UNIVERSITÉ DE STRASBOURG

ÉCOLE DOCTORALE DES CIENCES CHIMIQUES (ED 222)

Institut de Chimie et Procédés pour l'Energie, l'Environnement et la Santé

(ICPEES/CNRS UMR 7515)

THÈSE présentée par :

Francisco Javier IVAÑEZ CASTELLANO

soutenue le : **15 Septembre 2022**

pour obtenir le grade de : **Docteur de l'université de Strasbourg**

Discipline/ Spécialité : Chimie

Ru based photothermal catalysts for formic acid dehydrogenation and CO_2 methanation

THÈSE dirigée par :

[M. KELLER Nicolas]	Directeur de recherches CNRS, ICPEES, CNRS/Université de Strasbourg

RAPPORTEURS :

[Mme. EPRON Florence]	Directrice de recherches CNRS, IC2MP, CNRS/Université de Poitiers
[M. SCHNEIDER Raphaël]	Professeur, LRGP, CNRS/Université de Lorraine

---

AUTRES MEMBRES DU JURY :

[Mme. IGLESIAS JUEZ Ana]	Instituto de Catalisis y Petroleoquimica Investigator, ICP-CSIC, Madrid
[M. VERBRUGGEN Sammy]	Associate Professor, University of Antwerp
[M. KHODAKOV Andrei]	Directeur de recherches CNRS, Unité de catalyse et chimie du solide, CNRS/Université de Lille

ACKNOWLEDGMENTS

These 4 years of work could not be possible without the help of my BCFs: Marie, Maria, Clement, Marvin, Flo, JP, Xi, Leila, Justine, Nina, Maël, Caro and more people that have been part of the best photo-team in the world.

The beginnings in a new environment are not easy, when I felt the loneliest ever they came like a ray of sunshine: Fedyr, Anastasia, Rosanna and Alessia. Thank you for wonderful company (and for the shushi dinners).

I cannot forget the wonderful crew that I met in this journey. They are still part of my life even they left from Strasbourg: Irene, Elena and, of course, Patri. So many days (and nights) at Berthom that I will not forget. Thanks also to Thomas, Claire, Julien, Loïc. Special mention to Magdalena Brezinska. Despite she was not always in Strasbourg, she was present in my life.

Thanks to the Spanish speaker community: Camila, Wenziz, Marta, Jorge and Julia. You made me feel like at home.

Thanks to Vaso, Thierry Dintzer, Fabrice Vigneron, Sécou, Alain, Christophe Melart, Christophe Sutter, Valérie Caps, Valérie Keller, Dris Ihiawakrim and the rest of people who, somehow, have been part of this thesis too.

Thanks to the Initiative d'Excellence and International Doctoral Program for the PhD funding. Thanks also to Nicolas Keller for the supervision of this thesis, his endless patience and adaptability to make my study here much easier.

Last, I would like to dedicate some acknowledgments words to my family. Especially to my little sisters who I cannot be more proud of them. Thank you for your support and understanding.

Last (this time for sure), this thesis could not be possible without the support, strength, patience and love of Sara. Even with the distance, she was so close. If I achieved this is because she was there, all this time. Thank you for everything.

"Píntalo todo de negro
Cuando busques una luz

Restos de clavos ardiendo
Interminable cielo azul

Marineros del destierro
No dejéis de navegar

Por los que se fueron
Pero están"

Nubes Negras, La M.O.D.A

Table of contents

Introduction

During the last decades, environmental and energy issues increased in interest due to the global warming and climate change associated to the CO_2 emissions, as well as to the depletion of fossil resources. Therefore, the chemical and energy industry needs to address that societal concern in terms of process sustainability and must operate a difficult albeit vital environmental and energy transition from fossil-based resources towards a sustainable, environmentally benign chemicals and energy economy. This policy aims at reducing the fossil fuels dependency and at moving gradually towards a neutral carbon economy

Heterogeneous catalysis can be considered as the science of saving material and energy in chemistry. It is playing a pivotal role to find sustainable and greener pathways to supply energy (fuels) and to produce chemicals with the necessary reduction of the environmental and energetic footprint, with the highest atom efficiency. Heterogeneous photocatalysis emerged in the last decades as a valuable approach to provide sustainable reaction conditions for selectively driving chemical reactions in various environmental or energy-related fields.

However, heterogeneous photocatalysis demonstrated lower production or conversion rates than traditional (thermal) catalysis, what is unfavorable to its application in a wide span of fields, and especially for the chemical industry. Nevertheless, photocatalysis is a process that works at room temperature and demonstrated to be efficient in more sustainable conditions than (thermal) catalysis. In the recent years, the strategy of combining a dual photonic and thermal excitation in a one pot operation emerged for lowering the temperature conditions and enhancing sustainability of processes, increasing the reaction rates and potentially also orientating the reaction selectivity. This approach opened the door to a new field of heterogeneous catalysis, namely photothermal catalysis.

Photothermal catalysis is in consequence an emerging field that can be considered as one of the most promising and sustainable tools to reduce the carbon footprint in the energy and chemical industry. It consists in a simultaneous photonic and thermal activation (light and heat) of a photosensitive catalyst (i.e. light-responsive). Most of the systems rely on semiconductor materials, mostly decorated with metal nanoparticles. Any positive photothermal effect relies on a synergy potentially resulting from a combined (dual) activation of the catalyst that impact the (photo)catalytic behavior and modify catalytic reaction at the surface.

The main objectives of this thesis were first to demonstrate the ability of Ru-based catalysts to be used as photothermal catalysts under UV-A light for two gas-phase reactions of interest, namely the formic acid dehydrogenation to form hydrogen as main reaction and second the hydrogenation/methanation of CO_2 (Sabatier reaction). We aimed in consequence at obtaining a proof of evidence of a beneficial photothermal effect under UV-A light for both reactions, and to get better understanding to which extent the properties of the supported Ru catalysts can influence the photothermal behavior and the associated reaction mechanisms taking place under combined photonic and thermal excitation. Our objective was to pave the way for further studies and the development of novel photothermal catalysts.

This thesis was funded by the *Initiative d'Excellence* program (IdEX) of the University of Strasbourg. This work was realised at the *Institut de Chime des Procédés pour l'Energie, l'Environnement et la Santé* (ICPEES, UMR 7515 CNRS/University of Strasbourg, Strasbourg, France) under the supervision of Dr. Nicolas Keller.

This PhD thesis manuscript will consist in three main parts in regards to the catalysts used for both reactions of interest. As a result, this thesis is divided in five chapters:

The first chapter is a literature review devoted to the main contextual and topical aspects of this work in the field of photothermal catalysis. In the context of such an emerging field in heterogeneous catalysis, this chapter will describe to which extent photothermal catalysis derived from heterogeneous thermal- and photo-catalysis, with a series of definitions and principles brief description of both catalyses, as well as of the emerging field that is photo-thermal catalysis. The different strategies employed in photothermal catalysis depending on the energy sources are described and related to the catalyst design. The different methodologies reported for distinguishing electron- from thermal-driven mechanisms are summarized as well as the reactor aspects. Selected applications of photothermal catalysis are described, with a focus on formic acid decomposition and CO_2 methanation as reactions of interest and on the catalysts used. The chapter will conclude with a rational for the selection of Ru/TiO_2 as the reference photo-thermal catalyst in this work.

The second chapter will consist in the description of the main experimental procedures implemented during the thesis. This includes a description of the set up built and used for both photothermal formic acid decomposition and CO_2 methanation reactions together with the reaction protocols and the way of calculating the catalytic indicators. It is followed by a description of the different characterization techniques that are used in this work. The last part of the chapter will be devoted to the synthesis methods applied for the elaboration of the catalysts presented in this document and used for both reaction of interests.

The interest of using Ru/TiO_2 as photothermal catalyst under UV-A light will be first addressed in the third chapter, taking the gas-phase formic acid decomposition toward hydrogen (dehydrogenation) as first key-reaction. The Ru/TiO_2 catalyst prepared through a UV-A driven photo-assisted synthesis method will be used as reference catalyst. The catalytic behaviour will be discussed notably in terms of formic acid conversion, H_2 and CO production rates, as well as reaction selectivities. Screening additional studies varying the Ru content and the preparation method will be presented to improve the understanding of the Ru/TiO_2 systems under combined photonic/thermal excitation. The last part of the chapter consists in in-situ spectroscopy experiments conducted for getting knowledge on the possible mechanisms taking place at the surface of the Ru/TiO_2 catalyst in photothermal conditions.

Based on the results shown on the Ru/TiO_2 reference photothermal catalyst in the chapter three, the fourth chapter will examine the influence of the catalyst support in the (photothermal) formic acid decomposition reaction under UV-A light on different Ru-based catalysts. $g\text{-}C_3N_4$ and SiO_2 will be selected as supports of interest for the Ru nanoparticles. The main physico-chemical characterization of the catalysts are presented, as well as their catalytic behaviour at dark and illuminating conditions. The last part of the chapter will include the study of the in-situ infrared spectroscopy to highlight the differences in terms of reaction mechanisms under UV-A light for the hydrogen production for the three kinds of catalysts.

The fifth chapter will consist in investigating the ability of the Ru-based systems to be also used as photothermal catalysts under UV-A light in a second reaction of interest, namely the CO_2 methanation reaction. First, methanation experiments are conducted using Ru/TiO_2 as reference photothermal catalyst, before the investigations are extended to $g\text{-}C_3N_4$ and SiO_2 supported Ru catalyst. Using a span of commercially available titania materials, the last section will evidence the influence of the nature of the TiO_2 used as support for the Ru nanoparticles in the reaction in photothermal conditions, also with the help of an in situ DRIFT spectroscopy study for mechanistic aspects.

The final chapter of this thesis will be a general conclusion, with the main results obtained in these

investigations. Some perspectives and the possible future developments open by this work (some having been already successfully conducted but not reported in the PhD manuscript) are presented.

CHAPTER 1: Literature review

During the last decades, environmental and energy issues increased in interest due to the global warming and climate change, as well as to the depletion of fossil resources. The onset of the 3rd Millenium is already notable in regards of meteorological extremes, harbingers of anthropological climate change caused beyond a reasonable doubt by accumulating levels of atmospheric greenhouse gases, principally, carbon dioxide. Important agreements have been achieved like Kyoto Protocol (1997), Paris Agreement rulebook (2015) or Last UN Climate Change Conference (COP26) in 2021 where over 190 countries agreed to reduce the fossil fuel dependence, heading to a clean energy transition. The chemistry field and notably the chemical industry need to address those societal concerns in terms of clean chemical processes, environmental protection and energy transition. A difficult albeit vital transition must in consequence be made from fossil-based resources towards a sustainable, environmentally benign chemicals and energy economy. These objectives are based on concepts such as a neutral carbon economy where the undesired product is the promising reactant, reducing thus greenhouses gases emission and fossil fuels dependence.

To this end, heterogeneous catalysis, which is the science of saving material and energy in chemistry, is playing a pivotal role to find sustainable and greener pathways to supply energy (fuels) and to produce chemicals with the necessary reduction of the environmental and energetic footprint, and the highest atom efficiency. In parallel, heterogeneous photocatalysis appeared in the last decades as a valuable approach to provide sustainable reaction conditions for selectively driving chemical reactions in various environmental or energy-related fields.

This introductive chapter is divided into eight sections, with first a brief description of heterogeneous photo and thermal catalysis, followed by the definitions and principles of the emerging field that is photo-thermal catalysis. A third section describes different strategies employed in photo-thermal catalysis depending on the energy sources to catalyst design, while the potential methodologies to identify mechanisms in photo-thermal catalysis are summarized in the fourth section and reactors aspects are considered in the fifth section. A sixth section is devoted to some selected applications of photo-thermal catalysis, namely the reforming of oxygenates into hydrogen-rich mixtures and the CO_2 conversion, while a specific focus is made in the seventh section on formic acid decomposition and CO_2 methanation. Finally, the last section is the rational for the selection of Ru/TiO_2 as the reference photo-thermal catalyst in this work.

1. Heterogeneous photocatalysis and thermal catalysis.

Thermal and photo excitations have been perceived generally as different alternatives in overcoming activation energy barriers and driving reactions. Meanwhile thermal catalysis need a temperature increase to be activated, photocatalysis differs and may provide new routes at ambient conditions allowing for a saving in the process energy demand. The idea of combining both excitation processes in a unique catalyst to improve activity and reaction selectivity to desired the reaction products is a motivation for the research and development field, aiming at finding a catalytic solution able to accelerate the rate-determining step (rds) within a multiple elementary steps process.

1.1. Heterogeneous thermal catalysis

Nowadays, catalysis is involved in 95% of the manufactured chemical products [1]. This scientific discipline has been recognized and developed for many applications in the last centuries. Heterogeneous catalysis has been gradually improved in regards of characterization techniques [2] and of materials design, starting from metal powders to highly dispersed catalytically active components on high surface/porosity materials. However, traditional heterogeneous catalysis has limitations in being an efficient process in terms of activity and selectivity.

Most of the heterogeneous catalysts requires extreme conditions of temperature and pressure to carry out catalytic industrial reactions (with rare exceptions), requesting high process energies. The reaction conditions are in consequence often introducing un-wanted side-reactions detrimental to the reaction selectivity as well as to the catalyst activity and stability (e.g., coking, inhibitor poisons, and/or irreversible changes in the physico-chemical properties of the catalysts). Beside selectivity concerns, reversible or irreversible on-stream deactivation can be observed, while the process downtime for the regeneration/replacement of the catalyst is at the expend of a lower process sustainability.

1.2. Heterogeneous photocatalysis

In comparison with thermal catalysis, photocatalysis is a recent discipline in the chemistry field, capable to drive thermodynamically uphill reactions and to orientate reactions towards added-value molecules and high-prospect energetic compounds like hydrogen, as well as to drive degradation (environmental) reactions under soft/mild conditions. According to its restrictive definition (i.e. non IUPAC), heterogeneous photocatalysis is based on the absorption of photons by solid semi-conductor materials that promote electrons, also named hot electrons, from the valence band to the conduction band via photo-excitation processes when the photon energy is equal or higher to the semiconductor bandgap. The promotion of an electron generates a charge deficiency at the valence band also named as hole. Such hot carriers can interact with adsorbates after migration to the material surface where they drive reduction/oxidation reactions (**Fig. 1**) [3].

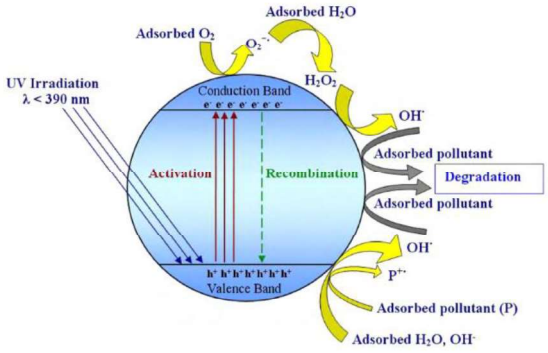

Fig. 1 *Generation of photocatalytic species in TiO2 semiconductor adapted from ref [3]*

The key limitation of this greener and sustainable process relies on the maximum optical power as natural solar insolation is around 1kW m^{-2} and on the need of high energetic photon flux utilization due to the large bandgap of the semiconductor materials currently used in photocatalysis. These limitations hinders its practice for industrial applications where the catalytic properties associated to selectivity, conversion and stability patterns plus a realistic space velocity is more than mandatory. Important progresses in the material science and engineering field led to the exploration of new

materials and hybrid assemblies, aiming at improving several properties like the absorption rate, the charge separation efficiency, the hot carrier lifetime or the sensitization of catalysts to the visible-light range, which accounts for around 50% of the solar light spectra.

1.3. Dual-mode excitation

Therefore, the strategy of coupling both photonic (solar) and thermal excitations in a one-pot operation (i.e. dual thermo/photo excitation) is logically aimed by the potential benefits of such synergetic systems in multiple catalytic applications, with enhanced activity and selectivity patterns. The aim is driven by the imperative of improving the chemical process sustainability with the lowering of the environmental and energetic footprint. This motivation is concretely materialized by the need of obtaining the same product yields at a lower temperature or more globally under milder conditions (softening of the reaction conditions), of accelerating the reaction rates under given reaction conditions for increasing production yields and reducing the processing times, and/or of orientating the reaction selectivities. Additionally, prolonging the lifetime of the catalyst is also a potential positive side-effect of the softening of the reaction conditions.

2. Photothermal Catalysis: definitions and principles.

In the last decade, research groups started to investigate the combination of a photo-excitation with temperature to probe the catalytic behaviors. This mixture of photo-excitation and thermal effects has not a “standardized” terminology yet and is not fitting with the ancient definitions of photocatalysis and thermal catalysis. Up to now, several very different phenomena were associated to the same terminology under the ‘photothermal’ umbrella, what can generate misunderstanding in the field. For example, Ghoussoub et al. (G. Ozin’s group) refers the photo-thermal term as the synergetic effect of simultaneous illumination under heating process [5]. Tang et al. associated photo thermal catalysis to a thermal acceleration of a photocatalytic reaction and to the photo-enhancement of a thermocatalytic reaction [6]. Nair et al. (Colmenares, Fernández-García and Luque) prefer to discriminate between photo-thermo-catalysis and thermo-photo-catalysis terms, where the first descriptor refers to a photo-effect on thermal catalysis and the second to a thermo-effect on photocatalysis [7]. In fact, the thermo- prefix is suitable for catalytic systems driven by heat to overcome an activation barrier, meanwhile the photo- prefix reveals more complexity because it strictly depends on the different reactions mechanisms involved, frequently unknown or ill-understood. Nair et al. summarized the key significance of their approach (howsoever named) as the implementation or exploitation of a ‘synergy between photocatalytic and (thermal) catalytic processes. From another perspective, Wang et al. (J. Ye’s group) concrete “Photo-thermal” as the localized heating process resulting from light absorption followed by a non-radiative relaxation [8].

Therefore, it is mandatory to search for and to adopt definitions able to take into account the different phenomena involved in photo-thermal catalysis and in the photo-thermal effect.

Kinetically-speaking, different synergistic (cooperative) effects that can operate under combined excitation in photothermal catalysis, may be distinguished through kinetics experiments :

- Type I. Meanwhile a reaction is driven by photo-excitation process through a low-energy transition state, thermal excitation is oriented to the “rds” of the dark type in the same overall sequence. In this case, the apparent activation energy (E_{app}) is expected to be lowered.

- Type II. The photo-excitation affects the steady-state equilibrium and modify the surface coverage by the intermediates species. This can be translated to an improvement of the rate due to a higher supply of the limiting reactant(s) on the catalytic surface or to the suppression of accumulated catalyst poisons. In this situation, no apparent activation energy change is expected.

- Type III. In this last scenario, the photo-excitation acts as a delivery mechanism of localized heat (via non-radiative relaxation process) and provides additional heating to the base (bulk) temperature, for a thermal catalytic process. It is important to mention that the apparent activation energy is not expected to be modified in this type.

Type III collects every process where photo-excitation is converted into an increase of temperature, in consequence supplying thermal energy as an internal source. Thus, several routes can be utilised in the photo-thermo catalytic process to provide thermal energy, by contrast to the light source, which is always an external irradiation (energy) source, either natural (sun) or artificial (UV lamps):

- through traditional heating by conventional operations, viz., conductive/convective transfer modes from reactor walls.
- by "optical heating", with the illumination of a light-absorbing component that dissipates thermal energy into the surrounding media due to non-radiative relaxation mechanisms of hot carriers generated by photonic energy absorption, also defined as *photothermal* effect. In that latter case, the thermal energy is supplied as internal energy source.

To sum up, photo-thermal catalysis is a combination of dual photo and thermal excitation in one pot operation where photo and thermocatalytic processes coexist to provide a synergetic effect over the different mechanisms and kinetics that are involved in the chemical reactions. However, it is important to remark the need of a classification of the different strategies where the photo-thermal effect is directly influenced by several factors such as the light source, the nature of the materials, etc.

3. Strategies in photo thermal catalysis: from energy source to catalyst design.

The essential property of a photo-thermal catalyst is that, at least one component must interact with light. Starting from this point, any design strategy must study the impact of photo-excitation with simultaneous heat.

It is possible to classify the different strategies according to a wide span of possibilities. For instance, Ma et al. classified the photo-thermal synergistic modes into 4 categories depending on the different contributions of both photo and thermochemical processes [9]:

- Thermal-assisted photo catalysis (TAPC) corresponds to the enhancement of photocatalytic processes by temperature increase,
- Photo-assisted thermal catalysis (PATC) where the light improves the thermal catalysis process,
- Photo-driven thermal catalysis (PDTC) is based on the photon-induced process to convert light energy to localized heat and drive thermal catalysis.
- Finally, photo-thermal co-catalysis (PTCC) where both photocatalysis and thermal catalysis coexist enhancing a higher conversion than the sum of them dividedly.

However, this kind of classification can be at the end quite chaotic, because of the similar names the strategies have and the overlapping between different groups in some situations. *Thermalization* process via photon absorption is part of the non-radiative decay phenomenon of excited electron-hole pairs. However, these charge carriers also can interact with molecular orbitals of the adsorbate at metal-adsorbate interface, promoting the conversion of the adsorbate into other chemical species. Both processes are commonly occurring simultaneously, what makes difficult to differentiate between them. Even thermalization (PDTC) can enhance the photocatalytic processes via an increase of the local temperature (TAPC). Then, there are some situations were several categories can co-exist simultaneously and this classification will not be suited. Therefore, to be able to classify several strategies that can be used simultaneously to perform photo-thermal catalysis, we propose a classification that depends on the different indirect and direct energy sources used. There are 3 different possibilities on how light and thermal energy sources can be combined:

- Unique photonic and thermal energy suppliers: The strategy consists in the use of a unique energy supplier that can provide photonic and thermal energies (such as sun or simulated solar light source), as it is shown in **Fig. 2**A. High energy photons (UV-Vis) interact with the photo-thermal catalyst with the promotion of hot carriers, while low-energy photons (Vis-NIR) increase globally the temperature at the catalytic surface. In this case, the global temperature is controlled and limited by the optical power and dispersion of the light source (filters, monochromatic devices, etc.). Nonetheless, optimizing the reactor design can enhance the temperature increase, notably through suited solar concentrators [10].

- Distinct photonic and thermal energy suppliers: This strategy (see **Fig. 2**B) is similar to the previous one with the exception that globally the temperature is not dependent on the light irradiance but can be better adjusted by conduction and convection processes from the reactor walls to the place where photo-thermal catalyst is located.

- Internal heat source by photon-flux irradiation (see **Fig. 2**C): As it has been previously described, some materials can increase the local temperature by non-radiative relaxation process after photon flux absorption [11]. In this case, the thermal energy source comes from the interaction between the materials and the photons. Under steady-state photon irradiation, a heat gradient will be established at the catalytic surface that depends on the thermal (diffusion) properties of the catalyst and the reactants. To ensure photo-thermal light-to-heat efficiency, mostly plasmonic nanostructure materials have been reported. However, it is important to mention the ability of several non-plasmonic materials to generate an increase of temperature.

Nevertheless, it is mandatory, before to distinguish among all the photochemical and thermochemical processes that can occur simultaneously or cooperatively and which are predominating in each photo-thermal reaction, to identify the different interactions that the catalyst can have with photons. Therefore, the next part of the section includes a classification based on the photonic properties of the materials (plasmonic, non plasmonic) and on their nature (noble and non-noble metals, metal oxides, etc.), that takes into account the phenomena associated with and arising from the absorption of the photon energy.

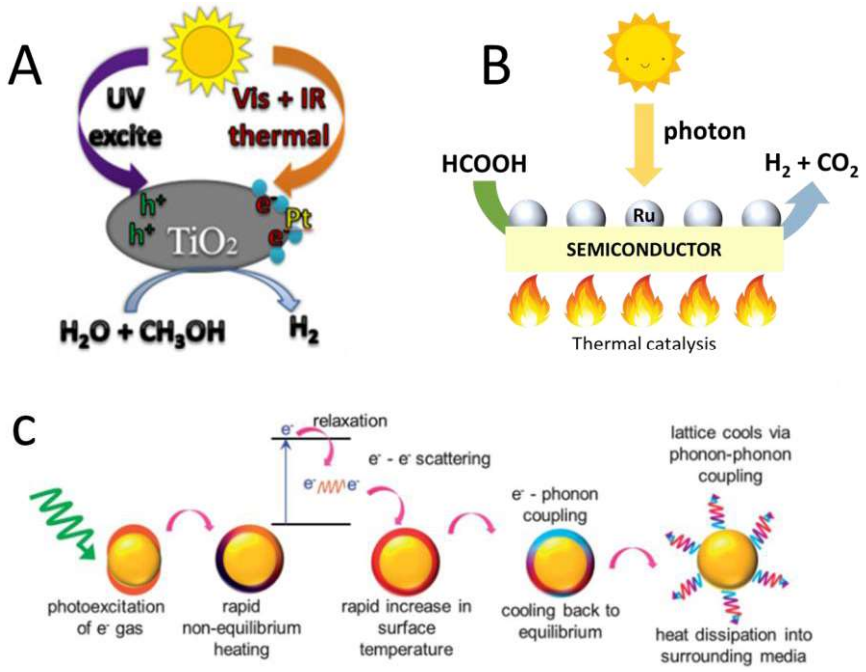

Fig. 2 *(A) First strategy with a unique photonic and thermal energy supplier, adapted and reproduced from ref [10], (B) second strategy with distinct photonic and thermal energy suppliers, and (C) third strategy with internal heat source by photon-flux irradiation, adapted and reproduced from ref [15].*

3.1. Plasmons and plasmonic materials for photothermal catalysis: Mechanisms.

The physics of the localized surface plasmon resonance (LSPR) phenomenon has been introduced through Gustav Mie and Drude-Maxwell models in 1908 [12,13]. According to these theories, free metal electrons can oscillate against a background of positive ion cores under the influence of the electromagnetic field of an external incident photonic irradiation. This produces an electron cloud as the sum of all the individual electron motions. This collective electron oscillation on the metal is named as surface plasmon [14]. Normally, the plasmon frequency, ω_p, is given by equation 1.1:

$$\omega_p = \left(\frac{Ne^2}{\varepsilon_0 m^*}\right)^{1/2} \qquad (1.1)$$

Where N is the density of charge carriers, m* their effective mass, e the electron charge and ε_0 the electric permittivity. In a metal nanoparticle surface, electrons are confined in a very limited area where the incident wavelength is larger than the nanoparticle size. Then, all electrons are subjected to the same electromagnetic field producing a positive and electron region as shown in **Fig. 3** [15]. In addition, if the incident electromagnetic field and the mode of electron cloud resonance oscillate at the same frequency, strong electric fields are created by the interaction of the resonant photons and the electrons on the metal surface. The amplification of these maximized local electric fields is named as “plasmonic hot-spots” and it has been widely studied for several applications such as biomedicine, raman and photocatalysis.

However, the plasmonic effect is not only related to the metal nature. Morphology properties like shape [16] and particle size [17], as well as the metal environment (dielectric constant), can also strongly influence the photon absorption properties by widening or narrowing the absorption range, modifying the plasmon intensity to lower values and blue or red-shifting maximum absorption peaks.

Several processes must be taken into account following the excitation:

- First, the energy stored by plasmons can decay as radiative process that emits photons with same wavelength as the resonance conditions.

- Secondly, the decay can occur through non-radiative processes: Electron-electron collisions, that increase the temperature [1], and electron-hole pair excitations. In this last process, the absorbed photon energy is used for the excitation of the ground state level electrons of the metal, with the associated formation of holes. Then, electron and hole can interact with the adsorbate to carry out photochemical reactions or they can "thermalize". Thermalization is the process where the charge carriers recombine after the electron promotion via electron-electron scattering that increase locally surface temperature, as shown in **Fig. 2**C, followed by electron-phonon scattering and lastly with phonon-phonon scattering that dissipates the thermal energy through the lattice.

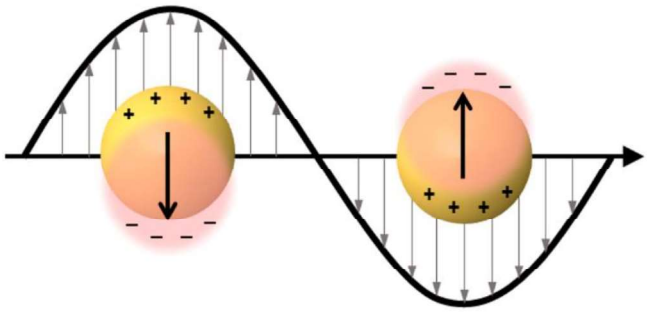

Fig. 3 Scheme of coherent localized oscillation of the electron density over the influence of an electromagnetic field on spherical plasmonic nanoparticles, from ref 18.

Charge carriers in plasmonic materials have several pathways where they can migrate or recombine depending on the metallic surface. There are three different scenarios: clean metal, metal/adsorbate and metal/semiconductor.

In a clean metal surface (see **Fig. 4**A), hot carriers are induced (photo-excitation) in a non-thermal distribution. Then, charge carriers can recombine (relaxation) generating inelastic *coulombic* electron-electron scattering, converting energy into heat in a 100 fs to 10ps period. At a different timescale, (low energy) electrons-lattice collisions increase the temperature of the metal lattice by the coupling of electrons and phonon modes. Then, heat is spread over the lattice via phonon-phonon scattering in

a period of 100 ps to 10 ns (see **Fig. 5**A), producing the *thermalization* process. This thermalization pathway has been already analyzed for potential application in cancer therapy [11,18]. However, in photocatalytic reaction conditions, other parameter can affect in this process like the presence of adsorbates on metallic surface.

In the case of metal/adsorbate systems, as shown in **Fig. 4**B, electrons can migrate from metal NPs if there is an electron-accepting orbital. In fact, reactants can be adsorbed at the metallic surface allowing electron migration from metal to the lowest unoccupied molecular orbital (LUMO) via direct or indirect transfer [15]. For an indirect transfer, hot electrons are first promoted in the metal nanoparticle and further transferred to the unoccupied molecular orbitals of the adsorbed molecules. On the contrary, if there is a strong interaction between the adsorbate and the metal, hot electrons can be directly generated at LUMO (electron-accepting state) of the adsorbate molecule by an additional dephasing channel called chemical interface damping (CID), induced by the coupling of unpopulated adsorbate states and excited surface plasmons (direct transfer)[15,19]. It is important to remark that only direct transfer really needs a strong orbital hybridization between the adsorbates and the metallic surface, which makes the indirect migration more favorable. Hot electrons can also thermalize through chemical interface scattering (CIS) where electrons scatter into and out of nearby unoccupied electronic states introduced by the coupling. In addition, hot electrons can deposit part of their energy at adsorbate molecular orbital. This remaining energy affects to the adsorbates that acquire a vibrational energy level higher than the equilibrium state, also named as hot adsorbates. These hot adsorbates can use their energy state level to overcome the reaction barrier and be converted into products at the metal surface. Otherwise, this energy can be also recovered back by the electrons when they are transferred back to adsorbate molecular states prolonging the time needed for thermalization processes (**Fig. 5**B) [1,9,15,19–21].

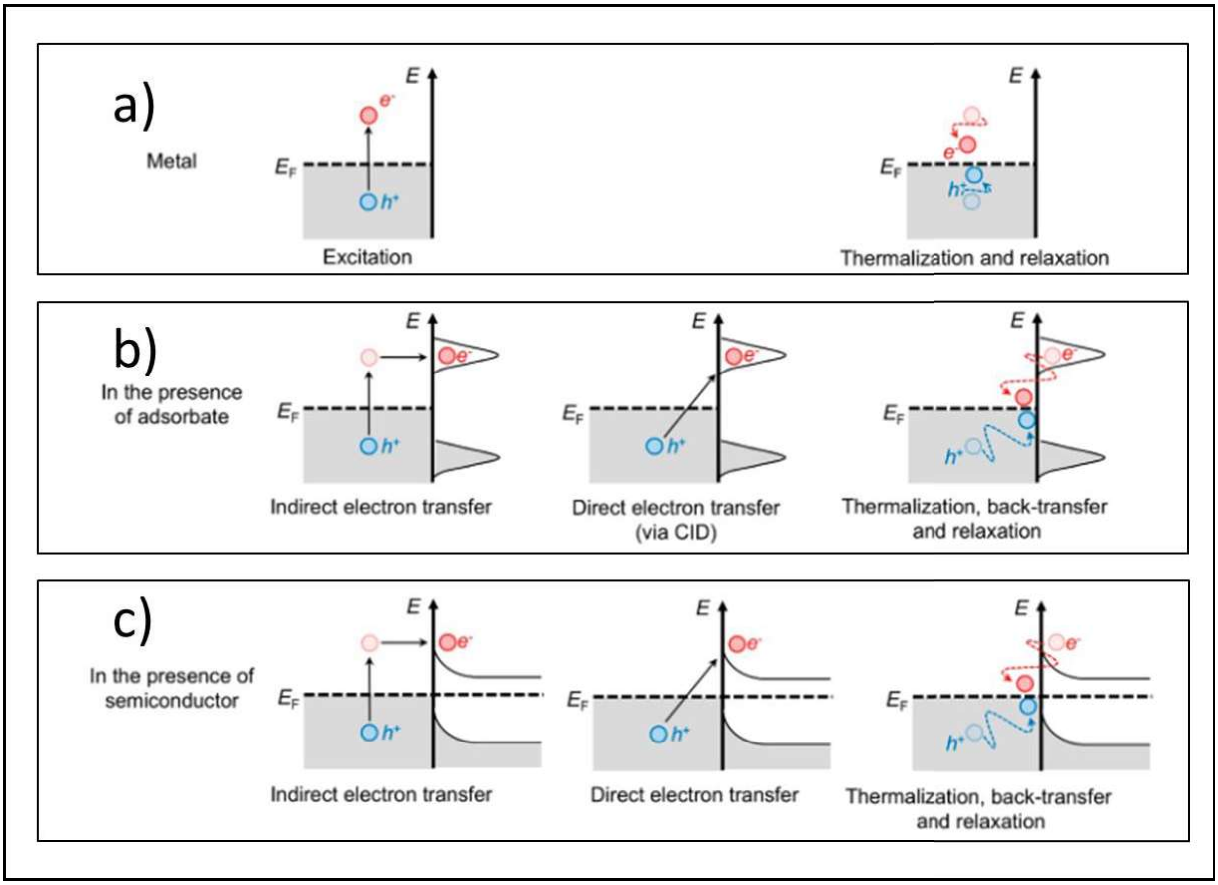

Fig. 4 *Hot carrier generation via plasmon-induced process and transfer/back-transfer processes of hot electrons and holes in different scenarios.*

A) *clean metal,*
B) *metal/adsorbate,*
C*)* *metal/semiconductor.*

In each scheme, the left side (relative to energy, y-axis) depicts the Fermi level (E_F) of the plasmonic metal. The right side (relative to energy y-axis) illustrates the highest occupied molecular orbital (HOMO) and the lowest unoccupied molecular orbital (LUMO) for the adsorbate (b), or the position of both conduction and valence bands of the semiconductor. The grey parts represent the population of electronic states. Figure based on ref [15].

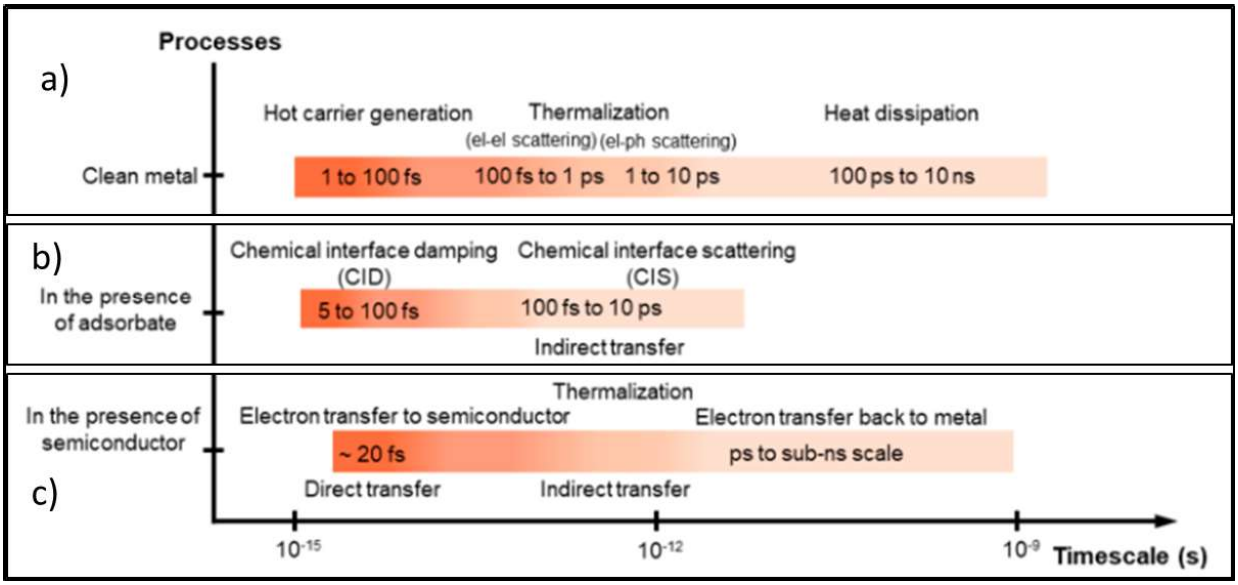

Fig. 5 *Time scales of the plasmon-induced hot carrier generation, the hot electron transfer, and the thermalization processes in the case of a clean metal NP as well as in the presence of an adsorbate or a semiconductor. From top to bottom: a series of time scales corresponding to the fate of hot carriers in a clean metal NP, additional events in a metal NP capped with an adsorbate, and the processes involved in a metal NP loaded on a semiconductor support via a Schottky contact are shown. Note: el stands for electron and ph stands for phonon. Figure based on ref* [15].

In the last scenario with a composite metal/semiconductor (**Fig. 4**C), hot electron migrates from the metal to the SC conduction band by indirect or direct transfer, as it occurs with adsorbates. In this particular case, the spatial separation between the holes (in the metal) and the electrons (in the semiconductor) prevents from charge carrier recombination and prolongs the electron lifetime to carry out chemical reaction at the catalyst surface [22]. When a junction between the semiconductor and the metal nanoparticle is formed, both materials Fermi levels align to enhance the charge redistribution. This valence and conduction band bending create the Schottky Barrier at the interface (SB), whose energy can be measured as the difference between the metal Fermi level and the conduction band at the semiconductor/metal interface.

When an electron is photo-excited, it can migrate from the metal to the semiconductor conduction band if its energy is higher than the Schottky barrier (see **Fig. 4**C). This process is the indirect transfer pathway. In addition, an adequate Schottky barrier is highly important to enhance the electron transfer and to inhibit the transfer back to the metal nanoparticle, for guaranteeing the spatial separation of the electron-hole pair. White and Catchpole have calculated that an overall quantum efficiency in indirect hot electron transfer from plasmon metal to semiconductor material below 8% [23]. Several research groups have evaluated the possibility of a single-step electron transfer based on the hot electron transfer to the acceptor orbital in the semiconductor upon plasmon dephasing in hybrid materials [24,25]. In comparison with the hot carrier transfer from the metal to the adsorbate, this pathway is more efficient due to the absence of electron-electron and electron-phonon scattering within the metal nanoparticle [26]. Although different studies have been performed and different theories reported, it is important to mention that there is actually no current method to discriminate between the electron transfer mechanisms in metal/semiconductor heterojunctions.

Last advances in LSPR highlighted that not only metals can be plasmonic materials. Semiconductor nanostructures [27,28] and 2D materials can have a behaviour similar to plasmonic effect on noble metals. For instance, ReO_3 type oxides, telluride or nitride materials present plasmonic properties in the visible-NIR region[27]. LSPR can be tuned by modifying the charge carriers density of these materials via doping and/or creating structural defects, shifting the absorption spectra to higher energy values. 2D materials proved to have a tuneable LSPR effect like in the case of graphene [14,29], which plasmon is localized in middle IR and terahertz regions. The overall plasmonic response of 2D materials is weaker than that of metals because of the thin atomic dimension, but it can be enhanced by electrostatic or chemical doping techniques. Modifying the carrier concentration with external electric gates, the dispersion and lifetime of surface plasmon in two-dimensional materials can be adjusted [30–32].

3.2. Non-plasmonic materials for photothermal catalysis.

Even if plasmonic structures have been grown in interest for photo-thermal application during the last years, they are not the only kind of materials where charge carriers "thermalize" after photon absorption. As it was previously described, electron promotion in plasmonic materials derived from the plasmon energy non-radiative decay process. Non-plasmonic elements can promote electrons via photon absorption through interband electronic transitions without the need of a prior surface plasmon resonance [15,33]. Among this group, metals such as Pd [34] or Ru [35] have been the most widely reported. However, we can cite materials as varied as e.g. carbon-based materials [36–39], metal-organic frameworks (MOFs)[40,41] and metal oxides.

In case of non-plasmonic metals, the photo-excited hot carriers can be transferred from the metal surface to an accepting orbital if the electrons have the enough energy to be injected in, as it similarly occurs in plasmonic metal materials [34]. For instance, Sarina et al. studied Pd, Pt, Rh and Ir supported nanoparticles on ZrO_2 as photocatalyst for several reactions [33]. In those cases, rate enhancement with light irradiation is mainly assigned to electrons transfer from metal NPs to unoccupied molecular orbital of the adsorbates as it was described in **Fig. 4**C. In addition, the photon wavelength plays an important role in the electron transfer because the electron can promote to higher or lower energy state depending on the energy of the photon and, therefore, can overcome the energy barrier to be transferred into the adsorbate. For this reason, with a higher photon energy (short photon wavelengths), the excited electron overcomes the energy barrier to be injected into the molecular orbital of the adsorbate. However, the promoted electrons cannot have enough energy to overcome the energy barrier if they have been excited by photons with not enough energy (normally corresponding to longer photon wavelengths), which contributes to the enhancement of reaction rates by means of thermal effects. Nevertheless, it is exceptionally possible that two photons promote one electron that can be transferred to the adsorbate at higher photon wavelength and high irradiance conditions.

It is important to mention that metal nanoparticles can be used not as "electron source" but as substrate materials. In this case, direct photo-excitations occurs in the gas-phase molecule as shown in **Fig. 6**. When the molecule is adsorbed onto the metal surface it can be bonded by strong and weak interactions [42,43]. When the molecule is weakly chemisorbed, as shown in **Fig. 6**A, the primary mechanism to drive photochemistry is the intraband promotion of electrons from the highest occupied molecular orbital (HOMO) to the LUMO. In comparison with non-chemisorbed gas phase molecules,

slightly decreased excitation energies are needed due to metal-induced perturbation of the molecular electronic states. This electron promotion is characteristically dependent of the photon wavelength. Strong chemisorption occurs through hybridization of metal and adsorbate orbitals to form bonding and antibonding states [44]. Then, the photoexcitation is targeted to the transition of electrons from bonding states to antibonding ones. This photoinduced excitation generally carries out selective heterocatalytic processes.

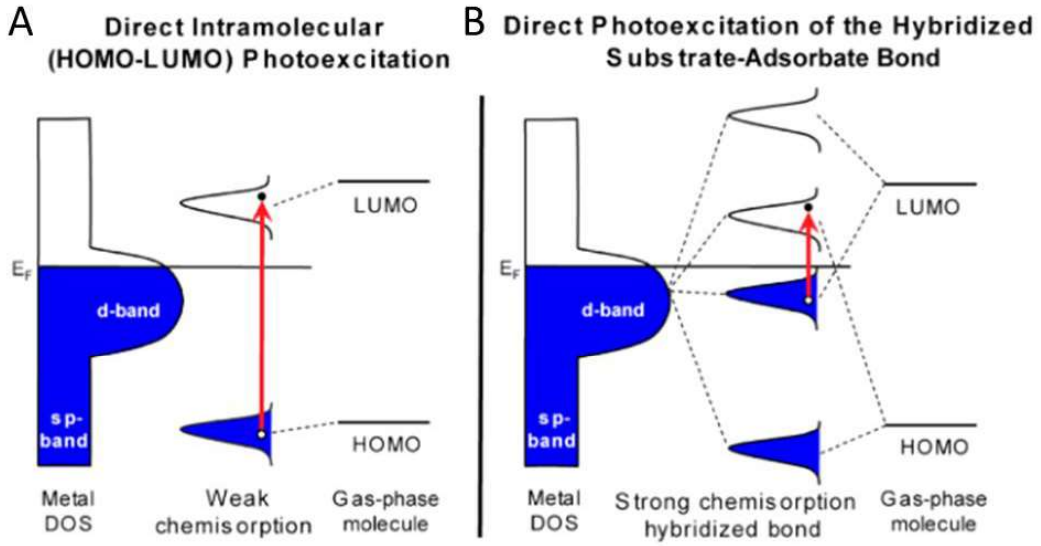

Fig. 6 *Schematic of the metal-adsorbate bond photoexcitation processes over metal surface adapted from ref* [44]. ***A)*** *Direct photoexcitation from the HOMO to the LUMO in the molecule when it is weakly chemisorbed with the metal surface.* ***B)*** *Direct photoexcitation of resonant hybridized bonds between metal and adsorbates when the molecule is strongly chemisorbed onto the metal surface.*

Metal oxide non-plasmonic materials can carry out photochemical process after charge generation. However, non-radiative decay compete with it. There are mainly two main possible recombination pathways in metal oxide non-plasmonic materials: Auger and Schockley-Read-Hall recombinations. Both are responsible of energy emission into the material lattice by phonon vibrations. The Auger recombination produces energy transfer, instead of light emission or heat dissipation, to a third charge carrier that thermalizes back emitting phonon vibrations in a scale of time from 10 to 100 ps [1,5]. The Shockley-Read-Hall recombination consists in two steps: first, a fast step where hot carriers thermalize back in a mid-gap energy state caused by defects and vacancies in the lattice. Then, a second step where the electron recombined at the valence band. When the charge carrier is at mid-gap state, its life-time is prolonged and it can interact with molecular adsorbates driving photocatalytic reactions [5,45].

To sum up, photo-thermal catalysis involves a broad range of materials that can absorb photo-irradiation to carry out photochemical and thermochemical reactions through different mechanisms and processes depending on their electronic properties and chemical nature. This diversity might provide promising results for catalysis and further applications like photovoltaics and solar thermal energy [46].

4. Methodologies to identify mechanisms in photo-thermal catalysis

Different computational and experimental methodologies can be used to distinguish between photochemical and thermochemical contributions in photo-thermal catalysis and to state which pathway drives mainly the process.

For instance, Density functional theory (DFT) framework is a computational quantum mechanical modelling method allowing for the investigation of the electronic structures of many systems, including here notably condensed phases (e.g. semiconductor/metal interface) or molecules (e.g. adsorbates at active sites).

Besides computational methodologies, the implementation of suited experimental procedures has been proved to be a powerful tool through the study of the influence of the light on photocatalytic systems, especially in plasmon-induced photocatalysis [47,48]. Those experimental procedures rely on:

- the implementation of specific reaction conditions for the catalytic tests. They are based on the identification of the electron-driven or thermal-driven processes through the modification of parameters such as light irradiance, photon-wavelength, and light beam radius or temperature.
- the use of external characterization technique setups like a spectrometer or a microscope in order to follow the features of the photo-thermal effect.

This section collects the main experimental methodologies that have been reported to distinguish between photo and thermochemical processes during photo-thermal catalysis.

4.1. Experimental conditions as methodologies.

The implementation of suited experimental conditions for the catalytic tests is a powerful tool for providing information about which process is dominant in photothermal catalysis. For example, a linear dependency between the reaction rate and the light intensity is sign of identity of an electron-driven process for plasmonic reactions [49–51]. The relationship between the reaction rate and the photon flux irradiance can be considered as representative of the electron-driven chemical transformations or the thermal enhancement at the catalytic surface. Four different kinetic regimes have been proposed by Christopher et al. depending on the relationship between the reaction rate and the photon flux irradiance [48]:

- Linear regime (rate $\propto$ I), shown in **Fig. 7** as blue line, is characteristic of electron-driven chemical transformations[49].
- Super-linear regime (rate $\propto I^n$, n>1)), shown in **Fig. 7** as red line, is also characteristic from chemical reaction driven by photo-generated hot carriers.[52]
- Sublinear regime (rate $\propto I^n$, n<1), shown in **Fig. 7** as green line, has only been reported in semiconductor materials and it corresponds to a high recombination of hot carriers[48].
- Exponential regime (rate $\propto e^{f(I)}$), shown in**Fig. 7** as violet line, corresponds to a thermally driven transformation [49,53].

Nevertheless, it is important to highlight operation conditions as a key-factor to determine the prevalence of each regime. For example, the Linic's group and Zhang et al. observed at higher light

intensity levels that the linear ("straight", constant slope) regime turned into superlinear. This behavior was ascribed in Zhang et al. to multiples excitations of the vibrational modes of adsorbed intermediates species by plasmon-induced hot electrons [49,52,54,55].

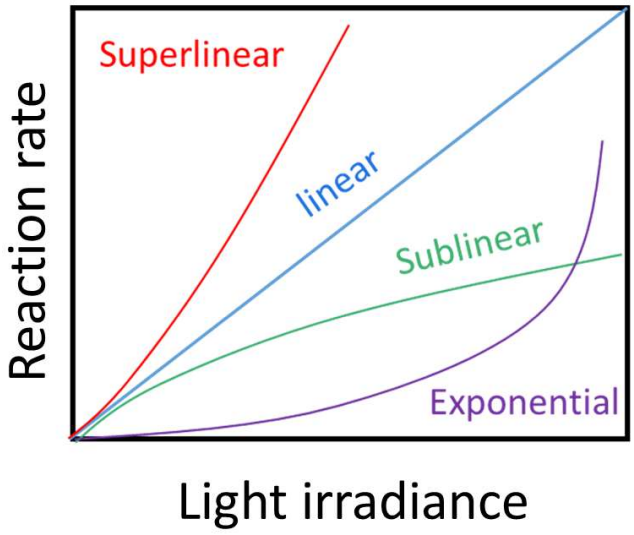

Fig. 7 *Linear (blue), superlinear (red) sublinear (green) and exponential (violet) regimes in the photon dependency of the reaction rate.*

In addition to the dependence with the light irradiance, an agreement between the action spectra of the catalyst (i.e. the wavelength-dependent reaction rate) and the absorption spectrum of the catalyst is also proposed as an evidence for electron-driven processes. As plasmonic and non-plasmonic materials can absorb photons with a determined wavelength to promote hot carriers, a variation of the photon wavelength within the UV-Vis-IR spectrum may provide useful information about which processes prevail over others if there is a correlation between the catalytic rate and the wavelength of the absorbed photons. For instance, Ye et al. studied the influence of the wavelength on the photo-thermal methanation with several supported metallic catalysts from group VIII [56]. No dependency of the CH_4 production rate on the photon wavelength was observed, so that they excluded any electron-driven mechanism and ascribed the photo-thermal enhancement to pure thermal effects. By contrast, the same group observed a direct agreement between the optical absorption spectrum of a Rh/TiO_2 catalyst and the quantum efficiency in the case of the photocatalytic steam reforming of methane, and suggested the role of the hot electrons from interband transition in the Rh nanoparticles [57]. Other groups [58,59] found also a correlation between the optical absorption of the photocatalyst and the reaction rate, in favor of electron-driven reaction mechanisms.

Both dependencies of the reaction rate with the wavelength and light irradiance might in consequence provide information on the hot electron-induced reaction mechanisms. Nevertheless, there are some controversial opinions in the field, arguing to which extent the direct implication of plasmonic hot-electrons in the drive of photo-thermal reactions is appropriately considered. For instance, Dubi and Sivan have done a theoretical study where only a small fraction of the catalytic rate was attributed to the generation of "hot-electrons" in plasmonic materials in comparison to the thermal-driven processes, and only an small part of the hot carriers in plasmonic materials are not thermalized and interact with the reactants [60]. Moreover, this group has compiled and re-treated

experimental data from other research publications (see ref [61,62]) according to their theoretical work. Of course, the relevance of these studies rapidly increases, and generates comments and additional discussion with researchers from the field [63,64].

Additionally, the analysis of selectivity patterns might be a way of evidencing the main pathway. Heat-mediated reactions lead to provide energy to all the different freedom degrees available, like vibrational, translational or rotational states, activating simultaneously many reaction pathways, while electron-driven processes may inject hot carriers to a selected adsorbate-metal bond modulating the reaction yield to a desired product [54]. In addition, it is reported by the Cronin's group that the selectivity in the artificial photosynthesis over Au/TiO_2 was influenced by the irradiation wavelength, and was switching from full CH_4 production to some derivatives like ethane, formaldehyde or methanol when the photon wavelength was lowered from 532 nm to 254 nm [65].

Alternative experimental procedures based on the variation of the light beam diameter have been proposed as useful tools to distinguish between the different contributions[66], following two different protocols: at a constant irradiance and by increasing the beam diameter with a proportional increase of the photon flux rate, or at a constant power while the photon flux irradiance keeps identical. Non-thermal and thermal contributions are proportional to the light beam radius when the photon irradiance is constant ; electron-driven processes rate has no relation with beam diameter at constant-power conditions and thermal driven reactions are inversely proportional to the beam area. Therefore, the bigger the beam radius is, the lower the local temperature. Thus, the variation of the beam diameter might appear to be successful to elucidate the underlying reaction mechanisms [66].

The determination of the Activation Energy can also provide valuable information on the reaction mechanism, and the activation barriers at illuminating and dark conditions can be compared. In general, a reduction of the activation energy is connected to a hot carrier driven-mechanism [54,57,67,68].

The implementation of isotopic labelling experiments was also reported as a suited strategy. Electron-driven processes can also have a significant effect with. Introducing labelled reactants as heavy isotopes results in a variation of the reaction rate in thermal catalysis, as a higher energy input is necessary for the heavy isotopes to reach the transition state. This gives rise to the kinetic isotope effect (KIE). Isotopic labelling can thus be a suited analytical tool for mechanistic studies, as electron-driven processes show higher KIE values (upon irradiation) than thermal catalysis (in the dark) [49,69,70]. This difference is obtained, because of the hot electrons, generated upon photon flux irradiation, that migrate from the metal to unoccupied molecular orbitals of the adsorbates. Then, they charge negatively the adsorbate that reaches a new equilibrium position. As the electron-residence time in the orbital is the same for both heavy and light isotopes, this pseudo-equilibrium position is different in lighter isotopes than in the heavier ones, because they are being accelerated faster and they tend to traverse longer distances. Once the electron is transferred back to the substrate, lighter isotopes are farer from their original equilibrium position. As result, they still conserve vibrational energy available for overcoming reaction barrier. Hence the higher KIE values. Therefore, comparing KIE values obtained upon irradiation and in dark conditions might be a good methodology to differentiate the different electron-driven and thermal-driven processes during photo-thermal catalytic reactions [49,57].

For instance, Linic et al. utilised labelled oxygen $^{18}O_2$ during kinetic isotope studies, hypothesizing that the O_2 dissociation over metal controls the overall catalytic rate for ethylene epoxidation on silver nanostructures [49]. They reported that, at steady state, the KIE effect (^{16}O rate/^{18}O rate) at 450K with light irradiation is higher than in dark conditions, with values of 1.19 ± 0.01 and 1.06 ± 0.02, respectively. They suggested that an electron transfer from silver to the antibonding O-O 2π' orbitals charge negatively the adsorbate, causing a change of the equilibrium position in favour of a larger O-O bond distance. During the electron back-transfer to the metal, additional vibrational energy remains in the O-O vibrational mode, what allows the molecule to react before the vibrational energy is dissipated, boosting in consequence the molecular dissociation of O_2 at a lower temperature than in dark conditions.

Interestingly, Fang et al. employed isotopic labelling experiments to explain the important H_2 production rate obtained from methanol/water mixtures under visible light irradiation (λ > 420 nm) over a Rh (1 wt.%)/TiO_2 (photo)catalyst at the temperature of 260°C compared to the corresponding rate value measured at room temperature [71]. The authors suggested that methanol, commonly used as sacrificial agent, was the main provider of H_2 at room temperature, while H_2 was mainly produced from water when coupling thermal and photo excitations. The same group explored a system consisting in NiO_x (metal core/oxide shell) on TiO_2 in the photo-thermal steam reforming of methanol, using Aeroxide TiO_2 P25 as support, with a final reductive treatment at 500°C under H_2 [72]. The optimal catalyst contained 5 wt.% Ni, and achieved a H_2 evolution rate of 54 mmol h^{-1} g_{cat}^{-1} under simulated AM 1.5 G sunlight at 260°C, 2.5 higher production than in dark conditions. In mechanistic investigations, isotope tracer experiments underlined that the enhancement of the H_2 production upon light irradiation was mainly by H-atom abstraction from water rather than dehydrogenation or reforming of methanol. Apparent quantum efficiencies (AQE) were wavelength-dependent, ranging from 66 % at 380 nm but falling to 15 % at 500 nm. Nonetheless, visible-light excitation still generated H_2 at a rate (27 mmol/h/g_{cat}) five orders of magnitude greater than at room temperature.

For the same photo-thermal reaction, Nikitenko et al. studied a metal-free Ti@TiO_2 core-shell catalyst, composed of 20-80 nm diameter quasi-spherical Ti particles coated by 5-15 nm crystals of defect-free anatase (with small amounts of rutile) [73]. Using isotopic studies with methanol-D_2O solutions, they proposed a mechanism involving a Ti inter-band transition followed by charge transfer to the semiconducting TiO_2 shell through the core-shell junction. The best catalytic performance in H_2 evolution from water, using methanol (25%) as sacrificial agent, was observed under the joint effect of Vis/NIR light, at an incident irradiance of 0.5 W/cm^2 (absorbed power = 0.38 W/mL), with mild heating at 60°C. The low value estimated for the apparent activation energy (17 ± 4 kJ.mol^{-1}) implied that the heating effect might be linked to a diffusional process (intermediate migration) as being rate-limiting. Nonetheless, since the oxidation (of methanol) was arrested at formic acid, the overall process appears as only *partial* reforming.

4.2. Experimental characterization techniques

In the previous subsection, several methodologies were discussed to provide useful information about photochemical and thermochemical contributions. However, external devices can be additionally used to characterize several features that are linked with electron-driven processes or

thermal surface enhancement. Globally, techniques based on microscopy, spectroscopy or luminescence have been reported as promising methods to distinguish both photo and thermochemical contributions.

The charge carriers, following their generation and recombination processes via the three different possible scenarios (clean metal, metal-adsorbate and metal/semiconductor), are characterized by their lifetime. Therefore, a study of charge carriers lifetime upon photo-irradiation at different photon wavelengths may suggest different photo and thermo-chemical processes. For instance, transient absorption spectroscopy (TAS) is a useful technique to study the dynamics of electron transfer phenomena. This technique consists on the study of the photo-generated excited absorption energies and corresponded lifetime of materials, molecules and devices. TAS can be used for metal-semiconductor materials at different wavelengths to observe the intensity of the electron transfer signal and the lifetime of the charge carriers, indicating several processes like successful migration of electron to semiconductor overcoming the Schottky Barrier or electron-hole recombination if the excitation energy of the photo-induced charge is not high enough. Ye and coworkers analyzed the ultrafast electron transfer from the metal to semiconductor material through the Schottky barrier in a Rh/TiO_2 catalyst upon laser excitation at 450 nm, what increased the hot carrier lifetime and consequently the possibility of an electron-driven reaction [57].

Direct, accurate and sensitive thermal measurements at the nanoscale at the catalytic surface (nanothermometry), are considered as high-prospect tools for discriminating between the thermochemical and photochemical contributions in photo-thermal catalysis processes. However, the development and implementation of such tools is still a highly challenging objective. They usually are itemized as non-luminescent or luminescent methods.

Among the different available tools, nanoscale probe tips for scanning thermal microscopy measure the surface temperature with a high spatial resolution in the range of 10 nm and a precision as good as 60 mK [74,75]. Also, scanning transmission electron microscopy (STEM) was used to obtain local temperature maps with a nanoscale resolution through the analysis of the temperature-dependent energy shift of plasmon peaks [76].

As Infrared (IR) thermography measures the temperature by detecting the energy emission of the sample, a thermal mapping by means of an IR camera can provide useful information about global and localized temperature at the catalyst surface. However, the low penetration of light and the non-uniform heat diffusion can lead to undesired temperature gradients [61,77].

Additionally, thermoreflectance and optical interferometry are methods using the light reflection for measuring the temperature, with a micro- and submicrometer scale, and with a high temporal and thermal resolution of about 10^{-1} μs and 10^{-2} K [78].

Photo-luminescence (PL) anti-Stokes (AS) nanothermometry is another useful technique to employ at the nanoscale. For instance, Barella et al. studied the photo-thermal response of a single Au nanoparticle by detecting the AS intensity variation under 532 nm laser irradiation through hyperspectral photoluminescence confocal images[79]. Using hyperspectral imaging (see**Fig. 8**A), they observed a linear dependency between the light irradiance and the local temperature (see **Fig. 8**B), with a photo-thermal coefficient (i.e. the slope) being influenced by the particle diameter and not by the external temperature (**Fig. 8**C). They showed further that the nature of the underlying support

(glass, sapphire, graphene) was influencing the photo-thermal coefficient, with apparently no predominant role played by the heat dissipation feature of the support (**Fig. 8**D).

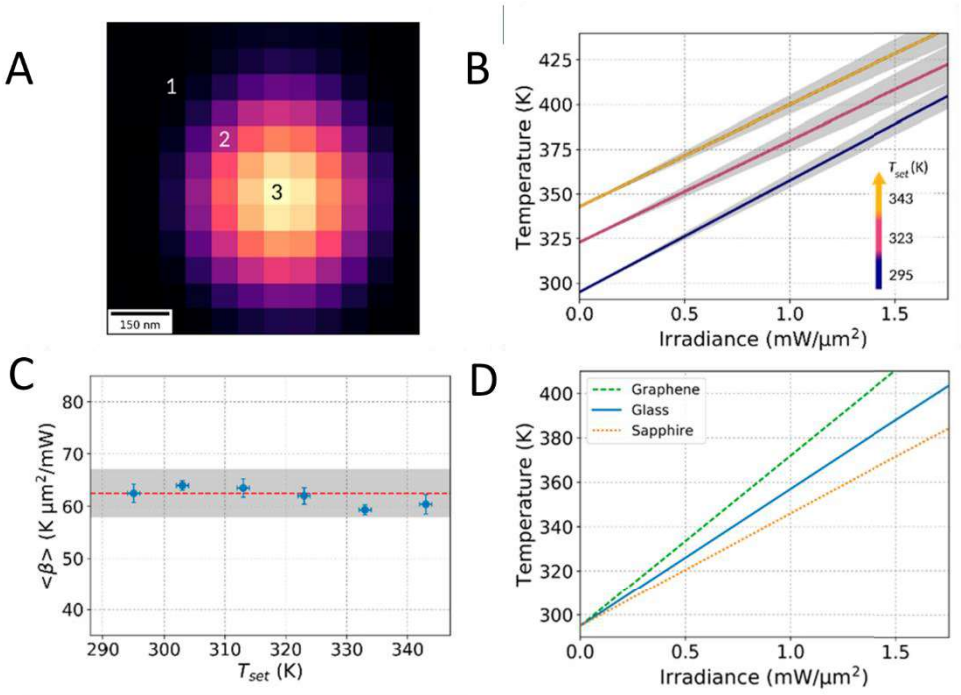

Fig. 8 *PL-AS nanothermometry applied to gold single particle under green laser irradiation results where a) is the hyperspectral image of a single Au nanoparticle, b) photon irradiance dependendance of the local temperature at different (global) temperatures, c) photothermal coefficient values at different set temperatures, and d) influence of the underlying substrate on the dependendance of the local temperature with the irradiance (Figure adapted from ref* [79]*)*

Espinosa et al. did a revolutionary work to determine the local temperature of single gold nanostructures and of hybrid Au-Fe_2O_3 systems (Fe_2O_3 core branched with Au nanoparticles in a Janus configuration) using X-Ray Absorption spectroscopy (XAS), when they are irradiated under a NIR laser beam (808 nm) with a irradiation power from 0.05 to 0.6 W [80]. Through extended X-ray absorption fine structure (EXAFS), they correlated the thermal movement of the atoms by the EXAFS Debye-Waller factor (σ), which is intrinsically temperature-dependent, with the temperature in the 10K to 350K range in dark conditions. **Fig. 9**A demonstrates a linear dependency between σ^2 and T. It was observable a linear tendency between the irradiation power and the σ^2, related to the local temperature increase on the gold surface under the NIR photons irradiance. Then, they attributed this change in the σ to the temperature increase as shown in **Fig. 9**B, which depicts the linear trend of irradiation power with the temperature by the Debye-Waller factor. Moreover, they used an IR thermographic camera at front and profile particle perspective to observe the different temperature gradients during laser excitation (**Fig. 9**C) obtaining similar values as in the EXAFS results, proofing two different and trustful approaches to be used as nanothermometry.

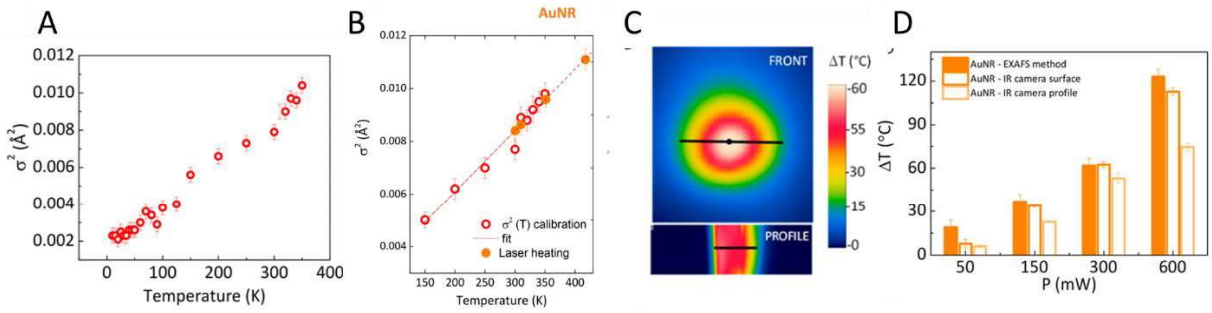

Fig. 9 *Experimental nanothermometry experiments on Au nanostructures.* ***A)*** *linear dependency of sigma at different temperature conditions,* ***B)*** *correlation between laser intensity and temperature by sigma square values for Au nanorods,* ***C)*** *IR thermography images of Au nanorods after 15 min of IR irradiation (808 nm) at 0.6 W and* ***D)*** *comparison of the temperature increments by the techniques used at different laser powers over Au nanorods. Adapted from ref* [80].

Raman spectroscopy can identify the temperature changes due to a linear response in the Raman shift. When the surface temperature increases, the vibrational mode peaks shift towards lower energy values together with an intensity loss. Therefore, any surface temperature increase should also be observable with this technique. For instance, the Abellan's group evidenced a clear linearity on antimonene nanosheets [81]. First, they stepwise recorded the spectra each 20K from 298K to 633K range at a constant 532 nm laser power (**Fig. 10**A), and further studied the influence of the laser power from 0.14 to 14 mW (**Fig. 10**B). By analyzing both A_{1g} and E_g modes at each temperature and laser power, they established a clear correlation between the laser power and the (local) temperature (**Fig. 10**C).

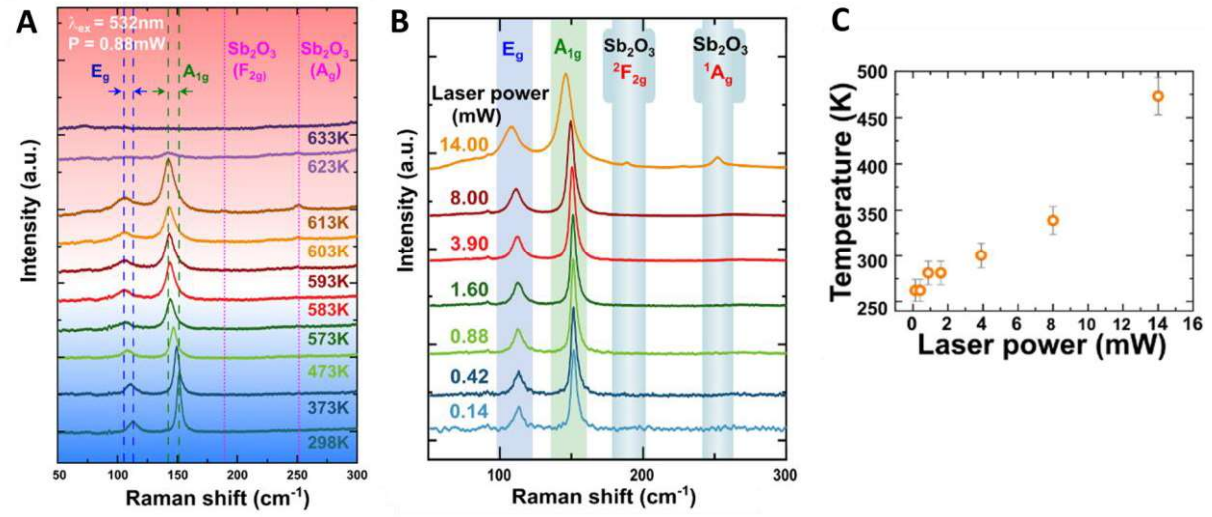

Fig. 10 *Raman spectra of antimonene nanosheets recorded* ***A)*** *at different temperatures,* ***B)*** *at different laser power values and* ***C)*** *the correlation between the laser power and the temperature. Figure adapted from ref* [81].

Even though the Raman spectroscopy principles are accurate and suitable for correlate light irradiance with thermal enhancement on the material surface, the use of low-percentage plasmonic metal nanostructures on the surface of the photo-thermal catalysts remains a limitation, due to a lack of sensitivity. Then, other characterization techniques based on Raman spectroscopy emerged to solve

this problem such as tip-enhanced Raman spectroscopy (TERS) and Surface-enhanced Raman spectroscopy (SERS).

Tip-enhanced Raman spectroscopy allows to elaborate precise local temperature maps at the nanometer scale and, therefore, enables the detection of thermal-driven processes. Surface-enhanced Raman spectroscopy can be also applied to observe the hot electron behaviors[82] through the coverage of metal nanostructures with molecules as adsorbates. When hot carriers are produced by non-radiative decay process using a probe with a wavelength that corresponds to the plasmon resonance, they can react with adsorbates on the surfaces, producing a difference in the intensity of the signal. Unfortunately, SERS is only useful for noble metals like Au, Pt or Ag, which when nanosized, tend to agglomerate during the reaction obstructing the analysis [83].

5. Reactors

Historically, the design and engineering of catalytic reactors has been a strong function of the primary excitation mode, viz., photonic or thermal, with little or no consideration for secondary activation options. Nonetheless, a photoreactor is under geometric design constraints, in terms of power optimization, spatial distribution, and delivery of the incident photon flux, certifying an appropriate access for reactants to optical excited states at the nano-dispersed absorber surfaces (high quantum yields), etc. Such considerations will clearly play a vital role in any realistic approach to design a photo-thermo reactor that can provide effective dual-mode excitation. Regardless of whether the photons are considered as a (immaterial) reactant – an aspect that remains a matter of debate –, the absorption of photons must be meticulously optimized in any system where the observed events are activated by photon irradiation [84].

In addition, the several choices available to supply heat offer good flexibility in respect of incorporating the thermal component. These include external (resistive) heating in radial symmetry (as per conventional jacketed tubular thermal catalytic reactors), heating from external absorber coatings, as in traditional solar-thermal units, or direct heat dissipation at the surface of an absorber catalyst (or support) working in photo-thermal conversion mode. Additional design factors and ancillary equipment must also be integrated according to the experimental objectives, be these of fundamental (mechanistic) concern or of a more applied type [3].

5.1. Solar thermal heating

In a reactor with no external resistive heating source, the main objectives in the design for optical heating are focused on the optimization of the capture geometry for increasing the incoming light flux and facilitating a rapid and highly efficient internal heat absorption. Solar thermal heating technologies use light-absorber materials and an associated infrastructure to collect selectively the heat resulting from the more abundant power components, i.e., the vis-IR components in the solar spectrum. The amplitude and spatial distribution of the localized temperature rise can be adjusted by suitable selection of light-absorber, receiver geometry and thermal (flow) characteristics. When the sun is the only source of photons, the optical element responsible for the harvesting and efficient channelling of solar photons into a catalytic reactor is known as a 'solar collector'. For instance, Malato et al. did extensive and well-documented studies on the use of this typology and applications, although the group's work focuses on the engineering of photocatalytic reactors for wastewater. They fall into 3 main categories offering different ranges of operating temperature, depending on the concentration factor (C), and thence on the suitability for specific types of catalytic application [85]. The

concentration degree of a solar collector is numerically equivalent to the ratio between the collector aperture area and absorber area. These are defined, respectively, as the area that intercepts the radiation and the area of the component that receives it. Solar collectors are usually classified into 3 main types:

(i) *Non-concentrating, low concentration* or *low temperature* collectors (T < 150°C). They are generally low-cost and easy to use. When non-concentrating, they are usually static, flat, facing the equator at fixed inclination and with no solar tracking. They can also be distinguished from others by a low concentration value (C < 1.5), and in that case very typical examples are the compound parabolic collectors (CPCs), given that these are ideal [86,87].

(ii) *Medium-concentrating*, or *medium-temperature* collectors (150 < T < 400°C). Concentration factors from 5 to 50 are typical and a single- or two-axis solar tracking system is mandatory to maintain stable and high levels of integrated optical input. Examples are parabolic-trough collectors, linear Fresnel lenses and holographic collectors. Tracking CPCs have the advantage of collecting *diffuse* light in the visible/near infrared wavelength range, which can amount to over half the annual total of terrestrial insolation depending on latitude and humidity level [88].

(iii) *High-concentrating*, or *high temperature* collectors (T > 400°C). These are based on a paraboloid with solar tracking, and demand a use of high-precision/quality optical components and rugged receiver materials for stable operation under concentration degrees as high as 10,000. Examples include parabolic dishes, central receiver (tower) systems and solar furnaces [86,89].

Depending on the scale of application and on the maximum working temperature, a typical layout for solar-thermal devices consists of a collector of suitable C value and a dimensionality compatible with that of the receiver. As shown in **Fig. 11**A, a popular selection is of the medium concentrating type (ii) combining a 2-dimensional parabolic trough and a tubular reactor receiver in annular configuration with the receiver positioned at the concentrator focus [90–92]. For an effective light-to-heat conversion, it is required a "black" material that not only absorbs along the wide range of the solar spectrum (ideally extending into the NIR), but also has high thermal diffusivity (to promote rapid and efficient heat transport to the central thermal fluid), and low thermal emissivity to minimize re-radiation losses. Well-designed tubular flow reactors heated by low-power (x5 - x10) solar concentrators can attain 240°C [10]. A recent advance in heat management has been to dispense with the conventional (external absorber layer) coating and to generate heat volumetrically throughout the thermal fluid by suspending nanoparticle ('nanofluid') absorbers offering a more efficient *direct* optical heating mode. Plasmonic noble metals are preferred over nanocarbon blacks as the latter have high thermal emissivity [93]. **Fig. 11**B collects various configurations for solar reactor systems. In these cases, they include layouts where the catalyst/reactor is physically remote, or decoupled, from the receiver (left), where the reactor/receiver is integrated with opaque side walls (middle), or where the catalyst itself is the exclusive or partial absorber exposed to direct illumination (right). This last case also provides prospects for photo/-thermal catalytic synergies depending on the chance of optical stimulation of electronic processes, which is a function of the absorber type.

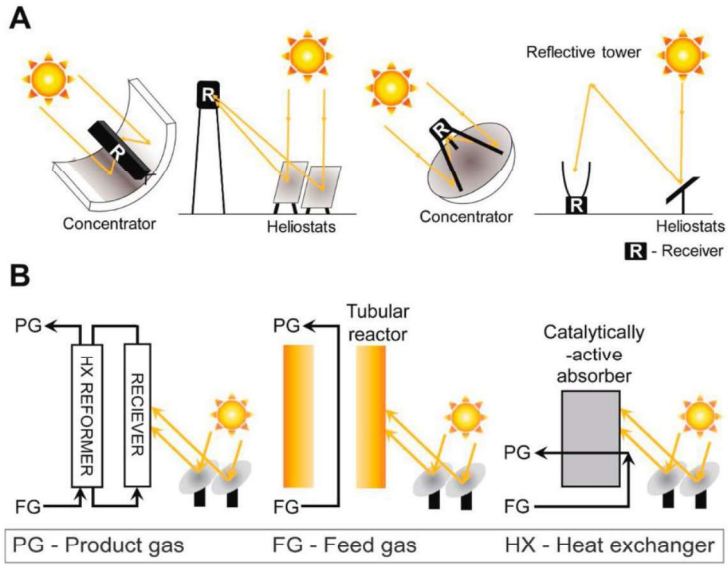

Fig. 11 (A) *Scheme of medium- to high- solar concentrator types, itemized from left to right as parabolic trough, central power tower (heliostats), parabolic dish, and double concentration systems. Parabolic troughs and dishes offer concentration factors from 30 to 100 and reach temperatures of 500–700 K. Double-concentrators (right), consisting of a heliostat field, a reflective tower and a ground collector, operate in the 5000-10000 concentration range and can reach temperatures as high as 1500 K ;* ***(B)*** *Different configurations for solar-thermal operations: (left) reactor decoupled from solar receiver system; (middle) integrated tubular reactor/receiver, and (right) catalytically active solar absorber. (reproduced from Kho et al.* [94]*)*

5.2. Photo-thermo microreactors

In recent years, advances in 3D printing technology has enabled flexibility in the design and the rapid, inexpensive and reproducible manufacture of structured reactors containing sub-millimetre-scale microchannel arrays, thus driving the development of process intensification. Compared to conventional ("macro") reactors, this small design largely reduces problems related to mass and heat transfer limitations, resulting in higher energy efficiency, higher conversion rates and yields, and increased safety (by facilitating the handling of high pressure conditions), as well as in a more precise definition of the reactor parameters and in a better control of the process [95]. For photocatalysts, such wide sideways dispersion and shallow depths serve to promote reactant/photon/catalyst encounters. A traditional inconvenience in the design of photo-reactors is how to minimize or delete the darkened section of the catalyst, i.e., sub-surface and bulk nanoparticle layers positioned below 'infinite depth', the terminology for the condition of full extinction because of absorption and scattering. For common indirect band-gap semiconductors like TiO_2, infinite depth is established already in the top *few microns*, i.e., the dimensional regime of single particles or agglomerates of nanoparticles. A planar rectangular microchannel array ('flat bed') can be efficient using external sunlight as photonic source, either as a direct beam or re-directed and intensified by a concentrator. Micro-channel reactors provide a good framework for catalyst dispersion (shallow depths and narrow cross-sectional sub-division), and are proven to offer high efficiencies in solar synthesis applications [96].

In **Fig. 12** it is illustrated an example of a photothermal microreactor with an authentically sunlight-driven structure. Castedo et al. have exploited 3D printing to obtain broad-spectrum (UV–vis-NIR) transparent silicone microreactors in both 9-channel and 32 channel ('scaled-out') versions, as it is shown in **Fig. 12**A [97,98]. These were compared in photo-dehydrogenation of ethanol/water vapour

mixtures over Au/TiO_2, in a laboratory set-up (inside an oven with LED lamp (UV-A) irradiation), and in the field under concentrated sunlight from a parabolic dish (**Fig. 12**B). Very respectable H_2 evolution rates (30- 350 µmol.min^{-1}g$_{cat}^{-1}$) were achieved over a range of temperatures from 323 to 423 K (the stability limit of the silicone) that resulted from optical heating in the solar concentrator system, as shown in **Fig. 12**C. Consistency in the apparent activation energies (25 ± 1 kJ mol^{-1}) between the Lab-based and field systems (see insert of **Fig. 12**C) certified the operational rigour of the latter (large) assembly. Further consistency in the H_2 evolution rates (~1 mmol.h $^{-1}$.cm^{-2}) between the 9- and 32-channel microreactors on an area-normalized irradiation basis was good evidence that a simple 'scaling-out' principle may apply to these modular devices.

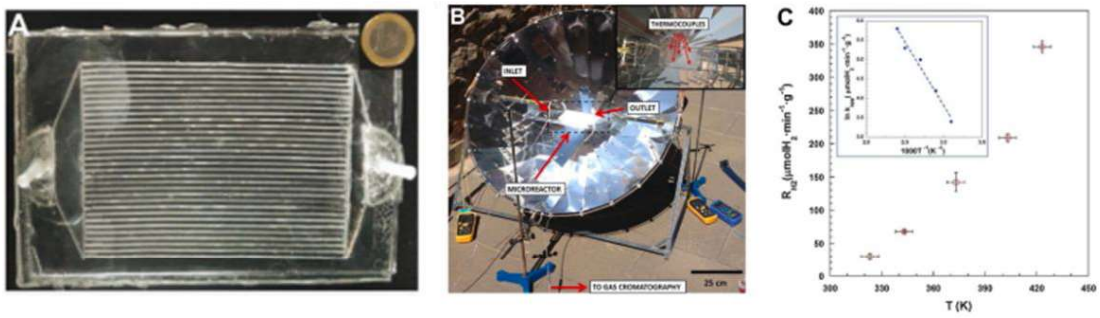

Fig. 12 (A) *Picture of the 3D-printed silicone microreactor with 32 microchannels of 500 µm (width) ×1 mm (depth) ×117.5 mm (length) used in* ***(B)*** *outdoor experimental test setup for H_2 production. The microreactor was placed in the collector focus, irradiating the top cover with sunlight gathered by the parabolic mirror and the bottom of the reactor with direct sunlight (commercial parabolic Al solar reflector: d = 1 m, aperture area = 0.8 m^2, AlSol K10, Spain).* ***(C)*** *Photocatalytic H_2 generation rates obtained using the experimental setup of (B) at different temperatures under sunlight irradiance (residence time 0.35 s, GHSV =10200 h^{-1}, H_2O:EtOH = 9:1 M). The photocatalytic tests were carried out in Barcelona (41.38°, 2.17°) with average solar and UV-A irradiance of 90 ±5 mW/cm^2 and 5.0 ± 0.5 mW/cm^2, respectively. (reproduced from ref* [97]*)*

5.3. Photo-thermo reactors with resistive heating

When external (resistive) heating is applied with light irradiation, a photo-thermo reactor must incorporate a window of similar dimension and aspect ratio to those of the catalyst bed and of the incident beam. It should preferably be made out of a strong thermal shock-resistant material like fused quartz. A good example from the work of Han and Hu is shown in **Fig. 13**A, in which the catalyst is dispersed on a light-diffuse-reflection-SiO_2 surface as substrate [99]. In another configuration from Ghuman et al., a borosilicate glass tubular reactor is heated by conduction using a copper block channel fastened within a custom-fabricated stainless steel brace, that enables the reactor heating from the walls and below (**Fig. 13**B) [100]. Alternatively, a more holistic arrangement for light exposure is to make the reactor by a transparent material and incorporate narrow bands of heat element tracery. Unfortunately, quartz is a brittle material not so amenable to machining (shaping), and so Pyrex glass usually serves instead, despite having an optical (UV) absorption starting below 350 nm. The group of Fernández-García developed a continuous flow annular Pyrex-glass thermo-photo-reactor using a centrally-positioned heater cartridge of extended length with a catalyst-coated inner wall [101,102] . As shown in **Fig. 14**, good illumination was achieved by 4 lamps symmetrically arrayed around the reactor.

Windows incorporated in thermo-photo reactors allow the main body to be fabricated from stainless steel, with the benefit to use a tough and chemically inert material classically employed in thermal reactors, and suited particularly for high-pressure work, so that they can work indifferently at

atmospheric pressure or under pressure. The use of quartz windows also provides flexibility in regulating the optical properties (spectral range and intensity) of the incoming light, e.g., with interposition of monochromators, cold mirrors and/or various kinds of optical filters. For instance, Zhao's group coated 100 mg of catalyst at the bottom of a stainless steel reactor comprising a quartz window of 110 mm of diameter to provide the irradiation of a simulated sunlight lamp to the reactor [103–105] and using iced water as a cooling down temperature system.

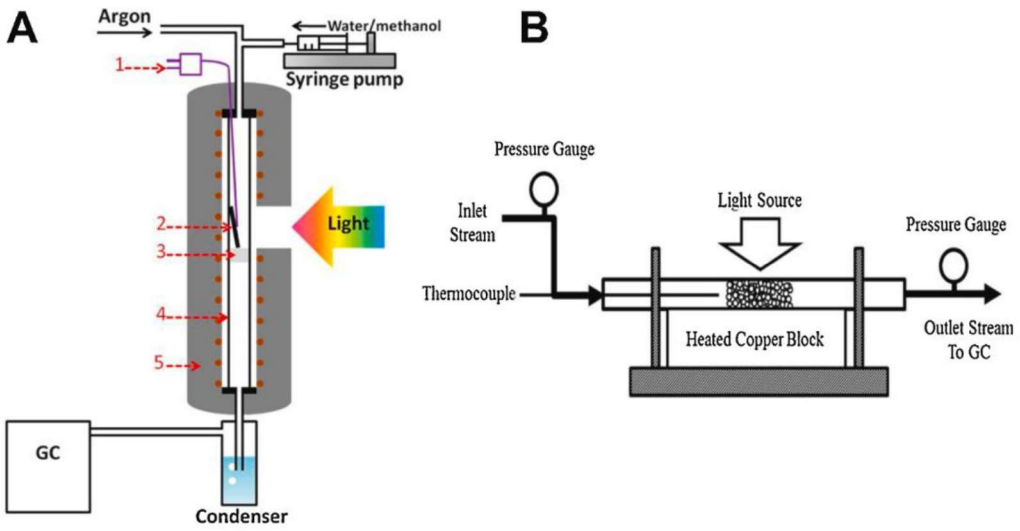

Fig. 13 (A) *Continuous flow annular thermo-photo reactor used for the temperature-induced photocatalytic H_2 production from H_2O with methanol as a sacrificial agent, with (1) thermocouple, (2) Pt/TiO_2 on SiO_2 substrate (used as light diffuse-reflection-surface, (3) quartz wool, (4) quartz tube reactor, and (5) electrical tube furnace. (reproduced from ref* [99]*)*
(B) *Gas-phase thermo-photo catalytic packed bed flow reactor comprising a borosilicate tube (3 mm outer diameter and 2.5 mm inner diameter) packed with 1 cm length catalyst bed, with quartz wool as support at both ends. A heated copper block was used to heat the tubular reactor via conduction, while the top of the reactor was exposed to light irradiation from a 300 W Xe lamp at a distance of 2 cm, with a light intensity of 1000 W/m². (reproduced from ref* [100]*)*

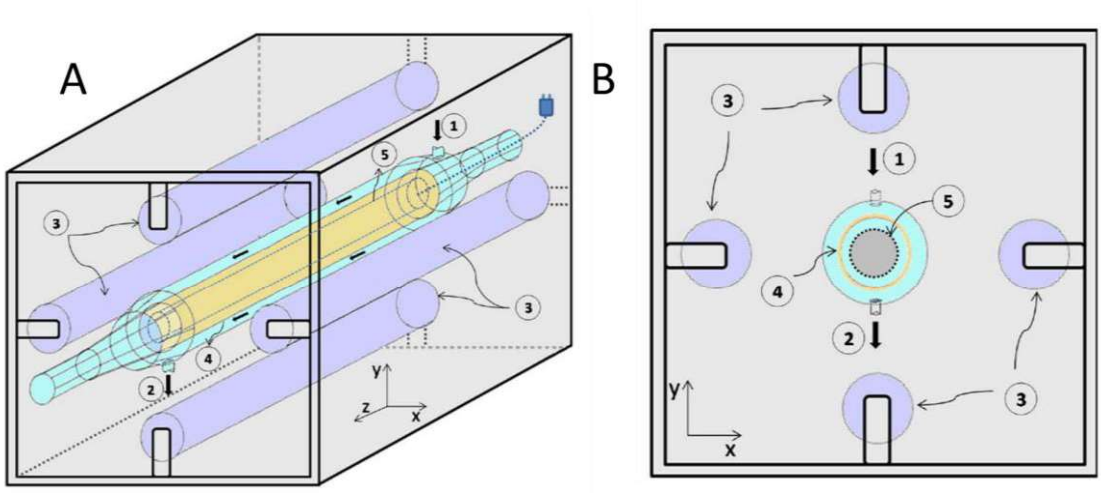

Fig. 14 *Photo-thermal annular reactor from Fernandez-Garcia's group. A) overall illustration perspective and B) front side view, where 1) and 2) are the inlet and outlet of the reactor, 3) are the UV light lamps, 4) is the catalyst coating and 5) is the heat cartridge. (reproduced from ref* [102]*).*

5.4. High Temperature (/pressure) reaction chambers

High Temperature (/pressure) reaction chambers are probably the most versatile and rugged commercial range of devices. They were designed originally for in-situ spectroscopic research of small powdered solid beds under extreme conditions. For instance, the High-Temperature reaction chamber series available from Harrick Technology can be used as photo-thermal reactors when the sample is a catalyst and the chamber turret is fitted with a 3rd 'observation' window (~1 cm^2) through which light may be directed (as from a lamp/filter/fibre optic combination). Built from stainless-steel alloy 316, models HVC-MRA-4 and -5 are the product of design evolution over 3 decades. By allowing operation from vacuum to 34.4 bar and 910°C, they are still continuing to prove invaluable in the hands of catalysis experts, although it has to be mention that at temperatures above 450°C, the heater lifetime is significantly reduced, and they can only operate at the maximal temperatures under vacuum conditions [54,106–108]. A snapshot of a typical plumbed-in Harrick device is shown in **Fig. 15** and details are provided in the suited section in chapter 2. The aim of conducting photo-thermo reactor testing along with in-situ or operando spectroscopic characterization (by Raman, FTIR, UV–vis, etc.) of reaction mechanisms via intermediate(s) detection, reactant-induced surface (structural and/or electronic) changes, etc., is as exciting as it will be challenging. This is partly due to its easy integration into complex on-line flow analysis configurations allowing e.g., mass spectrometric (MS) detection of products at very low levels.

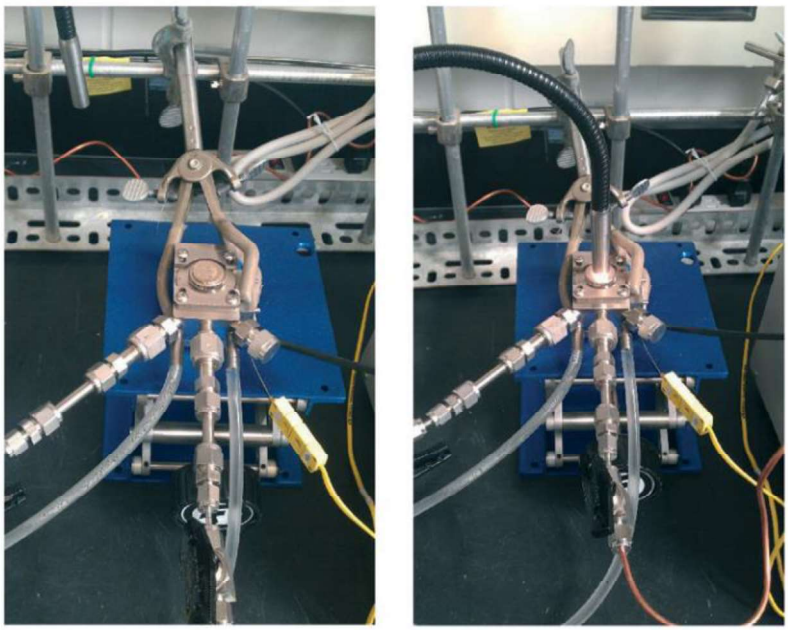

Fig. 15 *Harrick scientific (HVC-MRA) reactor at dark (left) and light (right) conditions adapted from ref* [108]

However, as a warning it must be pointed out that a good temperature definition, i.e., the absence of any thermal gradients in the catalyst bed is necessary for deriving accurate kinetic data, and is a serious challenge even having a well-positioned thermocouple in contact with the surface layer. The notoriously poor heat transport properties of powdered solids was the original motivation for implementing early solutions, such as the use of a continuous recycle reactor with a larger charge of catalyst in the loop having better temperature definition via tubular heating [109]. More recently, Li et al. [110] evaluated the temperature definition problem in studies on 3 different *in-situ* FTIR cells, and suggested effective correction methods. The tested cells were of both diffuse reflectance (DRIFTS) and transmission modes, custom-built and supplied from commercial sources (Harrick and Spectra-Tech.). The geometric layout of the different configurations is shown schematically in **Fig. 16**. With the aid of an optical (IR) pyrometer, they revealed by surface emissivity measurements from the catalyst bed that these three IR cells showed a significantly lower temperature than that of the corresponding thermocouple located in or close to the sample bed. The discrepancy amounted to some 35 degrees (T_{contr} =280 °C, T_{surf} =245 °C) in the Harrick cell, related mainly to the larger dimensions of its powdered bed (see **Fig. 16**C,D). The presence of significant thermal gradients, giving rise to variable effective mean reactor temperatures, were indicated by different methanation rates under identical (control) conditions. Fortunately, they also demonstrated that a systematic temperature correction was workable (e.g., T_{eff} = T_{contr} **-** 20°C for the Harrick cell) using calibration curves derived from rate measurements (CO methanation over 16 wt% Ni/Al_2O_3) obtained in a traditional packed-bed tubular (non-spectroscopic) reactor having a well-defined temperature. However, more complex cases of competing reactions (selectivities < 100 %) having different activation energies are bound to result in indissolubly-mixed kinetics and unreliable data under such temperature gradients.

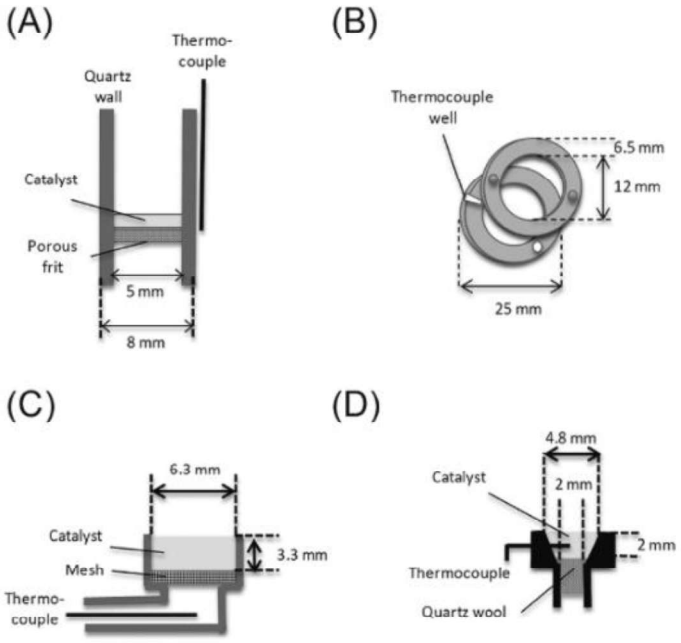

Fig. 16 *Various catalyst bed configurations studied in Li et al.:* ***(A)*** *in a conventional U-shaped quartz reactor,* ***(B)*** *in a "sandwich" transmission cell,* ***(C)*** *in the commercial Harrick DRIFTS cell and* ***(D)*** *in the commercial Spectra-Tech DRIFTS cell. (reproduced from ref* [110]*)*

6. Applications of photo-thermal catalysis

This section is an overview of last advances in *photo-thermal catalysis*, the default term we will use henceforth to describe the combination of dual (photon- and heat) excitation of the catalyst and any synergies issuing from it.

First of all, we can stress that the photothermal effect in the sense of a light-to-heat phenomena finds interest in high-prospect, emerging technologies such as cancer therapy, photovoltaic solar cells or even solar steam [36,41]. For instance, some groups have already used advantageously a photothermal effect in solar cells, which is a novelty in the field, as heat is commonly considered as a negative factor in classical photoelectric devices. The thermoelectric effect, based on the so-called Seebeck effect, has been recently applied in solar cells for heat recycling, and therefore, a new type of solar cell based on a photothermoelectric (PTE) effect was investigated [46]. In **Fig. 17**, it is represented a schematic illustration of a PTE device where gold nanoparticles absorb solar light to increase the local temperature [111].

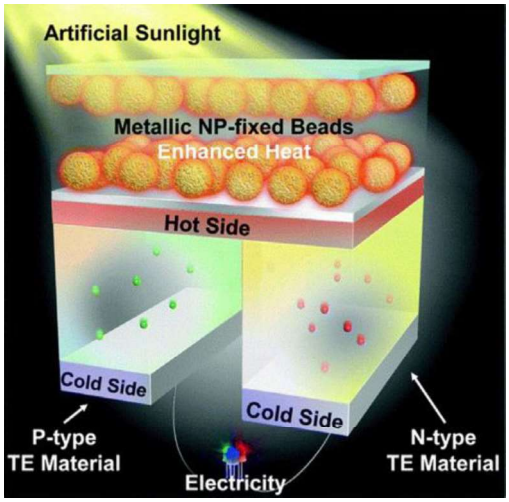

Fig. 17 *Schematic illustration of a solar thermoelectric device based on plasmonic collective phenomena, extracted from ref* [111].

In heterogeneous photo-thermal catalysis, synergies have been already reported in the frame of many reactions of interests, as shown in **Fig. 18**, in the fields of environmental chemistry (in gas-phase, like the degradation of volatile organic compounds, VOCs, [104,112–114] and in aqueous-phase like the degradation of methylene blue or 4-nitrophenol reduction [115–117]), valorization of bio-resources (e.g. biomass gasification, production of 5-hydroxymethylfurfural, lactic acid production) or selective oxidations, with molecular oxygen activation), the Haber-Bosch ammonia synthesis [118–120], methane activation or the Fischer-Tropsch reaction [35,121,122], among others. For more details on these and on other applications, there are excellent recent report works by Mateo et al.[1], Luo et al.[123] Colmenares et al.[7], Zeng et al. [124], Li et al. [125], Muñoz-Batista et al. [102], Hou et al. [126], Ma et al. [9], or Zhou et al.[127]. In this part of the chapter, we focus instead on processes expected to be of strategic importance in the establishment of H_2 production and CO_2 reduction.

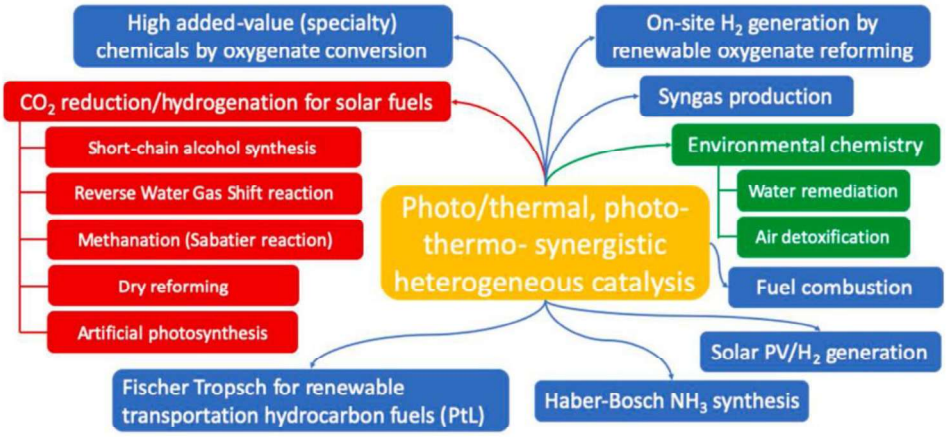

Fig. 18 *Scheme of a wide span of applications of photo-thermal catalysis.*

6.1. H_2 production by simple organic reforming reactions

Reforming of oxygenates into hydrogen-rich mixtures are endothermic processes and, consequently, good candidate reactions to take advantage from any light assistance. As well as a photocatalyst offers the special ability to carry out *endergonic* (thermodynamically uphill) processes, it became and store light energy in new chemical bonds with broader applications to any process that involves a dehydrogenation component to produce high value-added chemicals. The positive contribution of heating in a photocatalytic process was certified by several reports in the literature. Among them, Ye et al. nicely demonstrated that whereas photocatalytic activity in methanol reforming for H_2 production (1.2) over pristine TiO_2 under UV–vis illumination was low (< 2 µmol.h^{-1}) and actually decreased with rise in temperature from 10 to 40°C, a loading of 1 wt. % Pt onto TiO_2 raised the activity one hundred-fold and established a positive (Arrhenius-type) thermal response in the same temperature range (**Fig. 19**A)[128]. They interpreted this synergism in light-heat co-induced H_2 generation by suggesting that Pt could act as *co-catalyst* for the TiO_2 photocatalyst (to increase the lifetime of charge carriers efficiently upon UV light irradiation), and in its own right as *thermal* supported noble metal catalyst for (dark) methanol dehydrogenation. They surmised that the overall process efficiency should benefit from broad-band illumination over the entire solar spectrum, in which the short (UV) and longer (vis-IR) wavelength envelopes would in consequence also act in synergy, the second providing thermal enhancement of the catalytic H_2 production by localized optical heating. In a follow-up work [129], the same team demonstrated that optical heating, especially by inclusion of the infrared component, was powerful and efficient enough to render external resistive heating unnecessary. Full solar light spectrum irradiation raised the reactor temperature to 54°C (from 35°C under UV–vis light), thereby doubling the H_2 production rate until 25 mmol.g_{cat}^{-1} h^{-1}. Under pan-spectral excitation, they propose a fortuitous combination of photocatalysis (via electrons generated upon UV–A excitation of TiO_2 being transferred to surface Pt particles to reduce protons), while only the dark process of methanol oxidation (proceeding independently and in parallel) is enhanced by the heat provided by the vis–IR light (**Fig. 19**B).

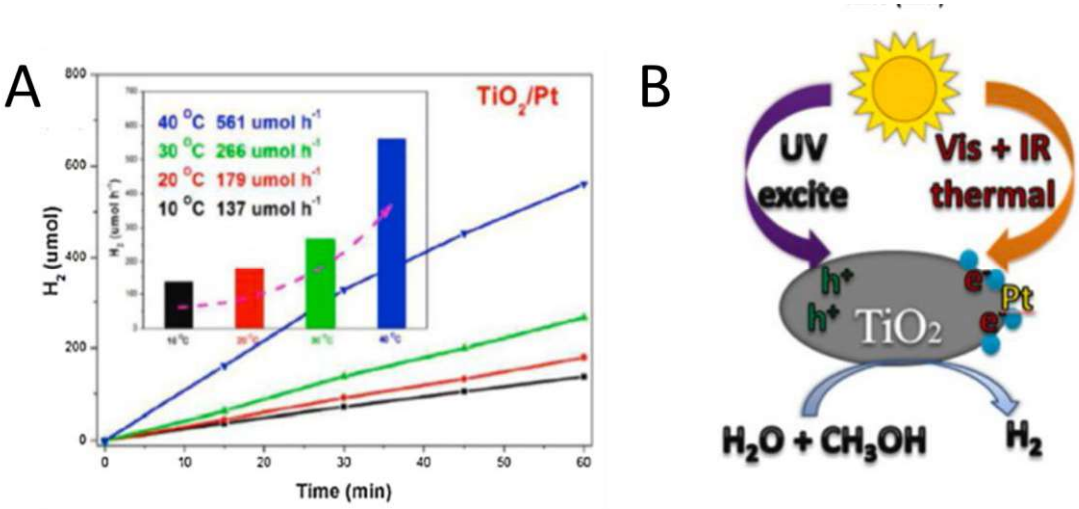

Fig. 19 (A) *Influence of the temperature (external heating) in the 10-40 °C range on the photocatalytic activity for H_2 production from a methanol-water (10 % v/v) solution upon UV–vis light (320-800 nm) over a Pt (1 wt.%)/TiO_2 catalyst (reproduced from ref* [128]*)* ***(B)*** *Combination of photonic- and (dark) thermal activation for H_2 production upon UV–vis–IR full spectrum irradiation (pan-spectral excitation) (adapted and reproduced from ref* [129]*).*

$$CH_3OH + H_2O \rightarrow 3H_2 + CO_2 \quad (1.2)$$

$$CH_3OH \rightarrow 2H_2 + CO \quad (1.3)$$

The use of the oxygenate methanol for producing H_2 is naturally not limited to reactions in the liquid state. Even higher quantum efficiencies (and H_2 evolution rates) have been reported in vapour-phase work up to 300°C by Han and Hu [99]. The authors claimed that their catalyst is based on 'black' TiO_2, a surface disorder-engineered material obtained by high-pressure hydrogenation of TiO_2 nanocrystals at temperature under H_2, that caused a media stir upon discovery a decade ago [130], even though interest cooled thereafter and debate is still open on this subject. However, it must be stressed that the H_2 treatment of their Pt/TiO_2 catalyst was not performed at high pressure. Over 1 wt.% Pt/TiO_2, the rate of H_2 evolution reached 700 $mmol.h^{-1}g^{-1}$ at 280°C with an overall (AM 1.5) quantum efficiency Φ = 0.78, that corresponds to a 5-fold photo-enhancement of a dark process offering a viable rate by thermal activation alone. Photo-thermo-catalysis of methanol decomposition (2) , targeting syngas (CO/H_2) production, was explored over a $Pt/SrTiO_3$ catalyst by Han et al. [131]. Highly dispersed Pt at 1-3 wt.% loading, acted as both co-catalyst and, due to its quasi-continuum absorption across the vis-NIR region, a thermal sensitizer, enabling the reactor temperature to reach 150°C in the absence of external heating under illumination from a 300 W Xe lamp at 530 mW/cm^2. The use of bandpass filters proved that most of the thermal effect was due to absorption of the NIR component beyond 800 nm. Sustainable and high H_2 evolution rates (~1 $mmol.h^{-1}$ over 100 mg catalyst) at such a low temperature, roughly 3-4 times higher than the analogous SiO_2-supported Pt control, was clear evidence of substantial photo-assistance. In batch recirculation tests, a high methanol conversion of 95.5 % was attained over 3% $Pt/SrTiO_3$, with a peak (initial) selectivity of 94.4 % towards syngas.

Caudillo-Flores et al. used their 4-lamp array photoreactor (see section 4.3) to assess the photo-thermo synergy in reforming of aqueous methanol vapour mixture over 1 to 10 wt.% Ru/TiO_2 catalysts in a continuous flow mode via combined UV-A light and external (resistive) heating[101]. They quantitated any synergism on the basis of 'excess' rate values (rates and quantum efficiencies, QE), given by any positive difference between dark and illuminated hydrogen production as compared to the sum of individual rates from each activation mode applied separately. Despite the performances obtained with their Ru/TiO_2 catalysts and notably the excess reaction rate resulting from dual UV-A light and thermal excitation of the catalysts were by far lower than those reported by Han and Hu with a Pt (1 wt.%/TiO_2) catalyst under solar light [99]. Nevertheless, they identified a strong synergy in co-excitation where the excess values reached maxima at 240°C. Heating above 200 °C enhanced the QE of photo-reforming (over ambient) by two orders of magnitude, while addition of illumination increased the dark rate at 240°C by a 40–50%. They attributed the synergy to the promotion of individual steps in the same overall mechanism, as studied by DRIFTS, in which a progressive conversion of methanol to CO occurs via formaldehyde and formate-type surface species, followed by water-gas shift conversion to H_2 and CO_2. From the perspective of global resource sustainability, there is now an encouraging trend towards the use of cheaper, earth-abundant non-noble metals as viable co-catalysts for H_2 production instead of noble metals based materials.

6.2. CO_2 conversion

The idea of convert anthropogenic carbon dioxide into synthetic fuels is a promising solution for reducing greenhouse gases (GHG) emissions and avoiding the use of fossil fuels in a carbon-neutral economy system where the undesired product is the reactant for another reaction. Therefore, emerging technologies like photo-thermal catalysis have been employed to face the arduous stability of CO_2 into promising chemicals that can act as fuels like methane, methanol, hydrogen, etc. Despite all the interesting and promising reactions such as Fischer-Tropsch synthesis [10,121,122,132–134], methane dry reforming [135–140] and artificial photosynthesis [141–145], Reverse Water Gas Shift (RWGS) [100,146–151], Methanol production [107,152–154] only a selection are commented in this subsection remarking interesting processes than occur during dual photo-thermal excitation.

CO_2 can be reduced through hydrogenation via Sabatier reaction (1.4), also named as methanation, reverse water gas shift reaction (RWGS) (1.5) and methanol production (1.6):

$$CO_2 + 4H_2 \rightarrow CH_4 + 2H_2O \qquad \Delta G_0 = -113 \text{ kJ mol}^{-1} \quad (1.4)$$

$$CO_2 + H_2 \rightarrow CO + H_2O \quad (1.5)$$

$$CO_2 + 3H_2 \rightarrow CH_3OH + H_2O \quad (1.6)$$

Last advances in the field of CO_2 hydrogenation stress that VIII elements (Rh, Ru, Co, Ni, Pt, Pd, Ir, and Fe) based catalysts may rise reaction rate to several orders of magnitude in comparison with classical photocatalysis systems improving the optical absorption along the solar light spectrum [3,123]. Ye and co-workers analysed different M/Al_2O_3 (where M=VIII group metal) catalyst for methanation and water gas shift reaction to obtain CH_4 and CO as solar fuels. Under a 300 W Xenon lamp irradiation they reached maximum values of CO_2 conversion higher than 90% (except in Pt, Fe and Ir) with special mention to Ru/Al_2O_3 being the less expensive noble metal reporting conversion and selectivity values to CH_4 of 95.75% and 99.22%, respectively [56]. A temperature monitoring over light irradiation demonstrated a temperature increase (see **Fig. 20**A), hypothesizing that hot carriers thermalization process was enhancing the CO_2 conversion via increasing local temperature, acting the metal nanoparticles as optical heating source after light absorption and any electron-driven mechanisms were involved. This hypothesis was strongly supported after the CH_4 evolution remained stable during a photon-wavelength study over Ru/Al_2O_3 catalyst using a monochromatic light source. Meanwhile, for an electron-driven chemical mechanisms, the CH_4 production rate should change in order to the UV-Vis spectrum of Ru/Al_2O_3 shown in **Fig. 20**B.

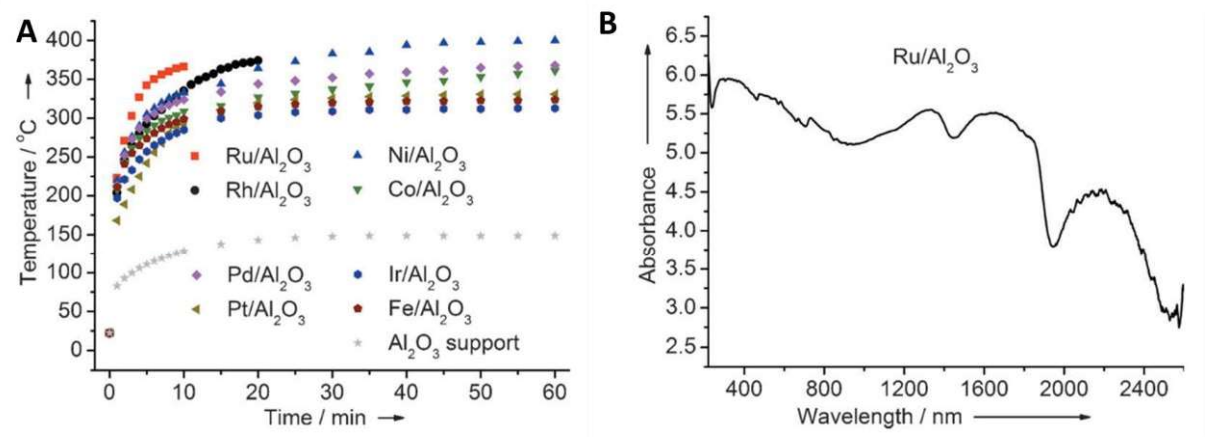

Fig. 20 *Photo-thermal methanation over group VIII catalysts. A) temperature monitoring during light irradiation and B) UV-Vis spectrum of Ru/Al_2O_3 catalyst, adapted from ref* [56].

In terms of advancing long-term sustainability in materials resources, it is essential that the development of plasmonic metals that are not based on expensive rare metals. Therefore, plasmonic transition metals like Fe, Co, Cu, Ni, Zn or weak metals like Al are promising materials for CO_2 reduction. A core/shell photo-thermo catalyst composed of earth-abundant elements ($Al@Cu_2O$) has been developed by Halas and colleagues for operation as 'antenna-reactor' nanostructures in which the light harvesting (Al) and catalysis (Cu_2O) components are separated but act in synergy [148]. Both thermal-driven and electron-driven processes were reported during the hydrogenation. For instance, HR-TEM imaging (**Fig. 21**A) demonstrates an increase of temperature at catalytic surface over a visible light illumination from a super continuum fibre laser at 10 W/cm^2 (equivalent to 100 suns), corresponded to a temperature monitoring (**Fig. 21**B) measuring a temperature increase till 175°C in Al particles caused by the thermalization of hot carriers at catalytic surface. However, thermal-driven process in dark conditions demonstrate to reduce carbon monoxide into a mixture of CO/CH_4 products, meanwhile over light-irradiation selectivity to CO production is ca 100%, suggesting electron-driven reaction a unique pathway for chemical bond activation that is based on effective hot-carrier migration from catalyst to adsorbate(s) species rather than photothermal heating. Additionally, photon-wavelength study proved a CO_2 conversion rate dependency with the photon-wavelength, increasing specially in the $Al@Cu_2O$ plasmon range. The authors suggests that the abundant generation of hot carriers might result from LSPR damping in the Al core or from near-field excitation in the Cu_2O shell, in both cases as a result of the Al/Cu_2O energy band alignment.

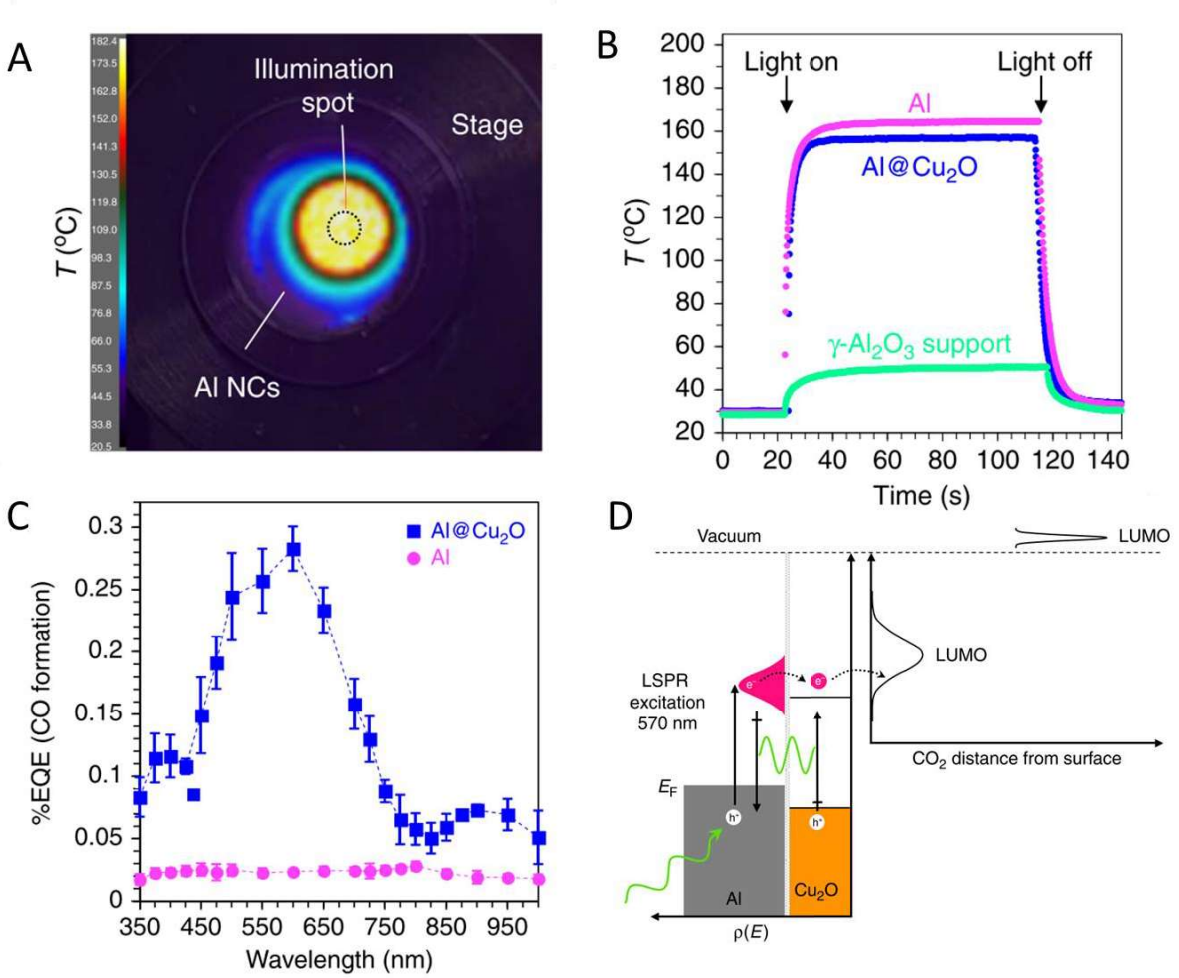

Fig. 21 *Thermal and photo-chemical processes in Al@Cu_2O where* ***A)*** *HR-TEM of particle over light irradiation with thermal gradient on particle surface,* ***B)*** *temperature monitoring at light conditions,* ***C)*** *wavelength dependency of EQE based on CO production through the visible-NIR spectra, and* ***D)*** *Energy band diagram of Al@Cu_2O for hot carrier generation for injection into unoccupied state of CO_2 for C–O bond photo-activation reproduced from ref* [148].

Lu et al. have recently made an interesting study of the RWGS reaction over Au/CeO_2 and with an unusual finding (**Fig. 22**) [150]. We believe it is the first reported case of a Type B effect (see section 2), in which a strong photo-enhancement seems to be connected with the favourable perturbation of pressure in reaction conditions. As shown in **Fig. 22**A, CO_2 conversion in the dark was quite poor, reaching only 3.2 % at 400 °C. Under irradiation, the conversion across the same temperature conditions (360−400 °C) was higher than an order of magnitude, reaching more than 40 % at 400 °C. Nevertheless, unlike the previous report of Ghuman et al. (**Fig. 22**C) [100], there no remarkable difference in E_{app} but a strong influence of the rate dependence on partial pressure of H_2. The exponent in P^n_{H2} rose from n = 0.63 in the dark to n = 1.52 under illumination **Fig. 22**D). Such a strong effect is clear proof that the dark process is H-supply-restricted, while photo-excitation eludes this limitation, possibly by promoting the growth of surface Au–H bonds, which was observed by in-situ DRIFTS. By analogy with the proposal of O'Brien et al. in CO_2 methanation [151], photo-induced charge carriers may open up a new route to key M–H intermediates by promoting heterolytic dissociation of H_2. Reconciling the conflicting but equally-convincing findings of Ghuman et al. [100] and Lu et al. [150] in the RWGS reaction lead to the remarkable and encouraging conclusion that a photo-thermo synergy

can enhance the same reaction via different mechanisms (type I [100] and/or type II [150]), possibly catalyst-dependent, which is a clear advance in the field.

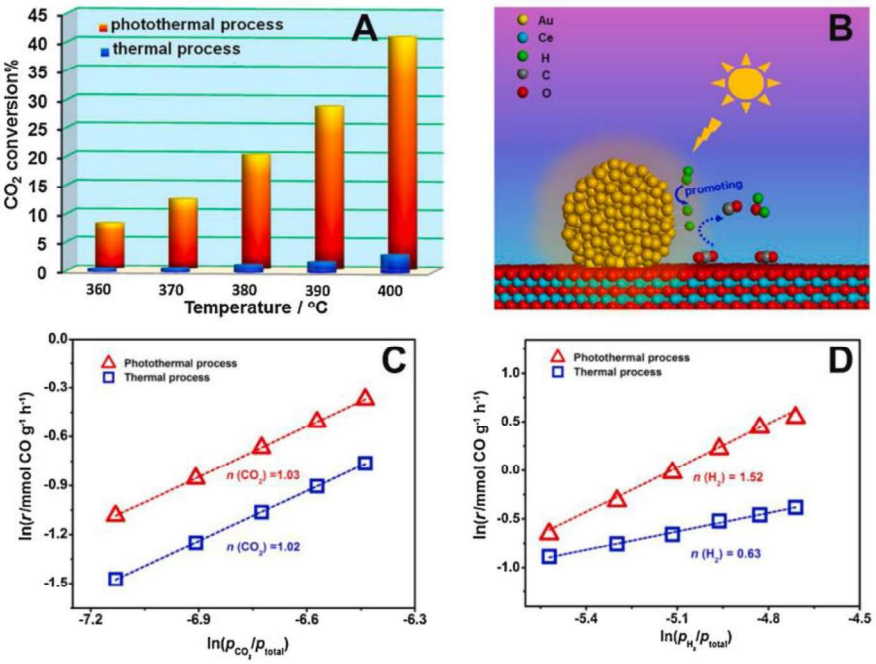

Fig. 22 A) *CO_2 conversion values in RWGS reaction over 0.9 at. % Au/CeO_2 from 360- 400 °C in the dark (blue) and under illumination (red) conditions.* ***B)*** *Mechanistic scheme showing the promotion of H_2 dissociation over Au atoms.* ***C)*** *Plot of CO production rate dependence on partial pressure of CO_2 in the dark and under illumination, and* ***D)*** *on partial pressure of H_2. (reproduced from ref.* [150]*)*

Artificial photosynthesis (AP) refers to the simulating-natural process to yield end-products of greater value and versatility in chemical industrial processing by reducing carbon dioxide with water as hydrogen provider by photonic excitation. This ambitious light-to-chemical process is marked by the advantage of employing unlimited reactants in natural resources as water and carbon dioxide are. However, it is important to take into account highly endergonic process of water splitting that is implicitly involved in the overall mechanism, which represents a technical obstacle for the advance of this process. In the domain of AP derived solar fuels are found methane, CH_4, carbon monoxide, CO, or methanol, CH_3OH, as the simplest chemical of valuable interest. Methanol production via artificial photosynthesis (1.7) is strongly dominated by the electron production from the water (1.8) that can reduce the CO_2 to produce methanol (1.9).

$$CO_2 + 2H_2O \rightarrow CH_3OH + 3/2O_2 \qquad E^0 = +1.21V \qquad (1.7)$$

$$3H_2O \rightarrow 6H^+ + 6e^- + 3/2O_2 \qquad E^0 = +1.23V \qquad (1.8)$$

$$CO_2 + 6H^+ + 6e^- \rightarrow CH_3OH + H_2O \qquad E^0 = -0.02V \qquad (1.9)$$

It is possible to find research articles that reported methanol production under dual photo/thermal excitation. For instance, the group of Zhao et al. [144] produced selectively methanol by CO_2 reduction

with water over a Mo-modified WO_3. In general, methane have been more reported as solar fuel product from artificial photosynthesis than methanol [142,145,155,156]. Alternatively, methanol can be sustainably generated by a two-step process. It consists of generating green hydrogen via water splitting that is after transferred for the followed carbon dioxide reduction, being the main reaction in this case $CO_2 + 3H_2 \rightarrow CH_3OH$. This two-step process is closer to the classical catalytic industrial methanol synthesis. Wang et al. and Xie et al. did some advances in this reaction over Cu/ZnO and $Cu/ZnO/Al_2O_3$ based catalyst, respectively [107,152]. Both studies highlighted the importance of the photon-induced carriers that activate key intermediate species adsorbed on the catalytic surface.

Photo-thermal CO_2 reduction has also been researched from the conversion of CH_4 and CO_2 to produce syngas products. This reaction is named as CO_2 dry reforming of methane (DRM) (1.10).

$$CO_2 + CH_4 \rightarrow 2CO + 2H_2 \quad (1.10)$$

DRM is an endothermic reaction ($\Delta H°_{298K}$=247 kJ/mol). Hence, the drawback of working at high temperatures and the need of photothermal catalysis as alternative process to lower the temperatures for avoiding undesired products as pollutant carbon species while syngas yield is kept or even improved. Group VIII metals have been used for this reaction like based materials on supported rhodium [57,157,158], platinum [139,159,160], nickel [161–164] or supported bimetallic structures such as Pt-Au [165] or Rh-Au [135,166] among others.

Beyond the importance of the supported metal as charge carrier promoter and the reforming metal catalyst, it is important to take into account the influence of the support. For instance, the use of semiconductor TaN as support have been reported as a beneficial for the lifetime prolongation of photo-induced charge carriers due to the transfer of electrons from metal to semiconductor, being CO_2 capable to be reduced and CH_4 by holes on the catalyst surface [8].

7. Photo thermal catalysis for formic acid dehydrogenation and CO_2 methanation.

Photo-thermal catalysis emerged as a promising process to reduce the energy consumption to carry out chemical conversion without efficiency and selectivity losses and its increase in interest by researchers from the field are solidifying its position as hot topic in the last years. However, it is still needed a long pathway to develop all the benefits of this new field into classical thermo and photochemical applications. For this purpose, we selected two different reactions of interest in the chemical field where light-assisted processes may result beneficial.

7.1. Formic acid dehydrogenation

This organic acid is abundant in biomass derivatives products and is a promising and renewable hydrogen carrier for hydrogen storage and as internal hydrogen source (hydrogen donor) for performing catalytic transfer hydrogenation reactions [167]. Hydrogen utilization as energy fuel has very well-known advantages such as high energetic combustion with zero carbon emissions after combustion (only H_2O as byproduct). However, its main limitations are associated with storage and delivering process. Then, formic acid, a glucose derivative issued from the lignocellulose biomass hydrolytic conversion chain, gained in interest as, in contrary to hydrogen, it is appropriate for storage and shipping. It has a high volumetric hydrogen content under ambient conditions, namely 53

g_{H2}/L[168] and H_2 can be produced via dehydrogenation/decarboxylation reaction (1.11). As shown in the scheme of **Fig. 23**, FA can be employed as energy storage molecule with the conversion of H_2, sustainably produced as solar fuel via water splitting, with captured CO_2. In this way, FA can be transported or stored in liquid medium as hydrogen source and be decomposed whenever it is needed to supply H_2.

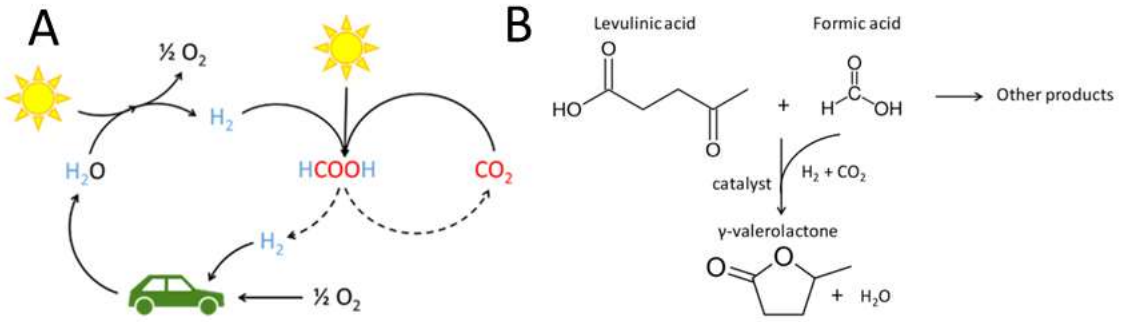

Fig. 23 *Proposed scheme for HCOOH as storage molecule of H_2 and H_2 supplier for energy applications from ref* [169] ***(A)*** *and as internal hydrogen donor for hydrogenation reactions(i.e., levulinic acid hydrogenation for GVL production) adapted from ref* [170] ***(B)***.

Its alternative application as hydrogen donor-mediated approach instead of using external pressurized hydrogen is a step forward in the design of sustainable hydrogenation processes enabling the production of high value-added chemicals. Nevertheless, formic acid can alternatively decompose as carbon monoxide and water via dehydration/decarbonylation (1.12).

$$HCOOH \rightarrow CO_2 + H_2 \quad (1.11)$$

$$HCOOH \rightarrow CO + H_2O \quad (1.12)$$

The absence of molecular hydrogen production and the presence of compounds that poison catalysts such as CO through the dehydration process makes it necessary to design a catalytic pathway that inhibits this reaction and favors the dehydrogenation one.

In the last years, FA dehydrogenation has increased in interest for heterogeneous catalysis processes, with studies devoted to noble metal based catalysts like Au [171–173], Pd [174–176], Pt [177] or Ru [178]. Recently some non-noble metal based materials have increased in interest for this reaction [179,180]. This heterogeneous catalytic reaction have been widely reported with formic acid in liquid phase, what limits the temperature range below 373K to avoid the evaporation of the reactant [181]. However, vapor-phase (gas-phase) formic acid by vapor saturation of the organic compound with an inert gas such as argon, helium, nitrogen, etc. have been proved as efficient process for unravelling the decarboxylation and decarbonylation reactions over catalytic materials due to advantages such as tuning the mass flow rate, modifying the FA concentration or widening the temperature range till 673K [169,177,182].

There are only a few studies devoted to the FA decomposition by photo-thermal catalysis. Han et al. studied the enhanced LSPR on Pt single atoms dispersed throughout Te nanowires (d=4-7nm) materials reaching a decomposition of formic acid (FA) via dehydrogenation process [167]. The authors stressed that the enhancement of formic acid decomposition under UV-light irradiation (Xe lamp, 250 mW/cm²)

in comparison with dark conditions (**Fig. 24**A,B) reaction at 25°C is carried mainly by photo-electron driven process than by a thermal-driven process caused by optical heating. However, they noted that the solution temperature increased after 40 min irradiation to values of 39°C, 38°C and 36°C with 1.1, 4.6 and 32% wt Pt/Te NWs catalysts, respectively, what is typical of the photo-thermal effect. Under dark conditions with a temperature value of 80°C, the higher the Pt loading, the higher the HCOOH decomposition. The behavior was different under light, where an optimal Pt wt. content of 1.1% on Te nanowires was observed. To distinguish between photochemical and thermochemical processes, they used some methodologies previously described in section 4. First, it is shown a correlation between the apparent quantum efficiency, AQE, and the UV-Vis spectrum (**Fig. 24**C), as well as a linear photon dependency with the reaction rate (Fig 20D) for the 1.1 wt% Pt/Te catalyst, that is related to electron driven mechanism. Nevertheless, this tendency is missing when the Pt loading increases to 32.0 wt.% (**Fig. 24**E,F), having a sublinearity which is more characteristic of thermal-driven processes. In addition, in-situ spectroscopy analysis were carried out by DRIFTS and XPS techniques to understand the different reaction steps at the catalytic surface. Then, researchers proposed the following mechanisms steps were indicated step (1.13) is the rds:

$$HCOOH^* \rightarrow HCOO^* + H^* \quad (1.13)$$

$$HCOO^* \rightarrow CO_2^{-\delta}* + H^* \quad (1.14)$$

$$CO_2^{-\delta}* \rightarrow CO_2 \quad (1.15)$$

$$2H^* \rightarrow H_2 \quad (1.16)$$

In a follow up work, the same group synthesized a noble metal free thermal catalyst to control the HCOOH adsorption tuning the oxygen coverage surfaces [38], lowering the energy barrier of HCOO* to CO_2* conversion and speeding up the HCOOH dehydrogenation process weakening the CO_2 and H_2 adsorption energy. Moskotiv and coworkers design nanocubes and nanosheets made of Pd to use its LSPR effect to produce hot charge carrier via non-radiative decay that improve formic acid dehydrogenation in an aqueous media [183]. In these conditions, water can provide some protons (H^+) to enhance the oxidation of $CO_2^{-\delta}$ to CO_2 and then desorb generating an H atom adsorb on the catalyst surface (1.17), which can react with other H atom to produce H_2.

$$H^+* + CO_2^{-\delta}* \rightarrow CO_2 + H^* \quad (1.17)$$

As it is shown in **Fig. 25**A, even if white light (AM 1.5) and visible light (>420 nm) irradiation conditions improve H_2 and CO_2 production values 5 and 120 times over nanosheets than in the absence of photons, stoichiometry between both products are far from the stoechiometrical one. For instance, H_2/CO_2 ratios were 0.59 and 0.54 in the dark and under AM1.5 illumination, respectively, in the case of Pd nanosheets. This phenomenon is mostly attributed to the properties of palladium to capture H_2, which also explains the decrease of the hydrogen production at longer times, as it is visible in **Fig. 25**B.

In **Fig. 25**C. it is presented a proposed mechanism to explain the important gain in hydrogen production between dark and illuminating conditions, where photo-induced electrons and holes generated via plasmonic non-radiative decay participate in the reaction. Hot electrons reduced the protonic ions at catalytic surface, meanwhile holes neutralize adsorbed CO_2^- species, which should also increase the CH bond breaking rate.

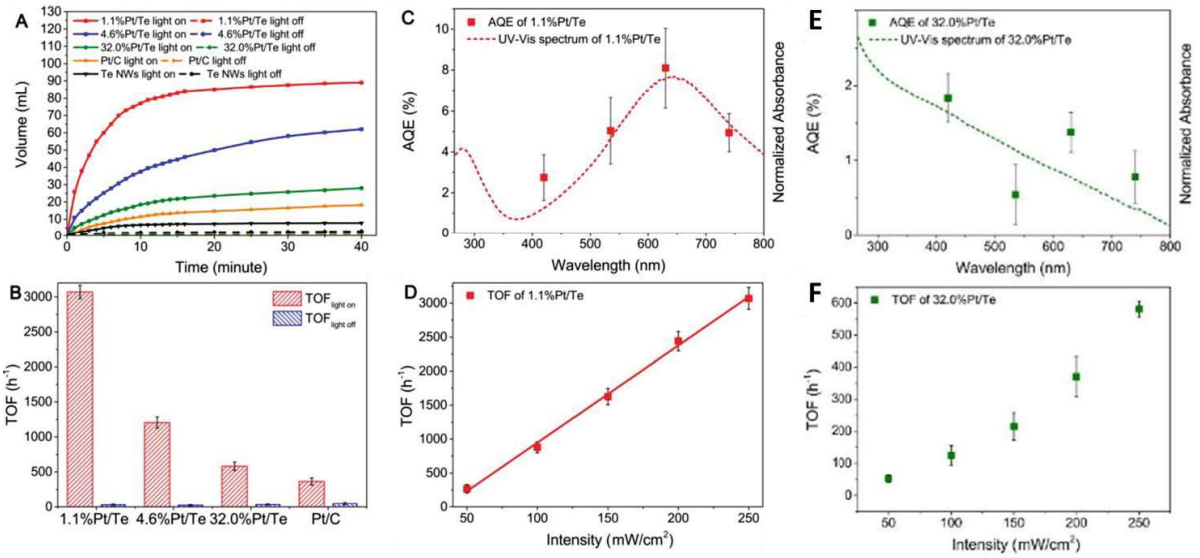

Fig. 24 A) *and* ***B)*** *Photo-thermal formic acid dehydrogenation reaction rate at dark and illuminating conditions over 1.1 to 32 wt.% Pt/Te nanowire catalysts,* ***C)*** *AQE in comparison with UV-Vis spectrum and* ***D)*** *rate photon dependence of 1.1 wt.%Pt/Te.* ***E)*** *AQE in comparison with UV-Vis spectrum and* ***F)*** *rate photon dependence of 32 wt. %Pt/Te. Figure based on ref* [167].

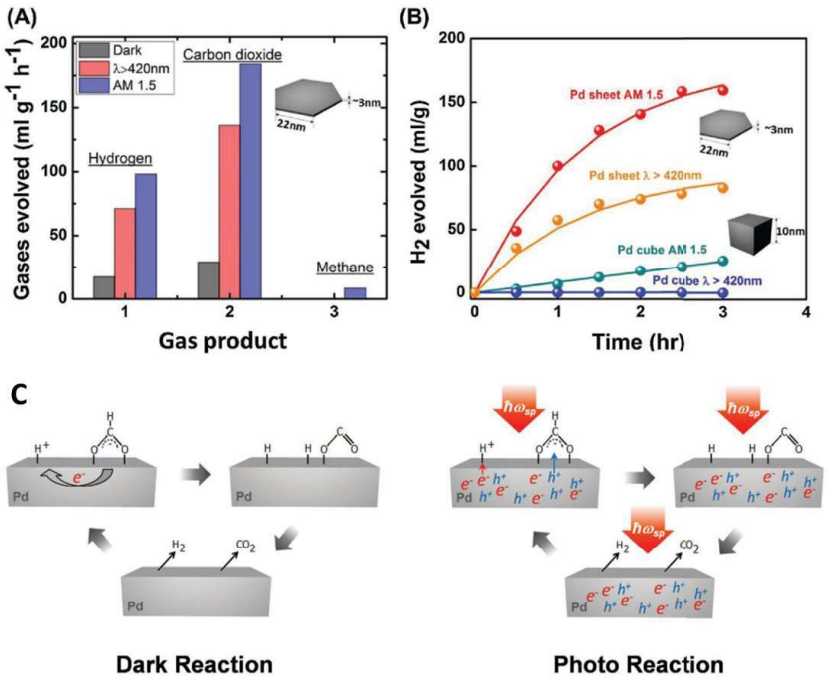

***Fig. 25 A**) Gases evolution during formic acid decomposition at dark (grey), visible light (pink) and sunlight (blue) conditions for Pd nanosheets. **B)** H_2 evolution over different Pd morphologies and light sources. **C)** Suggested mechanisms at light and dark reaction conditions. Adapted from ref* [183].

7.2. Sabatier reaction (methanation)

The CO_2 methanation (Eqn. 1.3) is a very challenging catalytic process in current chemistry advances. The hydrogenation of CO_2 to produce methane, also named as Sabatier reaction, is a spontaneous exothermic reaction that converts CO_2 into the valuable gaseous fuel SNG (synthetic natural gas) albeit at the expense of a high consumption of renewable H_2 [184]. Nevertheless, thermodynamic threshold does not allow carrying out carbon dioxide conversion at high-temperature range, and process intensification is in consequence necessary.

Moreover, we have to draw attention to the energetic request of CO_2 methanation, which needs a lot of process energy in terms of renewable H_2 supply, thus compromising process sustainability. Further advances in applied photo-thermal catalysis is also driving a reorientation in catalytic/optical materials design and synthesis. Traditional large-gap semiconductors (classically responsive to ultraviolet light irradiation) are increasingly absent or redundant components, although insulating (thermally stable) oxide supports remain important [94,185,186]. A significant exception is the study of Ru on black Si nanowires (Ru/SiNW) made by O'Brien et al [151]. A photo-enhancement of the CO_2 methanation rate to ~1 $mmol.h^{-1}.g_{cat}^{-1}$ at 150 °C, roughly double the activity at dark conditions, was investigated in more precisely with no resistive heating but thermal equilibration over 3 hours under illumination instead. Under increasing optical power (5–15 suns, 50–120 °C), the photo-enhancement over the dark case was more pronounced (x5 – x6) even though the apparent activation energy remained the same at ~54

kJ.mol^{-1}. They went on to show that only irradiation with super band-gap photons, i.e., those absorbable by Si at λ <1000 nm, contributed to the rate enhancement whereas continuum absorption by the Ru across the visible-NIR had no effect. The semiconductor photo-effect was attributed to heterolytic photoactivation of molecular H_2, and ensuing Ru-H surface bond enrichment, by charge carrier migration from the Si nanowires to the metal. The rate-determining step in the dark mechanism is believed to involve homolytic cleavage of H_2 directly on Ru and multi-step H-transfer to the active carbide Ru–C_x, itself obtained from successive dissociation of CO_2 and CO. The implied favourable alteration in the balance of steady-state (competitive) occupancy by Ru-H and Ru–C_x intermediates due to illumination should be verified by kinetic studies on the pressure exponents. This will allow proper categorization of what is likely a 'Type B' photo-thermo synergy (see Section 3).

In stark contrast, Sastre et al. have reported an extremely high "photo-thermo- activity" in CO_2 methanation over a similar catalyst, consisting of polydispersed Ru nanorods (aspect ratio ≈ 10/1) on γ-Al_2O_3 surface attributing this activity to shape-dependent visible-NIR plasmon optical absorption in Ru [187]. Under 1 sun irradiation at 150 °C the photo-enhancement was a factor of two, but on top of a very high dark conversion rate of ~50 mmol.h^{-1}.g_{cat}^{-1}. This was ascribed mainly to optical heating, whereas at higher intensities up to 8.5 suns (leading to temperatures above 200°C in combined heating mode) an excellent photo-thermo synergy became evident, producing rates 3 times higher than estimates for dark controls. The photon-to-methane conversion efficiency was high and temperature-dependent, ranging from 22.3 %, 25.0 %, to 54.8 % at catalyst temperatures of 212°C, 221°C, and 231°C, respectively. A similar photo-enhancement was observed by Wang et al. on Ru/TiO_2 catalysts upon AM1.5 sunlight illumination (1 sun) in the 150–300 °C temperature range, with a strong increase in CH_4 yield and the ability of the thermo-photo catalyst to produce CH_4 even at low temperature of 150 °C, while no CH_4 was formed in the dark [188]. The semi-conductor nature of the TiO_2 support was proposed to play a role, as no photo-enhancement was observed on a Ru/Al_2O_3 catalyst with large (> 8 eV) band bap support within an analogous temperature range. The results were explained in terms of thermodynamics and kinetics. The authors proposed that the insufficient driving forces for H_2 oxidation might be the main cause of the negligible activity obtained at room temperature for CO_2 hydrogenation. Then, they further suggested that the introduction of thermal energy, such as global temperature increase, can enhance the kinetic energy of the reactants, thus increasing the overall driving force and giving rise to substantially higher activities of CO_2 reduction in photo-thermo process mode over 150°C.

Last recent studies by the Amal's group on photo-thermal CO_2 methanation are based on the use of transition metals like Co or Ni on metal oxide materials supports widely reported for methanation like La_2O_3 and TiO_2 [189–193]. For instance, lanthanum promoted nickel catalyst (NiO_x/La_2O_3@TiO_2) is an excellent photo-thermal catalyst to selectively convert CO_2 into methane from 50°C to 400°C, having 8 times more CH_4 under solar light irradiation than in dark conditions at 200°C [193]. In-situ $^{13}CO_2$ DRIFTS revealed a strong photoactivation of HCO_2* intermediate specie. In fact, they attributed a dual function of La_2O_3, capturing CO_2 as proxy adsorption site and secondly sustaining the HCO_2* conversion by a strong interaction with NiO_x particles.

8. Rational for the selection of Ru/TiO_2 as reference photo-thermal catalyst in this work.

A photo-thermal catalyst must contain at least a photo-responsive material or component. For the two reactions of interest that have been described in the previous section, nanostructures of group VIII metals have been reported to be useful catalysts under dark and illuminating conditions. In contrast, a wide variety of supports has been used, ranging from classical bulk metal oxide supports to 2D structures or carbon based materials.

Ru is a metal catalyst of choice for several reactions (examples), including both reactions of interest selected, namely the formic acid decomposition and the CO_2 methanation. Ruthenium based catalysts have been reported for the formic acid decomposition in both homogeneous [194–196] and heterogeneous [197,198] phases. Its lower cost in comparison with other noble metals such as platinum or gold makes it more affordable to carry out industrial processes. It has been widely proved as an excellent metal catalyst for hydrogenation reactions (ref here), which makes it suitable for further applications of formic acid as internal hydrogen donor source. Furthermore, ruthenium is the most active unsupported metal for CO_2 methanation reaction [199]. In comparison with other metals, this high activity is related to the absence of deterioration during the reaction and absence of poisoning carbon deposition [200]. Extensive works on ruthenium demonstrate the possibility to tune its morphological shape, being found as spherical nanoparticles, nanorods or even doped into the support lattice [201].

Ruthenium based catalysts show evidence of being suitable for photothermal applications such as the CO_2 hydrogenation [56,151,188] or the valorization of biomass, with the conversion of microcrystalline cellulose into the 5-hydroxymethylfurfural (HMF) platform molecule [201]. However, there is not a clear consensus about the chemical processes occurring during light irradiation with these materials. For instance, Wang et al. reported a gain in the HMF yield from 18.7% to 31.0% over a $Ru/HY\text{-}SO_3H$ catalyst when is irradiated under visible light (300W Xe lamp with 420 nm cut-off filter) [202]. They assigned this improvement in the yield to the plasmon resonance effect by the supported Ru nanoparticles, promoting charge carriers to high-excited bands followed by a thermalization process. This hypothesis was supported by an increase of overall temperature on the surface from 36°C to 94°C during IR measurements. However, Guo et al. demonstrated a higher activity during Fischer Tropsch synthesis over supported Ru-wormlike particles on graphene under visible light irradiation (400-800 nm, 300 W Xe lamp) [35]. They assigned this enhancement to the photo-excited electron transfer from the metal to the $2\pi^*$ orbital of the adsorbed carbon monoxide, which can promote the C-O dissociation and then improve the catalytic activity. In addition, their selectivity values related to C_{5+} hydrocarbons increased under light irradiation, but decreased when the overall temperature were higher, what excludes any local temperature increase by light irradiation.

In contrast to the formic acid decomposition, there are some studies on CO_2 methanation with photothermal Ru based catalysts. For instance, Ye and co-workers demonstrate Ru/Al_2O_3 is enhancing the methane production via Sabatier reaction over light irradiation because the nanocatalyst is acting as an optical heater [56]. Using Ru/Si nanowires, O'Brien et al. attributed the boost of the methane production to the electron transfer from the silicon nanowire to metallic ruthenium that promotes the hydrogen activation on metal surface, considered as the rate-determining-step in dark conditions [151]. Therefore, the different photochemical and thermochemical processes that can influence a

reaction over ruthenium active sites under light irradiation makes this metal interesting to be studied for FA dehydrogenation and CO_2 methanation reactions.

As far as the support is concerned, titanium dioxide, TiO_2, is a support of interest in thermal catalysis for several kinds of reactions. It has been studied for over the last decades for a huge variety of applications, in more details in the photocatalysis field with a UV-A activation due to its photoelectronic properties as semiconductor material [4,203]. Nevertheless, TiO_2 is a support of interest in thermal catalysis for several kinds of reactions such as oxidation reactions [204–206], dehydrogenation reactions [207–209] or even industrial applications as the hydrodesulfurization of hydrocarbon oils [210] or selective catalytic reduction of NO by NH_3 [211], among others. TiO_2 presents nontoxicity, good mechanical resistance and stabilities in different environments such as acidic and oxidative ones [203], which make it suitable for use as heterogeneous catalyst support. As it is known that the properties of the support can strongly influence the performance of the catalysts, among others, reducible titania supports are considered as a versatile tool given a driving force for modifying the properties of the supported metal nanoparticles and consequently the activity of the catalysts.

For instance, in the case of the synthesis of lactone such as γ-butyrolactone or γ-valerolactone, Ru catalysts with different properties in terms of mean particle size, metal-support interaction strength or acidity were elaborated depending on the physico-physical properties of the titania support, including notably its rutile or anatase crystallographic nature, with direct influence on the catalytic behavior [212]. In the case of the hydrogenation of succinic acid, the presence of the rutile polymorph phase within the TiO_2 support was proposed not only to favor the formation of small Ru particles, but also to promote stronger metal–support interaction compared to the anatase polymorph, both features being key factors driving the performances of the Ru/TiO_2 catalysts [213].

Obviously, we have to say that the direct influence of the TiO_2 support nature does not remain restricted to Ru-based catalysts. Indeed, for the same reaction, the groups of Pinel and Epron showed that the nature of the TiO_2 support influenced the conversion obtained on Pd catalysts rather than the selectivity, the highest conversion being observed for anatase-supported samples and ascribed mainly to a good dispersion of the metal, while lower conversions were obtained using a mixed phase anatase/rutile TiO_2 support [214].

Photonic-thermal combination of the acetone oxidation reported good results over commercial pristine TiO_2 reported recently the enhancement by Lyulyukin et al. [215]. This relates to the higher bulk recombination, as well as to well known adsorption/desorption limitations for reactants and intermediates. This is a typical behavior of thermal intensification of pure photocatalysis, and should not be assigned to any photothermal effect. . The authors observed a good response in CO_2 production when they increased the temperature under UV-light irradiation. However, temperatures higher than 80-100 °C (depending on the TiO_2) caused a decrease in the conversion of acetone.

The benefit of a visible-light induced photothermal effect for the lactic acid production from a wide span of carbohydrates molecules (fructose, glucose, xylose, arabinose) was also reported by Cao et al. over a carbon-coated N-TiO_2 catalyst [216]. In this case, lactic acid yields raised over 84.9% at full conversion depending on the sugar substrate, and up to 98.9% in the particular case of pyruvaledhyde at 60°C with 10 W of simulated solar light. The authors suggested that carbon layers resulting from the incomplete burning of urea used for anionic doping of TiO_2 with nitrogen during the calcination process and wrapped around N-TiO_2 crystallites, were acting as light-to-heat antenna upon visible light

irradiation. In addition to visible light absorption, nitrogen doping was shown to favor charge separation and transfer. A thirty times upscaling experiment was successfully carried out over the carbon-coated N-TiO_2 photothermal catalyst using 3 g of saccharide substrate, that retained 71.8% of the yield to lactic acid originally obtained at the small lab-scale.

It is therefore worth investigating the combination of Ru as supported metal and of TiO_2 as support, namely by studying **Ru/TiO_2 photothermal catalysts**. The dual potential nature of TiO_2, that is here not only a semiconductor activable by UV-A light, but also a support of high interest in thermal catalysis, combined with the premises reported with supported Ru nanoparticles might favor positive synergistic effects upon combined photonic and thermal excitation. Further, Ru/TiO_2 systems are reported as excellent thermal catalysts for several applications as well as succinic acid hydrogenation [213], CO methanation [218,219] and hydrogenolysis of glycerol [220]. For instance, Ru/TiO_2 was recently reported as a very promising system capable of meeting the challenge of thermally catalyzing both the dehydrogenation of FA to H_2 and the hydrogenation of the levulinic acid biomass-derived platform molecule into the high value-added γ-valerolactone (GVL) at dark conditions [217]. Ru/TiO_2 systems are in consequence valuable to be studied as photothermal catalysts for the FA dehydrogenation, in view of their potential ability to favor the use of gas phase formic acid as internal hydrogen donor in a combined hydrogenation/dehydrogenation process. For instance, very recently, Bunrit et al. promisingly showed that Pt/TiO_2 can act as thermo- and photo catalyst for converting levulinic acid and its ester into γ-valerolactone in mild conditions using 2-propanol as hydrogen donor [221]. Unfortunately, they did not exploit this dual-functional character to explore the reaction under a dual-mode excitation.

In addition, as it was described in the previous section 7.2, Ru/TiO_2 could be used for convert CO_2 with high selectivity to methane production [188]. Further studies are needed to get a better understanding on the different mechanisms that occur during the photonic irradiation and how they can affect to the methanation enhancement. For instance, Wang et al. proposed electron-driven mechanisms for the CO_2 hydrogenation into methane on a Ru/TiO_2 catalyst. In this study, ruthenium is promoting hot electrons than can react with the adsorbates meanwhile the temperature conditions affects the kinetics, explaining the absence of methane at room temperature [188].

Additionally, and in parallel to the versatility of supports in thermal catalysis, the impact of the support materials on different properties during photo-thermal catalysis, like hot carrier lifetime, reactant adsorption or electron density in metal surface through hot carrier injection, can make appealing the study of ruthenium supported on other surfaces. For instance, it can be semiconductor materials like graphitic carbon nitride, g-C_3N_4, a 2D material that gained attention during the last decades due to its narrow band gap (2.7 eV), absorbing photons over the visible light spectra and it has been proved for photo-thermal catalysis for environmental applications [222]. Insulator materials are also worth supports. For instance, silicon dioxide share similar properties to TiO_2 as both are bulk metal oxide catalyst with strong surface basicity. Therefore, it can be interesting to take into account different catalytic supports to discuss on the different mechanisms that occur when formic acid is dehydrogenated, or CO_2 reduced.

References

[1] D. Mateo, J.L. Cerrillo, S. Durini, J. Gascon, Fundamentals and applications of photo-thermal catalysis, Chem. Soc. Rev. 50 (2021) 2173–2210. https://doi.org/10.1039/D0CS00357C.

[2] M. Beller, A. Renken, R.A. van Santen, Catalysis: From Principles to Applications, Wiley-VCH Verlag GmbH & Co. KGaA, Weinheim, Germany, 2012.

[3] N. Keller, J. Ivanez, J. Highfield, A.M. Ruppert, Photo-/thermal synergies in heterogeneous catalysis: Towards low-temperature (solar-driven) processing for sustainable energy and chemicals, Appl. Catal. B Environ. 296 (2021) 120320. https://doi.org/10.1016/j.apcatb.2021.120320.

[4] A.R. Khataee, M.B. Kasiri, Photocatalytic degradation of organic dyes in the presence of nanostructured titanium dioxide: Influence of the chemical structure of dyes, J. Mol. Catal. A Chem. 328 (2010) 8–26. https://doi.org/10.1016/j.molcata.2010.05.023.

[5] M. Ghoussoub, M. Xia, P.N. Duchesne, D. Segal, G. Ozin, Principles of photothermal gas-phase heterogeneous CO2 catalysis, Energy Environ. Sci. 12 (2019) 1122–1142. https://doi.org/10.1039/c8ee02790k.

[6] S. Tang, J. Sun, H. Hong, Q. Liu, Solar fuel from photo-thermal catalytic reactions with spectrum-selectivity: a review, Front. Energy. 11 (2017) 437–451. https://doi.org/10.1007/s11708-017-0509-z.

[7] V. Nair, M.J. Muñoz-Batista, M. Fernández-García, R. Luque, J.C. Colmenares, Thermo-Photocatalysis: Environmental and Energy Applications, ChemSusChem. 12 (2019) 2098–2116. https://doi.org/10.1002/cssc.201900175.

[8] Z. Wang, H. Song, H. Liu, J. Ye, Coupling of Solar Energy and Thermal Energy for Carbon Dioxide Reduction: Status and Prospects, Angew. Chem. Int. Ed. 59 (2020) 8016–8035. https://doi.org/10.1002/anie.201907443.

[9] R. Ma, J. Sun, D.H. Li, J.J. Wei, Review of synergistic photo-thermo-catalysis: Mechanisms, materials and applications, Int. J. Hydrogen Energy. 45 (2020) 30288–30324. https://doi.org/10.1016/j.ijhydene.2020.08.127.

[10] C. Jiang, L. Yu, S. Yang, K. Li, J. Wang, P.D. Lund, Y. Zhang, A Review of the Compound Parabolic Concentrator (CPC) with a Tubular Absorber, Energies. 13 (2020) 695. https://doi.org/10.3390/en13030695.

[11] J.A. Webb, R. Bardhan, Emerging advances in nanomedicine with engineered gold nanostructures, Nanoscale. 6 (2014) 2502. https://doi.org/10.1039/c3nr05112a.

[12] G. Mie, Beiträge zur Optik trüber Medien, speziell kolloidaler Metallösungen, Ann. Phys. 330 (1908) 377–445. https://doi.org/10.1002/andp.19083300302.

[13] P. Drude, Zur Elektronentheorie der Metalle, Ann. Phys. 306 (1900) 566–613. https://doi.org/10.1002/andp.19003060312.

[14] H. Yu, Y. Peng, Y. Yang, Z.Y. Li, Plasmon-enhanced light–matter interactions and applications, Npj Comput. Mater. 5 (2019) 1–14. https://doi.org/10.1038/s41524-019-0184-1.

[15] Y. Zhang, S. He, W. Guo, Y. Hu, J. Huang, J.R. Mulcahy, W.D. Wei, Surface-Plasmon-Driven Hot Electron Photochemistry, Chem. Rev. 118 (2018) 2927–2954. https://doi.org/10.1021/acs.chemrev.7b00430.

[16] J.J. Mock, M. Barbic, D.R. Smith, D.A. Schultz, S. Schultz, Shape effects in plasmon resonance

of individual colloidal silver nanoparticles, J. Chem. Phys. 116 (2002) 6755–6759. https://doi.org/10.1063/1.1462610.

[17] B.J. Wiley, S.H. Im, Z.Y. Li, J. McLellan, A. Siekkinen, Y. Xia, Maneuvering the surface plasmon resonance of silver nanostructures through shape-controlled synthesis, J. Phys. Chem. B. 110 (2006) 15666–15675. https://doi.org/10.1021/jp0608628.

[18] X. Huang, M.A. El-Sayed, Plasmonic photo-thermal therapy (PPTT), Alexandria J. Med. 47 (2011) 1–9. https://doi.org/10.1016/j.ajme.2011.01.001.

[19] O.A. Douglas-Gallardo, M. Berdakin, C.G. Sánchez, Atomistic Insights into Chemical Interface Damping of Surface Plasmon Excitations in Silver Nanoclusters, J. Phys. Chem. C. 120 (2016) 24389–24399. https://doi.org/10.1021/acs.jpcc.6b08519.

[20] C. Bauer, J.P. Abid, H.H. Girault, Hot adsorbate-induced retardation of the internal thermalization of nonequilibrium electrons in adsorbate-covered metal nanoparticles, J. Phys. Chem. B. 110 (2006) 4519–4523. https://doi.org/10.1021/jp060179l.

[21] C. Bauer, J.P. Abid, D. Fermin, H.H. Girault, Ultrafast chemical interface scattering as an additional decay channel for nascent nonthermal electrons in small metal nanoparticles, J. Chem. Phys. 120 (2004) 9302–9315. https://doi.org/10.1063/1.1710856.

[22] J.S. DuChene, B.C. Sweeny, A.C. Johnston-Peck, D. Su, E.A. Stach, W.D. Wei, Prolonged Hot Electron Dynamics in Plasmonic-Metal/Semiconductor Heterostructures with Implications for Solar Photocatalysis, Angew. Chem. Int. Ed. 53 (2014) 7887–7891. https://doi.org/10.1002/anie.201404259.

[23] T.P. White, K.R. Catchpole, Plasmon-enhanced internal photoemission for photovoltaics: Theoretical efficiency limits, Appl. Phys. Lett. 101 (2012). https://doi.org/10.1063/1.4746425.

[24] Y. Tian, X. Wang, D. Zhang, X. Shi, S. Wang, Effects of electron donors on the performance of plasmon-induced photovoltaic cell, J. Photochem. Photobiol. A Chem. 199 (2008) 224–229. https://doi.org/10.1016/j.jphotochem.2008.05.025.

[25] L. Du, A. Furube, K. Yamamoto, K. Hara, R. Katoh, M. Tachiya, Plasmon-Induced Charge Separation and Recombination Dynamics in Gold−TiO 2 Nanoparticle Systems: Dependence on TiO 2 Particle Size, J. Phys. Chem. C. 113 (2009) 6454–6462. https://doi.org/10.1021/jp810576s.

[26] K. Wu, J. Chen, J.R. Mcbride, T. Lian, Efficient hot-electron transfer by a plasmon-induced interfacial charge-transfer transition, 349 (2015) 3584–3588.

[27] J.A. Faucheaux, A.L.D. Stanton, P.K. Jain, Plasmon resonances of semiconductor nanocrystals: Physical principles and new opportunities, J. Phys. Chem. Lett. 5 (2014) 976–985. https://doi.org/10.1021/jz500037k.

[28] L. Yang, Y. Peng, Y. Yang, J. Liu, Z. Li, Y. Ma, Z. Zhang, Y. Wei, S. Li, Z. Huang, N.V. Long, Green and Sensitive Flexible Semiconductor SERS Substrates: Hydrogenated Black TiO2 Nanowires, ACS Appl. Nano Mater. 1 (2018) 4516–4527. https://doi.org/10.1021/acsanm.8b00796.

[29] Q. Guo, C. Li, B. Deng, S. Yuan, F. Guinea, F. Xia, Infrared Nanophotonics Based on Graphene Plasmonics, ACS Photonics. 4 (2017) 2989–2999. https://doi.org/10.1021/acsphotonics.7b00547.

[30] Y. Wang, J.Z. Ou, A.F. Chrimes, B.J. Carey, T. Daeneke, M.M.Y.A. Alsaif, M. Mortazavi, S. Zhuiykov, N. Medhekar, M. Bhaskaran, J.R. Friend, M.S. Strano, K. Kalantar-Zadeh, Plasmon Resonances of Highly Doped Two-Dimensional MoS 2, Nano Lett. 15 (2015) 883–890.

https://doi.org/10.1021/nl503563g.

[31] J. Miao, W. Hu, Y. Jing, W. Luo, L. Liao, A. Pan, S. Wu, J. Cheng, X. Chen, W. Lu, Surface Plasmon-Enhanced Photodetection in Few Layer MoS 2 Phototransistors with Au Nanostructure Arrays, Small. 11 (2015) 2392–2398. https://doi.org/10.1002/smll.201403422.

[32] Z. Liu, K. Aydin, Localized Surface Plasmons in Nanostructured Monolayer Black Phosphorus, Nano Lett. 16 (2016) 3457–3462. https://doi.org/10.1021/acs.nanolett.5b05166.

[33] S. Sarina, H.Y. Zhu, Q. Xiao, E. Jaatinen, J. Jia, Y. Huang, Z. Zheng, H. Wu, Viable photocatalysts under solar-spectrum irradiation: Nonplasmonic metal nanoparticles, Angew. Chem. - Int. Ed. 53 (2014) 2935–2940. https://doi.org/10.1002/anie.201308145.

[34] Q. Xiao, S. Sarina, A. Bo, J. Jia, H. Liu, D.P. Arnold, Y. Huang, H. Wu, H. Zhu, Visible light-driven cross-coupling reactions at lower temperatures using a photocatalyst of palladium and gold alloy nanoparticles, ACS Catal. 4 (2014) 1725–1734. https://doi.org/10.1021/cs5000284.

[35] X.Y.X.N. Guo, Z.F. Jiao, G.Q. Jin, X.Y.X.N. Guo, Photocatalytic fischer-tropsch synthesis on graphene-supported worm-like ruthenium nanostructures, ACS Catal. 5 (2015) 3836–3840. https://doi.org/10.1021/acscatal.5b00697.

[36] B. Zhu, H. Kou, Z. Liu, Z. Wang, D.K. MacHaria, M. Zhu, B. Wu, X. Liu, Z. Chen, Flexible and Washable CNT-Embedded PAN Nonwoven Fabrics for Solar-Enabled Evaporation and Desalination of Seawater, ACS Appl. Mater. Interfaces. 11 (2019) 35005–35014. https://doi.org/10.1021/acsami.9b12806.

[37] J. Yao, G. Yang, An efficient solar-enabled 2D layered alloy material evaporator for seawater desalination, J. Mater. Chem. A. 6 (2018) 3869–3876. https://doi.org/10.1039/C7TA10832J.

[38] T. Hou, Q. Luo, Q. Li, H. Zu, P. Cui, S. Chen, Y. Lin, J. Chen, X. Zheng, W. Zhu, S. Liang, J. Yang, L. Wang, Modulating oxygen coverage of Ti3C2Tx MXenes to boost catalytic activity for HCOOH dehydrogenation, Nat. Commun. 11 (2020). https://doi.org/10.1038/s41467-020-18091-7.

[39] Y. Jin, J. Chang, Y. Shi, L. Shi, S. Hong, P. Wang, A highly flexible and washable nonwoven photothermal cloth for efficient and practical solar steam generation, J. Mater. Chem. A. 6 (2018) 7942–7949. https://doi.org/10.1039/C8TA00187A.

[40] J.D. Xiao, H.L. Jiang, Metal-Organic Frameworks for Photocatalysis and Photothermal Catalysis, Acc. Chem. Res. 52 (2019) 356–366. https://doi.org/10.1021/acs.accounts.8b00521.

[41] G. Chen, Z. Jiang, A. Li, X. Chen, Z. Ma, H. Song, Cu-based MOF-derived porous carbon with highly efficient photothermal conversion performance for solar steam evaporation, J. Mater. Chem. A. 9 (2021) 16805–16813. https://doi.org/10.1039/d1ta03695e.

[42] X.-L. Zhou, X.-Y. Zhu, J.M. White, Photochemistry at adsorbate/metal interfaces, Surf. Sci. Rep. 13 (1991) 73–220. https://doi.org/10.1016/0167-5729(91)90009-M.

[43] B. Hammer, J.K. Nørskov, Theoretical surface science and catalysis—calculations and concepts, in: 2000: pp. 71–129. https://doi.org/10.1016/S0360-0564(02)45013-4.

[44] M.J. Kale, T. Avanesian, H. Xin, J. Yan, P. Christopher, Controlling catalytic selectivity on metal nanoparticles by direct photoexcitation of adsorbate-metal bonds, Nano Lett. 14 (2014) 5405–5412. https://doi.org/10.1021/nl502571b.

[45] L. Wang, Y. Dong, T. Yan, Z. Hu, A.A. Jelle, D.M. Meira, P.N. Duchesne, J.Y.Y. Loh, C. Qiu, E.E. Storey, Y. Xu, W. Sun, M. Ghoussoub, N.P. Kherani, A.S. Helmy, G.A. Ozin, Black indium oxide a photothermal CO2 hydrogenation catalyst, Nat. Commun. 11 (2020) 2432. https://doi.org/10.1038/s41467-020-16336-z.

[46] Y. Zhao, A. Dunn, J. Lin, D. Shi, Photothermal Effect of Nanomaterials for Efficient Energy Applications, Elsevier Inc., 2018. https://doi.org/10.1016/B978-0-12-814497-8.00013-8.

[47] M.J. Kale, P. Christopher, Plasmons at the interface, Science. 349 (2015) 587–588. https://doi.org/10.1126/science.aac8522.

[48] M.J. Kale, T. Avanesian, P. Christopher, Direct photocatalysis by plasmonic nanostructures, ACS Catal. 4 (2014) 116–128. https://doi.org/10.1021/cs400993w.

[49] P. Christopher, H. Xin, S. Linic, Visible-light-enhanced catalytic oxidation reactions on plasmonic silver nanostructures, Nat. Chem. 3 (2011) 467–472. https://doi.org/10.1038/nchem.1032.

[50] K.H. Kim, K. Watanabe, D. Mulugeta, H.J. Freund, D. Menzel, Enhanced photoinduced desorption from metal nanoparticles by photoexcitation of confined hot electrons using femtosecond laser pulses, Phys. Rev. Lett. 107 (2011) 20–23. https://doi.org/10.1103/PhysRevLett.107.047401.

[51] M.J. Landry, A. Gellé, B.Y. Meng, C.J. Barrett, A. Moores, Surface-Plasmon-Mediated Hydrogenation of Carbonyls Catalyzed by Silver Nanocubes under Visible Light, ACS Catal. 7 (2017) 6128–6133. https://doi.org/10.1021/acscatal.7b02128.

[52] P. Christopher, H. Xin, A. Marimuthu, S. Linic, Singular characteristics and unique chemical bond activation mechanisms of photocatalytic reactions on plasmonic nanostructures, Nat. Mater. 11 (2012) 1044–1050. https://doi.org/10.1038/nmat3454.

[53] C. Wang, O. Ranasingha, S. Natesakhawat, P.R. Ohodnicki, M. Andio, J.P. Lewis, C. Matranga, Visible light plasmonic heating of Au–ZnO for the catalytic reduction of CO2, Nanoscale. 5 (2013) 6968–6974. https://doi.org/10.1039/c3nr02001k.

[54] X. Zhang, X. Li, D. Zhang, N.Q. Su, W. Yang, H.O. Everitt, J. Liu, Product selectivity in plasmonic photocatalysis for carbon dioxide hydrogenation, Nat. Commun. 8 (2017) 14542. https://doi.org/10.1038/ncomms14542.

[55] T. Olsen, J. Schiøtz, Origin of Power Laws for Reactions at Metal Surfaces Mediated by Hot Electrons, Phys. Rev. Lett. 103 (2009). https://doi.org/10.1103/PhysRevLett.103.238301.

[56] X. Meng, T. Wang, L. Liu, S. Ouyang, P. Li, H. Hu, T. Kako, H. Iwai, A. Tanaka, J. Ye, Photothermal conversion of CO2 into CH4 with H2 over Group VIII nanocatalysts: An alternative approach for solar fuel production, Angew. Chem. - Int. Ed. 53 (2014) 11478–11482. https://doi.org/10.1002/anie.201404953.

[57] H. Song, X. Meng, Z.J.Z. Wang, Z.J.Z. Wang, H. Chen, Y. Weng, F. Ichihara, M. Oshikiri, T. Kako, J. Ye, Visible-Light-Mediated Methane Activation for Steam Methane Reforming under Mild Conditions: A Case Study of Rh/TiO2 Catalysts, ACS Catal. 8 (2018) 7556–7565. https://doi.org/10.1021/acscatal.8b01787.

[58] P. Li, G. Xiao, Y. Zhao, H. Su, Tuning the Product Selectivity of the α-Alkylation of Ketones with Primary Alcohols using Oxidized Titanium Nitride Photocatalysts and Visible Light, ACS Catal. 10 (2020) 3640–3649. https://doi.org/10.1021/acscatal.9b04921.

[59] J. Guo, Y. Zhang, L. Shi, Y. Zhu, M.F. Mideksa, K. Hou, W. Zhao, D. Wang, M. Zhao, X. Zhang, J. Lv, J. Zhang, X. Wang, Z. Tang, Boosting Hot Electrons in Hetero-superstructures for Plasmon-Enhanced Catalysis, J. Am. Chem. Soc. 139 (2017) 17964–17972. https://doi.org/10.1021/jacs.7b08903.

[60] Y. Dubi, Y. Sivan, “Hot” electrons in metallic nanostructures—non-thermal carriers or

heating?, Light Sci. Appl. 8 (2019). https://doi.org/10.1038/s41377-019-0199-x.

[61] Y. Sivan, J. Baraban, I.W. Un, Y. Dubi, Comment on "Quantifying hot carrier and thermal contributions in plasmonic photocatalysis," Science. 364 (2019) eaaw9367. https://doi.org/10.1126/science.aaw9367.

[62] Y. Dubi, I.W. Un, Y. Sivan, Thermal effects – an alternative mechanism for plasmon-assisted photocatalysis, Chem. Sci. 11 (2020) 5017–5027. https://doi.org/10.1039/C9SC06480J.

[63] P.K. Jain, Comment on "Thermal effects – an alternative mechanism for plasmon-assisted photocatalysis" by Y. Dubi, I. W. Un and Y. Sivan, Chem. Sci. , 2020, 11 , 5017, Chem. Sci. 11 (2020) 9022–9023. https://doi.org/10.1039/D0SC02914A.

[64] Y. Dubi, I.W. Un, Y. Sivan, Reply to the "Comment on 'thermal effects-an alternative mechanism for plasmon-assisted photocatalysis'" by P. Jain,: Chem. Sci., 2020, 11, DOI: 10.1039/D0SC02914A, Chem. Sci. 11 (2020) 9024–9025. https://doi.org/10.1039/d0sc03335a.

[65] W. Hou, W.H. Hung, P. Pavaskar, A. Goeppert, M. Aykol, S.B. Cronin, Photocatalytic conversion of CO2 to hydrocarbon fuels via plasmon-enhanced absorption and metallic interband transitions, ACS Catal. 1 (2011) 929–936. https://doi.org/10.1021/cs2001434.

[66] G. Baffou, I. Bordacchini, A. Baldi, R. Quidant, Simple experimental procedures to distinguish photothermal from hot-carrier processes in plasmonics, Light Sci. Appl. 9 (2020). https://doi.org/10.1038/s41377-020-00345-0.

[67] L. Zhou, J.M.P. Martirez, J. Finzel, C. Zhang, D.F. Swearer, S. Tian, H. Robatjazi, M. Lou, L. Dong, L. Henderson, P. Christopher, E.A. Carter, P. Nordlander, N.J. Halas, Light-driven methane dry reforming with single atomic site antenna-reactor plasmonic photocatalysts, Nat. Energy. 5 (2020) 61–70. https://doi.org/10.1038/s41560-019-0517-9.

[68] H. Song, X. Meng, T.D. Dao, W. Zhou, H. Liu, L. Shi, H. Zhang, T. Nagao, T. Kako, J. Ye, Light-Enhanced Carbon Dioxide Activation and Conversion by Effective Plasmonic Coupling Effect of Pt and Au Nanoparticles, ACS Appl. Mater. Interfaces. 10 (2018) 408–416. https://doi.org/10.1021/acsami.7b13043.

[69] M. Bonn, S. Funk, C. Hess, D.N. Denzler, C. Stampfl, M. Scheffler, M. Wolf, G. Ertl, Phonon-versus electron-mediated desorption and oxidation of CO on Ru(0001), Science. 285 (1999) 1042–1045. https://doi.org/10.1126/science.285.5430.1042.

[70] S. Funk, M. Bonn, D.N. Denzler, C. Hess, M. Wolf, G. Ertl, Desorption of CO from Ru(001) induced by near-infrared femtosecond laser pulses, J. Chem. Phys. 112 (2000) 9888–9897. https://doi.org/10.1063/1.481626.

[71] S. Fang, Y. Liu, Z. Sun, J. Lang, C. Bao, Y.H. Hu, Photocatalytic hydrogen production over Rh-loaded TiO2: What is the origin of hydrogen and how to achieve hydrogen production from water?, Appl. Catal. B Environ. 278 (2020) 119316. https://doi.org/10.1016/j.apcatb.2020.119316.

[72] S. Fang, Z. Sun, Y.H. Hu, Insights into the Thermo-Photo Catalytic Production of Hydrogen from Water on a Low-Cost NiOx-Loaded TiO2 Catalyst, ACS Catal. 9 (2019) 5047–5056. https://doi.org/10.1021/acscatal.9b01110.

[73] S.I. Nikitenko, T. Chave, C. Cau, H.P. Brau, V. Flaud, Photothermal Hydrogen Production Using Noble-Metal-Free Ti@TiO2 Core-Shell Nanoparticles under Visible-NIR Light Irradiation, ACS Catal. 5 (2015) 4790–4795. https://doi.org/10.1021/acscatal.5b01401.

[74] D.G. Cahill, P. V. Braun, G. Chen, D.R. Clarke, S. Fan, K.E. Goodson, P. Keblinski, W.P. King, G.D.

Mahan, A. Majumdar, H.J. Maris, S.R. Phillpot, E. Pop, L. Shi, Nanoscale thermal transport. II. 2003–2012, Appl. Phys. Rev. 1 (2014) 011305. https://doi.org/10.1063/1.4832615.

[75] F. Menges, P. Mensch, H. Schmid, H. Riel, A. Stemmer, B. Gotsmann, Temperature mapping of operating nanoscale devices by scanning probe thermometry, Nat. Commun. 7 (2016) 1–6. https://doi.org/10.1038/ncomms10874.

[76] M. Mecklenburg, W.A. Hubbard, E.R. White, R. Dhall, S.B. Cronin, S. Aloni, B.C. Regan, Nanoscale temperature mapping in operating microelectronic devices, Science. 347 (2015) 629–632. https://doi.org/10.1126/science.aaa2433.

[77] L. Zhou, D.F. Swearer, H. Robatjazi, A. Alabastri, P. Christopher, E.A. Carter, P. Nordlander, N.J. Halas, Response to Comment on "Quantifying hot carrier and thermal contributions in plasmonic photocatalysis," Science. 364 (2019). https://doi.org/10.1126/science.aaw9545.

[78] C.D.S. Brites, P.P. Lima, N.J.O. Silva, A. Millán, V.S. Amaral, F. Palacio, L.D. Carlos, Thermometry at the nanoscale, Nanoscale. 4 (2012) 4799–4829. https://doi.org/10.1039/c2nr30663h.

[79] M. Barella, I.L. Violi, J. Gargiulo, L.P. Martinez, F. Goschin, V. Guglielmotti, D. Pallarola, S. Schlücker, M. Pilo-Pais, G.P. Acuna, S.A. Maier, E. Cortés, F.D. Stefani, In Situ Photothermal Response of Single Gold Nanoparticles through Hyperspectral Imaging Anti-Stokes Thermometry, ACS Nano. 15 (2021) 2458–2467. https://doi.org/10.1021/acsnano.0c06185.

[80] A. Espinosa, G.R. Castro, J. Reguera, C. Castellano, J. Castillo, J. Camarero, C. Wilhelm, M.A. García, Á. Muñoz-Noval, Photoactivated Nanoscale Temperature Gradient Detection Using X-ray Absorption Spectroscopy as a Direct Nanothermometry Method, Nano Lett. 21 (2021) 769–777. https://doi.org/10.1021/acs.nanolett.0c04477.

[81] M. Fickert, M. Assebban, J. Canet-Ferrer, G. Abellan, Phonon properties and photo-thermal oxidation of micromechanically exfoliated antimonene nanosheets, 2D Mater. 8 (2021). https://doi.org/10.1088/2053-1583/abb877.

[82] J.-L. Yang, H.-J. Wang, H. Zhang, Z.-Q. Tian, J.-F. Li, Probing Hot Electron Behaviors by Surface-Enhanced Raman Spectroscopy, Cell Reports Phys. Sci. 1 (2020) 100184. https://doi.org/10.1016/j.xcrp.2020.100184.

[83] X. Tan, J. Melkersson, S. Wu, L. Wang, J. Zhang, Noble-Metal-Free Materials for Surface-Enhanced Raman Spectroscopy Detection, ChemPhysChem. 17 (2016) 2630–2639. https://doi.org/10.1002/cphc.201600286.

[84] G.C. Roda, V. Loddo, L. Palmisano, F. Parrino, Chapter 6. Special needs and characteristic features of (photo)catalytic reactors with a review of the proposed Solutions, in: Heterog. Photocatal. Relationships with Heterog. Catal. Perspect., Elsevier B.V., 2019: pp. 177–213. https://doi.org/10.1016/B978-0-444-64015-4.00006-7.

[85] A. Rabl, Active solar collectors and their applications, Oxford University Press, New York, 1985.

[86] S. Malato Rodríguez, J. Blanco Gálvez, M.I. Maldonado Rubio, P. Fernández Ibáñez, D. Alarcón Padilla, M. Collares Pereira, J. Farinha Mendes, J. Correia de Oliveira, Engineering of solar photocatalytic collectors, Sol. Energy. 77 (2004) 513–524. https://doi.org/10.1016/j.solener.2004.03.020.

[87] W.T. Welford, R. Winston, D.C. Sinclair, The Optics of Nonimaging Concentrators: Light and Solar Energy, Phys. Today. 33 (1980) 56–57. https://doi.org/10.1063/1.2914121.

[88] S.E. Berrizbeitia, E. Jadraque Gago, T. Muneer, Empirical Models for the Estimation of Solar Sky-Diffuse Radiation. A Review and Experimental Analysis, Energies. 13 (2020) 701. https://doi.org/10.3390/en13030701.

[89] M. Geyer, V. Quaschning, Solar thermal power: the seamless solar link to the conventional power world, Renew. Energy World. 3 (2000) 184–191.

[90] M. Gao, P.K.N. Connor, G.W. Ho, Plasmonic photothermic directed broadband sunlight harnessing for seawater catalysis and desalination, Energy Environ. Sci. 9 (2016) 3151–3160. https://doi.org/10.1039/C6EE00971A.

[91] Y.L. He, J. Xiao, Z.D. Cheng, Y.B. Tao, A MCRT and FVM coupled simulation method for energy conversion process in parabolic trough solar collector, Renew. Energy. 36 (2011) 976–985. https://doi.org/10.1016/j.renene.2010.07.017.

[92] Z.D. Cheng, Y.L. He, F.Q. Cui, R.J. Xu, Y.B. Tao, Numerical simulation of a parabolic trough solar collector with nonuniform solar flux conditions by coupling FVM and MCRT method, Sol. Energy. 86 (2012) 1770–1784. https://doi.org/10.1016/j.solener.2012.02.039.

[93] W. Chamsa-ard, S. Brundavanam, C. Fung, D. Fawcett, G. Poinern, Nanofluid Types, Their Synthesis, Properties and Incorporation in Direct Solar Thermal Collectors: A Review, Nanomaterials. 7 (2017) 131. https://doi.org/10.3390/nano7060131.

[94] E.T. Kho, T.H. Tan, E. Lovell, R.J. Wong, J. Scott, R. Amal, A review on photo-thermal catalytic conversion of carbon dioxide, Green Energy Environ. 2 (2017) 204–217. https://doi.org/10.1016/j.gee.2017.06.003.

[95] A. Castedo, E. Mendoza, I. Angurell, J. Llorca, Silicone microreactors for the photocatalytic generation of hydrogen, Catal. Today. 273 (2016) 106–111. https://doi.org/10.1016/j.cattod.2016.02.053.

[96] M. Oelgemöller, Solar Photochemical Synthesis: From the Beginnings of Organic Photochemistry to the Solar Manufacturing of Commodity Chemicals, Chem. Rev. 116 (2016) 9664–9682. https://doi.org/10.1021/acs.chemrev.5b00720.

[97] A. Castedo, A. Casanovas, I. Angurell, L. Soler, J. Llorca, Effect of temperature on the gas-phase photocatalytic H2 generation using microreactors under UVA and sunlight irradiation, Fuel. 222 (2018) 327–333. https://doi.org/10.1016/j.fuel.2018.02.128.

[98] E. Taboada, I. Angurell, J. Llorca, Dynamic photocatalytic hydrogen production from ethanol–water mixtures in an optical fiber honeycomb reactor loaded with Au/TiO2, J. Catal. 309 (2014) 460–467. https://doi.org/10.1016/j.jcat.2013.10.025.

[99] B. Han, Y.H. Hu, Highly Efficient Temperature-Induced Visible Light Photocatalytic Hydrogen Production from Water, J. Phys. Chem. C. 119 (2015) 18927–18934. https://doi.org/10.1021/acs.jpcc.5b04894.

[100] K.K. Ghuman, T.E. Wood, L.B. Hoch, C.A. Mims, G.A. Ozin, C.V. Singh, Illuminating CO2 reduction on frustrated Lewis pair surfaces: investigating the role of surface hydroxides and oxygen vacancies on nanocrystalline In2O3−x(OH)y, Phys. Chem. Chem. Phys. 17 (2015) 14623–14635. https://doi.org/10.1039/C5CP02613J.

[101] U. Caudillo-Flores, G. Agostini, C. Marini, A. Kubacka, M. Fernández-García, Hydrogen thermo-photo production using Ru/TiO2: Heat and light synergistic effects, Appl. Catal. B Environ. 256 (2019) 117790. https://doi.org/10.1016/j.apcatb.2019.117790.

[102] M.J. Muñoz-Batista, A.M. Eslava-Castillo, A. Kubacka, M. Fernández-García, Thermo-photo

degradation of 2-propanol using a composite ceria-titania catalyst: Physico-chemical interpretation from a kinetic model, Appl. Catal. B Environ. 225 (2018) 298–306. https://doi.org/10.1016/j.apcatb.2017.11.073.

[103] J. Hou, Y. Li, M. Mao, Y. Yue, G. Neville Greaves, X. Zhao, Full solar spectrum light driven thermocatalysis with extremely high efficiency on nanostructured Ce ion substituted OMS-2 catalyst for VOCs purification, Nanoscale. 7 (2015) 2633–2640. https://doi.org/10.1039/c4nr06410k.

[104] M. Zeng, Y. Li, F. Liu, Y. Yang, M. Mao, X. Zhao, Cu doped OL-1 nanoflower: A UV–vis-infrared light-driven catalyst for gas-phase environmental purification with very high efficiency, Appl. Catal. B Environ. 200 (2017) 521–529. https://doi.org/10.1016/j.apcatb.2016.07.042.

[105] L. Lan, Y. Li, M. Zeng, M. Mao, L. Ren, Y. Yang, H. Liu, L. Yun, X. Zhao, Efficient UV–vis-infrared light-driven catalytic abatement of benzene on amorphous manganese oxide supported on anatase TiO2 nanosheet with dominant {001} facets promoted by a photothermocatalytic synergetic effect, Appl. Catal. B Environ. 203 (2017) 494–504. https://doi.org/10.1016/j.apcatb.2016.10.047.

[106] X. Zhang, X. Li, M.E. Reish, D. Zhang, N.Q. Su, Y. Gutiérrez, F. Moreno, W. Yang, H.O. Everitt, J. Liu, Plasmon-Enhanced Catalysis: Distinguishing Thermal and Nonthermal Effects, Nano Lett. 18 (2018) 1714–1723. https://doi.org/10.1021/acs.nanolett.7b04776.

[107] B. Xie, R.J. Wong, T.H. Tan, M. Higham, E.K. Gibson, D. Decarolis, J. Callison, K.-F. Aguey-Zinsou, M. Bowker, C.R.A. Catlow, J. Scott, R. Amal, Synergistic ultraviolet and visible light photo-activation enables intensified low-temperature methanol synthesis over copper/zinc oxide/alumina, Nat. Commun. 11 (2020) 1615. https://doi.org/10.1038/s41467-020-15445-z.

[108] A.A. Upadhye, I. Ro, X. Zeng, H.J. Kim, I. Tejedor, M.A. Anderson, J.A. Dumesic, G.W. Huber, Plasmon-enhanced reverse water gas shift reaction over oxide supported Au catalysts, Catal. Sci. Technol. 5 (2015) 2590–2601. https://doi.org/10.1039/c4cy01183j.

[109] J.G. Highfield, M. Prairie, A. Renken, In-situ drift spectroscopy in a continuous recycle reactor: a versatile tool for catalytic process research, Catal. Today. 9 (1991) 39–46. https://doi.org/10.1016/0920-5861(91)85005-S.

[110] H. Li, M. Rivallan, F. Thibault-Starzyk, A. Travert, F.C. Meunier, Effective bulk and surface temperatures of the catalyst bed of FT-IR cells used for in situ and operando studies, Phys. Chem. Chem. Phys. 15 (2013) 7321. https://doi.org/10.1039/c3cp50442e.

[111] A. Kosuga, Y.Y. Yamamoto, M. Miyai, M. Matsuzawa, Y. Nishimura, S. Hidaka, K. Yamamoto, S. Tanaka, Y.Y. Yamamoto, S. Tokonami, T. Iida, A high performance photothermal film with spherical shell-type metallic nanocomposites for solar thermoelectric conversion, Nanoscale. 7 (2015) 7580–7584. https://doi.org/10.1039/c5nr00943j.

[112] Y. Li, J. Huang, T. Peng, J. Xu, X. Zhao, Photothermocatalytic Synergetic Effect Leads to High Efficient Detoxification of Benzene on TiO2 and Pt/TiO2 Nanocomposite, ChemCatChem. 2 (2010) 1082–1087. https://doi.org/10.1002/cctc.201000085.

[113] X. Wang, D. Zeng, C. Xie, Temperature-dependent photothermocatalytic mineralization of gaseous benzene based on rutile TiO2 nanorod array, Mater. Lett. 139 (2015) 336–339. https://doi.org/10.1016/j.matlet.2014.10.071.

[114] M. Bellardita, R. Fiorenza, L. D'Urso, L. Spitaleri, A. Gulino, G. Compagnini, S. Scirè, L. Palmisano, Exploring the Photothermo-Catalytic Performance of Brookite TiO2-CeO2 Composites, Catalysts. 10 (2020) 765. https://doi.org/10.3390/catal10070765.

[115] J. Kim, K.M. Twaddle, J. Hu, H. Byun, Sunlight-Induced Synthesis of Various Gold Nanoparticles and Their Heterogeneous Catalytic Properties on a Paper-Based Substrate, (2014).

[116] Y. Gu, Y. Jiao, X. Zhou, A. Wu, B. Buhe, H. Fu, Strongly coupled Ag/TiO2 heterojunctions for effective and stable photothermal catalytic reduction of 4-nitrophenol, Nano Res. 11 (2018) 126–141. https://doi.org/10.1007/s12274-017-1612-5.

[117] G. Wang, B. Huang, Z. Lou, Z. Wang, X. Qin, X. Zhang, Y. Dai, Valence state heterojunction Mn3O4/MnCO3: Photo and thermal synergistic catalyst, Appl. Catal. B Environ. 180 (2016) 6–12. https://doi.org/10.1016/j.apcatb.2015.06.010.

[118] Y. Lu, Y. Yang, T. Zhang, Z. Ge, H. Chang, P. Xiao, Y. Xie, L. Hua, Q. Li, H. Li, B. Ma, N. Guan, Y. Ma, Y. Chen, Photoprompted Hot Electrons from Bulk Cross-Linked Graphene Materials and Their Efficient Catalysis for Atmospheric Ammonia Synthesis, ACS Nano. 10 (2016) 10507–10515. https://doi.org/10.1021/acsnano.6b06472.

[119] C. Mao, L. Yu, J. Li, J. Zhao, L. Zhang, Energy-confined solar thermal ammonia synthesis with K/Ru/TiO2-xHx, Appl. Catal. B Environ. 224 (2018) 612–620. https://doi.org/10.1016/j.apcatb.2017.11.010.

[120] X. Li, X. Zhang, H.O. Everitt, J. Liu, Light-Induced Thermal Gradients in Ruthenium Catalysts Significantly Enhance Ammonia Production, Nano Lett. 19 (2019) 1706–1711. https://doi.org/10.1021/acs.nanolett.8b04706.

[121] W. Gao, R. Gao, Y. Zhao, M. Peng, C. Song, M. Li, S. Li, J. Liu, W. Li, Y. Deng, M. Zhang, J. Xie, G. Hu, Z. Zhang, R. Long, X.-D. Wen, D. Ma, Photo-Driven Syngas Conversion to Lower Olefins over Oxygen-Decorated Fe5C2 Catalyst, Chem. 4 (2018) 2917–2928. https://doi.org/10.1016/j.chempr.2018.09.017.

[122] L. Wang, Y. Zhang, X. Gu, Y. Zhang, H. Su, Insight into the role of UV-irradiation in photothermal catalytic Fischer–Tropsch synthesis over TiO2 nanotube-supported cobalt nanoparticles, Catal. Sci. Technol. 8 (2018) 601–610. https://doi.org/10.1039/C7CY02304A.

[123] S. Luo, X. Ren, H. Lin, H. Song, J. Ye, Plasmonic photothermal catalysis for solar-to-fuel conversion: current status and prospects, Chem. Sci. 12 (2021) 5701–5719. https://doi.org/10.1039/d1sc00064k.

[124] M. Zeng, Y. Li, M. Mao, J. Bai, L. Ren, X. Zhao, Synergetic effect between photocatalysis on TiO2 and thermocatalysis on CeO2 for gas-phase oxidation of benzene on TiO2/CeO2 nanocomposites, ACS Catal. 5 (2015) 3278–3286. https://doi.org/10.1021/acscatal.5b00292.

[125] J.J. Li, E.Q. Yu, S.C. Cai, X. Chen, J. Chen, H.P. Jia, Y.J. Xu, Noble metal free, CeO2/LaMnO3 hybrid achieving efficient photo-thermal catalytic decomposition of volatile organic compounds under IR light, Appl. Catal. B Environ. 240 (2019) 141–152. https://doi.org/10.1016/j.apcatb.2018.08.069.

[126] J. Hou, Y. Li, M. Mao, Y. Yue, G. Neville Greaves, X. Zhao, Full solar spectrum light driven thermocatalysis with extremely high efficiency on nanostructured Ce ion substituted OMS-2 catalyst for VOCs purification, Nanoscale. 7 (2015) 2633–2640. https://doi.org/10.1039/c4nr06410k.

[127] Y. Zhou, D.E. Doronkin, Z. Zhao, P.N. Plessow, J. Jelic, B. Detlefs, T. Pruessmann, F. Studt, J.D. Grunwaldt, Photothermal Catalysis over Nonplasmonic Pt/TiO2 Studied by Operando HERFD-XANES, Resonant XES, and DRIFTS, ACS Catal. 8 (2018) 11398–11406. https://doi.org/10.1021/acscatal.8b03724.

[128] L. Ye, K.H. Chu, B. Wang, D. Wu, H. Xie, G. Huang, H.Y. Yip, P.K. Wong, Noble-metal loading

reverses temperature dependent photocatalytic hydrogen generation in methanol–water solutions, Chem. Commun. 52 (2016) 11657–11660. https://doi.org/10.1039/C6CC05689J.

[129] X. Liu, L. Ye, Z. Ma, C. Han, L. Wang, Z. Jia, F. Su, H. Xie, Photothermal effect of infrared light to enhance solar catalytic hydrogen generation, Catal. Commun. 102 (2017) 13–16. https://doi.org/10.1016/j.catcom.2017.08.014.

[130] X. Chen, L. Liu, P.Y. Yu, S.S. Mao, Increasing Solar Absorption for Photocatalysis with Black Hydrogenated Titanium Dioxide Nanocrystals, Science. 331 (2011) 746–750. https://doi.org/10.1126/science.1200448.

[131] X. Han, L. Song, H. Xu, S. Ouyang, Light-driven low-temperature syngas production from CH3OH and H2O over a Pt@SrTiO3 photothermal catalyst, Catal. Sci. Technol. 8 (2018) 2515–2518. https://doi.org/10.1039/C8CY00539G.

[132] Y. Zhao, W. Gao, S. Li, G.R. Williams, A.H. Mahadi, D. Ma, Solar- versus Thermal-Driven Catalysis for Energy Conversion, Joule. 3 (2019) 920–937. https://doi.org/10.1016/j.joule.2019.03.003.

[133] Y. Zhao, B. Zhao, J. Liu, G. Chen, R. Gao, S. Yao, M. Li, Q. Zhang, L. Gu, J. Xie, X. Wen, L.-Z. Wu, C.-H. Tung, D. Ma, T. Zhang, Oxide-Modified Nickel Photocatalysts for the Production of Hydrocarbons in Visible Light, Angew. Chem. Int. Ed. 55 (2016) 4215–4219. https://doi.org/10.1002/anie.201511334.

[134] Y. Wang, Q. Xia, Fischer-Tropsch Synthesis Steps into the Solar Era: Lower Olefins from Syngas, Chem. 4 (2018) 2741–2743. https://doi.org/10.1016/j.chempr.2018.11.020.

[135] H. Liu, X. Meng, T.D. Dao, H. Zhang, P. Li, K. Chang, T. Wang, M. Li, T. Nagao, J. Ye, Conversion of Carbon Dioxide by Methane Reforming under Visible-Light Irradiation: Surface-Plasmon-Mediated Nonpolar Molecule Activation, Angew. Chem. Int. Ed. 54 (2015) 11545–11549. https://doi.org/10.1002/anie.201504933.

[136] H. Liu, M. Li, T.D. Dao, Y. Liu, W. Zhou, L. Liu, X. Meng, T. Nagao, J. Ye, Design of PdAu alloy plasmonic nanoparticles for improved catalytic performance in CO2 reduction with visible light irradiation, Nano Energy. 26 (2016) 398–404. https://doi.org/10.1016/j.nanoen.2016.05.045.

[137] H. Liu, H. Song, X. Meng, L. Yang, J. Ye, Light irradiation enhanced CO2 reduction with methane: A case study in size-dependent optical property of Ni nanoparticles, Catal. Today. 335 (2019) 187–192. https://doi.org/10.1016/j.cattod.2018.11.005.

[138] B. Han, W. Wei, L. Chang, P. Cheng, Y.H. Hu, Efficient Visible Light Photocatalytic CO2 Reforming of CH4, ACS Catal. 6 (2016) 494–497. https://doi.org/10.1021/acscatal.5b02653.

[139] F. Pan, X. Xiang, W. Deng, H. Zhao, X. Feng, Y. Li, A Novel Photo-thermochemical Approach for Enhanced Carbon Dioxide Reforming of Methane, ChemCatChem. 10 (2018) 940–945. https://doi.org/10.1002/cctc.201701565.

[140] H. Liu, H. Song, W. Zhou, X. Meng, J. Ye, A Promising Application of Optical Hexagonal TaN in Photocatalytic Reactions, Angew. Chem. Int. Ed. 57 (2018) 16781–16784. https://doi.org/10.1002/anie.201810886.

[141] L. Wang, Y. Wang, Y. Cheng, Z. Liu, Q. Guo, M.N. Ha, Z. Zhao, Hydrogen-treated mesoporous WO3 as a reducing agent of CO2 to fuels (CH4 and CH3OH) with enhanced photothermal catalytic performance, J. Mater. Chem. A. 4 (2016) 5314–5322. https://doi.org/10.1039/C5TA10180H.

[142] M.N. Ha, G. Lu, Z. Liu, L. Wang, Z. Zhao, 3DOM-LaSrCoFeO 6−δ as a highly active catalyst for the thermal and photothermal reduction of CO 2 with H 2 O to CH 4, J. Mater. Chem. A. 4 (2016) 13155–13165. https://doi.org/10.1039/C6TA05402A.

[143] E. Fabbri, A. Habereder, K. Waltar, R. Kötz, T.J. Schmidt, Developments and perspectives of oxide-based catalysts for the oxygen evolution reaction, Catal. Sci. Technol. 4 (2014) 3800–3821. https://doi.org/10.1039/C4CY00669K.

[144] L. Wang, M.N. Ha, Z. Liu, Z. Zhao, Mesoporous WO3 modified by Mo for enhancing reduction of CO2 to solar fuels under visible light and thermal conditions, Integr. Ferroelectr. 172 (2016) 97–108. https://doi.org/10.1080/10584587.2016.1176507.

[145] D. Zheng, G. Wei, L. Xu, Q. Guo, J. Hu, N. Sha, Z. Zhao, LaNixFe1-xO3 (0 ≤ x ≤1) as photothermal catalysts for hydrocarbon fuels production from CO2 and H2O, J. Photochem. Photobiol. A Chem. 377 (2019) 182–189. https://doi.org/10.1016/j.jphotochem.2019.03.045.

[146] J. Ren, S. Ouyang, H. Xu, X. Meng, T. Wang, D. Wang, J. Ye, Targeting Activation of CO2 and H2 over Ru-Loaded Ultrathin Layered Double Hydroxides to Achieve Efficient Photothermal CO2 Methanation in Flow-Type System, Adv. Energy Mater. 7 (2017) 1–7. https://doi.org/10.1002/aenm.201601657.

[147] S. Kattel, W. Yu, X. Yang, B. Yan, Y. Huang, W. Wan, P. Liu, J.G. Chen, CO2 Hydrogenation over Oxide-Supported PtCo Catalysts: The Role of the Oxide Support in Determining the Product Selectivity, Angew. Chem. - Int. Ed. 55 (2016) 7968–7973. https://doi.org/10.1002/anie.201601661.

[148] H. Robatjazi, H. Zhao, D.F. Swearer, N.J. Hogan, L. Zhou, A. Alabastri, M.J. McClain, P. Nordlander, N.J. Halas, Plasmon-induced selective carbon dioxide conversion on earth-abundant aluminum-cuprous oxide antenna-reactor nanoparticles, Nat. Commun. 8 (2017) 1–9. https://doi.org/10.1038/s41467-017-00055-z.

[149] H. Zhang, T. Wang, J. Wang, H. Liu, T.D. Dao, M. Li, G. Liu, X. Meng, K. Chang, L. Shi, T. Nagao, J. Ye, Surface-Plasmon-Enhanced Photodriven CO2Reduction Catalyzed by Metal-Organic-Framework-Derived Iron Nanoparticles Encapsulated by Ultrathin Carbon Layers, Adv. Mater. 28 (2016) 3703–3710. https://doi.org/10.1002/adma.201505187.

[150] B. Lu, F. Quan, Z. Sun, F. Jia, L. Zhang, Photothermal reverse-water-gas-shift over Au/CeO2 with high yield and selectivity in CO2 conversion, Catal. Commun. 129 (2019) 105724. https://doi.org/10.1016/j.catcom.2019.105724.

[151] P.G. O'Brien, A. Sandhel, T.E. Wood, A.A. Jelle, L.B. Hoch, D.D. Perovic, C.A. Mims, G.A. Ozin, Photomethanation of gaseous CO2 over ru/silicon nanowire catalysts with visible and near-infrared photons, Adv. Sci. 1 (2014) 1–7. https://doi.org/10.1002/advs.201400001.

[152] Z. jun Wang, H. Song, H. Pang, Y. Ning, T.D. Dao, Z. Wang, H. Chen, Y. Weng, Q. Fu, T. Nagao, Y. Fang, J. Ye, Photo-assisted methanol synthesis via CO2 reduction under ambient pressure over plasmonic Cu/ZnO catalysts, Appl. Catal. B Environ. 250 (2019) 10–16. https://doi.org/10.1016/j.apcatb.2019.03.003.

[153] S. Kattel, P.J. Ramírez, J.G. Chen, J.A. Rodriguez, P. Liu, Active sites for CO2 hydrogenation to methanol on Cu/ZnO catalysts, Science. 355 (2017) 1296–1299. https://doi.org/10.1126/science.aal3573.

[154] S. Kattel, P. Liu, J.G. Chen, Tuning Selectivity of CO2 Hydrogenation Reactions at the Metal/Oxide Interface, J. Am. Chem. Soc. 139 (2017) 9739–9754. https://doi.org/10.1021/jacs.7b05362.

[155] F. Yu, C. Wang, H. Ma, M. Song, D. Li, Y. Li, S. Li, X. Zhang, Y. Liu, Revisiting Pt/TiO2 photocatalysts for thermally assisted photocatalytic reduction of CO2, Nanoscale. 12 (2020) 7000–7010. https://doi.org/10.1039/c9nr09743k.

[156] K. Wang, R. Jiang, T. Peng, X. Chen, W. Dai, X. Fu, Modeling the effect of Cu doped TiO2 with carbon dots on CO2 methanation by H2O in a photo-thermal system, Appl. Catal. B Environ. 256 (2019) 117780. https://doi.org/10.1016/j.apcatb.2019.117780.

[157] Y. Cho, S. Shoji, A. Yamaguchi, T. Hoshina, T. Fujita, H. Abe, M. Miyauchi, Visible-light-driven dry reforming of methane using a semiconductor-supported catalyst, Chem. Commun. 56 (2020) 4611–4614. https://doi.org/10.1039/d0cc00729c.

[158] S. Shoji, X. Peng, A. Yamaguchi, R. Watanabe, C. Fukuhara, Y. Cho, T. Yamamoto, S. Matsumura, M.W. Yu, S. Ishii, T. Fujita, H. Abe, M. Miyauchi, Photocatalytic uphill conversion of natural gas beyond the limitation of thermal reaction systems, Nat. Catal. 3 (2020) 148–153. https://doi.org/10.1038/s41929-019-0419-z.

[159] B. Han, W. Wei, L. Chang, P. Cheng, Y.H. Hu, Efficient Visible Light Photocatalytic CO2 Reforming of CH4, ACS Catal. 6 (2016) 494–497. https://doi.org/10.1021/acscatal.5b02653.

[160] M. Mao, Q. Zhang, Y. Yang, Y. Li, H. Huang, Z. Jiang, Q. Hu, X. Zhao, Solar-light-driven CO2 reduction by methane on Pt nanocrystals partially embedded in mesoporous CeO2 nanorods with high light-to-fuel efficiency, Green Chem. 20 (2018) 2857–2869. https://doi.org/10.1039/c8gc01058g.

[161] H. Liu, T.D. Dao, L. Liu, X. Meng, T. Nagao, J. Ye, Light assisted CO2 reduction with methane over group VIII metals: Universality of metal localized surface plasmon resonance in reactant activation, Appl. Catal. B Environ. 209 (2017) 183–189. https://doi.org/10.1016/j.apcatb.2017.02.080.

[162] H. Liu, X. Meng, T.D. Dao, L. Liu, P. Li, G. Zhao, T. Nagao, L. Yang, J. Ye, Light assisted CO2 reduction with methane over SiO2 encapsulated Ni nanocatalysts for boosted activity and stability, J. Mater. Chem. A. 5 (2017) 10567–10573. https://doi.org/10.1039/c7ta00704c.

[163] Q. Zhang, M. Mao, Y. Li, Y. Yang, H. Huang, Z. Jiang, Q. Hu, S. Wu, X. Zhao, Novel photoactivation promoted light-driven CO2 reduction by CH4 on Ni/CeO2 nanocomposite with high light-to-fuel efficiency and enhanced stability, Appl. Catal. B Environ. 239 (2018) 555–564. https://doi.org/10.1016/j.apcatb.2018.08.052.

[164] Z. Rao, Y. Cao, Z. Huang, Z. Yin, W. Wan, M. Ma, Y. Wu, J. Wang, G. Yang, Y. Cui, Z. Gong, Y. Zhou, Insights into the Nonthermal Effects of Light in Dry Reforming of Methane to Enhance the H 2 /CO Ratio Near Unity over Ni/Ga 2 O 3, ACS Catal. 11 (2021) 4730–4738. https://doi.org/10.1021/acscatal.0c04826.

[165] H. Song, X. Meng, T.D. Dao, W. Zhou, H. Liu, L. Shi, H. Zhang, T. Nagao, T. Kako, J. Ye, Light-Enhanced Carbon Dioxide Activation and Conversion by Effective Plasmonic Coupling Effect of Pt and Au Nanoparticles, ACS Appl. Mater. Interfaces. 10 (2018) 408–416. https://doi.org/10.1021/acsami.7b13043.

[166] B. László, K. Baán, E. Varga, A. Oszkó, A. Erdőhelyi, Z. Kónya, J. Kiss, Photo-induced reactions in the CO2-methane system on titanate nanotubes modified with Au and Rh nanoparticles, Appl. Catal. B Environ. 199 (2016) 473–484. https://doi.org/10.1016/j.apcatb.2016.06.057.

[167] L. Han, L. Zhang, H. Wu, H. Zu, P. Cui, J. Guo, R. Guo, J. Ye, J. Zhu, X. Zheng, L. Yang, Y. Zhong, S. Liang, L. Wang, Anchoring Pt Single Atoms on Te Nanowires for Plasmon-Enhanced Dehydrogenation of Formic Acid at Room Temperature, Adv. Sci. 6 (2019).

https://doi.org/10.1002/advs.201900006.

[168] C. Guan, Y. Pan, T. Zhang, M.J. Ajitha, K.W. Huang, An Update on Formic Acid Dehydrogenation by Homogeneous Catalysis, Chem. - An Asian J. 15 (2020) 937–946. https://doi.org/10.1002/asia.201901676.

[169] J.T. Gray, S.W. Kang, J. Il Yang, N. Kruse, J.S. McEwen, J. Chan Park, S. Ha, Unravelling the reaction mechanism of gas-phase formic acid decomposition on highly dispersed Mo2C nanoparticles supported on graphene flakes, Appl. Catal. B Environ. 264 (2020). https://doi.org/10.1016/j.apcatb.2019.118478.

[170] A. García, R. Sanchis, F.J. Llopis, I. Vázquez, M.P. Pico, M.L. López, I. Álvarez-Serrano, B. Solsona, Ni supported on natural clays as a catalyst for the transformation of levulinic acid into γ-valerolactone without the addition of molecular hydrogen, Energies. 13 (2020). https://doi.org/10.3390/en13133448.

[171] T. Kecskés, J. Raskó, J. Kiss, FTIR and mass spectrometric study of HCOOH interaction with TiO2 supported Rh and Au catalysts, Appl. Catal. A Gen. 268 (2004) 9–16. https://doi.org/10.1016/j.apcata.2004.03.021.

[172] M. Yadav, Q. Xu, Liquid-phase chemical hydrogen storage materials, Energy Environ. Sci. 5 (2012) 9698–9725. https://doi.org/10.1039/c2ee22937d.

[173] S. Singh, S. Li, R. Carrasquillo-Flores, A.C. Alba-Rubio, J.A. Dumesic, M. Mavrikakis, Formic acid decomposition on Au catalysts: DFT, microkinetic modeling, and reaction kinetics experiments, AIChE J. 60 (2014) 1303–1319. https://doi.org/10.1002/aic.14401.

[174] H. jin Jeon, Y.M. Chung, Hydrogen production from formic acid dehydrogenation over Pd/C catalysts: Effect of metal and support properties on the catalytic performance, Appl. Catal. B Environ. 210 (2017) 212–222. https://doi.org/10.1016/j.apcatb.2017.03.070.

[175] Z. Chang, G. Thornton, Effect of Pd on the interaction of formic acid with TiO2(110), Surf. Sci. (2000). https://doi.org/10.1016/S0039-6028(00)00458-1.

[176] J. García-Aguilar, M. Navlani-García, Á. Berenguer-Murcia, K. Mori, Y. Kuwahara, H. Yamashita, D. Cazorla-Amorós, Evolution of the PVP-Pd surface interaction in nanoparticles through the case study of formic acid decomposition, Langmuir. 32 (2016) 12110–12118. https://doi.org/10.1021/acs.langmuir.6b03149.

[177] F. Solymosi, Á. Koós, N. Liliom, I. Ugrai, Production of CO-free H2 from formic acid. A comparative study of the catalytic behavior of Pt metals on a carbon support, J. Catal. 279 (2011) 213–219. https://doi.org/10.1016/j.jcat.2011.01.023.

[178] M. Zacharska, O.Y. Podyacheva, L.S. Kibis, A.I. Boronin, B. V. Senkovskiy, E.Y. Gerasimov, O.P. Taran, A.B. Ayusheev, V.N. Parmon, J.J. Leahy, D.A. Bulushev, Ruthenium Clusters on Carbon Nanofibers for Formic Acid Decomposition: Effect of Doping the Support with Nitrogen, ChemCatChem. 7 (2015) 2910–2917. https://doi.org/10.1002/cctc.201500216.

[179] C. Tang, A.E. Surkus, F. Chen, M.M. Pohl, G. Agostini, M. Schneider, H. Junge, M. Beller, A Stable Nanocobalt Catalyst with Highly Dispersed CoNx Active Sites for the Selective Dehydrogenation of Formic Acid, Angew. Chem. - Int. Ed. 56 (2017) 16616–16620. https://doi.org/10.1002/anie.201710766.

[180] S. Li, J. Scaranto, M. Mavrikakis, On the Structure Sensitivity of Formic Acid Decomposition on Cu Catalysts, Top. Catal. 59 (2016) 1580–1588. https://doi.org/10.1007/s11244-016-0672-1.

[181] X. Wang, Q. Meng, L. Gao, Z. Jin, J. Ge, C. Liu, W. Xing, Recent progress in hydrogen production

from formic acid decomposition, Int. J. Hydrogen Energy. 43 (2018) 7055–7071. https://doi.org/10.1016/j.ijhydene.2018.02.146.

[182] S. Bhandari, S. Rangarajan, C.T. Maravelias, J.A. Dumesic, M. Mavrikakis, Reaction Mechanism of Vapor-Phase Formic Acid Decomposition over Platinum Catalysts: DFT, Reaction Kinetics Experiments, and Microkinetic Modeling, ACS Catal. 10 (2020) 4112–4126. https://doi.org/10.1021/acscatal.9b05424.

[183] B. Wu, J. Lee, S. Mubeen, Y.S. Jun, G.D. Stucky, M. Moskovits, Plasmon-Mediated Photocatalytic Decomposition of Formic Acid on Palladium Nanostructures, Adv. Opt. Mater. 4 (2016) 1041–1046. https://doi.org/10.1002/adom.201600055.

[184] P. Frontera, A. Macario, M. Ferraro, P.L. Antonucci, Supported catalysts for CO2 methanation: A review, Catalysts. 7 (2017) 1–28. https://doi.org/10.3390/catal7020059.

[185] X. Meng, L. Liu, S. Ouyang, H. Xu, D. Wang, N. Zhao, J. Ye, Nanometals for Solar-to-Chemical Energy Conversion: From Semiconductor-Based Photocatalysis to Plasmon-Mediated Photocatalysis and Photo-Thermocatalysis, Adv. Mater. 28 (2016) 6781–6803. https://doi.org/10.1002/adma.201600305.

[186] X. Wang, F. Wang, Y. Sang, H. Liu, Full-Spectrum Solar-Light-Activated Photocatalysts for Light-Chemical Energy Conversion, Adv. Energy Mater. 7 (2017) 1700473. https://doi.org/10.1002/aenm.201700473.

[187] F. Sastre, C. Versluis, N. Meulendijks, J. Rodríguez-Fernández, J. Sweelssen, K. Elen, M.K. Van Bael, T. den Hartog, M.A. Verheijen, P. Buskens, Sunlight-Fueled, Low-Temperature Ru-Catalyzed Conversion of CO2 and H2 to CH4 with a High Photon-to-Methane Efficiency, ACS Omega. 4 (2019) 7369–7377. https://doi.org/10.1021/acsomega.9b00581.

[188] C. Wang, S. Fang, S. Xie, Y. Zheng, Y.H. Hu, Thermo-photo catalytic CO2 hydrogenation over Ru/TiO2, J. Mater. Chem. A. 8 (2020) 7390–7394. https://doi.org/10.1039/C9TA13275A.

[189] S. Ullah, E.C. Lovell, T.H. Tan, B. Xie, P. V. Kumar, R. Amal, J. Scott, Photoenhanced CO2 methanation over La2O3 promoted Co/TiO2 catalysts, Appl. Catal. B Environ. 294 (2021) 120248. https://doi.org/10.1016/j.apcatb.2021.120248.

[190] S. Jantarang, E.C. Lovell, T.H. Tan, B. Xie, J. Scott, R. Amal, Altering the influence of ceria oxygen vacancies in Ni/CexSiyO2for photothermal CO2methanation, Catal. Sci. Technol. 11 (2021) 5297–5309. https://doi.org/10.1039/d1cy00136a.

[191] B. Xie, E. Lovell, T.H. Tan, S. Jantarang, M. Yu, J. Scott, R. Amal, Emerging material engineering strategies for amplifying photothermal heterogeneous CO2 catalysis, J. Energy Chem. 59 (2021) 108–125. https://doi.org/10.1016/j.jechem.2020.11.005.

[192] S. Jantarang, S. Ligori, J. Horlyck, E.C. Lovell, T.H. Tan, B. Xie, R. Amal, J. Scott, Plasma-induced catalyst support defects for the photothermal methanation of carbon dioxide, Materials (Basel). 14 (2021). https://doi.org/10.3390/ma14154195.

[193] T.H. Tan, B. Xie, Y.H. Ng, S.F.B. Abdullah, H.Y.M. Tang, N. Bedford, R.A. Taylor, K.F. Aguey-Zinsou, R. Amal, J. Scott, Unlocking the potential of the formate pathway in the photo-assisted Sabatier reaction, Nat. Catal. 3 (2020) 1034–1043. https://doi.org/10.1038/s41929-020-00544-3.

[194] A. Boddien, B. Loges, H. Junge, F. Gärtner, J.R. Noyes, M. Beller, Continuous Hydrogen Generation from Formic Acid: Highly Active and Stable Ruthenium Catalysts, Adv. Synth. Catal. 351 (2009) 2517–2520. https://doi.org/10.1002/adsc.200900431.

[195] A. Boddien, B. Loges, H. Junge, M. Beller, Hydrogen Generation at Ambient Conditions: Application in Fuel Cells, ChemSusChem. 1 (2008) 751–758. https://doi.org/10.1002/cssc.200800093.

[196] B. Loges, A. Boddien, H. Junge, M. Beller, Controlled Generation of Hydrogen from Formic Acid Amine Adducts at Room Temperature and Application in H 2 /O 2 Fuel Cells, Angew. Chem. Int. Ed. 47 (2008) 3962–3965. https://doi.org/10.1002/anie.200705972.

[197] L. Deng, Y. Zhao, J. Li, Y. Fu, B. Liao, Q.X. Guo, Conversion of levulinic acid and formic acid into γ-valerolactone over heterogeneous catalysts, ChemSusChem. 3 (2010) 1172–1175. https://doi.org/10.1002/cssc.201000163.

[198] W. Gan, P.J. Dyson, G. Laurenczy, Heterogeneous Silica-Supported Ruthenium Phosphine Catalysts for Selective Formic Acid Decomposition, ChemCatChem. 5 (2013) 3124–3130. https://doi.org/10.1002/cctc.201300246.

[199] S. Rönsch, J. Schneider, S. Matthischke, M. Schlüter, M. Götz, J. Lefebvre, P. Prabhakaran, S. Bajohr, Review on methanation – From fundamentals to current projects, 166 (2016) 276–296. https://doi.org/10.1016/j.fuel.2015.10.111.

[200] P.J. Lunde, F.L. Kester, Carbon Dioxide Methanation on a Ruthenium Catalyst, Ind. Eng. Chem. Process Des. Dev. 13 (1974) 27–33. https://doi.org/10.1021/i260049a005.

[201] D.C. Upham, A.R. Derk, S. Sharma, H. Metiu, E.W. McFarland, CO2 methanation by Ru-doped ceria: the role of the oxidation state of the surface, Catal. Sci. Technol. 5 (2015) 1783–1791. https://doi.org/10.1039/C4CY01106F.

[202] A. Wang, P. Berton, H. Zhao, S.L. Bryant, M.G. Kibria, J. Hu, Plasmon-Enhanced 5-Hydroxymethylfurfural Production from the Photothermal Conversion of Cellulose in a Biphasic Medium, ACS Sustain. Chem. Eng. 9 (2021) 16115–16122. https://doi.org/10.1021/acssuschemeng.1c04592.

[203] S. Bagheri, N. Muhd Julkapli, S. Bee Abd Hamid, Titanium dioxide as a catalyst support in heterogeneous catalysis, Sci. World J. 2014 (2014). https://doi.org/10.1155/2014/727496.

[204] J. Huang, S. Wang, Y. Zhao, X. Wang, S. Wang, S. Wu, S. Zhang, W. Huang, Synthesis and characterization of CuO/TiO2 catalysts for low-temperature CO oxidation, Catal. Commun. 7 (2006) 1029–1034. https://doi.org/10.1016/j.catcom.2006.05.001.

[205] Y.-L. Shen, S.-Y. Chen, J.-M. Song, I.-G. Chen, Ultra-long Pt nanolawns supported on TiO2-coated carbon fibers as 3D hybrid catalyst for methanol oxidation, Nanoscale Res. Lett. 7 (2012) 237. https://doi.org/10.1186/1556-276X-7-237.

[206] Y.P.G. Chua, G.T.K.K. Gunasooriya, M. Saeys, E.G. Seebauer, Controlling the CO oxidation rate over Pt/TiO2 catalysts by defect engineering of the TiO2 support, J. Catal. 311 (2014) 306–313. https://doi.org/10.1016/j.jcat.2013.12.007.

[207] A.H.S. Kootenaei, J. Towfighi, A. Khodadadi, Y. Mortazavi, Stability and catalytic performance of vanadia supported on nanostructured titania catalyst in oxidative dehydrogenation of propane, Appl. Surf. Sci. 298 (2014) 26–35. https://doi.org/10.1016/j.apsusc.2013.12.172.

[208] G. Liang, L. He, H. Cheng, W. Li, X. Li, C. Zhang, Y. Yu, F. Zhao, The hydrogenation/dehydrogenation activity of supported Ni catalysts and their effect on hexitols selectivity in hydrolytic hydrogenation of cellulose, J. Catal. 309 (2014) 468–476. https://doi.org/10.1016/j.jcat.2013.10.022.

[209] M. Setnička, P. Čičmanec, R. Bulánek, A. Zukal, J. Pastva, Hexagonal mesoporous

titanosilicates as support for vanadium oxide—Promising catalysts for the oxidative dehydrogenation of n-butane, Catal. Today. 204 (2013) 132–139. https://doi.org/10.1016/j.cattod.2012.07.028.

[210] R. Palcheva, L. Dimitrov, G. Tyuliev, A. Spojakina, K. Jiratova, TiO2 nanotubes supported NiW hydrodesulphurization catalysts: Characterization and activity, Appl. Surf. Sci. 265 (2013) 309–316. https://doi.org/10.1016/j.apsusc.2012.11.001.

[211] S. Okazaki, M. Kumasaka, J. Yoshida, K. Kosaka, K. Tanabe, Effect of sulfate ion on the catalytic activity of molybdenum oxide-titanium dioxide (MoOx-TiO2) for the reduction of nitric oxide with ammonia, Ind. Eng. Chem. Prod. Res. Dev. 20 (1981) 301–304. https://doi.org/10.1021/i300002a013.

[212] A.M. Ruppert, J. Grams, M. Jędrzejczyk, J. Matras-Michalska, N. Keller, K. Ostojska, P. Sautet, Titania-Supported Catalysts for Levulinic Acid Hydrogenation: Influence of Support and its Impact on γ-Valerolactone Yield, ChemSusChem. 8 (2015) 1538–1547. https://doi.org/10.1002/cssc.201403332.

[213] M. Brzezinska, J. Niemeier, Y. Louven, N. Keller, R. Palkovits, A.M. Ruppert, TiO2 supported Ru catalysts for the hydrogenation of succinic acid: influence of the support, Catal. Sci. Technol. 10 (2020) 6860–6869. https://doi.org/10.1039/D0CY01446J.

[214] B. Tapin, F. Epron, C. Especel, B.K. Ly, C. Pinel, M. Besson, Study of Monometallic Pd/TiO 2 Catalysts for the Hydrogenation of Succinic Acid in Aqueous Phase, ACS Catal. 3 (2013) 2327–2335. https://doi.org/10.1021/cs400534x.

[215] M. Lyulyukin, N. Kovalevskiy, I. Prosvirin, D. Selishchev, D. Kozlov, Thermo-photoactivity of pristine and modified titania photocatalysts under UV and blue light, J. Photochem. Photobiol. A Chem. 425 (2022) 113675. https://doi.org/10.1016/j.jphotochem.2021.113675.

[216] Y. Cao, D. Chen, Y. Meng, S. Saravanamurugan, H. Li, Visible-light-driven prompt and quantitative production of lactic acid from biomass sugars over a N-TiO2 photothermal catalyst, Green Chem. 23 (2021) 10039–10049. https://doi.org/10.1039/D1GC03057D.

[217] J. Wojciechowska, M. Jędrzejczyk, J. Grams, N. Keller, A.M. Ruppert, Enhanced Production of γ-Valerolactone with an Internal Source of Hydrogen on Ca-Modified TiO 2 Supported Ru Catalysts, ChemSusChem. 12 (2019) 639–650. https://doi.org/10.1002/cssc.201801974.

[218] P. Panagiotopoulou, D.I. Kondarides, X.E. Verykios, Mechanistic study of the selective methanation of CO over Ru/TiO 2 catalyst: Identification of active surface species and reaction pathways, J. Phys. Chem. C. 115 (2011) 1220–1230. https://doi.org/10.1021/jp106538z.

[219] P. Panagiotopoulou, D.I. Kondarides, X.E. Verykios, Mechanistic aspects of the selective methanation of CO over Ru/TiO 2 catalyst, Catal. Today. 181 (2012) 138–147. https://doi.org/10.1016/j.cattod.2011.05.030.

[220] J. Feng, J. Wang, Y. Zhou, H. Fu, H. Chen, X. Li, Effect of base additives on the selective hydrogenolysis of glycerol over Ru/TiO2 catalyst, Chem. Lett. 36 (2007) 1274–1275. https://doi.org/10.1246/cl.2007.1274.

[221] A. Bunrit, T. Butburee, M. Liu, Z. Huang, K. Meeporn, C. Phawa, J. Zhang, S. Kuboon, H. Liu, K. Faungnawakij, F. Wang, Photo–Thermo-Dual Catalysis of Levulinic Acid and Levulinate Ester to γ-Valerolactone, ACS Catal. 12 (2022) 1677–1685. https://doi.org/10.1021/acscatal.1c04959.

[222] P. Chen, F. Dong, M. Ran, J. Li, Synergistic photo-thermal catalytic NO purification of MnOx/g-C3N4: Enhanced performance and reaction mechanism, Cuihua Xuebao/Chinese J. Catal. 39 (2018) 619–629. https://doi.org/10.1016/S1872-2067(18)63029-3.

CHAPTER 2: Experimental procedure

1. Catalytic activity

1.1. Reactor and light source

The catalytic tests were performed in a continuous-flow mode in a photo-thermo reactor consisting in a Harrick Scientific HVC-MRA 5 reaction chamber made from SS-316 alloy material, as it is represented in **Fig. 26**. The catalyst is placed into the reactor as a thin layer at a given surface density (depending on the catalyst mass used) on a stainless meshed grid (400 x 400 mesh, pore size 0.038 mm, 6.3 mm diameter), which is homogeneously heated using an external cartridge heater monitored by a K-type thermocouple (±1 °C), and using a high flow rate water cooling system for maintaining a constant (bulk) temperature. The location of both inlet and outlet flows makes the catalyst operating in a downstream flow-through mode. The catalyst was irradiated *via* a SiO_2 window (13 x 2 mm) using a Thorlab M365LP1 LED (λ = 365 nm) with tuneable and calibrated irradiance within the 0-400 mW/cm^2 range. The emission spectrum of the Thorlab M365LP1 LED is shown in **Fig. 26**A.

The photon flux to which the catalyst was exposed, was measured by locating the sensor of a radiometer (1919-R optical power meter, Newport) at the place of the catalyst bed.

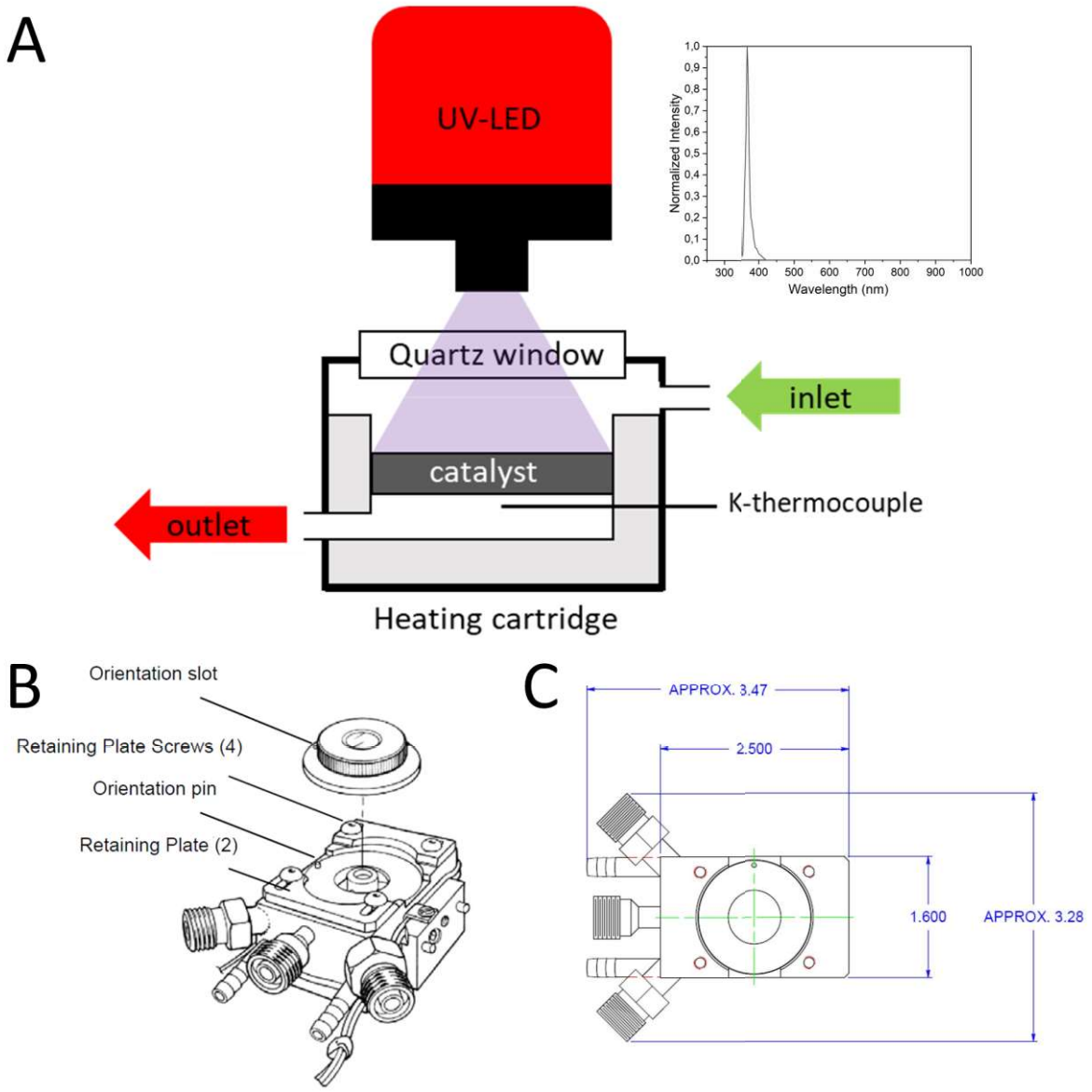

Fig. 26 *Schemes of the Harrick Scientific HVC-MRA 5 reaction chamber used as photo-thermal reactor A) during the catalytic process where green and red arrows correspond to inlet and outlet respectively. Emission spectrum of the LED UV-source appears in the inlet figure. B) the different pieces that compose the reactor and C) top-view of the reactor with length values in inches.*

1.2. Dehydrogenation of formic acid to H_2

A scheme of the set-up used for conducting the catalytic tests is presented in **Fig. 27**. The catalytic tests were carried out with a FA concentration of 4600 ppmv and employing argon as carrier gas with a total flow rate of 14.7 mL/min. The FA-containing inlet flow was obtained by diluting a concentrated FA/Ar flow with a pure Ar carrier flow. To achieve this, an Ar flow (Air Liquide, ALPHAGAZ™ 1, ≥ 99,999 %) was bubbled in a temperature-controlled saturator containing liquid-phase formic acid (HCOOH, FA, Sigma Aldrich, >95 %) at 15 °C and atmospheric pressure conditions. Therefore, the concentration of gas phase HCOOH was related to the vapour pressure of HCOOH at the working temperature and pressure conditions. This concentrated FA/Ar flow was further mixed with an additional Ar flow to obtain the required FA concentration at the working flow rate, corresponding to a Weight hourly space velocity (WHSV) of 4.24 h^{-1}, calculated as follows:

$$\text{WHSV} = \frac{flow\ rate\ \left(\frac{ml}{h}\right) * [FA]_0 * MW_{FA}}{m_{catalyst} * 24.43} \quad (2.1)$$

Where $[FA]_0$ is the initial concentration of formic acid in the flow, MW_{FA} is the molecular weight of formic acid and $m_{catalyst}$ is the mass of the catalyst.

In-Flow Bronkhorst flow meter (Bronkhorst® High-Tech, the Netherlands) allowed the control of the FA-containing air flow, while the main Ar carrier flow was controlled *via* a Brooks 5850 massflow meter.

Most of the tests were performed with a catalyst mass of 1.8 mg, that corresponded to a surface density of 5.77 mg/cm^2 and to a FA specific molar rate of 67.2 mmol g^{-1}h^{-1}.

Prior to any experiment, residual oxygen was removed by flushing the reactor under Ar. All lines were thermostated to avoid adsorption of reactants or products, or water condensation. The photo-/thermo- catalytic behavior was obtained by *on-line* quantification of the outlet flow using a R3000A gas micro-chromatography (SRA instruments), equipped with micro-TCDs, and allowing the quantification of CH_4, HCOOH, H_2, O_2, CO, CO_2 and organics on 5A molecular sieve, OV1, PoraPlotQ and Stabilwax columns. The activity of the catalyst was expressed in terms of FA conversion, H_2 selectivity, as well as of H_2, CO_2 and CO production in mmol g^{-1} h^{-1}, calculated as follows (Eqs. 2.2-2.4).

$$FA\ conversion\ (\%) = \frac{[H_2] + [CO]}{[FA_{in}]} \cdot 100 \quad (2.2)$$

$$H_2\ selectivity\ (\%) = \frac{[H_2]}{[H_2] + [CO]} \cdot 100 \quad (2.3)$$

$$X\ production\ (mmol\ g^{-1} h^{-1}) = \frac{\left[\frac{[X](ppm) * flow\ rate\ (\frac{ml}{\min})}{24.43(\frac{ml}{mmol})} \cdot 60\left(\frac{\min}{h}\right) \cdot 10\text{^}(-6)\right]}{m_{catalyst}(g)} \quad (2.4)$$

Where [X] corresponds to concentration of the product *X* in the flow, namely here H_2, CO and CO_2.

The carbon balance was calculated as follows:

$$C\ balance\ (\%) = \frac{[CO_2]+[CO]+[FA_{out}]}{[FA_{in}]} \cdot 100 \quad (2.5)$$

where $[FA_{in}]$ and $[FA_{out}]$ are, respectively, the inlet and outlet FA concentrations, while $[H_2]$, [CO] and $[CO_2]$ correspond to the concentrations of hydrogen, carbon monoxide and CO_2, respectively, in the outlet flow.

It must be said that whatever the reaction conditions (temperature and light irradiance), H_2 and CO_2 were formed with an equimolar ratio associated to the dehydrogenation path (see the corresponding figures in both Chapters 3 and 4), so that H_2 or CO_2 can be independently chosen for calculating both FA conversion and H_2 selectivity. The carbon balance was calculated within the 98–102 % range for all catalytic tests.

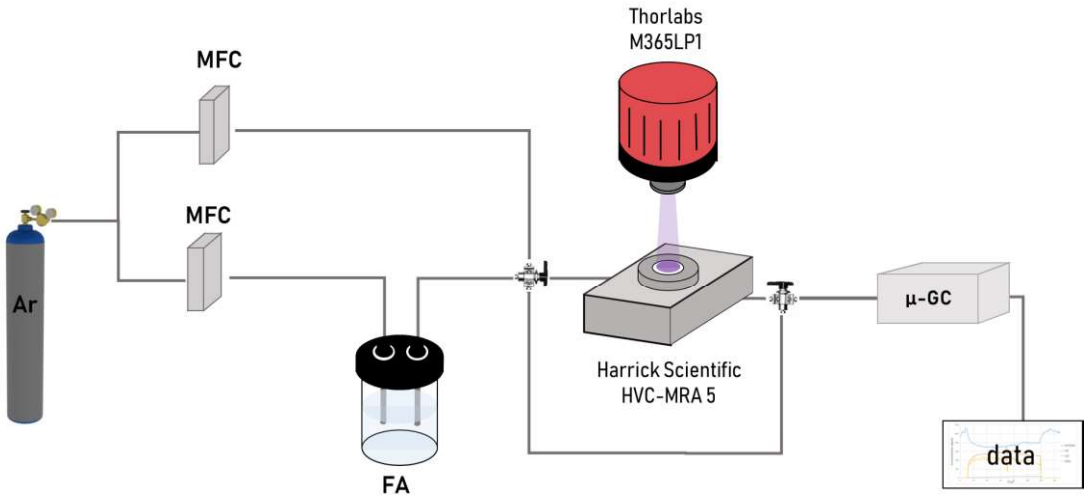

Fig. 27 Scheme *of the photo thermal catalytic set up for FA conversion.*

1.3. CO_2 methanation

In the methanation catalytic tests, gas cylinders of 2% CO_2 in Ar (Air Liquide) and pure H_2 (Air products, 99.995%) were used. Both flows were mixed following a 12.5:1 flow ratio, resulting in a CO_2 and H_2 concentrations of 1.9% and 7.7%, respectively, with a total flow of 5.1 ml/min. An in-Flow Bronkhorst flow meter (Bronkhorst® High-Tech, the Netherlands) was utilised for the control of the pure hydrogen flow, while the 2%CO_2/Ar flow was controlled *via* a Brooks 5850 massflow meter.

For the methanation tests, the catalyst mass was 5 mg, corresponding to a surface density of 16 mg/cm^2.

The photo-/thermo- catalytic behavior was obtained by *on-line* quantification of the outlet flow using a R3000A gas micro-chromatography (SRA instruments), equipped with micro-TCDs, and allowing the quantification of CH_4, H_2, O_2, CO, CO_2 and organics on 5A molecular sieve, OV1, PoraPlotQ and Stabilwax columns. The activity of the catalyst was expressed in terms of CO_2 conversion, CH_4 selectivity, as well as of CH_4 and CO production in mmol g^{-1} h^{-1}, calculated as follows (Eqs. 2.5,2.6,2.7).

$$X\ Production\ (mmol\ g^{-1}h^{-1}) = \frac{\left[\frac{[X](ppm)*flow\ rate\ (\frac{ml}{\min})}{24.43(\frac{ml}{mmol})} \cdot 60\left(\frac{\min}{h}\right) \cdot 10\text{^}(-6)\right]}{m_{catalyst}(g)} \quad (2.6)$$

[X] corresponds to the concentration of the product *X* in the flow, namely here methane or carbon monoxide.

$$CO_2\ conversion\ (\%) = \frac{[CO_2]_{in} - [CO_2]_{out}}{[CO_2]_{in}} \cdot 100 \quad (2.7)$$

$$CH_4\ selectivity\ (\%) = \frac{[CH_4]}{[CH_4] + [CO]} \cdot 100 \quad (2.8)$$

The carbon balance was calculated as follows:

$$C\ balance\ (\%) = \frac{[CO_2]_{out} + [CO] + [CH_4]}{[CO_2]_{in}} \cdot 100 \quad (2.9)$$

where $[CO_2]_{in}$ and $[CO_2]_{out}$ correspond to the inlet and and outlet concentrations of carbon dioxide, respectively, while [CO] and $[CH_4]$ correspond to the concentrations of carbon monoxide and methane, respectively, in the outlet flow.

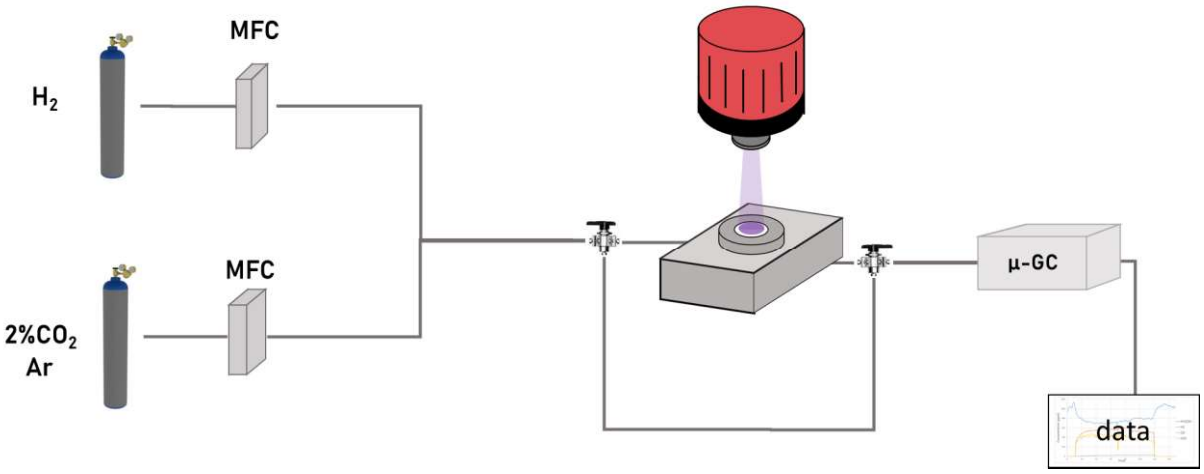

Fig. 28 *Scheme of the photo thermal catalytic set up for CO_2 methanation.*

2. Characterization techniques

2.1. X-ray diffraction

X-ray powder diffraction (XRD) is a non-destructive analytical technique that allows notably identifying the different crystallized phases of a material. The principles are based on the constructive interferences generated by the diffraction of monochromatic X-rays by a crystalline sample. A metallic anode generates X-rays that are filtered to get a monochromatic incident beam, collimated to concentrate and further directed to the sample. Constructive interferences are satisfying the Bragg's law in terms of diffracted X-rays, as follows:

$$n\lambda = 2dsin\theta \quad (2.10)$$

where n is an integer, λ is the wavelength of incident x-ray, θ is the incident (and scattering) angle and d is the interplanar spacing for lattice planes. The crystallographic structure of the powders has been characterized by X- ray diffraction patterns (XRD) recorded on a D8 Advance Bruker diffractometer in a θ/θ mode and using the $K_{\alpha 1}$ radiation of a Cu anticathode (λ = 1.5406 Å). The diffractograms were recorded from 10 to 90° in 2θ with steps of 0.01581° and 0.5 s per step.

2.2. N_2 physisorption

The specific surface area, SSA, of a material is a physical property that affects to reactant-catalyst surface interactions. Adsorption techniques can be used to characterize catalyst surface. Among them, N_2 physisorption allows to identify not only SSA, also the porosity of the sample by the Brunauer-Emmet-Teller (BET) theory. This technique consist on the physical adsorption of nitrogen at 77K (-196°C) at different pressure conditions, performing hysteresis loops into the isothermal experiment. SSA is determined using the BET equation:

$$\frac{1}{V_a(\frac{P}{P_0}-1)} = \frac{C-1}{V_m C} \cdot \frac{P_0}{P} + \frac{1}{V_m C} \qquad (2.11)$$

where:

V_a - Volume of specific gas adsorbed at standard temperature and pressure, in mL/g
P - Partial vapour pressure of adsorbate gas in equilibrium with the surface at boiling point of liquid nitrogen, in Pa.
P_0 - Saturated vapor pressure of adsorbate gas at given temperature, in Pa
V_m - Volume of a monolayer of gas adsorbed per gram of solid, in mL/g
C – adsorption constant

The specific surface area measurements have been carried on a Micromeritics ASAP 2420 using N_2 as adsorbent at −196°C with a prior outgassing at 150°C overnight in order to desorb the impurities or moisture. The Brunauer-Emmett-Teller (BET) specific surface area values has been obtained from the N_2 adsorption isotherm.

2.3. Chemical adsorption

Chemisorption, or chemical adsorption, is a traditional characterization technique used in material science and catalysis to provide information on the material surface, such as acidity and basicity, or active sites.

Chemisorption experiments were carried out in a Micrometrics Autochem II 2920 device (**Fig. 29**) on-line with a downstream PFEIFFER VACUUM Prisma™ mass spectrometer (MS). For each test, a catalyst amount of about 60 mg was mounted between quartz wool plugs in a U-type quartz reactor. Aside from the additional MS, chemisorption device includes a thermal conductivity detector (**Fig. 29**D) to analyse gases adsorption/desorption. The experimental results were analysed using the AutoChem II 2920 V3.05 software, which is also used to control the chemisorption device.

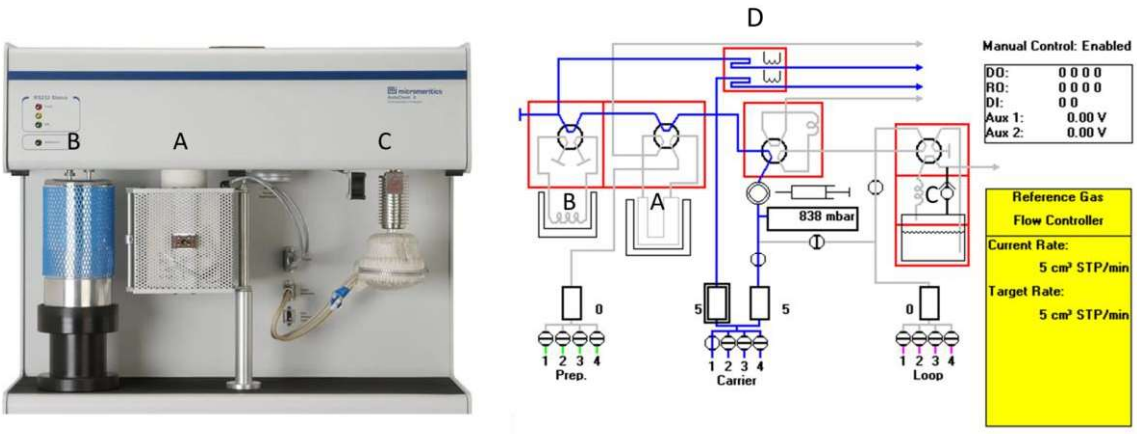

Fig. 29 *At the left, Micrometrics Autochem II 2920 device used for chemisorption analysis where* ***A)*** *is the reactor placed,* ***B)*** *the water trap and* ***C)*** *the vapour generation. At the right, internal scheme of the device where blue and grey represent the stainless steel lines where the gasses pass through. TCD is marked as* ***D)***

2.3.1. CO chemisorption

Carbon monoxide easy bonds with noble metal surface like Ru, Au or Pt at standard pressure and temperature conditions. CO chemisorption is extensively used to quantify the active metal sites of the catalyst surface. Once it is known the quantity of CO uptake by the metal and the number of active sites on the catalyst, it is possible to calculate the dispersion (Eq. 13) and the particle size (Eq. 14).

CO chemisorption measurements were realized in pulse mode to determine the CO uptake of each catalyst. After submitting the catalyst to a cleaning pre-treatment to remove any pollutant from the metal surface, controlled pulsed CO injections into the flow were carried out and the CO uptake by the catalyst was monitored for each pulse until the output CO peak signal remained constant, that is the surface of the catalyst cannot uptake more CO.

CO-pulses tests were carried out following a sample pre-treatment with a 50 mL/min flow of 10% H_2/Ar (Air Liquide) at 100°C for 1 h, with a temperature ramp of 10°C/min. Then, the samples were cooled down to 40°C in a 50 mL/min He gas flow. For the pulses analysis, each injection corresponded to a volume of 0.5 cm^3 of 1%CO/He mixture (Air Liquide) or of 4%CO/He (Air Liquide) mixture into the He carrier flow. The outgoing CO gas was detected and quantified by thermal conductivity detector, TCD. The analysis was completed when the output CO pulse signal remained stable. The CO uptake was determined as the sum up of the differences between the CO output concentration in each pulse, $[CO]_{n,i}$, and the CO inlet pulse concentration, $[CO]_0$, as it is shown below.

$$CO_{uptake} = \sum_{i=0}^{n} [CO]_0 - [CO]_{n,i} \qquad (2.12)$$

To determine the Ru dispersion parameter, the equation is given below:

$$\gamma = \frac{CO_{uptake}}{[Ru]\cdot F} \qquad (2.13)$$

Where γ is the dispersion, calculated from experimental moles of CO adsorbed on the catalytic surface divided per total moles of ruthenium in the catalyst with a Ru/CO factor, F, of 1. Once the dispersion is known, it is possible to calculate the mean crystallite/particle size with the following equation:

$$d = \frac{6v_m}{\gamma A_m} \quad (2.14)$$

Where d is the mean crystallite size, A_m is the surface area occupied by a metal atom and v_m the volume occupied by a metal atom with values of 8.6 10^{-2} nm² and 13.65 10^{-3} nm³, respectively [1].

2.4. Temperature programmed desorption

Temperature programmed desorption (TPD) experiments provide useful information about the strength of acid and basic active sites on catalytic surface. The principle consists on the covering of the material surface by a gas that is acid or basic. Depending on the strength of the sites on the surface, the adsorbed species are desorbed in a specific temperature. As higher is the temperature, stronger is the active sites on the surface.

TPD experiments are divided in 4 steps:

- Sample pre-treatment: Before the TPD, high temperatures are employed to remove any residual species in the surface like carbonates, formates, etc. Depending on the sample and its properties, the carrier gas can be inert (Ar, He, N_2), oxidizing (diluted O_2) or reducing (H_2).
- Pre-adsorption of the gas: At low temperatures, the carrier gas includes basic or acid gases (depending on the test) that are adsorbed on the sample surface.
- Evacuation of the gas in the flow: An inert gas is employed in the same temperature as the pre-adsorption process to remove the physisorbed species and the residual adsorption gas in the flow.
- Temperature programmed analysis: Once there is no adsorption gas in the carrier flow, the test starts with an increase of the temperature to observe the different desorbed species.

In temperature program desorption (TPD) experiments, NH_3 is a basic gas that is widely used for characterizing surface acid sites [2], as CO_2 is useful for the basic ones. Prior each chemisorption test, 60 mg of sample mass was submitted to a thermal treatment at 300°C for 1 h in He (Air Liquide ALPHAGAZ2, 99.9999%) gas flow using a temperature ramp of 10°C/min to desorb any pollutant molecules on surface and then cooled to 50°C. Then, the samples were exposed to CO_2 (Air Liquide, 99.99995%) and 10% NH_3 in He (Air Liquide) for CO_2-TPD and NH_3-TPD, respectively, during 30 min to bond the gases to the surface sites, before a He purge for 1 h was applied to remove not-bonded or weakly-bonded gases (as physisorbed species). Lastly, TPD tests were performed from 50°C to 850°C by ramping the temperature at 25°C/min. NH_3 or CO_2 desorption was detected by monitoring the mass spectrometry signals for m/z = 17 and m/z = 44, respectively. A final temperature of 500°C was applied for the g-C_3N_4 based catalysts to avoid the support decomposition.

2.5. Temperature programmed reduction

Temperature programmed reduction, TPR, has been widely reported as an efficient method to identify the different oxidized species at the catalyst surface. In TPR experiments, the catalyst is submitted to a flow of a reducing agent, commonly hydrogen, with thermal heating until high temperature values. The reduction of oxidized species generates water and are associated with hydrogen consumption, which produces a difference of thermal conductivity visible by a TCD. In TPR, the same mass quantity as in section 2.4. is used for the experiments. First, the sample was submitted to a thermal pre-treatment at 200°C under synthetic air flow (50 ml/min) during 30 min with a temperature ramp of 10°C/min to clean the surface and to oxidize the catalyst. Then, the quartz reactor was cooled down to 50°C and the gas flow was changed to 10% H_2/Ar (Air Liquide) at 20 ml/min until stabilization. The water trap downstream of the reactor consisted in dry ice mixed with acetone solution (**Fig. 29**B) to condense any water molecule, so that any TCD signal variation was related to hydrogen consumption. The temperature was increased till 800°C in the case of catalysts based on metal oxide supports with a ramp temperature of 10°C/min. Similarly to the TPD, a final temperature of 500°C was applied for the g-C_3N_4 based catalysts to avoid the support decomposition.

2.6. Spectroscopy techniques

2.6.1. Diffuse Reflectance Infrared Fourier Transform Spectroscopy

As it is shown in **Fig. 30**A, employing an IR beam over a fine particle material, light can be reflected from the top of the sample or it can penetrate into sample particles followed by a scattering of the matrix of sample, which is the diffuse reflectance process. In situ Diffusion Reflectance Infrared Fourier Transform (DRIFT) spectroscopy provide useful information about which organic functional groups are present and the different adsorbed species on the material surface. In DRIFTS, sample preparation properties such as the shape of particles and surface, compactness, etc. play an important role on the spectra quality. That is the main reason of a good sample preparation using e.g. grinding process or IR transparent material to dilute the sample, allowing a deeper light incidence over sample cup and higher diffusion.

DRIFTS experiments were conducted in a homemade elevated-pressure cell with a Fourier Transform infrared spectrometer (Bruker Vertex 70). The top cell was composed of a dome (Harrick Scientific) with two KBr windows for both inlet and outlet infrared beams, and a UV quartz window for UV-A light irradiation (Fig 5B). The sample was carefully placed in the cup until it overflowed the top of the cup. The sample was homogenously heated using a halogen lamp with reflector MR16 (OSRAM 64635 HLX) monitored by K-thermocouple (±1°C), and using a water-cooling system with a high flow rate for a constant (bulk) temperature maintenance. The experimental results were analysed using the OPUS 8.5 Software.

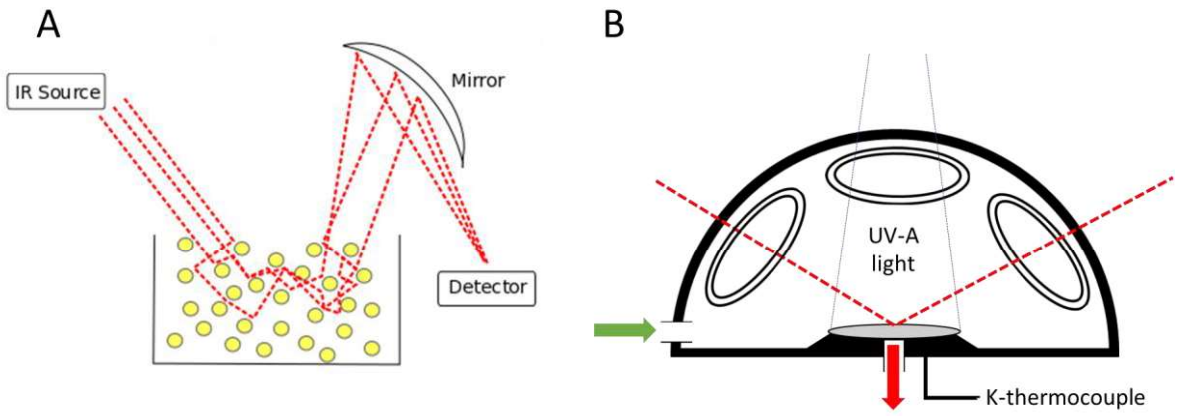

Fig. 30 A) *Modified scheme of diffuse reflectance FTIR technique where the red dash line corresponds to IR beams and yellow circles to the grounded sample and* ***B)*** *Schematic in-situ DRIFTS process where green and red arrow corresponds to inlet and outlet lines.*

2.6.1.1. FA adsorption and decomposition followed by In situ DRIFTS

The monitoring of the formic acid decomposition in dark and illuminating conditions by In situ DRIFTS aims at observing the differences between pure thermal driven reaction and light-induced derived processes on the catalyst surface, including aspects like how formic acid is adsorbed, which species predominate during the decomposition, intermediates, etc. In these experiments, the objective is to understand how the formic acid is adsorbed and decomposed over the catalyst surface and the different possible mechanism under light irradiation and dark conditions.

For these experiments, the catalyst was submitted to an argon flow (Air Liquide, ALPHAGAZ 1, >99.999%) at a flow rate of 14.7 ml/min for 30 min at 25°C and further for 30 min at 100°C, before the background spectrum was recorded. Then, 14.7 ml/min Ar gas flow was allowed to bubble in liquid-phase HCOOH (Sigma-Aldrich, >95%) in an ice bath and atmospheric pressure to generate the inlet FA/Ar flow to flow through the IR cell for 30 min at 25 °C to determine the gas-phase FA continuous flow spectrum and the adsorbed species onto the catalyst surface. Then, a 10°C/min temperature ramp rate was set until 150 °C with 30 min of plateau at 110°C, 130°C and 150°C temperature values at dark and illuminating conditions for Ru based catalysts. In case of bare TiO_2, the temperature ramp was until 350 °C. Spectra were recorded from 6000 cm^{-1} to 600 cm^{-1} with a resolution of 4 cm^{-1}, every spectra was the result of 32 scans meanwhile the background was recorded with 64 scans.

2.6.1.2. CO_2 methanation followed by In situ DRIFTS

CO_2 conversion into methane is based on several intermediate steps where DRIFT spectroscopy can provide information on the different surface species. Similarly to the previous subsection, the reaction is studied at illuminated and dark conditions to observe any differences at the catalyst surface. For this group of experiments, CO_2 (ALPHAGAZ N48, Air Liquide) and H_2 (Air Products, 99.995%) were mixed with Ar (Air Liquide, ALPHAGAZ 1, >99.999%) in a 1:4:5 proportion with a total 10 ml/min flow rate, to provide a CO_2/H_2 ratio of 1:4. The catalyst was diluted in a KBr matrix (8.5 % wt.) by grinding both materials in an agate mortar. A pre-treatment with argon (10 ml/min) flow at 110°C for 1 h with a ramp rate of 10°C/min was applied to desorb pollutants from the surface, and the flow was subsequently turned to $H_2/CO_2/Ar$ at 25°C. Then, the methanation reaction was performed from 120°C to 200°C with a stability of 30 min at each dark and illuminated conditions. Spectra were recorded from 4000 cm^{-1} to

1100 cm^{-1} with a resolution of 4 cm^{-1}, every spectra was the result of 32 scans meanwhile the background was recorded with 64 scans.

2.6.1.3. CO_2 adsorption and desorption followed by In situ DRIFTS

DRIFTS can also be used to observe the different CO_2 based adsorbed species on the catalyst surface such as bicarbonates, carbonates, formates, etc. Adsorption and desorption studies can indicate species stability at different conditions in CO_2 or inert gas atmosphere and how they are desorbed from the surface.

In case of CO_2 adsorption, sample pre-treatment consisted on inert argon flow into the reactor with a flow rate of 10 ml/min at 25 °C during 30 min. Then, the temperature was set at 400°C for 30 min with a temperature ramp of 20°C/min to desorb any pollutant molecules on surface followed by a cooling down process to achieve a temperature of 25°C in the reactor cell. After an argon flush for 1 h, the reactor was submitted at 25°C to a CO_2/Ar flow (1:10) with a total flow rate of 5.5 ml/min for 20 min to observe the CO_2 adsorbed species. The reactor was further submitted to Ar flow at 10 mL/min and the CO_2 desorption was monitored. A temperature ramp of 10 °C/min was set until 400 °C to observed the different species desorbed by the infrared detector. Spectra were recorded from 4000 cm^{-1} to 1100 cm^{-1} with a resolution of 4 cm^{-1}. Each spectra is the result of 32 scans, while the background spectra is recorded with 64 scans.

2.6.2. X-Ray Photoelectron Spectroscopy

X-ray Photoelectron spectroscopy (XPS) is a semi-quantitative and non-destructive technique currently used for analysis of the surface of solid materials, to get information on the elemental composition and the chemical and electronic state of the elements at the surface of samples. The chemical environment of atoms impacts on their electronic and oxidation state, what leads to a chemical shift, explained by electronegativity differences in the electrostatic model of atoms. The principle is based on the measurement of the kinetic energy of electrons that are emitted from a solid under the impact of a photon beam of X-rays of energy hv. Any electron (from core or valence state) having a binding energy less than hv will be ejected. Classical analysis depth is less than 10 nm (but depending on the inelastic mean free path), and the detection limit is of 0.1 atom %.

X-ray photoelectron spectroscopy measurements were performed on a ThermoVG Multilab ESCA 3000 spectrometer (ultra-high vacuum, base pressure P=1x10^{-9} mbar), equipped with a RESOLVE 120 MCD5 hemispherical electron analyzer. Al Kα line (hv=1486.6 eV) of a dual anode X-ray source was used as incident radiation. The constant pass energy mode, with pass energies of 100 and 20 eV values, was used to record survey and high resolution spectra, respectively. The samples powders were mounted on the sample holders using carbon tapes. No pre-treatment was applied on the samples before or during measurements. The experimental results were analysed using the CasaXPS 2.3.23 software. Decompositions were obtained using contributions with Doniach–Sunjic shape [3] and a S-shaped Shirley [4] type background. The energy shift due to electrostatic charging was adjusted using the adventious sp2 carbon C 1 s band at 284.6 eV.

The Ru/Ti surface atomic ratio (SAR) was calculated as follows:

$$\frac{S_{Ru}/F_{Ru}}{S_{Ti,}/F_{Ti}} \quad (2.15)$$

where S_{Ru} correspond to the total integrated surface in the spectrum that are related to ruthenium species, S_{Ti} for titanium species and F_{Ru} and F_{Ti} the empirically sensitivity factors as determined by Wagner et al. at 2.15 and 1.2, respectively [5].

2.6.3. Inductively coupled plasma optical emission spectroscopy

The ruthenium loadings were determined by chemical analysis through inductively coupled plasma optical emission spectroscopy (ICP-OES) carried out on a Optima 7000 DV spectrometer (Perkin Elmer) at the IPHC analytical platform for inorganics, Strasbourg. The samples were subjected first to a microwave-assisted acidic dissolution in aqua regia at 185 °C under autogenic pressure.

2.6.4. UV-Vis spectroscopy

Solid-state UV-Vis spectroscopy is widely used to analyse the electronic properties of a photosensitive material such as the bandgap or the plasmonic resonance range.

The measurements were performed with a PerkinElmer Lambda 950 UV-Vis spectrometer equipped with a dual light source of deuterium and tungsten to cover the wavelength spectrum from 800 to 200 nm. Every test were done with a sensitivity of 1 nm with a preliminary calibration of the device with $BaSO_4$. Data treatment was done with the UV Winlab™ software.

2.7. Transmission Electron Microscopy (TEM)

Electron microscopy is based on the use of an electron beam to pass through a column in ultra-high vacuum conditions where the sample is placed. Electron beam is focused and magnified by lenses before and after the sample. The imprinted image is a result of the beam variation caused by the sample interaction. This technique provides information about morphology, size and distribution of nanomaterials in a fine scale. A JEOL 2100F electron microscope with a point-to-point resolution of 0.2 nm was used to obtain TEM images. The sample preparation consists first in sonicating the sample in ethanol, before to deposit a drop of the suspension onto a copper grid covered by holey carbon membrane. The particle size distribution histograms, with mean particle size and standard deviation values calculations, were derived from the analysis of 250 particles using the ImageJ software.

3. Supports and catalysts

3.1. Supports

Graphitic carbon nitride, g-C_3N_4, was synthesized by thermal polycondensation of melamine (99%, Aldrich) in a covered alumina crucible at 550°C for 4h under static air within a muffle furnace using a heating ramp of 5°C/min. In a typical experiment, 14 g of melamine was used in a 60 mL ceramic

crucible. After natural cool-down to room temperature, the as-synthesized bulk g-C_3N_4 was further thermally exfoliated at 550°C for 4 h in similar conditions.

Aeroxide® TiO_2 P25 and Aeroxide® TiO_2 P90 were obtained from Evonik® (Evonik Resource Efficiency GmbH, Germany). TiO_2 MPT625 and TiO_2 UV-100 (Hombikat) were obtained from ISK (Japan) and Sachtleben (Germany), respectively.

Fumed silicon dioxide, SiO_2, was purchased from Sigma-Aldrich (>99.98%).

Cerium dioxide, CeO_2, was purchased from Solvay (HSA 5)

3.2. Catalysts prepared by wet impregnation

The wet impregnation method was used for preparing Ru/SiO_2 and Ru/TiO_2 catalysts. Typically, 500 mg of SiO_2 or TiO_2 was dispersed in a 15 ml aqueous solution of ruthenium (III) chloride hydrate ($RuCl_3 \cdot xH_2O$, 40% Ru min. content, Sigma-Aldrich) under vigorous stirring till solvent evaporation at room temperature (ca. 24 h). Then, the remaining solid was dried under air in a drying oven at 100°C for 1h, and further submitted in an open crucible in a tubular furnace to a reductive treatment at 500°C for 1 h under pure hydrogen flow (18 mL/min) using a temperature ramp of 5°C/min. **Fig. 31** shows a scheme of the wet impregnation synthesis process.

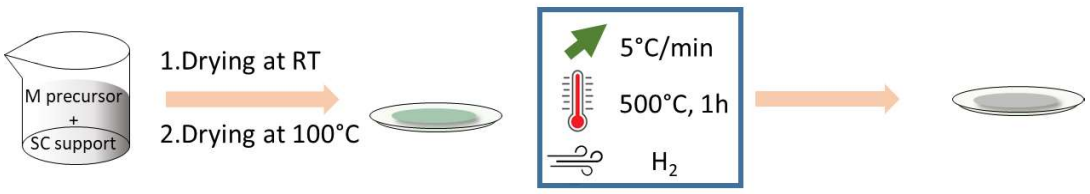

Fig. 31 *Scheme of the wet impregnation method used for the catalyst preparation.*

3.3. Catalysts prepared by the photo-assisted synthesis method

Ru/TiO_2 and Ru/g-C_3N_4 photo-thermal catalysts were prepared with a nominal Ru content ranging from 0.25 wt.% to 5 wt.% according to a UV-A light-assisted synthesis method that allows a fine control of the Ru nanoparticle size distribution [6].

In a typical experiment, ruthenium (III) chloride hydrate ($RuCl_3 \cdot xH_2O$, 40% Ru min. content, Sigma-Aldrich) in the appropriate amount was used as Ru precursor and dissolved under stirring in 100 mL of an aqueous solution with 10% v/v methanol as sacrificial agent in a beaker-type glass reactor. Then, 100 mg of semiconductor support, TiO_2 or g-C_3N_4, was dispersed into the solution at a concentration of 1 g/L and maintained under vigorous stirring for 1 h in dark conditions to ensure the establishment of the adsorption/desorption equilibrium. After, saturated NaOH solution was employed to modify pH of the dispersion to a value of 8. The pH modification was followed by a pH-meter (METLER TOLEDO). Once it is determined a pH 8, the dispersion is stirring during one hour more. After, the suspension was exposed under stirring to UV-A light at 69.6 W/m² irradiance within an irradiation chamber composed of 5 UV lamps (λ_{max} = 365 nm, Philips 24 W/10/4P). **Fig. 32**shows a scheme of the photo-assisted synthesis process. In addition, tracing of ruthenium precursor concentration in solution via UV-vis spectrophotometry (VWR UV-3100 PC, Radnor, PA, USA) was used sampling 0.5 ml of dispersion and filtering to remove the solid phase each test at different irradiation time to determine the absence of precursor in solution.

Once there is no ruthenium precursor signal detected, the suspension was filtered in vacuum followed by washing several times with distilled water and stored in drying oven at 100°C under air atmosphere during 12h.

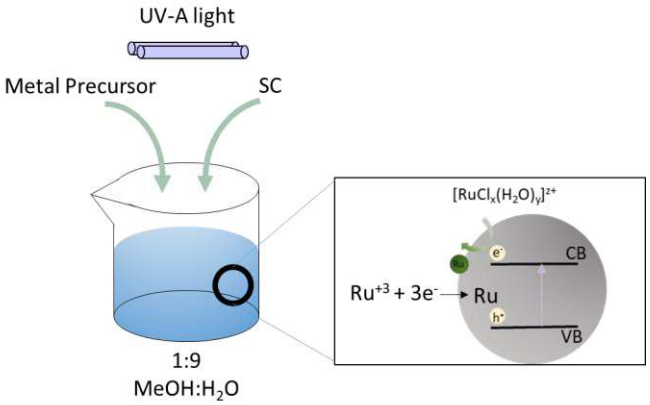

Fig. 32 *Scheme of the photo-assisted method used for the preparation of* Ru/TiO_2 *and* $Ru/g\text{-}C_3N_4$ *catalysts*

References

[1] X. Shen, L.J. Garces, Y. Ding, K. Laubernds, R.P. Zerger, M. Aindow, E.J. Neth, S.L. Suib, Behavior of H2 chemisorption on Ru/TiO2 surface and its application in evaluation of Ru particle sizes compared with TEM and XRD analyses, Appl. Catal. A Gen. 335 (2008) 187–195. https://doi.org/10.1016/j.apcata.2007.11.017.

[2] A.W. Chester, E.G. Derouane, Zeolite Characterization and Catalysis: a tutorial, Springer, Dordrecht Heidelberg London New York, 2010. https://doi.org/10.1016/s1351-4180(10)70329-9.

[3] S. Doniach, M. Sunjic, Many-electron singularity in X-ray photoemission and X-ray line spectra from metals, J. Phys. C Solid State Phys. 3 (1970) 285–291. https://doi.org/10.1088/0022-3719/3/2/010.

[4] D.A. Shirley, High-Resolution X-Ray Photoemission Spectrum of the Valence Bands of Gold, Phys. Rev. B. 5 (1972) 4709–4714. https://doi.org/10.1103/PhysRevB.5.4709.

[5] C.D. Wagner, R.H. Raymond, L.H. Gale, Empirical Atomic Sensitivity Factors for Quantitative Analysis by Electron Spectroscopy for Chemical Analysis, 3 (1981) 211–225.

[6] J. Wojciechowska, M. Jędrzejczyk, J. Grams, N. Keller, A.M. Ruppert, Enhanced Production of γ-Valerolactone with an Internal Source of Hydrogen on Ca-Modified TiO 2 Supported Ru Catalysts, ChemSusChem. 12 (2019) 639–650. https://doi.org/10.1002/cssc.201801974.

CHAPTER 3: Photo-thermal formic acid decomposition over Ru/TiO_2 catalyst.

Introduction

This chapter is focused on the study of Ru/TiO_2 systems as photothermal catalysts for the gas-phase formic acid decomposition. It includes the first evidence that a dual photonic/thermal excitation can boost the hydrogen production via dehydrogenation.

It is divided into 5 sections. The first section is devoted to the proof of concept of the ability of Ru/TiO_2 materials to be used as photothermal catalysts, and to which extent the catalytic behavior is affected by a dual photonic/thermal excitation.

Second and third short sections are presenting the influence of some synthesis parameters (namely the irradiation time, the synthesis method and the Ru loading), and investigate to which extent the catalytic behavior and the photothermal effect are influenced by the surface properties of the catalyst.

Fourth section is devoted to an in-situ DRIFTS study of the photothermal decomposition of formic acid, conducted on bare TiO_2 and Ru/TiO_2 systems under illuminating and dark conditions to increase the knowledge on possible mechanisms. Finally, fifth section briefly concludes and summarizes the chapter.

1. Formic acid decomposition over the $Ru(0.5\%)/TiO_2$ (PA) reference catalyst

The first study conducted in order to demonstrate the interest of a dual photonic (UV-A) and thermal activation of a Ru/TiO_2 catalyst via the occurrence of a beneficial photothermal effect, has been performed using TiO_2 P25 Aeroxide (Degussa-Evonik) as reference TiO_2 support and a weight content in Ru of 0.5 %. TiO_2 P25 is an anatase-rutile mixed phase material with a micropore-free specific surface area of 55 m^2/g. Composition among crystalline phases is 80% and 20% of anatase and rutile polymorphs, respectively. It was measured to contain ca. 7% of amorphous phase, as determined by the method developed in the group of Lillo-Rodenas and Roman-Martinez [1].

TiO_2 P25 Aeroxide is indeed one of the reference TiO_2 in the field of photocatalysis under UV-A light. It was also reported to be an advantageous support in comparison to many other TiO_2 materials (other commercial titania, sol-gel titania, hydrothermally-prepared titania, etc…) in a wide span of catalytic reactions, including hydrogenation ones [2–6], mainly in the case of supported metal nanoparticles prepared with a final thermal reduction in hydrogen.

The reason for that is still being investigated by many research groups, but it has been proposed that this might result from several factors, lying to both the way of preparing the supported nanoparticles, the phase composition of the support with notably the co-existence of both anatase and rutile phases, and the catalytic activity itself of the nanoparticles in contact with the support phase. For instance, it has been shown that using thermal reduction in hydrogen requires the presence of the rutile phase within the TiO_2 support for synthesizing relatively small-size Ru nanoparticles ; the presence of the rutile phase in the support is also reported to reduce the reducibility of the supported Ru phase during the preparation of the catalyst [4]. A stronger Support Metal Support Interaction (SMSI) effect has already been reported for the anatase polymorph in comparison to its rutile counterpart, what can reduce the availability of the supported active phase, and in consequence the catalyst activity. The

beneficial co-presence of both anatase and rutile polymorphs results in some cases in the existence of a composition optimum, that in several cases corresponds to the TiO_2 P25 Aeroxide material.

For the reference catalyst, a weight loading of 0.5% of Ru was selected, by reference to previous works in the laboratory [7]. As reference, the catalyst was prepared through a photo-assisted synthesis method, that is an elegant and sustainable alternative to classical methods for preparing small size supported metal nanoparticles, provided that the support is a semi-conductor material. The method uses the redox photoactivity of the host TiO_2 semiconductor under UV-A light for promoting electrons to the conduction band of the semiconductor, further able to reduce pre-adsorbed Ru-based ions at the surface. This offers a potential control over the supported nanoparticle size, their distribution and their oxidation state [8]. This is of importance, as classical wet impregnation method is usually providing a badly-defined control of the dispersion and/or size in the case of the Ru/TiO_2 systems [2,7]. This reference catalyst is labeled as $Ru(0.5\%)/TiO_2$ (PA).

1.1. Synthesis and characterization of the $Ru(0.5\%)/TiO_2$ (PA) reference catalyst.

The synthesis of the $Ru(0.5\%)/TiO_2$ (PA) catalyst is monitored through photo-spectrometry, by following the evolution with time under irradiation of the relative concentration of the Ru precursor and of the corresponding UV-vis absorbance spectra upon UV-A light illumination (**Fig. 33**). The favored adsorption at pH 8 is visualized by the strong decrease in the absorbance at λ=324 nm, due to the negative charge of the TiO_2 surface at a pH above the IEP of TiO_2, and the positive charge of chloro-complexes, as the Ru species are most probably present as a mixture of $RuCl_3(H_2O)_3$, and of $RuCl_2(H_2O)_4^+$ and $RuCl(H_2O)_5^{2+}$ species [9–11]. Complete disappearance of the Ru precursor was observed upon UV-A illumination of the TiO_2 support suspension for a reaction time of 2 h. The content of 0.46 wt.% Ru was determined by ICP-OES, in agreement with the nominal targeted value of 0.5 wt.% Ru (see **Table 1**).

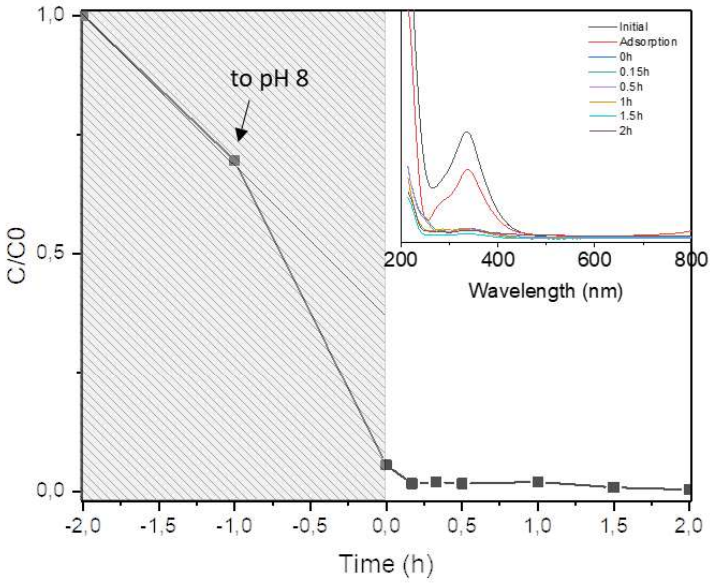

Fig. 33 *Photo-assisted synthesis of the $Ru(0.5\%)/TiO_2$ (PA) reference catalyst followed by UV-Vis spectrophotometry where the remaining Ru precursor was assigned to the peak at wavelength λ=324 nm.*

Fig. 34 shows TEM pictures of the Ru(0.5%)/TiO_2 (PA) catalyst. They evidenced that the catalyst is characterized by a very high and homogeneous nanoparticle dispersion (no formation of aggregates being observed). The synthesis led to sub-nanometric particles of Ru with an extreme narrow particle size distribution of 0.6 nm, with a Full With at Half Maximum (FWHM) of 0.16 nm, which does not differ significantly from crystallite size obtained by chemisorption, taking into account the approximation of the method. Indeed, the CO pulses chemisorption study (shown in **Fig. 35**) provided CO uptake values indicating a ruthenium dispersion onto the titania surface of 90%, with a crystallite size of 1.1 nm (see **Table 1**). We are aware that the dispersion value and the crystallite size remain indicative, due to the assumptions of the model used for the calculations. For instance, a theoretical value of 0.6 nm of mean particle size corresponds to a dispersion value higher than 100%. Nevertheless, this dispersion value is interesting to keep for further comparison with other catalysts. The metallic nature of the Ru nanoparticles was confirmed by XPS surface characterization and high resolution TEM (performed on slightly larger Ru nanoparticles). The 2.1 Å interplane distance characteristic of the (101) planes of metallic Ru [7,12,13] was visualized.

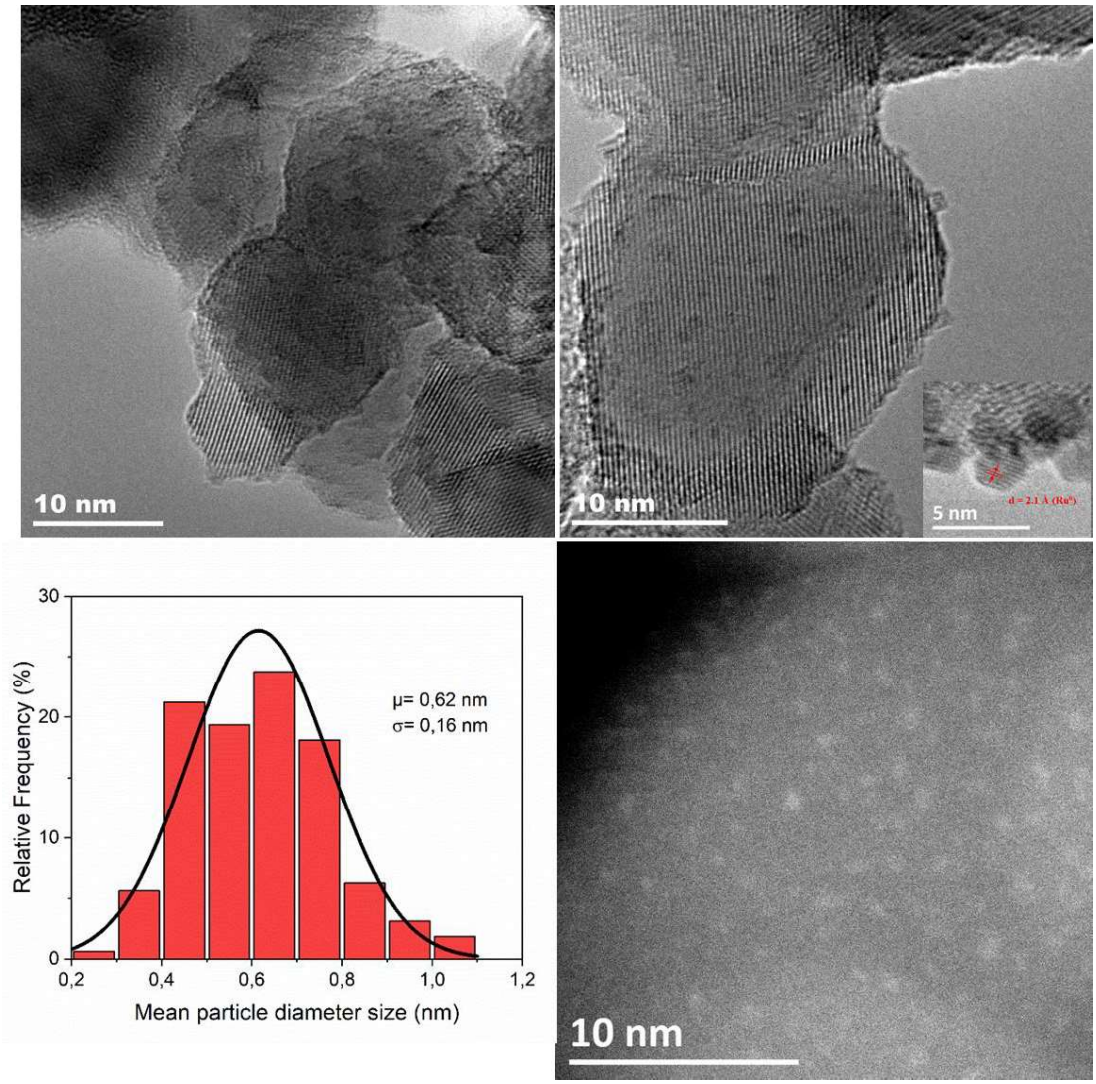

Fig. 34 *TEM analysis of the Ru(0.5 %)/TiO_2 (PA) reference catalyst. At the top: HRTEM pictures. At the bottom: histogram of the Ruthenium particle size distribution and STEM image.*

As far as X-Ray photon spectroscopy measurements are concerned, shown in **Fig. 36**A., the binding energy overlap between both C 1s and Ru 3d regions, as well as that between both Ti 2p and Ru 3p regions, is known to complexify the investigation on the surface state of Ru/TiO_2 systems, and complex multi-contribution envelopes are usually observed [14–18]. However, the Ru 3d primary region spectra exhibit two doublet contributions at 280.4 and 282.0 eV with a 4.1 eV spin orbit splitting constant, corresponding to Ru 3d5/2-Ru 3d3/2 orbital doublet contributions, in addition to the multi-contribution environment attributed to atmospheric carbon species adsorbed (adventious carbon).[19] They are assigned to Ru^0 and $Ru^{\delta+}$ species, respectively.

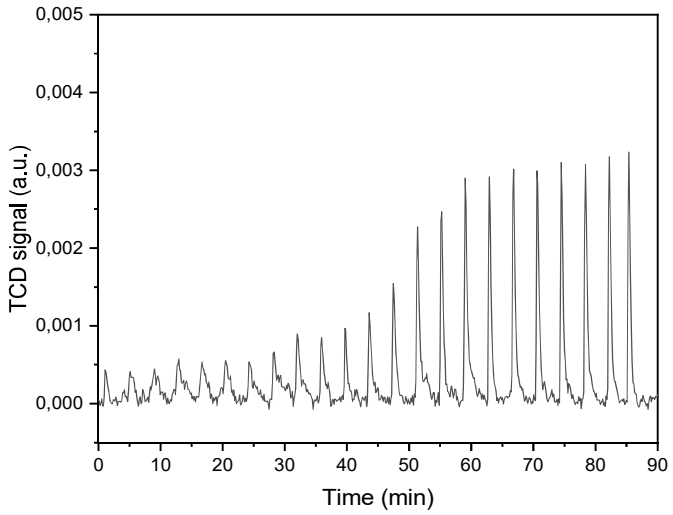

Fig. 35. *TCD signal during CO chemisorption pulses on the Ru(0.5%)/TiO_2 (PA) catalyst. Each peak corresponds to the outlet CO concentration in the flow after each pulse injection.*

A $Ru^0/Ru^{\delta+}$ surface concentration ratio was calculated at 79/21 ± 6. The presence of $Ru^{\delta+}$ species resulted from the natural surface oxidation of the metallic Ru species, as metallic Ru undergoes oxidation very easily when exposed to the air, and more globally as reported for many supported noble metals. It might also find its origin in the formation of interfacial bonds Ti-O-Ru upon the irradiation and the related reaction between the adsorbed Ru complexes and the promoted electrons. Both the high intensity Ru metal peak in the Ru 3d orbital spectrum and the high surface atomic ratio Ru/Ti value of 0.037 for this Ru loading are commonly related to a high dispersion of the elemental species onto the surface and to the very small size of the Ru nanoparticles.

The Cl 2p XPS spectra (**Fig. 36**B) did not reveal the presence of any residual chlorine species, evidencing the efficiency of the synthesis and of the washing protocols, although we have to stress that ultra-traces of chlorine species were analysed by ToF-SIMS. This discrepancy probably finds its origin in the by far smaller analysis thickness in ToF-SIMS when compared to that of XPS. Analysis of selected ions suggested that the residual top-surface Cl species are in interaction with the TiO_2 support rather than with the Ru nanoparticles, as evidenced by the detection of the characteristic TiO_2Cl^- ion and the absence of any characteristic $Ru_xCl_y^-$ and $RuO_2Cl_y^-$ ions (data not shown).

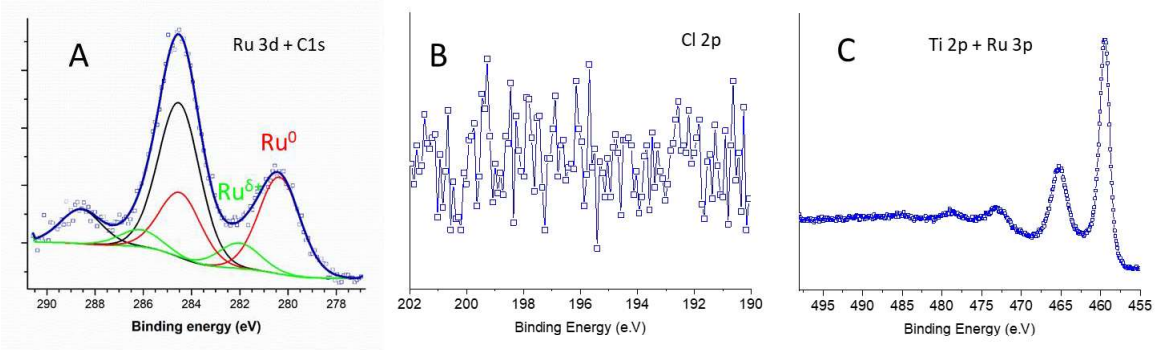

Fig. 36 *X-ray photoelectron spectra of Ru(0.5 %)/TiO_2 (PA) where* ***A)*** *shows the Ru 3d + C1s orbitals with red: Ru^0 (3d); green: oxidized $Ru^{\delta+}$ (3d); black: multi-contribution envelope of adventious carbon (1s)* [19]*,* ***B)*** *Cl 2p orbitals and* ***C)*** *Ti 2p + Ru 3p orbitals ranges.*

The values of metal dispersion, distribution and chemical state demonstrated the successful synthesis of highly dispersed ruthenium metal nanoparticles onto the titania surface with the desired loading, by a green and sustainable synthesis method that does not require any high temperature conditions or any external reducing agent to prepare the catalyst.

wt. % Ru[1]	$Ru^0/Ru^{\delta+}$ [2]	SAR $_{Ru/Ti}$[2]	Dispersion (%)[3]	Crystallite size (nm)[3]	Particle size (nm)[4]
0.46	79/21	0.036	90	1.1	0.6 ± 0.2

Table 1 *Data of different properties of the Ru(0.5%)/TiO_2 (PA) catalyst obtained by 1. ICP-OES, 2. XPS, 3. CO pulses chemisorption and 4. TEM characterization techniques.*

1.2. Thermal decomposition of FA over the Ru(0.5%)/TiO_2 (PA) reference catalyst.

Formic acid decomposition was first performed in the dark over the Ru(0.5%)/TiO_2 (PA) reference catalyst prepared by the photo-assisted synthesis method. The results obtained as a function of the reaction temperature over the 25-210°C range are shown in **Fig. 37**A, and expressed as FA conversion, and productions of H_2, CO and CO_2. First it must be said that no deactivation was observed with time on stream whatever the temperature conditions. The increase in temperature was accompanied by an increase in the FA conversion and in the production of CO, CO_2 and H_2, as a result of dehydration and dehydrogenation reactions, respectively. Values of H_2 and CO_2 production were always obtained in an equimolar ratio, meaning that no side reactions that would contribute to lower the selectivity to H_2 occurred (Eqs 3.1-3.3) in the reaction conditions [17]. Sum up of the CO and CO_2 formed and unconverted FA provided a carbon balance within the 98–102 % range regardless of the temperature.

$$CO + 3H_2 \rightarrow CH_4 + H_2O \quad (3.1)$$

$$CO_2 + 4H_2 \rightarrow CH_4 + 2H_2O \quad (3.2)$$

$$2HCOOH \rightarrow HCHO + CO_2 + H_2O \quad (3.3)$$

No product formation could be observed in the 25-110°C range, and the reaction products started to be detected for temperatures above 130°C, at which a FA conversion of 1.6% was obtained, reaching exponentially values of 37% at 190°C, and 64 % at 210°C. The reaction products increased as well exponentially in the temperature range, to reach at 210°C a production of 20.4, 21.4 and 21.5 mmol $g^{-1}h^{-1}$ for H_2, CO_2 and CO, respectively. The increase in the conversion with the temperature is accompanied by an increase in the selectivity to dehydrogenation (H_2 and CO_2), from 8.3% at 130°C up to 48.7% at 210°C (**Fig. 37**B). All data are summarized in Table 2.

Temperature	**FA conversion**	**H_2 production**	**CO production**	**CO_2 production**	**H_2 selectivity**
°C	%	$mmolg^{-1}h^{-1}$	$mmolg^{-1}h^{-1}$	$mmolg^{-1}h^{-1}$	%
25	0	0	0	0	-
70	0	0	0	0	-
90	0	0	0	0	-
110	0	0	0	0	-
130	1.6	0.1	0.1	0.1	8.3
150	5.1	0.5	2.8	0.6	18.0
170	12.2	2.9	4.2	4.0	40.9
190	36.8	10.1	13.4	11.3	43.0
210	63.9	20.4	21.5	21.4	48.7

Table 2 *Formic acid decomposition over the Ru(0.5%)/TiO_2 (PA) reference catalyst at dark conditions.*

The dehydrogenation reaction takes place at the metal surface, producing metal-formate species, that undergo β-hybride elimination with the formation of CO_2 and H^- that bonds with a previously adsorbed H^+ to get H_2 production [20,21].

The **Fig. 37**C depicts the Arrhenius plot used for deriving the apparent activation energy, AE_{app}, for dehydrogenation and dehydration reactions, as it represents the slope of the logarithmic rate of both decomposition reactions versus the inverse of the temperature. Apparent activation energies of 64 ± 8 and 106 ± 11 kJ/mol were obtained for the dehydration and dehydrogenation reactions, respectively. This reflects the fact that the Ru(0.5%)/TiO_2 (PA) reference catalyst is a relatively poor thermal catalyst when considering the selectivity to H_2, and favors the dehydration pathway in dark conditions, with the extensive formation of CO.

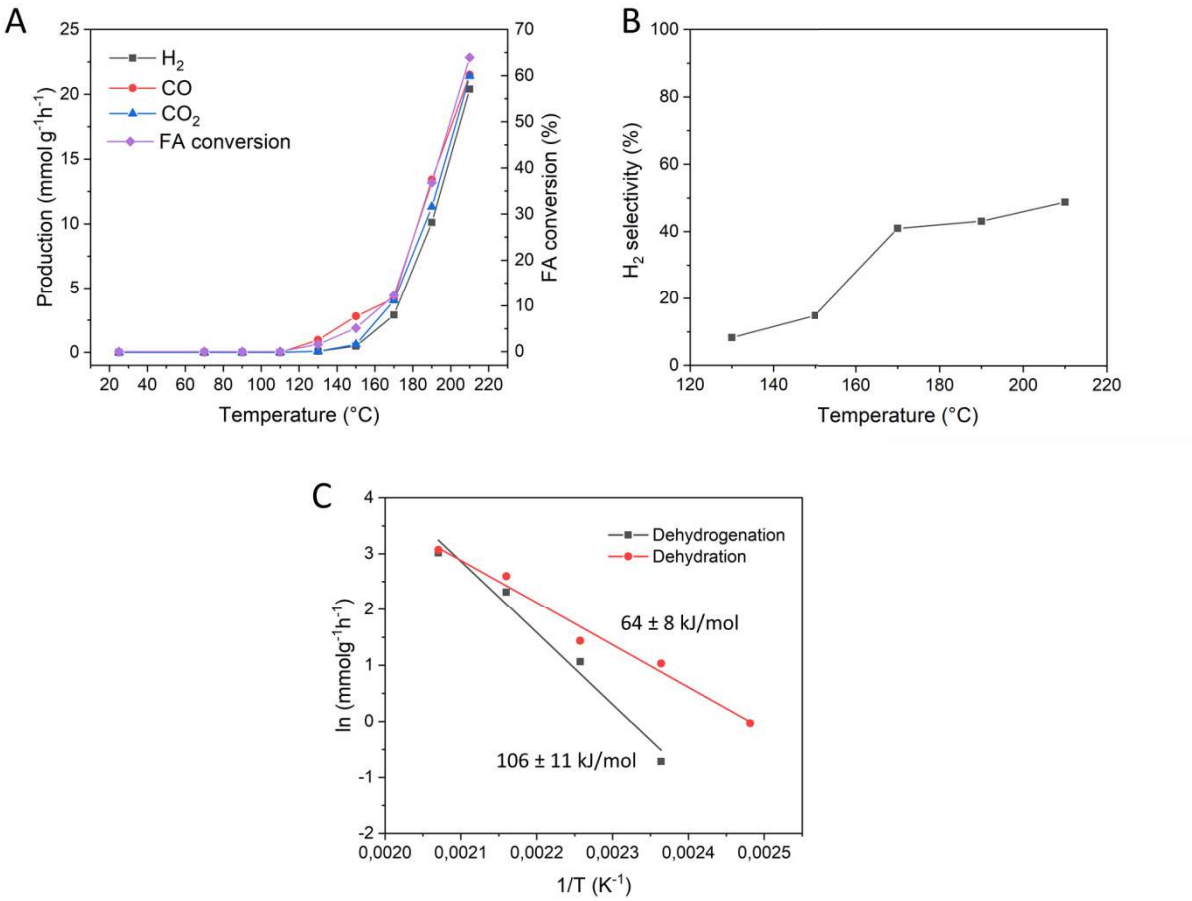

Fig. 37 *Influence of the temperature within the 25-210°C range in the dark on the Ru(0.5 %)/TiO_2 (PA) reference catalyst prepared by the photo-assisted synthesis method. FA decomposition in terms of* ***A)*** *production of H_2 (black), CO (red), CO_2 (blue) and conversion of FA (purple),* ***B)*** *selectivity to dehydrogenation products,* ***C)*** *Arrhenius plot used for deriving the apparent activation energy for dehydrogenation (black) and dehydration (red) reactions. Reaction conditions: [FA]=4600 ppm_v, total Ar flow of 14.7 mL, 1.8 mg of catalyst, FA specific molar rate of 67.2 mmol $g^{-1}h^{-1}$.*

1.3. Light-effect on FA decomposition.

Fig. 38 depicts the influence of the reaction temperature and of the UV-A light irradiance (0-365 mW/cm²). All data are summarized in **Table A 1** in annex (to not duplicate here with the different graphs).

Regardless of the temperature reaction, the results showed that the formic acid conversion is clearly enhanced under illumination in comparison to dark conditions. In addition, it is important to mention that, the higher the light irradiance, the stronger the enhancement upon illumination. For example, at 130°C, FA conversion was 1.6% at dark conditions, and it raised a value of 70% at 365 mW/cm² (**Fig. 38**A). This enhancement allows FA conversion to be observed under illumination even for temperatures at which no reaction products were observed in the dark, like at 25°C, with a conversion of 9% at a 365 mW/cm² irradiance.

Whatever the temperature and the light irradiance, carbon balances within the 98–102 % range are calculated. The enhanced conversion is associated to an increase in both H_2 and CO productions (H_2 and CO_2 productions are still obtained in an equimolar ratio, as it is shown in **Fig. 38**B,C).

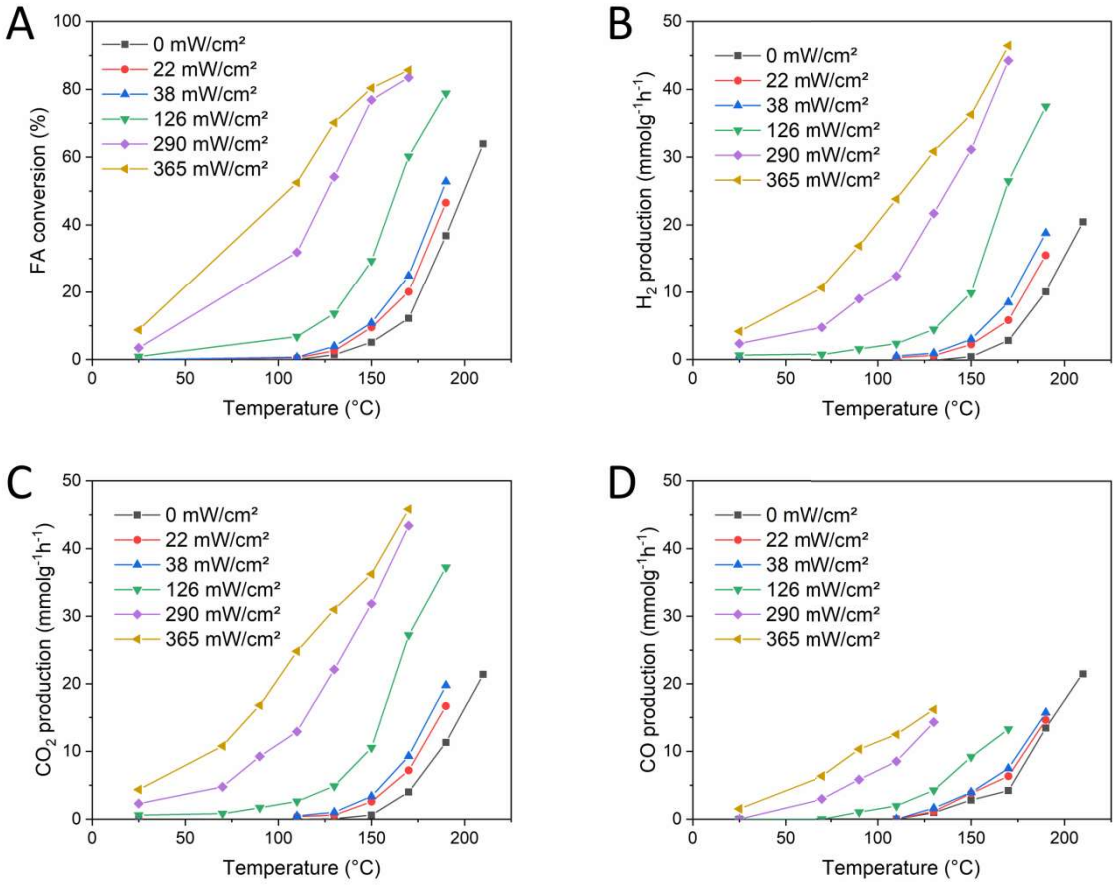

Fig. 38 *Influence of the UV-A light irradiance in the 0-365 mW/cm² range and of the reaction temperature on the photothermal FA decomposition on the Ru(0.5 %)/TiO_2 (PA) reference catalyst prepared by the photo-assisted synthesis method.* ***A)*** *FA conversion,* ***B)*** *production of H_2,* ***C)*** *production of CO_2, and* ***D)*** *production of CO. Reaction conditions: [FA]=4600 ppm_v, total Ar flow of 14.7 mL, 1.8 mg of catalyst, FA specific molar rate of 67.2 mmol $g^{-1}h^{-1}$.*

Independently of the temperature, the enhancement of the FA conversion under photon flux irradiation conditions was accompanied by a strong increase in the selectivity to H_2, as it is shown in **Fig. 39**A. For instance, FA conversion reached 86% with 46.4 mmol/g/h and 11.7 mmol/g/h of H_2 and CO formation, respectively, at 170°C with 365 mW/cm², which corresponds to an important H_2 selectivity increase up to 80%.

The different catalytic indicators can also be presented as a function of the light irradiance as it is shown in **Fig. 39**B-D. Based on the regimes reported in the literature [22–24], it is possible to distinguish different regimes depending on the reaction temperature. We propose that the regime is turning from a superlinear regime at low temperatures to a sublinear regime at high temperatures, and potentially a linear regime at intermediate temperatures. In the specific case of the production of CO, the change of regime remains less visible, as the CO production values are smaller than those of H_2.

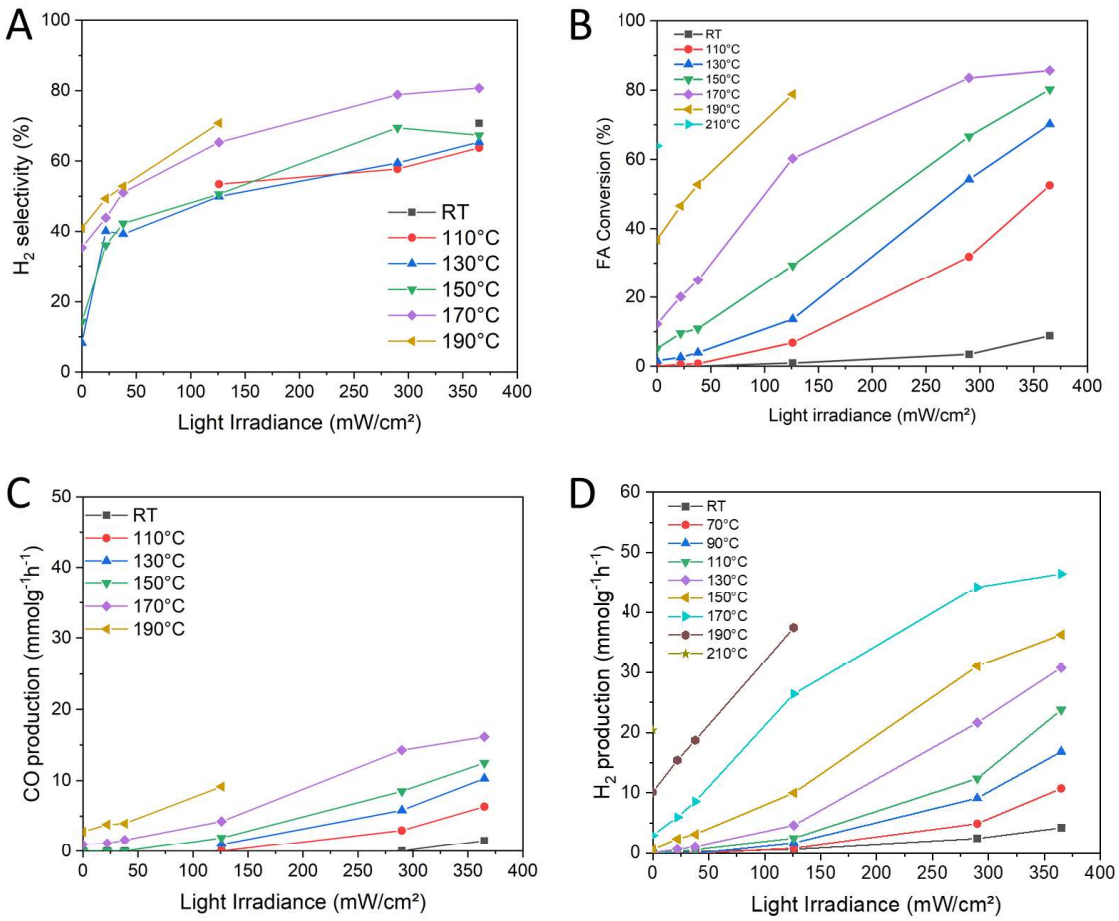

Fig. 39 *Representation as a function of the light irradiance of the photothermal FA decomposition over the Ru(0.5 %)/TiO_2 (PA) reference catalyst prepared by the photo-assisted synthesis method.* ***A)*** *Selectivity to dehydrogenation products (H_2),* ***B)*** *FA conversion,* ***C)*** *production of CO, and* ***D)*** *production of H_2. Reaction conditions: [FA]=4600 ppm_v, total Ar flow of 14.7 mL, 1.8 mg of catalyst, FA specific molar rate of 67.2 mmol $g^{-1}h^{-1}$.*

The results evidenced that a dual-mode excitation allows for the increase in the FA conversion, and therefore the H_2 production, in comparison to the thermocatalytic conditions in the dark. The higher the irradiance, the stronger the enhancement. It means that similar H_2 levels and FA conversions can be obtained at a lower bulk temperature upon illumination, namely under milder operating conditions. For example, the H_2 production at 170°C in dark conditions corresponded to that obtained at room temperature at a 290 mW/cm² irradiance, and the CO production at 170°C in dark conditions corresponded to that obtained at 130°C at a 126 mW/cm² irradiance.

The low-temperature shift and the gain in selectivity to H_2 obtained when the Ru/TiO_2 catalyst operates at a lower temperature for achieving a similar conversion than that obtained in the dark, can be extrapolated from **Fig. 38**. They are quantified and depicted in **Fig. 40**. **Fig. 40**A proves that the low-temperature shift under illumination conditions is all the more pronounced when the irradiance is high, but also when the reference temperature in the dark is low (within the range of tested temperatures). In addition, this low-temperature shift was positively accompanied by an important gain in H_2 selectivity (**Fig. 40**B), which is globally more pronounced since irradiation is high. The strongest increase in H_2 selectivity upon illumination was observed at 150°C. As a result of the low-temperature shift while keeping the same FA conversion and the simultaneous increase in H_2 selectivity, the gain in catalytic activity upon illumination allowed in consequence for an even more

pronounced lowering of the temperature, obtaining under light the same H_2 production level than was reached in the dark conditions at a far higher reaction temperature value (**Fig. 40**C).

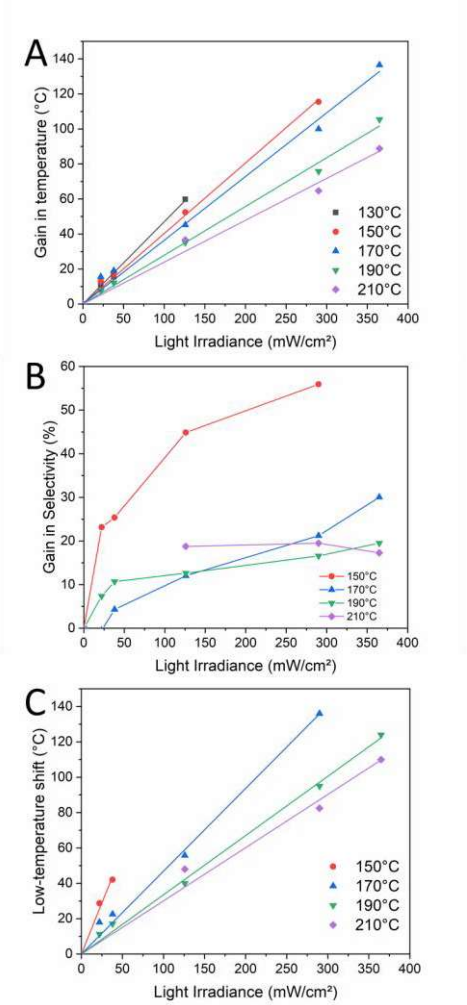

Fig. 40 *Results extrapolated from the FA conversion, H_2 and CO productions over Ru (0.5 %)/TiO_2 (PA) catalyst shown in Fig 3A,B and D, in order to depict:*

(A) *The influence of the irradiance on the low-temperature shift under light while achieving a similar FA conversion as that in the dark thanks to the higher catalytic activity. The low-temperature shift is plotted by comparison to the different reaction temperatures in the dark (130-210°C);* ***(B)*** *The gain in H_2 selectivity obtained by enabling the catalyst to operate at the lower temperature plotted in* ***(A)*** *thanks to the photonic excitation. The gain in H_2 selectivity is plotted by comparison to the selectivity obtained at the different temperatures in the dark (150-210°C);* ***(C)*** *The influence of the irradiance on the low-temperature shift under light while achieving a similar H_2 production level as that in the dark. The low-temperature shift is plotted by referring to the different reaction temperatures in the dark (150-210°C).*

Reaction conditions: [FA]=4600 ppm_v, total Ar flow of 14.7 mL, 1.8 mg of catalyst, FA specific molar rate of 67.2 mmol $g^{-1}h^{-1}$.

It must be said that performing the reaction under light did not change the performances of the catalyst in the dark. Indeed, after a cycle of tests at different irradiances, no significant differences were observed when performing again the tests at dark conditions. Only excursion at high temperatures (>190°C) resulted in small changes in conversion and H_2 production, associated to a slight increase and broadening of the nanoparticles size distribution.

1.4. FA decomposition over bare TiO_2 (P25)

Fig. 41 depicts the influence of both the reaction temperature in the 130−190°C range and the UV-A irradiance (0−365 mW/cm^2) on the catalytic activity of the pure TiO_2-P25 support in the gas phase formic acid decomposition. The results obtained revealed that the FA decomposition only occurred through the dehydration pathway, CO being the only reaction product detected, neither H_2 nor CO_2 being formed, independently of the reaction temperature, and whether the reaction is performed in the dark or under irradiation. Higher the reaction temperature, higher the FA conversion, with an increase of the conversion from 3% to 33 % accompanied by an increase in the CO formation from 2 to 22 mmol/g/h when the reaction temperature was increased from 130°C to 190°C in the dark. Performing the reaction under irradiation enhanced the conversion and the corresponding CO formation, both being all the more pronounced as the irradiance is high. Here, the FA conversion reached 85 % with a CO formation of 57 mmol/g/h at a temperature of 190°C with an irradiance of 365 mW/cm^2.

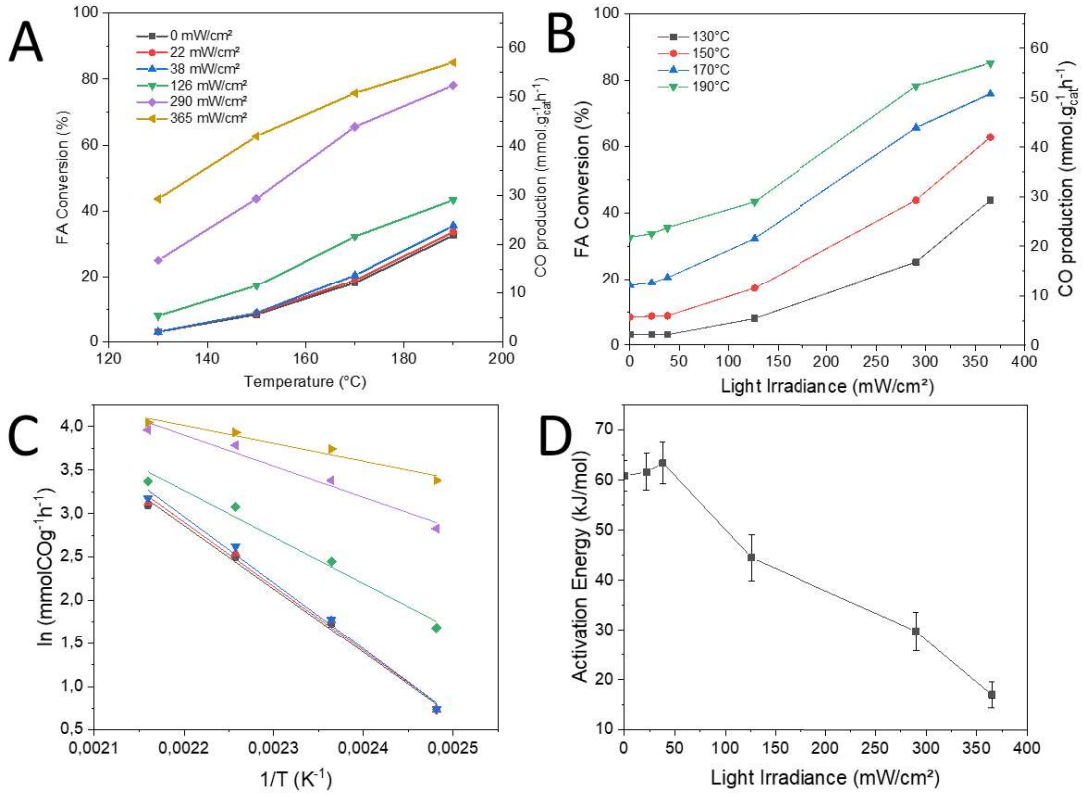

Fig. 41 *Influence of both the reaction temperature in the 130-190°C range and the UV-A irradiance (0-365 mW/cm^2) on the catalytic activity of the pure TiO_2-P25 support in the gas phase FA decomposition, expressed in terms of FA conversion and CO formation in mmol/g/h,* ***(A)*** *temperature dependency and* ***(B)*** *light irradiance dependency.* ***(C)*** *Arrhenius plot at each light irradiance condition and* ***(D)*** *Activation energy dependency with the light irradiance.*

Reaction conditions: [FA]=4600 ppm$_v$, total Ar flow of 14.7 mL, 1.8 mg of catalyst, FA specific molar rate of 67.2 mmol g^{-1}h^{-1}.

Literature has already reported some possible formic acid decomposition mechanisms over titanium dioxide. For instance, Henderson proposed a mechanism involving a complex set of chemical reactions, with the formation of water and the creation of oxygen vacancies by the reaction of the acid proton

with the oxide lattice (Eqs. 3.4,3.5), and subsequently with the decomposition of the adsorbed formate with the release of CO (Eqs. 3.6-3.8)[25].

$$2HCOOH + 2O^{2-}_{lattice} \rightarrow 2HCOO^{-}_{ad} + 2OH^{-}_{lattice} \quad (3.4)$$

$$2OH^{-}_{lattice} \rightarrow H_2O + O^{2-}_{lattice} + vac \quad (3.5)$$

$$2HCOO^{-}_{ad} \rightarrow 2CO + 2OH^{-}_{ad} \quad (3.6)$$

$$2OH^{-}_{ad} \rightarrow H_2O + O^{2-}_{ad} \quad (3.7)$$

$$O^{2-}_{ad} + vac \rightarrow O^{2-}_{lattice} \quad (3.8)$$

Studies are ongoing for elucidating the mechanism responsible for the light/heat synergistic effect enhancing the dehydration activity of the bare TiO_2 support. Hypotheses may involve the implication of the photogenerated charge carriers of TiO_2 or the possible change in the surface chemistry upon illumination.

Taking into account the above-mentionned equations, we can also put forward the capacity of light to activate lattice oxygen. This effect is nowadays reported as one of the factors explaining most of the recent advances in the field of environmental remediation (e.g. mineralization of volatile organic compounds) obtained by photothermal catalysis. In thermal catalysis, the activation of the oxygen species occurs with the implementation of Mars-van Krevelen redox mechanism where the surface reducible oxygens of the catalyst directly participate in the oxidation. This was put forward by Palmisano and coll. who demonstrated notably that brookite TiO_2-CeO_2 composites considerably lower the conversion temperatures for a variety of volatile organic compounds under light [26]. Similarly, Fiorenza et al. reported that the T_{90} temperature was also decreased on noble metal-free MnO_x-ZrO_2 catalysts in the case of gaseous toluene and ethanol [27]. In Zhang et al., the light was proposed to activate oxygen lattice in Pt-embedded CoO/g-C_3N_4 ternary multifunctional catalysts for the degradation of gaseous toluene under simulated solar light (300 W Xe lamp) [28]. The positive role of the photoactivation of lattice oxygen was also suggested for a $LaTi_{0.6}Mn_{0.4}O_{3+\delta}$ photothermal catalyst in the toluene degradation [29].

Formic acid decomposition over titania has been studied by considering the role of Ti−O site pairs, which consist of five-coordinate Ti (Ti_{5c}) and two-coordinate O (O_{2c}) on the surface. Kwon et al. analysed by kinetics and isotopics methods with DFT the different transition steps during the formic acid decomposition at the surface of rutile (101) and anatase (101) crystalline phases [30]. With the theoretical and experimental results obtained in their study, they proposed the FA decomposition over TiO_2 surface scheme that is shown in **Fig. 42**. They indicated that the cleavage of C-O and O-H bonds in molecularly adsorbed formic acid (HCOOH*) is the kinetically-relevant step. They also observed by infrared spectroscopy that this molecularly adsorbed species can also dissociate into bidentate formate (*HCOO*) with a coadsorbed proton on a O_{2c} atom. These species are more thermodynamically stable than HCOOH*. However, large DFT-derived energy barriers were calculated for the CO formation via *HCOO* decomposition, which inhibits kinetically this route for the dehydration reaction. In this case, the authors suggested back reaction to *HCOOH species from *HCOO that finally decompose into CO and H_2O as shown in the scheme of the **Fig. 42**. Last step is the water formation from the recombination (condensation) of H/OH* at Ti_{5c}-O_{2c} pair and its desorption to obtain back the bare surface.

Therefore, considering the activation of the oxygen lattice by light (previously mentioned), the involvement of the O_{2c} atoms in the formic acid adsorption and decomposition (with water formation/desorption from the surface) might also be proposed to explain the enhancement of the formic acid decomposition under light irradiation conditions.

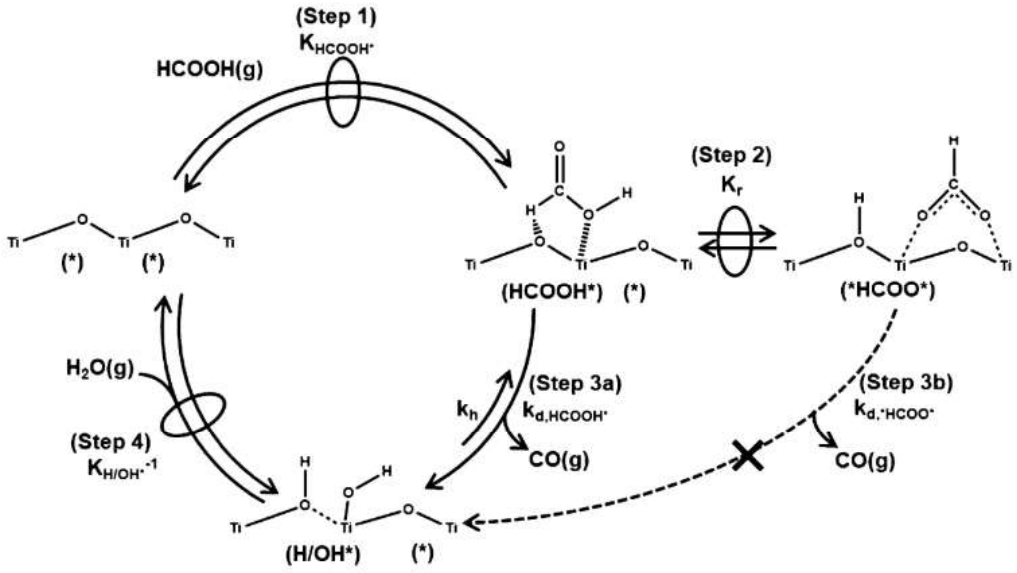

Fig. 42 *Proposed scheme from ref* [30] *about the mechanistic steps of formic acid adsorption and decomposition into dehydration products over titanium dioxide surface.*

1.5. Possible light-induced mechanisms in FA photothermal decomposition

Methodologies used to discriminate electron-driven from thermal-driven reaction pathways during dehydrogenation and dehydration processes in photo-thermal reaction (see Introduction section 4) are useful tools for mechanistic aspects. Superlinear and linear regimes in light-dependency plots indicate electron-driven processes prevalence above thermal driven to carry out catalytic reaction under illuminating conditions [23].

Literature reports that selectivity changes upon illumination can also be the sign of electron-driven mechanisms [31]. In our case, dehydrogenation reaction have been more benefited from the irradiation than the dehydration reaction. However, selectivity to H_2 under dark conditions is also temperature-dependent as shown in **Fig. 37**B, so that looking on selectivity aspects cannot provide us clear information whether electron-driven or termalization mechanisms are predominant.

According to literature, apparent activation energy values are lowered through electron-driven processes [31–34] where the combined (dual) excitation is taking advantage of the photonic excitation for allowing the reaction to be conducted through an alternative low-energy transition state, and the thermal excitation to subsequently operate on a new dark-type rate-determining-step. **Fig. 43** depicts Arrhenius equation plot graphs of both dehydrogenation (**Fig. 43**A) and dehydration (**Fig. 43**B) reactions. In a prevalence of “hot carriers” thermalization increasing locally temperature over electron-

driven reaction, no change in apparent activation energy is expected, and the reaction would process under combined excitation through a similar mechanism than that operating in the dark, but not at the bulk temperature. As shown in **Fig. 43**C, the apparent activation energy for the dehydrogenation reaction decreased from 106 kJ/mol in the dark down to 18 kJ/mol at the highest irradiation of 365 mW/cm^2, while the same trend was observed for the dehydration reaction, for which the apparent activation energy was reduced from 64.1 kJ/mol in the dark down to 17.3 kJ/mol at 365 mW/cm^2. While the apparent activation energy for dehydrogenation overcomes strongly that for dehydration in the dark, the increase in the light irradiance strongly reduced this gap, so that the selectivity to H_2 significantly enhanced, with values in the 8–40% range in the dark increasing up to the 60–80% range under light depending on the reaction temperature.

If we consider that most of the CO formed resulted from the dehydration activity of the TiO_2 support itself, the enhancement of the H_2 selectivity upon illumination might result from the occurrence of two fully different mechanisms for the CO and H_2 formation, that are in consequence differently enhanced under light. The more pronounced enhancement of the Ru-based pathway over the TiO_2-based one, could explain the strong increase in the H_2 selectivity upon illumination.

We must stress that the change of the regime into a sublinear regime observed in some conditions (at very light conversion) cannot be used to derive a mechanism change, due to the very high conversions achieved.

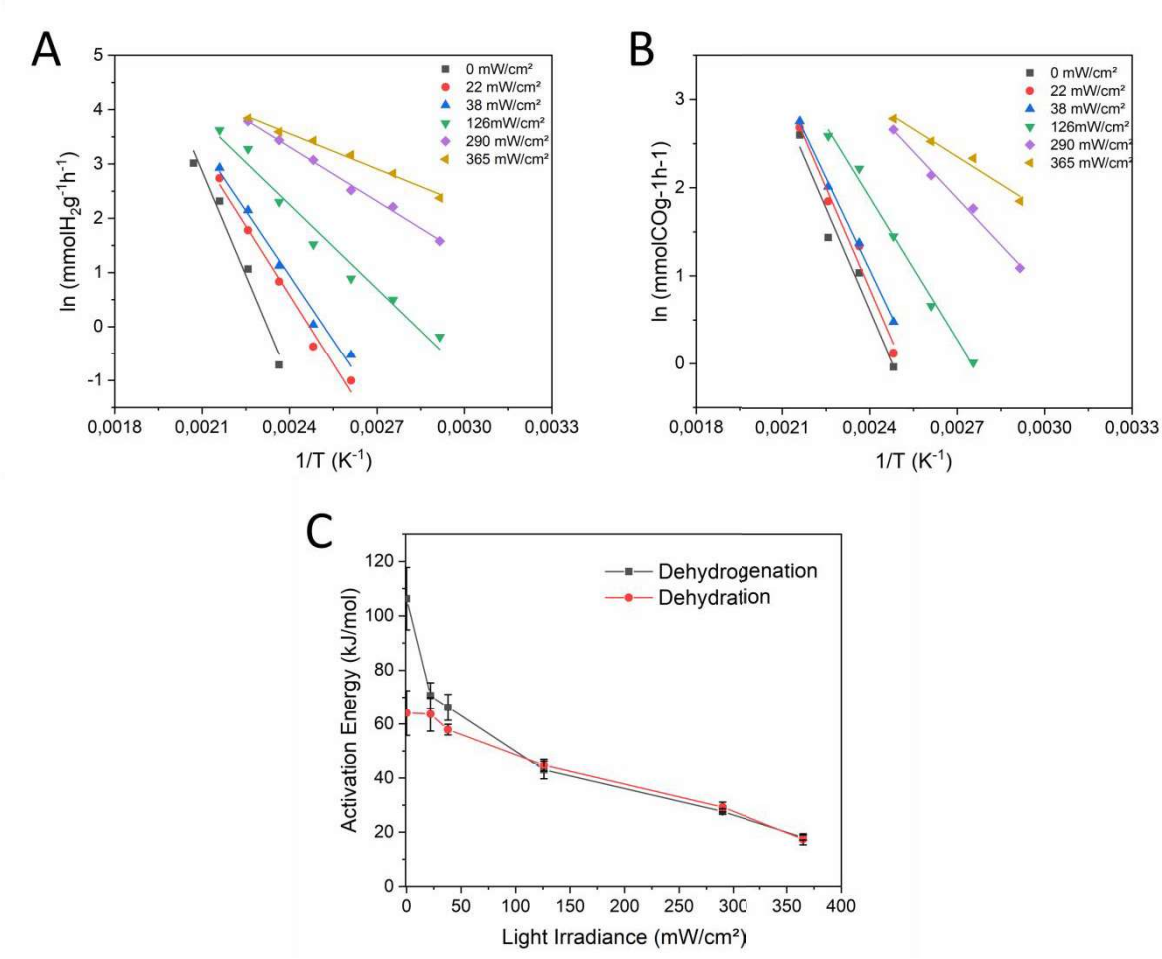

Fig. 43 *Arrhenius plot graphs of* ***(A)*** *dehydrogenation and* ***(B)*** *dehydration reactions.* ***(C)*** *Influence of the light irradiance on the apparent activation energy calculated for both dehydration and dehydrogenation reactions on the Ru (0.5 %)/TiO_2 (PA) reference catalyst prepared by the photo-assisted synthesis method.*

Reaction conditions: [FA]=4600 ppm_v, total Ar flow of 14.7 mL, 1.8 mg of catalyst, FA specific molar rate of 67.2 mmol $g^{-1}h^{-1}$.

To sum up, we demonstrated for the first time that a photothermal effect can be used on a Ru(0.5 %)/TiO_2 (PA) catalyst to boost the decomposition of gas-phase formic acid into H_2 under UV-A photon flux irradiation. Enhanced catalytic formic acid conversion and selectivity to dehydrogenation products were achieved under light and resulted from new possible phenomena induced by the photo excitation. The photon-dependency and the lowering of activation energy values suggest a predominance of electron-driven processes over thermal-driven ones. The occurrence of two different mechanisms for CO and H_2 productions (both being enhanced under combined excitation) taking place on two different surfaces (namely the TiO_2 support and the Ru nanoparticles, respectively) might explain the positive change in selectivity upon irradiation.

The performances of the Ru(0.5%)/TiO_2 (PA) reference catalyst are however suffering from the intrinsic activity of the TiO_2 support as dehydration catalyst, further enhanced in photothermal conditions. Therefore, further studies about the catalyst have to be conducted to gain knowledge on the different processes that occur during the dual photo/thermal excitation.

2. Complementary study on the influence of synthesis aspects.

This complementary (additional) study has been conducted in order to investigate to which extent the catalytic behavior and the photothermal effect are influenced by the surface properties of the catalyst, as both Ru and TiO_2 materials that compose the catalyst are photo-sensitive to UV-A light, and exhibited photothermal effects upon irradiation.

The properties of both the Ru nanoparticles and the Ru/TiO_2 catalysts can be influenced by the synthesis protocols. For instance, previous studies on Ru/TiO_2 catalysts synthesized via the solar light-assisted method demonstrated that the nanoparticle growth was impacted by the light irradiation time, the longer the irradiation time, the larger the particle size [9]. As it has been reported in the case of plasmonic materials, particle size of metal nanoparticles may influence the light absorption properties as photon wavelength range or absorption intensity [35]. Therefore, this section is studying the influence of two synthesis factors on the behavior of the Ru/TiO_2 photothermal catalysts and the H_2 production under dual photo/thermal excitation, namely the irradiation time used for the photo-assisted synthesis, and the preparation method itself.

2.1. Influence of the irradiation time in the light-assisted synthesis of the Ru/TiO_2 catalysts.

Ru(0.5%)/TiO_2 (PA) catalysts were synthesized as described in Chapter 2 following three different irradiation times, i.e. 1, 2 and 7 h. CO pulses chemisorption demonstrated a lower adsorption of CO on the catalyst prepared with larger irradiation time in comparison to that observed for the reference catalyst prepared for 2 h, as shown in **Fig. 44**. The calculated dispersion value in the 7 h irradiation time sample is 20 %, largely lower than irradiation time of 2 h (90 %). We know from previous studies conducted in the lab that shorter irradiation times led to smaller-size Ru nanoparticles. Unfortunately, the small size of Ru nanoparticles for an irradiation time of 1 h (the 'nanoparticles' terminology remains here questionable, as maybe nano-clusters might be preferred ?) makes difficult their characterization via classical techniques, and we can just assume the smallest Ru size for the sample prepared for 1 h *vs.* 2 h of synthesis.

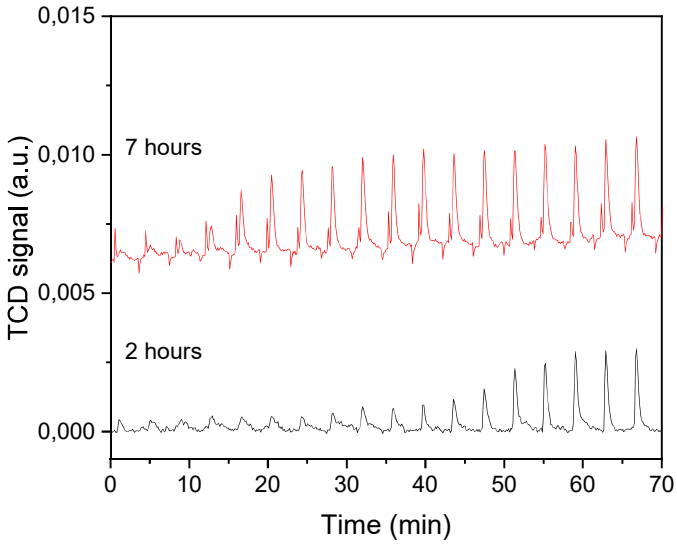

Fig. 44 *CO pulses chemisorption tests over Ru (0.5%)/TiO_2 (PA) catalysts synthesized by the photo-assisted method with an irradiation time of 2 h (black) and 7 h (red).*

Fig. 45 and **Fig. 46** depict respectively the H_2 and CO production from formic acid decomposition within the 110-150°C temperature range obtained on the three different Ru (0.5)/TiO_2 catalysts. It must be said that a photothermal effect was observed for all catalysts, as both H_2 and CO produced increased upon irradiation, the effect being all the more pronounced than the irradiation was high. However, it was worth nothing that their behavior differed strongly whether the H_2 or the CO production was concerned. Indeed, whatever the temperature and the light irradiance, the same CO production level was obtained for the three Ru/TiO_2 catalysts, meaning that the CO production and its enhancement through photothermal effect were not influenced by the size of the Ru nanoparticles. By contrast they were both influenced in the case of the H_2 production. This difference is well visualized in **Fig. 47** and **Fig. 48**, in terms of Arrhenius plots for both the H_2 and CO productions.

This was in agreement and supported our suggestion that H_2 and CO productions (i.e. dehydrogenation and dehydration reactions) might occur through two fully different mechanisms, involving the Ru nanoparticles and the TiO_2 support surface, respectively, both being enhanced under light.

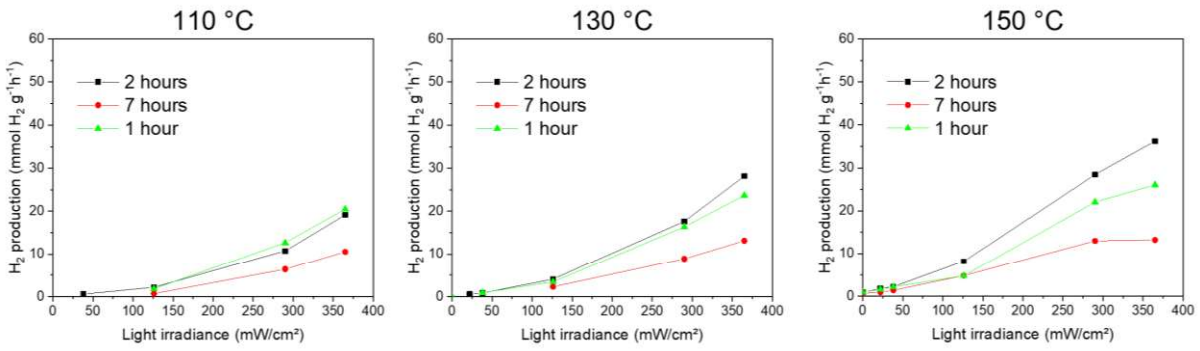

Fig. 45*. Light irradiance dependence of the catalytic H_2 production at 110, 130 and 150°C on the Ru(0.5%)/TiO_2 (PA) catalyst synthesized by the light-assisted method for 1 h (green line), 2 h (black line) and 7 h (red line). Reaction conditions: [FA]=4600 ppm_v, total Ar flow of 14.7 mL, 1.8 mg of catalyst, FA specific molar rate of 67.2 mmol $g^{-1}h^{-1}$.*

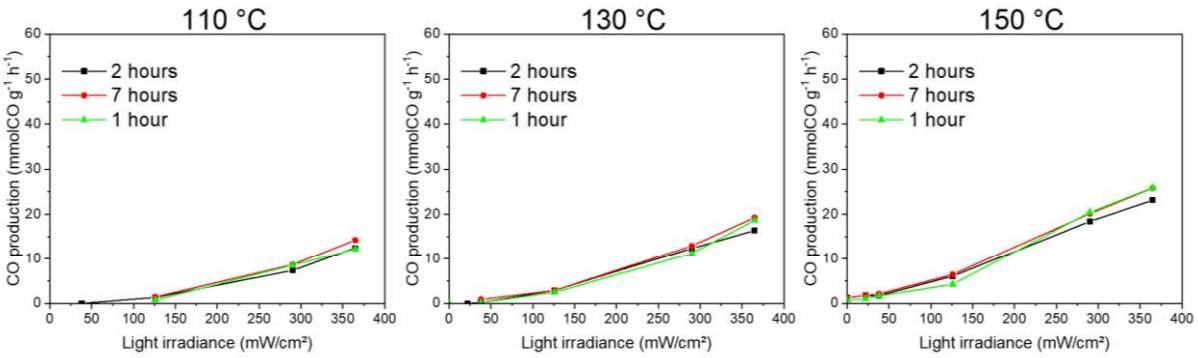

Fig. 46 *Light irradiance dependence of the catalytic CO production at 110, 130 and 150°C on the Ru(0.5%)/TiO_2 (PA) catalyst synthesized by the light-assisted method for 1 h (green line), 2 h (black line) and 7 h (red line). Reaction conditions: [FA]=4600 ppm_v, total Ar flow of 14.7 mL, 1.8 mg of catalyst, FA specific molar rate of 67.2 mmol $g^{-1}h^{-1}$.*

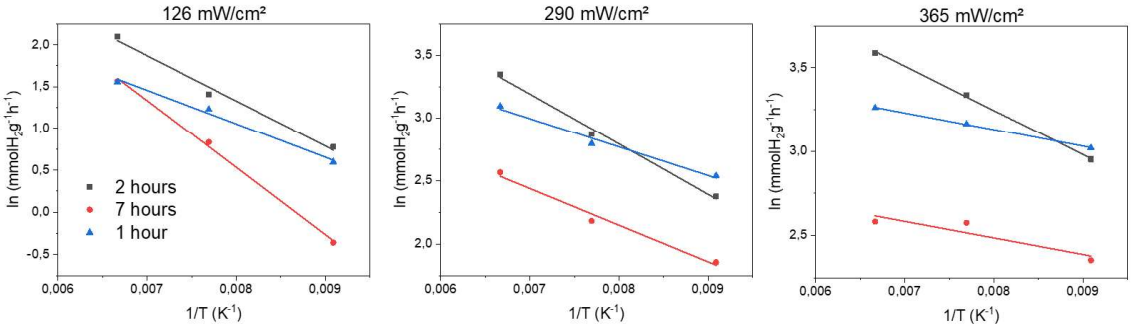

Fig. 47 *Arrhenius plot of H_2 production under 126 W/cm², 290 mW/cm² and 365 mW/cm² irradiance on the Ru(0.5%)/TiO_2 (PA) catalyst by the light-assisted method for 1 h (blue line), 2 h (black line) and 7 h (red line). Reaction conditions: [FA]=4600 ppm_v, total Ar flow of 14.7 mL, 1.8 mg of catalyst, FA specific molar rate of 67.2 mmol $g^{-1}h^{-1}$.*

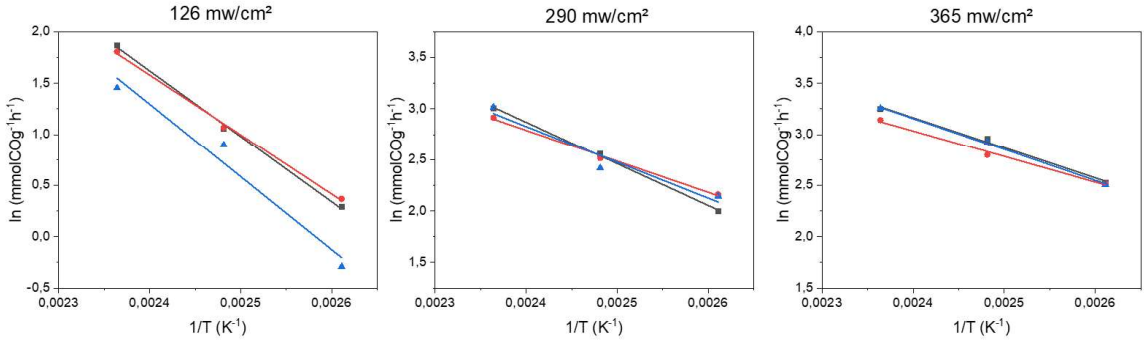

Fig. 48 *Arrhenius plot of CO production under 126 W/cm², 290 mW/cm² and 365 mW/cm² irradiance on the the Ru(0.5%)/TiO_2 (PA) catalyst by the light-assisted method for 1 h (blue line), 2 h (black line) and 7 h (red line). Reaction conditions: [FA]=4600 ppm_v, total Ar flow of 14.7 mL, 1.8 mg of catalyst, FA specific molar rate of 67.2 mmol $g^{-1}h^{-1}$.*

2.2. Influence of the synthesis method : wet impregnation vs. light-assisted method

A wet impregnation method with final thermal reduction under H_2 has been used as a classical catalyst preparation method to be compared to the photo-assisted synthesis method for getting knowledge to which extent the surface metal properties can affect to H_2 production and the photothermal effect. **Table 3** shows the main properties of the Ru(0.5%)/TiO_2 catalysts prepared via both methods. The catalyst prepared by Wet Impregnation (WI) method has a Ru loading of 0.53 wt. %, in agreement with the desired (nominal) value of 0.5 wt.% close to that of 0.46 wt.% obtained through the photo-assisted synthesis method.

TEM pictures, shown in **Fig. 49**B, reveal a larger Ru particle size with a broader size distribution at the surface of the titanium dioxide compared to the sample prepared by the photo-assisted synthesis method, namely a mean particle size of 1.2 nm *vs.* 0.6 nm. **Fig. 49**A depicts the X-ray photon spectra of the catalyst prepared by wet impregnation (C1s and Ru 3d orbital energy range). In comparison to the catalyst prepared following the photo-assisted method, the binding energy of metallic Ru is shifted towards lower binding energy values from 1.2 eV, at 279.2 eV. This downward energy shift of the $Ru^{(0)}$ binding energy observed with respect to the accepted value of 279.9 eV for bulk metallic Ru [36–38], was proposed to result from the existence of metal–support interactions, which have been ascribed to a charge transfer in the substrate (support) to the supported nanometer-size metallic particles, as usually observed for TiO_2 support after a high-temperature reduction step in H_2, notably due to the high mobility of surface titanium atoms. Even if we have no high-resolution microscopy evidence of the partial decoration of Ru nanoparticles by titanium atoms, this metal–support interaction could correspond to the well-admitted Strong Metal-Support Interaction, SMSI, effect [39], caused by high-temperature reduction processes during the catalyst preparation. This SMSI effect have been reported for Ru/TiO_2 systems, as well as with other noble metals as gold [40–42] and platinum [43–46] , or non-noble such as cobalt [47–49]. The energy shift strongly depends on the nature of the oxide support and can also be understood from the literature in terms of difference of electronegativity values. In case of systems with a supported metals exhibiting a higher electronegativity than that of the cation (M^{n+}) from the metal oxide support (2.2 *vs.* 1.5, although logically lower than that of the oxygen at 3.5), the supported metal (here Ru) acts as electron acceptor in competition with the surface oxygen atoms, with respect to the titanium cations from the support surface [50].

Table 3 shows that the catalyst exhibits a lower Ru/Ti SAR of 0.017 *vs.* 0.036 for the catalyst prepared by the photo-assisted synthesis method, in agreement with the larger mean Ru nanoparticle size. Therefore, the high-temperature reduction process generates larger metallic Ru nanoparticles with a broader distribution of the particle size, as well as with a stronger interaction with the TiO_2 support in comparison to the photo-assisted method.

Catalyst synthesis method	**wt. % Ru[1]**	**Particle size (nm) [2]**	**Ru^0 B.E. (eV)[3]**	**$Ru^0/Ru^{\delta+}$ [3]**	**SAR $_{Ru/Ti}$[3]**
Photo-assisted (2h)	0.46	0.6 ± 0.2	280.4	79/21	0.036
Wet impregnation	0.53	1.2 ± 0.4	279.2	68/32	0.017

Table 3*. Data of different properties of Ru(0.5%)/TiO_2 catalysts synthesized by both catalyst preparation methods obtained by 1.ICP-OES, 2 TEM characterization techniques and 3. XPS*

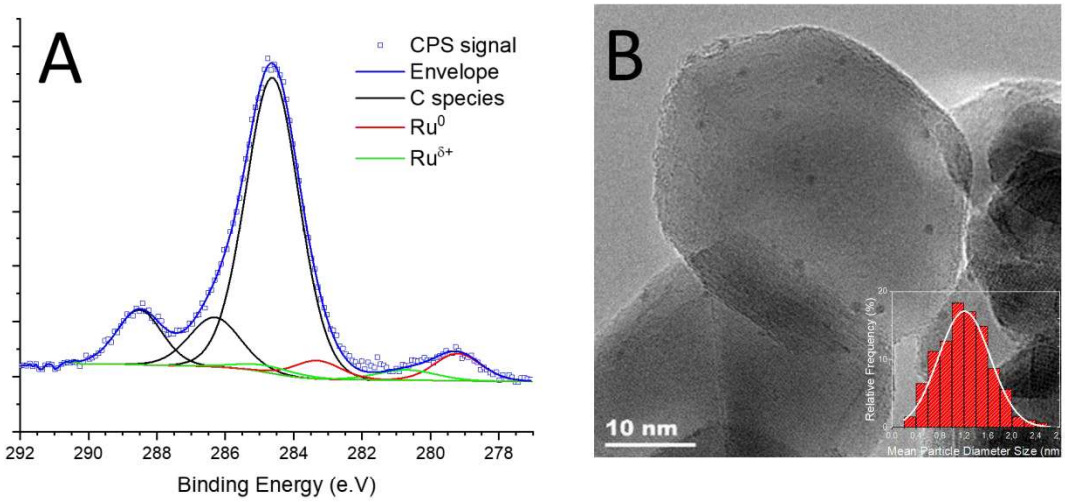

Fig. 49(A) *Ru 3d + C 1s orbitals XPS profile of the Ru(0.5%)/TiO_2 (WI) catalyst, with red: Ru^0 (3d); green: oxidized $Ru^{\delta+}$ (3d); black: multi-contribution envelope of adventious carbon (1s);* ***(B)*** *TEM picture of Ru particles at the surface of the TiO_2 support and histogram of the particle size measurement.*

In regards to the photo-thermal catalytic decomposition, there is a wide difference between the two catalysts. **Fig. 50**A,B and **Fig. 50**C,D depict the H_2 and CO productions over both Ru(0.5%)/TiO_2 catalysts. In dark conditions, the WI catalyst exhibited performances overcoming those obtained on the catalyst prepared via the photo-assisted method, for both the H_2 and CO production levels. For instance, H_2 values of 16 $mmolH_2\,g^{-1}h^{-1}$ are obtained at 150°C with the WI catalyst versus less than 1 $mmolH_2\,g^{-1}h^{-1}$ in the absence of UV-A light irradiation on the PA catalyst, respectively. More investigation are necessary to determine if this relates more to a Ru size effect or to a change of the electronic properties of Ru nanoparticles due to the interaction with the TiO_2 support. This was not the aim of this short study. However, it was noteworthy that the catalyst prepared by the WI method also benefited from a photothermal effect for boosting its catalytic performances in the FA decomposition, similarly to the case of the Ru(0.5 %)/TiO_2 (PA) reference catalyst.

The Arrhenius plots and the associated activation energy graphs shown in **Fig. 51** are evidencing that both catalysts seem to follow the same behaviour:

- first, in dark conditions, a higher activation energy for the dehydrogenation reaction *vs.* that of the dehydration reaction that favours the formation of CO and led to a low selectivity to H_2.
- a gradual decrease in activation energy for both reactions upon irradiation, being more pronounced in the case of the dehydrogenation reaction, so that the selectivity to H_2 was enhanced with the increase of the light irradiance.

It was noted in **Fig. 50**E,F that the Ru/TiO_2 (WI) catalyst allowed a higher selectivity to H_2 to be obtained in the dark in comparison to the Ru/TiO_2 (PA) counterpart. By contrast the selectivity enhancement upon illumination was more pronounced for the Ru/TiO_2 (PA) catalyst, and strongly higher selectivities were achieved for temperatures as high as 170°C-190°C. This is in particular interesting for an application of the FA decomposition such as for use as internal hydrogen carrier, although a slightly lower activity was observed. The reasons of that behaviour still need to be investigated, but are probably related to the role of the Ru-TiO_2 interface in the electronic properties of the Ru nanoparticles and/or to a size effect, with different behaviour in terms of photothermal effect.

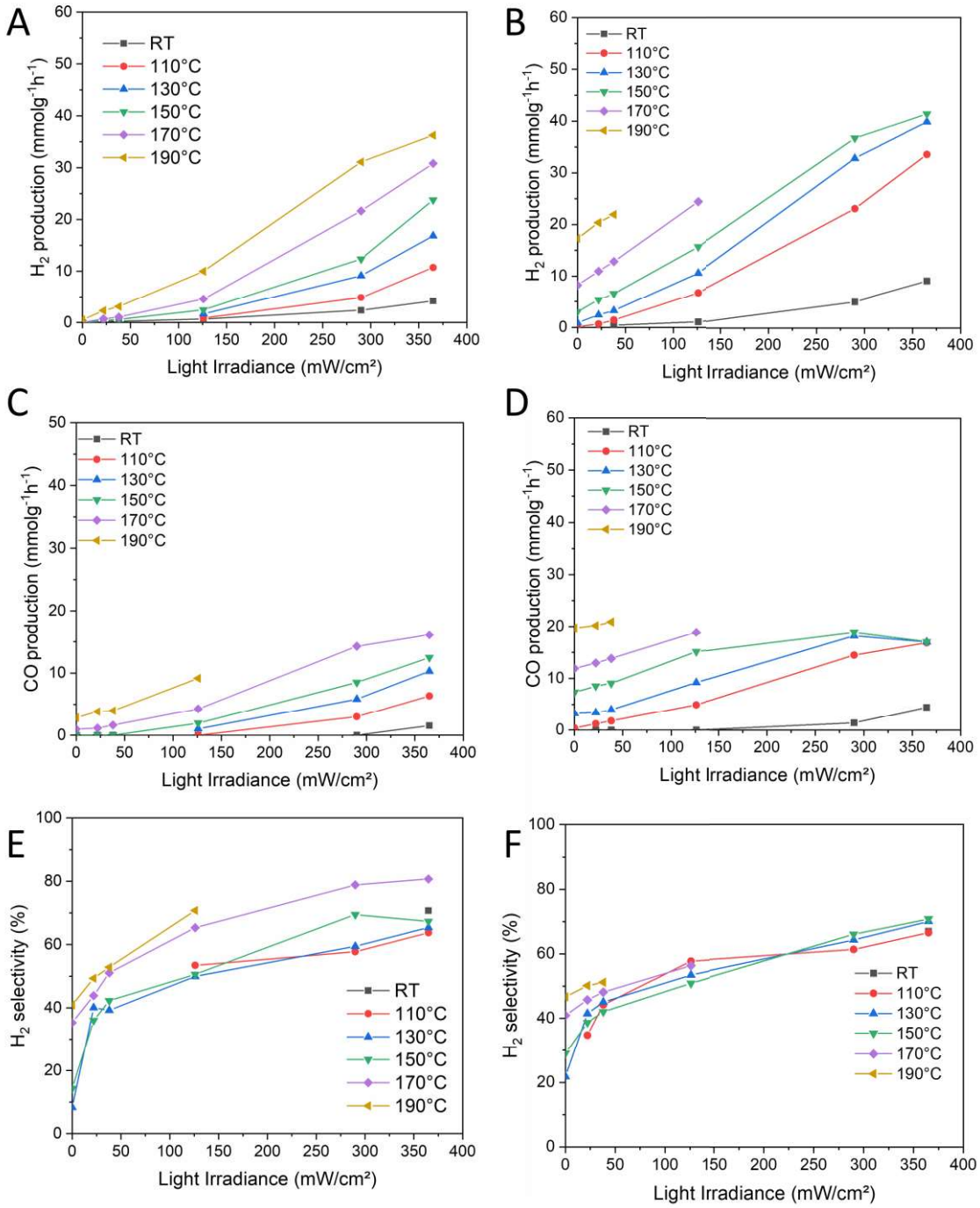

Fig. 50 *Light-dependence FA decomposition via dehydrogenation* ***(A, B)*** *and dehydration* ***(C, D)*** *processes, and Selectivity to* H_2 ***(E, F)*** *obtained on the Ru(0.5%)/*TiO_2 *catalyst prepared following the photo-assisted synthesis method* ***(left)*** *and the wet impregnation method* ***(right)****.*

Reaction conditions: [FA]=4600 ppm_v*, total Ar flow of 14.7 mL, 1.8 mg of catalyst, FA specific molar rate of 67.2 mmol* $g^{-1}h^{-1}$*.*

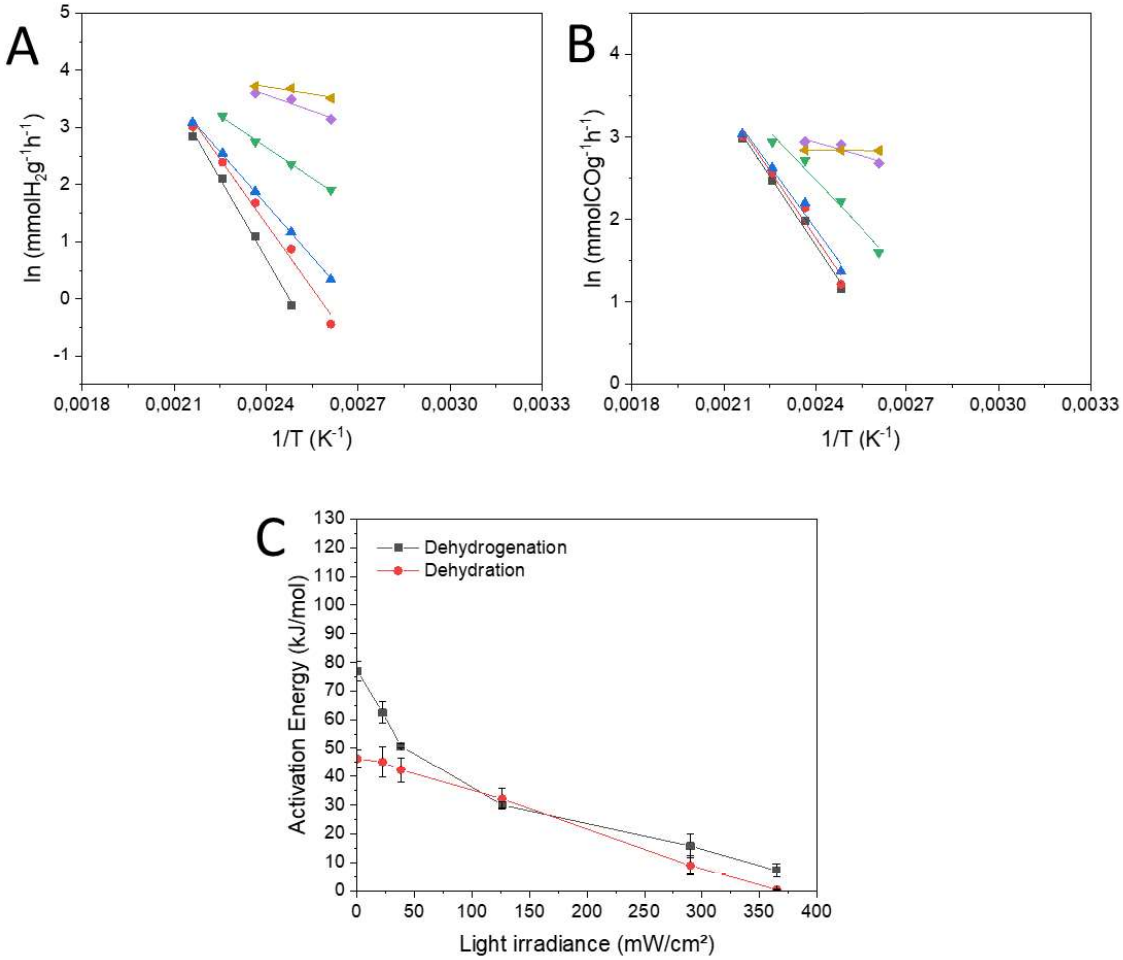

Fig. 51 Arrhenius plot for H_2 production **(A)** and CO production **(B)** on the Ru (0.5 %)/TiO_2 (WI) catalyst with the apparent activation energies of both reactions as function of the light irradiance **(C)**.

Reaction conditions: [FA]=4600 ppm$_v$, total Ar flow of 14.7 mL, 1.8 mg of catalyst, FA specific molar rate of 67.2 mmol g^{-1}h^{-1}.

3. Influence of the ruthenium loading

Following the works reported in the previous section, here is reported a short study conducted in order to investigate to which extent the catalytic behavior and the photothermal effect are influenced by the Ru loading, taking the photo-assisted synthesis as reference method for elaborating the catalyst. TiO_2 supported ruthenium catalysts with different loadings within the 0-1 wt. % range were synthesized by the photo-assisted method with a similar irradiation duration of 2 h. Chemical analysis values demonstrated a Ru loading similar to the desired (nominal) value for each catalyst, shown in **Table 4**. **Fig. 53**A, C, E depicts the Ru 3d and C 1s region spectra in XPS for the 0.25, 0.5 and 1 wt.% Ru/TiO_2 catalysts, respectively. The Ru 3d peaks intensity is commonly related to the metal concentration at the support surface and the nanoparticle dispersion (nanoparticle size). No significant difference was observed in terms of binding energy for the Ru 3d5/2-Ru 3d3/2 orbital doublet contributions, as metallic Ru^0 species and its surface oxidized $Ru^{\delta+}$ form. The spectra differ in terms of Ru/Ti surface atomic ratios (i.e. relative peak intensities). Ru/Ti surface atomic ratios of 0.011, 0.036 and 0.022 were obtained for Ru contents of 0.25%, 0.5% and 1%, respectively. In regards of Ru nanoparticle size, TEM images (**Fig. 34** and **Fig. 52**) and the corresponding size histograms show mean nanoparticle diameter

size of 0.6 nm, 0.6 nm and 0.8 nm, respectively (**Fig. 53**B, D and F). Both characterization data are in good agreement. In addition, it was possible to observe the metallic Ru (101) planes on the 1% Ru/P25 catalyst. This supports that, even a higher Ru concentration, the photo-assisted method is an efficient method to synthesize metallic Ru nanoparticles over TiO_2.

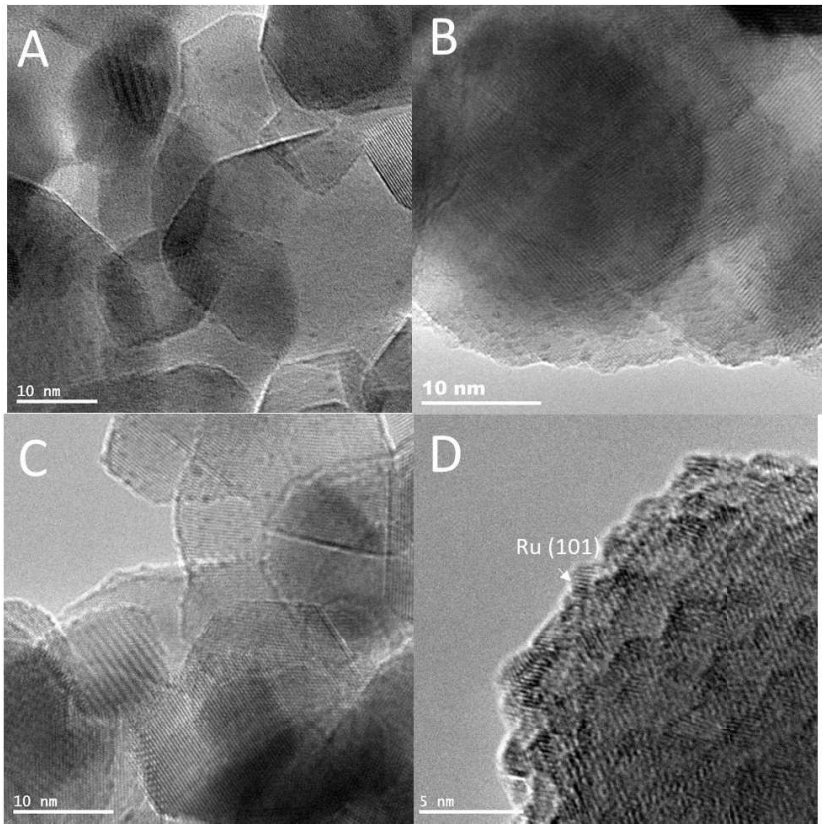

Fig. 52 *TEM images of* ***(A,B)*** *Ru (0.25%)/TiO_2 (PA) and* ***(C,D)*** *Ru (1%)/TiO_2 (PA).*

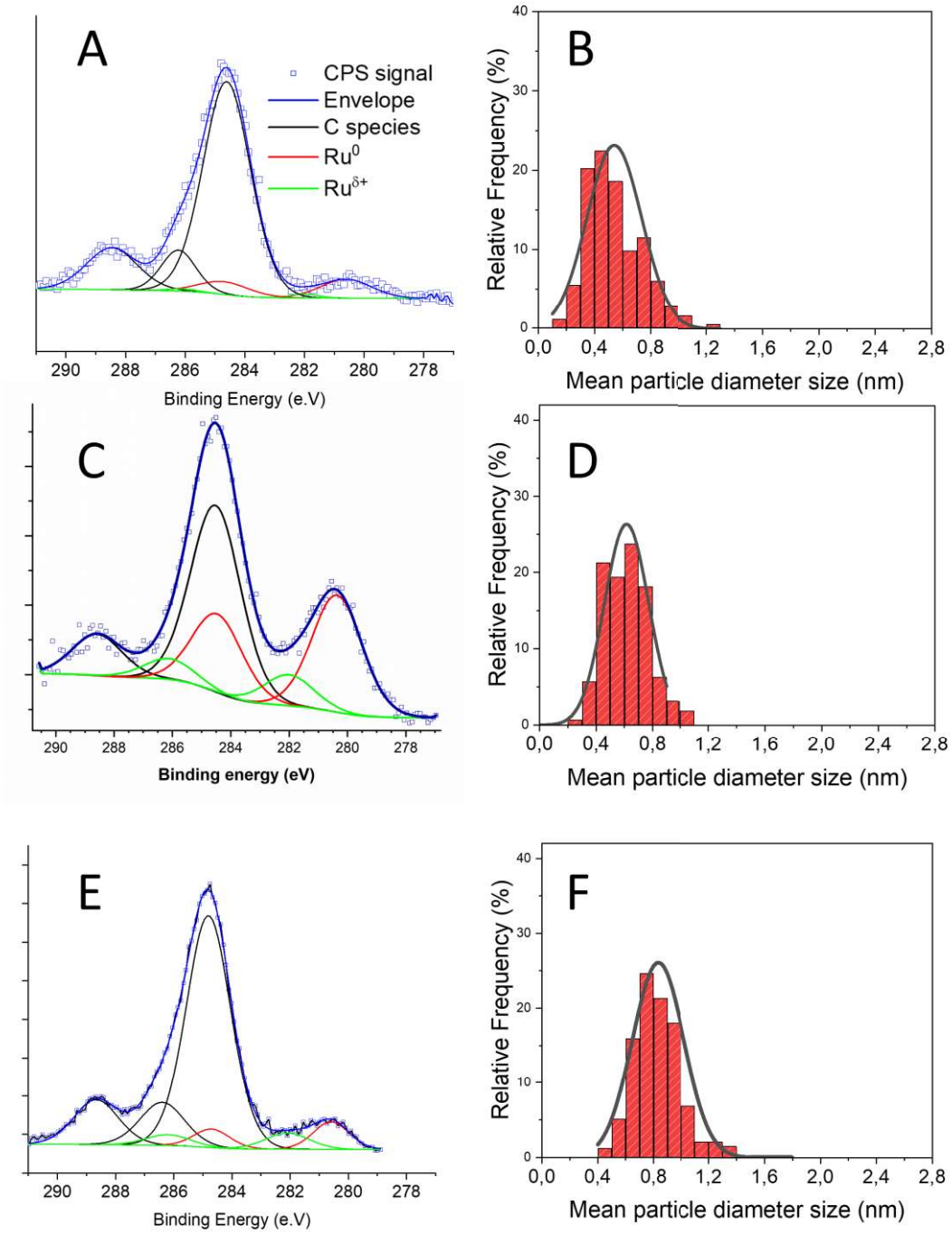

Fig. 53 (left) *Ru 3d + C 1s orbitals XPS profile of the Ru/TiO_2 (PA) catalyst and* ***(right)*** *histograms pf the Ru nanoparticle size distribution derived from TEM pictures for* ***(A, B)*** *0.25 wt.%,* ***(C, D)*** *0.5 wt.% and* ***(E, F)*** *1 wt.%, Ru/TiO_2 catalysts.*

wt. % Ru[1]	**Particle size (nm) [2]**	**Ru^0 B.E. (eV)[3]**	**$Ru^0/Ru^{\delta+}$ [3]**	**SAR $_{Ru/Ti}$[3]**
0.26	0.6 ± 0.2	280.6	90/10	0.011
0.46	0.6 ± 0.2	280.4	79/21	0.036
0.98	0.8 ± 0.2	280.6	58/42	0.022

Table 4 *Data of different properties of the Ru(0.5%)/TiO_2 (PA) catalysts obtained by 1.ICP-OES, 2 TEM characterization techniques and 3. XPS*

Fig. 54 and **Fig. 55** depict the light irradiance dependency of both H_2 and CO productions from formic acid decomposition over the three different catalysts at 25, 110, 130 and 150°C. As noticed before, no H_2 production was detected over bare TiO_2 that acts only as dehydration catalyst whatever the temperature, CO being the main product and with a significant photothermal effect on the CO production level upon illumination. At the low temperatures studied here, no H_2 production was obtained in the dark regardless of the Ru content.

By contrast, for instance, a catalytic H_2 production rate of 11.1, 23.8 and 20.3 $mmolH_2\ g^{-1}h^{-1}$ was measured on the catalysts with 0.25%, 0.5% and 1 wt. % Ru, respectively, at 110°C with a 365 mW/cm^2 irradiance. Increasing the Ru content with a mean particle size of 0.6 nm for both 0.25% and 0.5% Ru content, allowed to evidence a strong enhancement of the H_2 production level under light. The use of a higher Ru content of 1% led to an increase in the particle size to 0.8 nm, but did not allow for a further photothermal enhancement of the H_2 production. In first assumption, the similar binding energy of the metallic Ru^0 species at the surface obtained for the three Ru-based catalysts led to consider the catalytic behavior in terms of number of surface Ru sites exposed at the surface. For the 1% Ru catalyst, we can suggest that the increase in the number of surface Ru sites resulting from the increased Ru loading, might be compensated by its reduction due to the increase in the mean nanoparticle size. Obviously we cannot fully ruled out the occurrence of a lower intensity electron-driven photothermal effect when increasing the Ru nanoparticle size from 0.6 nm to 0.8 nm.

As far as the CO production was concerned, a similar photothermal enhancement was observed at the four temperatures studied for the three Ru-based catalysts, independently of the Ru content and of the Ru nanoparticle size. This is in agreement with the hypothesis that the CO formation resulted mostly (only) from the catalytic activity of the TiO_2 support itself, that is enhanced under light through a specific mechanism.

Superlinear (or linear) regimes were identified for the photon-dependency curves independently of the Ru loading and the reaction temperature, indicating the predominance of electron-driven processes in the photothermal enhancement of the formic acid decomposition at those temperatures. This correlated well with the Arrhenius plots shown in **Fig. 56**, with a decrease in the apparent activation energies for both H_2 and CO productions.

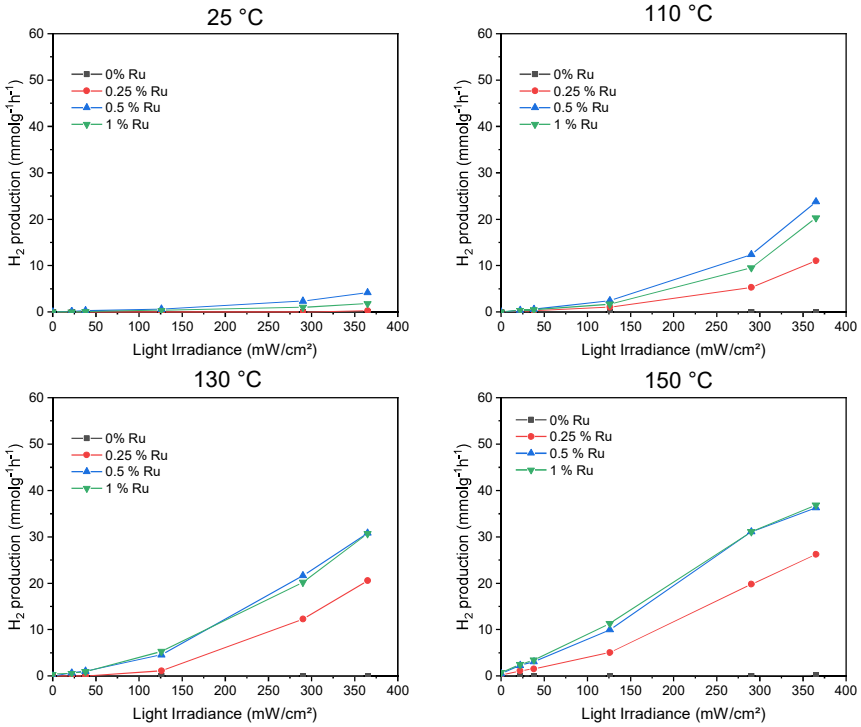

Fig. 54. *Photo-thermal catalytic FA dehydrogenation reaction with the H2 production values as a function of the UV-A light irradiance over bare TiO_2 (black), 0.25 wt.% Ru (red), 0.5 wt.% Ru (blue) and 1% wt. % Ru (green) at 25°C, 110°C, 130°C and 150°C.*

Reaction conditions: [FA]=4600 ppm_v, total Ar flow of 14.7 mL, 1.8 mg of catalyst, FA specific molar rate of 67.2 mmol $g^{-1}h^{-1}$.

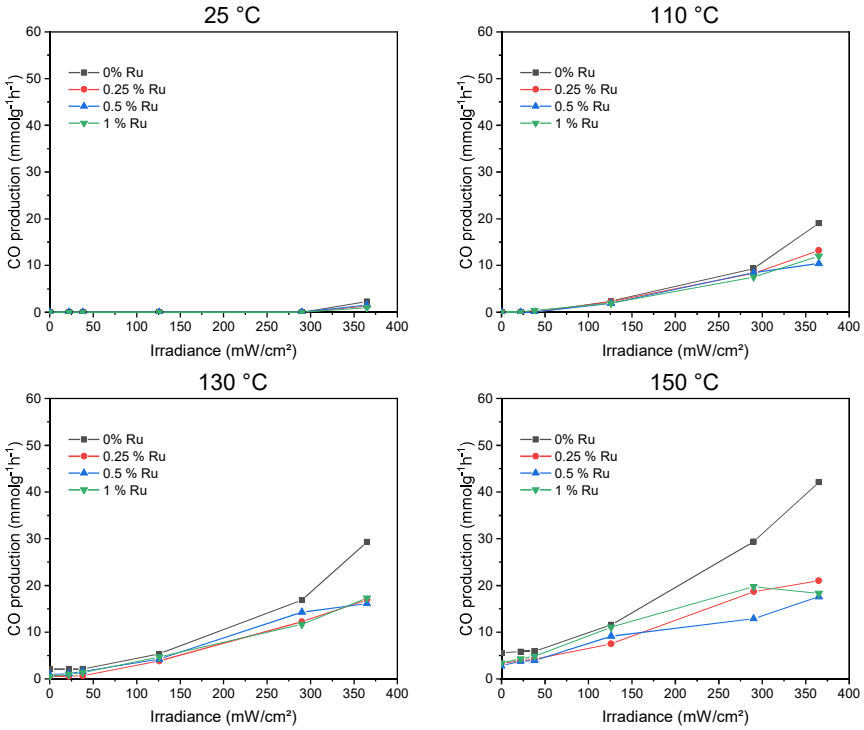

Fig. 55 *Photo-thermal catalytic FA dehydration reaction with the CO production values as a function of the UV-A light irradiance over bare TiO_2 (black), 0.25 wt.% Ru (red), 0.5 wt.% Ru (blue) and 1% wt. % Ru (green) at 25°C, 110°C, 130 °C and 150 °C.*

Reaction conditions: [FA]=4600 ppm_v, total Ar flow of 14.7 mL, 1.8 mg of catalyst, FA specific molar rate of 67.2 mmol $g^{-1}h^{-1}$.

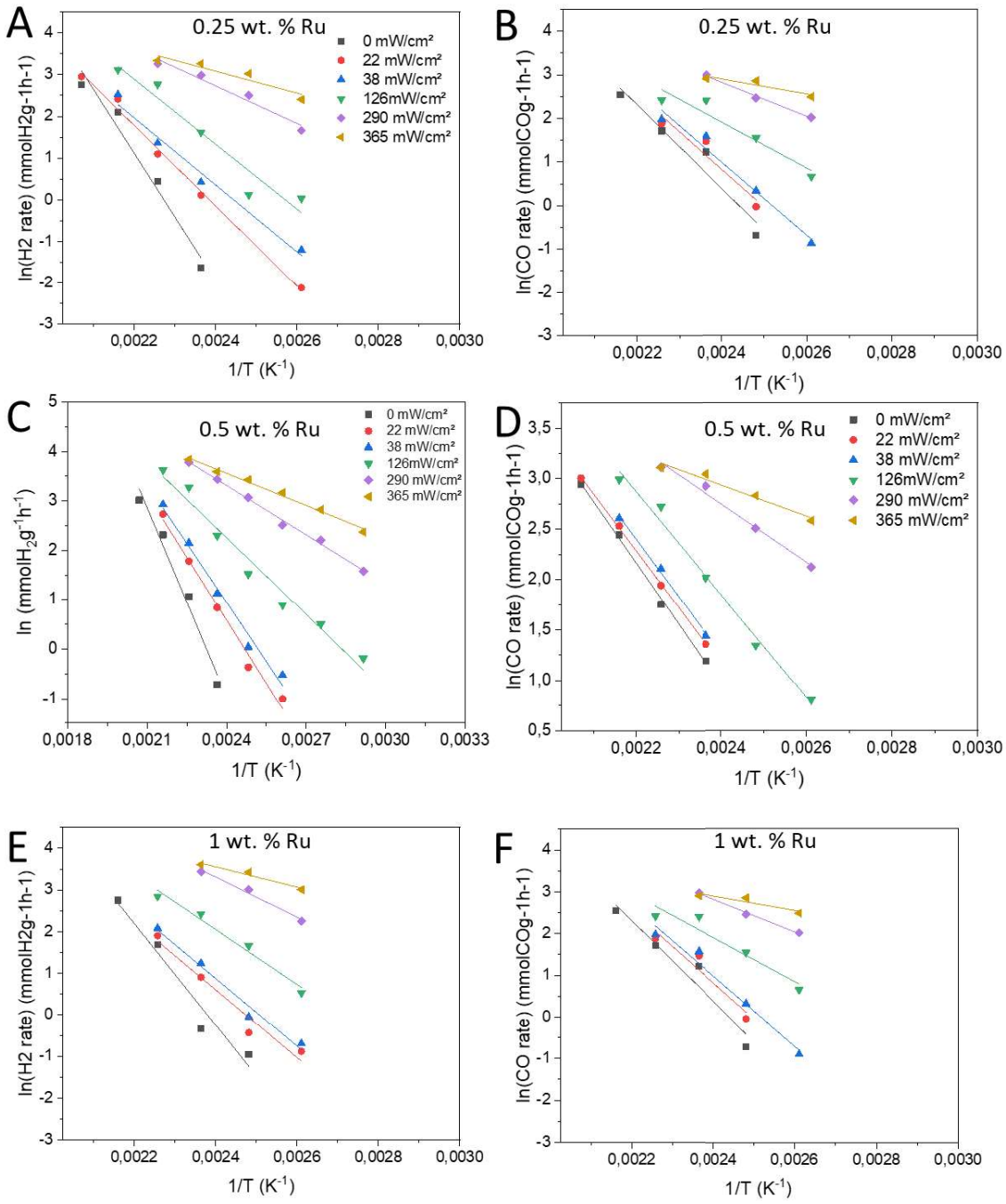

Fig. 56 *Arrhenius plot graphs for H_2 production (**A,C,E**) and CO production (**B,D,F**) at different Ru loadings at the TiO_2 surface.*

4. In-situ DRIFTS study of the formic acid decomposition on Ru/TiO_2 photothermal catalysts

In situ diffuse reflectance infrared Fourier-transform spectroscopy is a useful technique to determine the presence and adsorption of organic species at the catalytic surface under operating (working) conditions. UV-A photonic irradiation can induce electron-driven processes that can affect the mechanism by, for example, the generation of new intermediates species. Therefore, the use of

Fourier-transform infrared spectroscopy to analyze the catalytic surface during the formic acid decomposition (with preliminary tests on bare TiO_2) may provide useful information about the species adsorbed at illuminating and dark conditions.

This section is divided into three parts. First part is focused on the adsorption of the formic acid at the surface of bare titania. Second, the thermal and photothermal decompositions of formic acid over TiO_2 P25 are studied. Third, the thermal and photothermal decompositions of formic acid are investigated on the Ru(0.5%)/TiO_2 (PA) catalyst.

4.1. Formic acid adsorption over bare TiO_2 (P25): gaseous and adsorbed species.

Main absorption bands recorded during the in-situ DRIFTS analysis of FA adsorption over bare TiO_2 (P25), with the wavenumbers, the respective vibrational modes and the assigned species according to the literature are collected in **Table 5**. **Fig. 57** depicts the formic acid adsorption over the bare TiO_2 material. At early adsorption time over TiO_2, three bands at 1684 cm^{-1}, 1552 cm^{-1} and 1375 cm^{-1} are evidenced and assigned to ν(CO) in molecularly adsorbed (MA) HCOOH, and ν_a(OCO) and ν_a(OCO) in bidentate formate species, $HCOO_{ad}$, respectively [30,51–53]. This indicates how the formic acid is adsorbed at first contact with the titania surface. Spectra baseline is slightly shifted to higher absorbance values until formic acid signal is stable. Beside the increase in absorbance of the bands assigned to MA and bidentate formate at longer adsorption time, bands around 1740 cm^{-1} and 1215 cm^{-1} considerably increased in absorbance in the corresponding spectra, related to gaseous dimeric formic acid in the IR chamber [54]. Bands at 1389 cm^{-1} and 1339 cm^{-1} can be assigned to the vibrational mode of δ(CH) gas-phase and molecularly adsorbed (MA) formic acid, respectively [52]. Another vibrational mode of monomer gas-phase formic acid has been reported at 1788 cm^{-1} [55], associated to ν(CO), indicating a dimeric and monomer equilibrium gas-phase formic acid species. The shift of the ν(C=O) band from 1788 to 1684 cm^{-1} when the formic acid is molecularly bonded to TiO_2 surface can be related to a strong interaction between the O atom from the C=O bond and the protons adsorbed at the O_{2c} centers on the TiO_2 lattice. These protons were formed after the formic acid dissociation into bidentate formate [30].

Then, we can conclude that the gas phase is a mixture of both monomer and dimer forms of formic acid. In contact with bare TiO_2 surface, formic acid is adsorbed as MA or as bidentate formate. In **Fig. 58** it is shown the steps of formic acid adsorption from gas phase to bidentate formate, molecularly adsorbed formic acid being considered both not only as adsorbate species and as intermediate species towards the formation of bidentate formate.

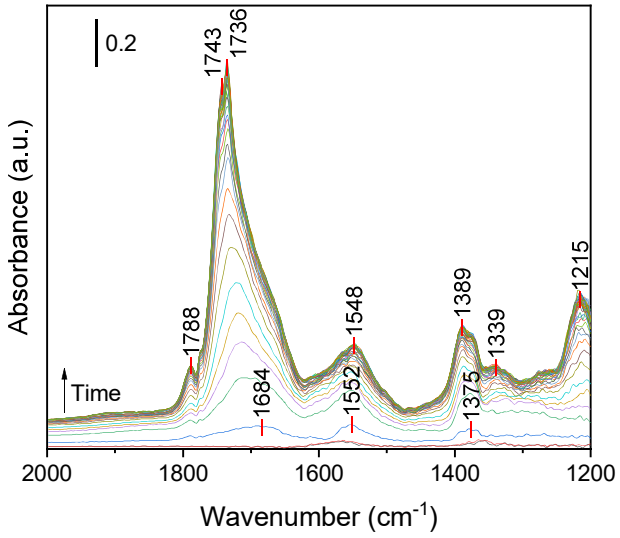

Fig. 57 *DRIFT spectra of formic acid adsorption over bare TiO_2, every spectra were recorded each 30 s approximately.*

Wavenumber (cm^{-1})	Species	Vibrational mode	References
1788	Monomer formic acid	ν(C=O)	[55]
1740	Dimer formic acid	ν(C=O)	[54]
1684	MA formic acid	ν(C=O)	[30,51–53]
1550	bidentate formate species	ν_a(OCO)	[30,51–53]
1389	Monomer formic acid	δ(CH)	[52]
1375	bidentate formate species	ν_a(OCO)	[30,51–53]
1339	MA formic acid	δ(CH)	[52]
1215	Dimer formic acid	ν(C-O)	[54]

Table 5 *Main absorption bands recorded during the in-situ DRIFTS analysis of FA adsorption over bare TiO_2 (P25), with the wavenumbers, the respective vibrational modes and the assigned species according to the literature.*

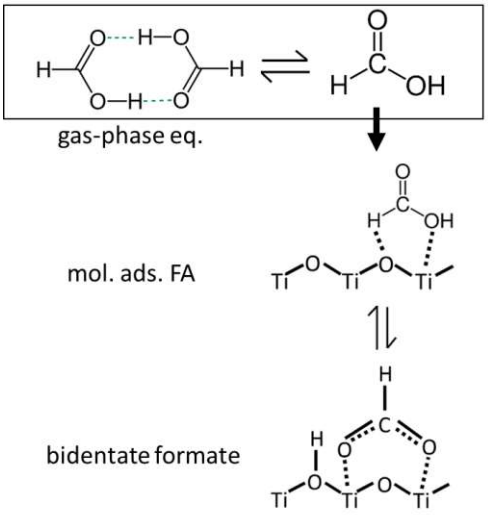

Fig. 58 *Scheme with the proposed mechanism of formic acid adsorption over TiO_2 surface.*

4.2. Formic acid decomposition over bare TiO_2 (P25)

In this part of the study, the spectrum that was recorded with stabilized infrared bands at long time of adsorption at 25°C in the dark (**Fig. 57**) is used as reference (absorbance=0). From now, the DRIFTS spectra shown in this part of the chapter are differential spectra, namely the spectra recorded at a specific reaction condition subtracted from this reference spectrum. Then, concave curves (absorbance >0) in the spectra correspond to an increase of the population of the related species, and convex curves (absorbance< 0) are associated to a decrease of that population.

First, at dark conditions, **Fig. 59**A depicts differential FTIR spectra recorded from room temperature to 350°C during the thermal degradation of formic acid. With the temperature ramp, a slight baseline shift to lower absorbance values was observed, so that curves have been adjusted with a baseline correction in the flat 1800-1900 cm^{-1} region. With the temperature ramp it is possible to appreciate changes in the gas phase equilibrium between dimer and monomer formic acid at low-mild temperatures conditions. With the temperature increase, the bands associated to dimer formic acid (1743 and 1736 cm^{-1}) decreased in intensity meanwhile those assigned to the gaseous monomer (1790 and 1774 cm^{-1}) increased until reaching maximum absorbance values around 180°C. Above this temperature, both dimer and monomer bands have similar decreasing trend in absorbance. This difference in the equilibrium can be associated to a thermal dissociation of dimer to monomer formic acid in gas phase and/or at the titania surface. The band assigned to the v(C=O) stretching of molecularly adsorbed formic acid at 1684 cm^{-1} was observable until high temperatures where the FA conversion reach maximum values, however with difficulty to estimate the evolution as being only a shoulder from the main peak.

The differential spectra show as well the emergence of a broad band (1500-1600 cm^{-1}) with maximum absorbance around 1524 cm^{-1} at temperatures above 150-180°C, as also well visualized in the temperature mapping graph of **Fig. 59**B. This can be assigned to bidentate formates on TiO_2, some authors suggesting even a specific adsorption on the rutile (110) phase at that wavenumber [56,57]. The slight increase in intensity at 1352 cm^{-1} might also be attributed to bidentate formates, however to a lesser extent, so that it is less visible on the temperature mapping. The mapping shows as well an

absorbance decrease around 1395 cm^{-1}, that might correspond to other adsorption modes of formates being temperature-dependent. According to literature, a change in formate bond configuration at the catalyst or support surface can cause significant shift in wavenumbers, without providing more accurate details [51,58]. This remained questionable, as in addition, we have to contemplate the influence of the gas phase formic acid consumption in this region of the spectra, as a band at 1389 cm^{-1} can be assigned to this species.

More remarkable is the evidence in **Fig. 59**C of the presence of two bands at 2177 and 2120 cm^{-1} that correspond to physisorbed CO at the titania surface. CO bands absorbance values increased with increasing the temperature as shown in the temperature map of **Fig. 59**D, raising the maximum absorbance values at 350°C. Furthermore, no bands were recorded at 2400-2250 cm^{-1}, which points out the absence of CO_2 production, being the formic acid decomposition completely selective to dehydration products as it was observed and monitored by chromatography in the previous sections.

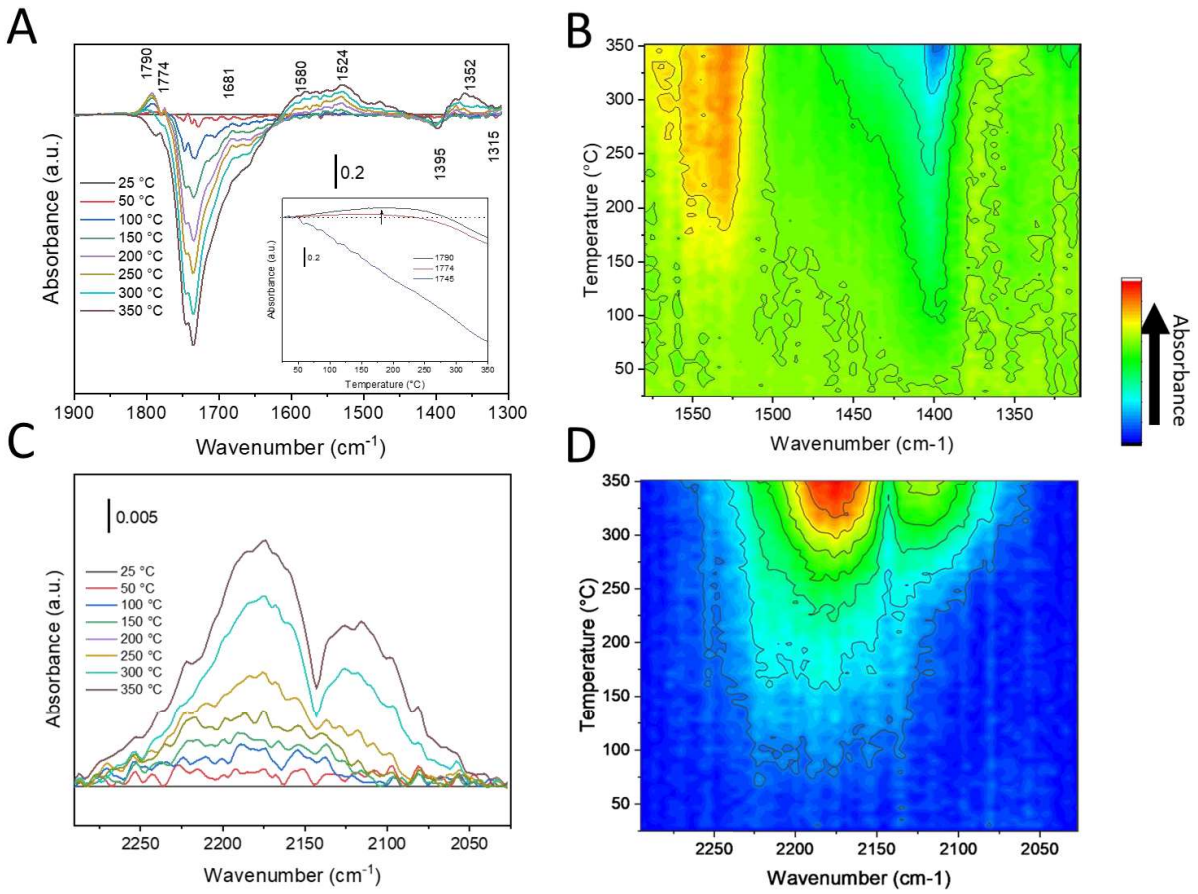

Fig. 59 *In situ differential DRIFT spectra of the formic acid decomposition over TiO_2 obtained by subtracting the reference spectra (at 25°C) from the spectra recorded at different temperatures (up to 350°C), where* ***(A)*** *shows the 1900-1300 cm^{-1} range with* ***(B)*** *the 2D mapping graph from 1580 to 1300 cm^{-1}, and where* ***(C)*** *shows the 2280-2030 cm^{-1} range with* ***(D)*** *the respective 2D mapping graph for the same wavenumber range.*

Second, under light irradiation, **Fig. 60**A depicts the differential DRIFT spectra of the formic acid decomposition on bare TiO_2 under UV-A light irradiation (i.e. subtracted from the reference spectrum obtained in the dark after long adsorption time). Upon irradiation, a slight baseline shift to lower

absorbance values was observed, so that curves have been adjusted with a baseline correction in the flat 1800-1900 cm^{-1} region. Under light a strong decrease in the main dimer formic acid band was observed with a simultaneous small increase in the intensity of the monomer formic acid band. The shoulder at 1683 cm^{-1} was observed whatever the irradiation time, with no significant intensity change in the molecularly adsorbed formic acid.

Similar temperature values have been set as in the experiments of pure thermal catalytic decomposition of formic acid. With the temperature ramp, a slight baseline shift to lower absorbance values was observed, so that curves in **Fig. 60**B have been also adjusted with a baseline correction in the flat 1800-1900 cm^{-1} region. Similar spectra patterns were observed in the 1900-1300 cm^{-1} region in comparison to dark conditions (**Fig. 59**A).

Remarkable, is the evolution under light at different temperatures of the CO bands located in the 2250-2050 cm^{-1} range during the formic acid decomposition, as shown in **Fig. 60**C. In comparison to dark conditions (**Fig. 59**C,D), higher intensity CO bands were observed for a similar reaction temperature upon the UV-A photon flux irradiation as visualized in **Fig. 60**D, that compares the band absorbances at 2177 cm^{-1} of wavenumber recorded during both experiments. The CO band absorbance was higher in photothermal conditions than in thermal conditions until temperatures of ca. 320-350°C at which the formic acid conversion was completed. Similarly to dark conditions, no bands associated to CO_2 were observed in the appropriate region, confirming the high selectivity of the reaction toward dehydration at the surface of the bare TiO_2 material.

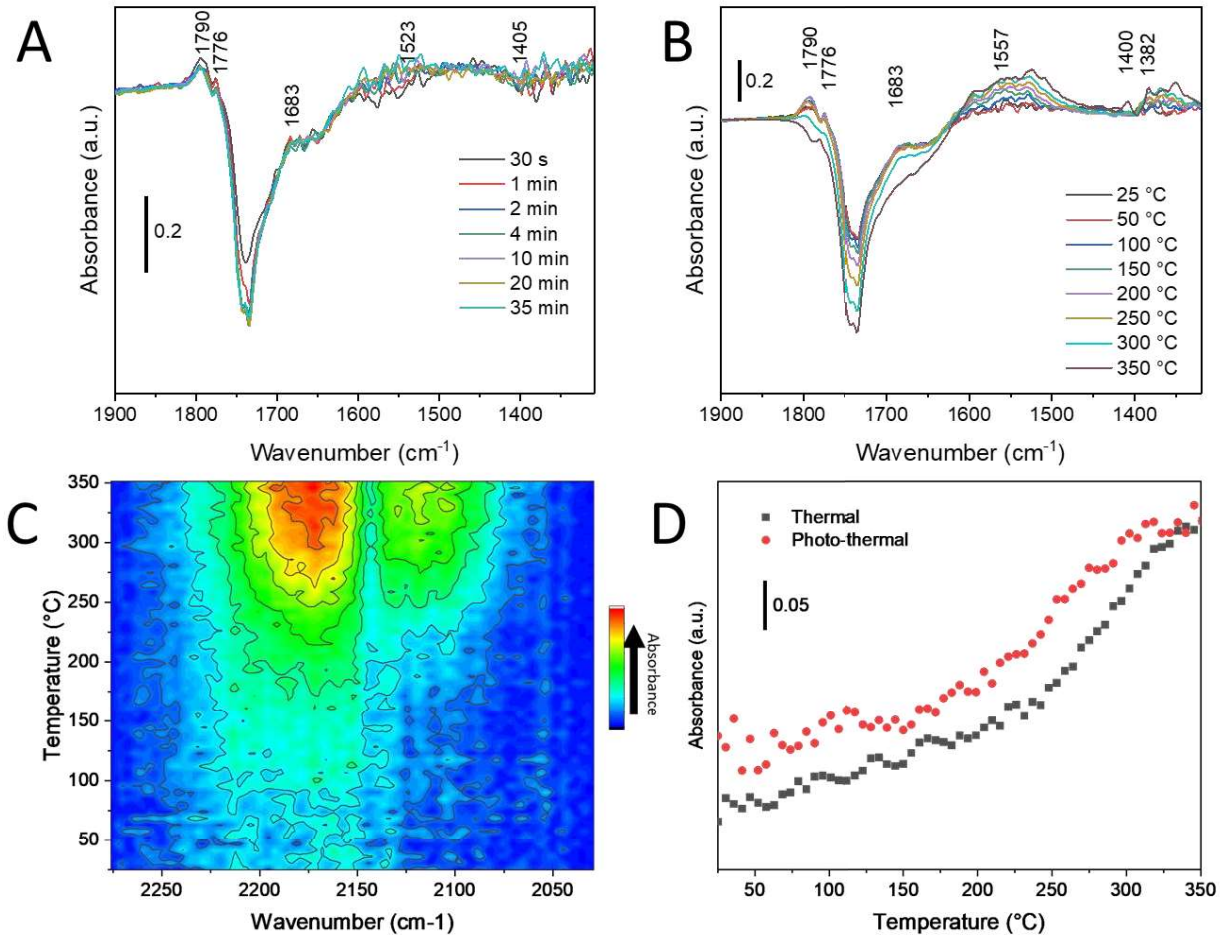

Fig. 60 *In situ differential DRIFT spectra of the formic acid decomposition over TiO_2 spectra obtained by subtracting the reference spectrum at 25°C in dark conditions from that obtained spectra under UV-A light irradiation (ca. 365 mW/cm²)* ***(A)*** *at 25°C* ***(B)*** *from 25°C to 350°C in the 1900-1300 cm^{-1} range,* ***(C)*** *2D mapping graph of CO assigned bands in the 2275-2020 cm^{-1} range and* ***(D)*** *comparison of main CO band absorbance (at 2177 cm^{-1}) in photo-thermal (red) and thermal (black) conditions.*

4.3. Formic acid decomposition over Ru(0.5%)/TiO_2 (PA) catalyst

Finally, in-situ DRIFTS study of the photo-thermal formic acid decomposition on the Ru(0.5%)/TiO_2 (PA) catalyst was conducted. Infrared spectra were recorded at 110°C, 130°C and 150°C after 30 min of stabilization with and without UV-A light irradiation (ca. 365 mW/cm²). **Fig. 61**A depicts the differential spectra in the wavenumber range of 1900-1300 cm^{-1}, by subtracting the reference spectrum (after 30 min of FA/Ar flow at 25°C in dark conditions) from the obtained spectra recorded in specific reaction conditions. At dark conditions, the convex envelope with bands assigned to monomer formic acid (1790 cm^{-1}, 1774 cm^{-1}) was visible at each temperature, like the concave peaks associated to the dimer (1740 cm^{-1}), with the shoulder at lower wavenumber being molecularly adsorbed formic acid.

Under light, both the monomer and dimer FA bands decreased in absorbance, what can indicate a strong consumption of both monomer and dimer formic acid simultaneously. This behaviour was previously observed with bare TiO_2 as (dehydration) photothermal catalyst at high temperatures where CO bands were visible. Possible changes in the wavenumber region corresponding to adsorbed formates in bidentate or monodentate configurations were not clearly evidenced [57].

Remarkable is the possibility, by comparing both dark and light conditions, to discriminate and group bands depending on the conditions where they emerged. Bands that only appear at illuminating

conditions (whatever the reaction temperature) are named as **"light" bands** (highlighted in blue) and the bands that appear with the temperature increase named as **"thermal" bands** (highlighted in red). When the temperature is high enough, thermal bands are already visible in the dark, and their intensity is enhanced under light.

Fig. 61B shows physisorbed CO_2 bands in the 2356-2332 cm^{-1} interval that appear in light irradiation conditions exclusively. By contrast no CO band associated to CO physisorbed on TiO_2 was observed at 2177 cm^{-1} under light, what reflects the improvement of the H_2 selectivity in photo-thermal conditions, as well as a possible preferential adsorption at the Ru-TiO_2 interface. Indeed, Ru-CO bands have been observed for both photo-thermal and thermal conditions in the range of 2150-1950 cm^{-1}, obtaining higher absorbance values at illuminating conditions. Both "thermal" and 'light" bands have been observed for CO.

The temperature affects directly the absorbance values of "thermal" Ru-CO bands. For instance, no Ru-CO bands are reported at 110°C in dark conditions but the temperature increase allows to observe Ru-CO bands at 2085 cm^{-1}, assigned to linear Ru^{n+}-CO, and 2005 cm^{-1}. This second band is composed of overlapped bands at 2020 cm^{-1} and 1984 cm^{-1} shoulder, which can be assigned to dicarbonyl CO species on Ru actives sites and to linearly-adsorbed CO on defects sites or on Ru^0 surrounded by partially oxidized Ru [4,59].

At illuminating conditions, it is possible to appreciate the emergence of three "light" bands at 2138, 2053 cm^{-1} and 1950 cm^{-1}. According to literature [4,60], the band at 2053 cm^{-1}, which is the most intense under irradiation, can be assigned to linear Ru^0-CO bands. Other bands assigned to bridge-bonded CO Ru_2-(CO) or TiO_2(Ru)-(CO) and Tricarbonyl CO species on Ru^{n+}, [$Ru^{n+}(CO)_3$, n=1-3] appeared during illuminating conditions at 1950 cm^{-1} and 2138 cm^{-1}, respectively. The presence of these bands only at illuminating conditions can be related to electron-driven mechanisms where the electron transfer from ruthenium to carbonyl adsorbed at the metallic surface triggers the adsorbate conversion into the dehydrogenation products. An electron transfer back from the adsorbate LUMO to the metal can let remaining energy in the adsorbate that can be used to overcome the energy reaction barrier.

In addition, this back-transfer to the metal can induce electron-electron scattering at the surface, inducing the thermalization process that locally increases the temperature in the surrounding media activating the rest of different Ru-CO bonds in the metal/adsorbate interface. This thermalization effect can also occur by the promotion of hot carriers at metal surface by light irradiation that do not migrate to the LUMO of the adsorbate. Then, these hot carriers recombine converting this absorbed energy to local temperature increase. This explanation is supported by the presence of "thermal bands" under light irradiation at low temperatures, conditions where they were not visual during light absence. In addition, it is possible to appreciate an increase of absorbance of these Ru-CO bands at high-mild temperatures. This difference in "thermal" Ru-CO bands absorbance values between dark and illuminating conditions can be a fingerprint of higher temperature over metal surface than overall temperature in the cell by the thermalization effect.

Then, electrons that migrates to the LUMO adsorbate and they are transferred back and the electrons that remain in the metal participates into the mechanisms for the local temperature increase, which enhance the "thermal bands" absorbance under light irradiation.

The observation of both the so-called "thermal" and "light" bands can suggest the occurrence of both electron-driven and thermalization mechanisms in the case of the Ru(0.5%)/TiO_2 (PA) catalyst.

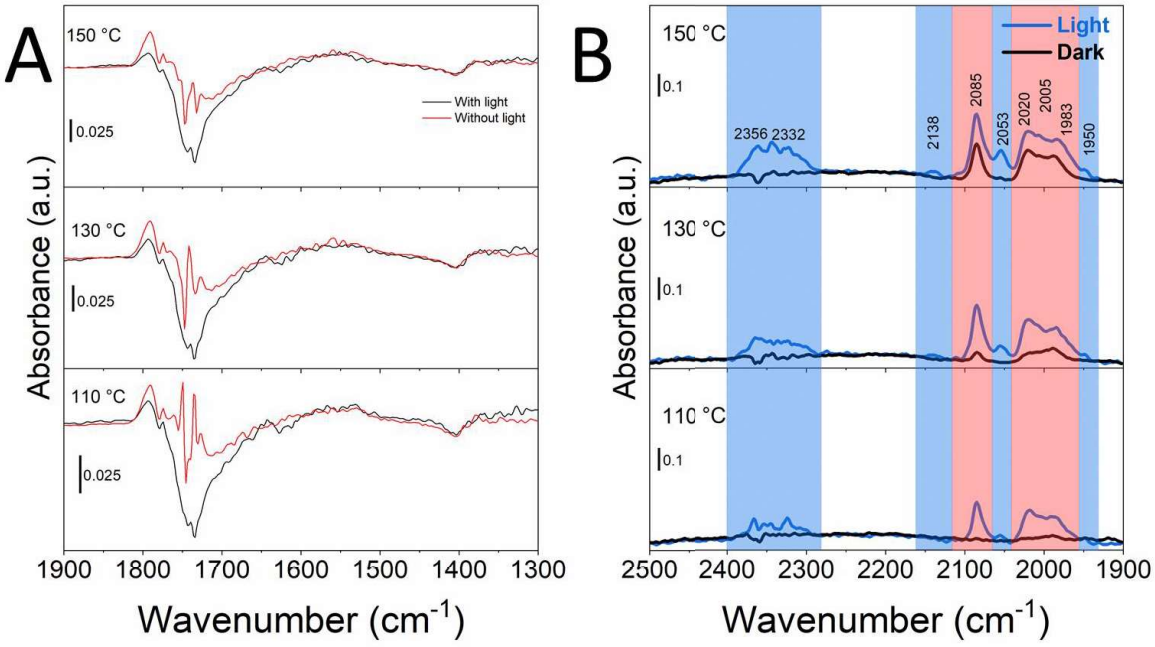

Fig. 61 *Differential DRIFT spectra during the formic acid decomposition on Ru(0.5%)/TiO_2 (PA) at dark (red) and illuminating (black) conditions in the ranges of* ***(A)*** *1900-1300 cm^{-1} and* ***(B)*** *2500-1900 cm^{-1}, at 110°C, 130°C and 150°C.*

5. Conclusions and further aspects

In conclusion, Ru/TiO_2 systems demonstrated to be effective photothermal catalysts for the FA decomposition. The combined (dual) photonic/thermal excitation in a one-pot operation was proved to boost the catalytic decomposition of gaseous FA, the H_2 production rates and the selectivity towards dehydrogenation. This enhanced performances allowed further to lower the reaction temperature. Particular focus was made on the Ru(0.5 %)/TiO_2 (PA) catalyst, but photothermal enhancement was observed independently of the preparation method, of the metal content, as well as of the Ru nanoparticle size and the metal-support interaction. However, those chemical and surface properties influenced the intensity of the photothermal enhancement.

However, not only H_2 production but also CO production has been benefited from the synergistic photothermal effect, lowering the activation energy similarly as the dehydrogenation reaction via light-assisted processes. Studies of FA decomposition over different supported Ru catalysts provided insight on the role and predominance of the TiO_2 support itself as dehydrating surface limiting intrinsically the performances of the photothermal catalysts. It was proposed that two different mechanisms occurred for H_2 and CO productions on the Ru nanoparticles and the dehydrating TiO_2 surface, respectively, both being enhanced upon irradiation, explaining the improvement of the H_2 selectivity.

Different methodologies have been used to get knowledge on the possible electron-driven and thermal-driven processes during FA conversion, such as photon-dependency experiments, apparent activation energy determination at different light irradiances or in situ DRIFT spectroscopy.

Photon-dependency experiments and apparent activation energy determination at different light irradiances supported the hypothesis of dominant electron-driven processes during the formic acid conversion. In situ DRIFT spectroscopy of FA adsorption and decomposition at the catalyst surface

evidenced the photothermal enhancement of the catalytic dehydrating activity of the bare TiO_2 support. On Ru/TiO_2 catalysts, the evidence of CO (on Ru) and CO_2 bands appearing only upon irradiation and CO bands enhanced under light but already observed in the dark, suggested the occurrence of both electron-driven and thermal-driven mechanisms. However, relative quantification of both kinds of processes could not be conducted. We suggested in consequence the co-existence of both processes, with the predominance of electron-driven mechanisms.

Considering the intrinsic limitation of the (dehydrating) TiO_2 surface, next chapter 4 will be devoted to the study of alternative materials to be used as supports for Ru nanoparticles.

References

[1] L. Cano-Casanova, A. Amorós-Pérez, M. Ouzzine, M.A. Lillo-Ródenas, M.C. Román-Martínez, One step hydrothermal synthesis of TiO_2 with variable HCl concentration: Detailed characterization and photocatalytic activity in propene oxidation, Appl. Catal. B Environ. 220 (2018) 645–653. https://doi.org/10.1016/j.apcatb.2017.08.060.

[2] A.M. Ruppert, J. Grams, M. Jędrzejczyk, J. Matras-Michalska, N. Keller, K. Ostojska, P. Sautet, Titania-Supported Catalysts for Levulinic Acid Hydrogenation: Influence of Support and its Impact on γ-Valerolactone Yield, ChemSusChem. 8 (2015) 1538–1547. https://doi.org/10.1002/cssc.201403332.

[3] M. Przydacz, M. Jędrzejczyk, M. Brzezińska, J. Rogowski, N. Keller, A.M. Ruppert, Solvothermal hydrodeoxygenation of hydroxymethylfurfural derived from biomass towards added value chemicals on Ni/TiO2 catalysts, J. Supercrit. Fluids. 163 (2020) 104827. https://doi.org/10.1016/j.supflu.2020.104827.

[4] M. Brzezinska, J. Niemeier, Y. Louven, N. Keller, R. Palkovits, A.M. Ruppert, TiO_2 supported Ru catalysts for the hydrogenation of succinic acid: influence of the support, Catal. Sci. Technol. 10 (2020) 6860–6869. https://doi.org/10.1039/D0CY01446J.

[5] R. Tao, B.-Q. Shan, H.-D. Sun, M. Ding, Q.-S. Xue, J.-G. Jiang, P. Wu, K. Zhang, Surface Molecule Manipulated Pt/TiO 2 Catalysts for Selective Hydrogenation of Cinnamaldehyde, J. Phys. Chem. C. 125 (2021) 13304–13312. https://doi.org/10.1021/acs.jpcc.1c03026.

[6] B. Wang, Y. Cui, C. Wen, X. Chen, Y. Dong, W.-L. Dai, Role of copper content and calcination temperature in the structural evolution and catalytic performance of Cu/P25 catalysts in the selective hydrogenation of dimethyl oxalate, Appl. Catal. A Gen. 509 (2016) 66–74. https://doi.org/10.1016/j.apcata.2015.10.022.

[7] J. Wojciechowska, Ru/TiO2-based catalysts for the hydrogenation of levulinic acid using formic acid as internal hydrogen source, University of Strasbourg, Politechnika Łódzka, 2018.

[8] K. Wenderich, G. Mul, Methods, Mechanism, and Applications of Photodeposition in Photocatalysis: A Review, Chem. Rev. 116 (2016) 14587–14619. https://doi.org/10.1021/acs.chemrev.6b00327.

[9] J. Wojciechowska, E. Gitzhofer, J. Grams, A.M. Ruppert, N. Keller, Solar light induced photon-assisted synthesis of TiO2 supported highly dispersed Ru nanoparticle catalysts, Materials (Basel). 11 (2018) 1–14. https://doi.org/10.3390/ma11112329.

[10] R.. Connick, Advances in the Chemistry of the Coordination Compounds, Macmillan, New York, 1961.

[11] K. Viljoen, Ruthenium(III) Aqua-Chloro Complex Chemistry: The Interconversion of the Hexachlororuthenate(III) and Aquapentachlororuthenate(III) Species, University of Stellenbosch, 2003.

[12] J. Okal, K. Adamska, Thermal Stability of Ru–Re NPs in H_2 and O_2 Atmosphere and Their Activity in VOCs Oxidation: Effect of Ru Precursor, Catal. Letters. 152 (2022) 55–74. https://doi.org/10.1007/s10562-021-03607-7.

[13] B. Coşkuner Filiz, E.S. Gnanakumar, A. Martínez-Arias, R. Gengler, P. Rudolf, G. Rothenberg, N.R. Shiju, Highly Selective Hydrogenation of Levulinic Acid to Γ-Valerolactone Over Ru/ZrO_2 Catalysts, Catal. Letters. 147 (2017) 1744–1753. https://doi.org/10.1007/s10562-017-2049-x.

[14] J.C. Calderón, G. García, L. Calvillo, J.L. Rodríguez, M.J. Lázaro, E. Pastor, Electrochemical

oxidation of CO and methanol on Pt–Ru catalysts supported on carbon nanofibers: the influence of synthesis method, Appl. Catal. B Environ. 165 (2015) 676–686. https://doi.org/10.1016/j.apcatb.2014.10.077.

[15] Y. Zhou, G. Yang, H.-B. Pan, C. Zhu, S. Fu, Q. Shi, D. Du, X. Cheng, J. Yang, C.M. Wai, Y. Lin, Ultrasonic-assisted synthesis of carbon nanotube supported bimetallic Pt–Ru nanoparticles for effective methanol oxidation, J. Mater. Chem. A. 3 (2015) 8459–8465. https://doi.org/10.1039/C5TA00695C.

[16] M.-Y. Chen, Y.-B. Huang, H. Pang, X.-X. Liu, Y. Fu, Hydrodeoxygenation of lignin-derived phenols into alkanes over carbon nanotube supported Ru catalysts in biphasic systems, Green Chem. 17 (2015) 1710–1717. https://doi.org/10.1039/C4GC01992J.

[17] A.M. Ruppert, M. Jędrzejczyk, O. Sneka-Płatek, N. Keller, A.S. Dumon, C. Michel, P. Sautet, J. Grams, Ru catalysts for levulinic acid hydrogenation with formic acid as a hydrogen source, Green Chem. 18 (2016) 2014–2028. https://doi.org/10.1039/c5gc02200b.

[18] H. Liu, H. Song, X. Meng, L. Yang, J. Ye, Light irradiation enhanced CO_2 reduction with methane: A case study in size-dependent optical property of Ni nanoparticles, Catal. Today. 335 (2019) 187–192. https://doi.org/10.1016/j.cattod.2018.11.005.

[19] A. Kim, C. Sanchez, G. Patriarche, O. Ersen, S. Moldovan, A. Wisnet, C. Sassoye, D.P. Debecker, Selective CO2 methanation on Ru/TiO_2 catalysts: unravelling the decisive role of the TiO_2 support crystal structure, Catal. Sci. Technol. 6 (2016) 8117–8128. https://doi.org/10.1039/C6CY01677D.

[20] M. Ojeda, E. Iglesia, Formic Acid Dehydrogenation on Au-Based Catalysts at Near-Ambient Temperatures, Angew. Chem. Int. Ed. 48 (n.d.) 4800–4803. https://doi.org/10.1002/anie.200805723.

[21] P. Mars, J.J.F. Scholten, P. Zwietering, The Catalytic Decomposition of Formic Acid, in: J. Phys. Chem., 1963: pp. 35–113. https://doi.org/10.1016/S0360-0564(08)60338-7.

[22] M.J. Kale, T. Avanesian, P. Christopher, Direct photocatalysis by plasmonic nanostructures, ACS Catal. 4 (2014) 116–128. https://doi.org/10.1021/cs400993w.

[23] P. Christopher, H. Xin, S. Linic, Visible-light-enhanced catalytic oxidation reactions on plasmonic silver nanostructures, Nat. Chem. 3 (2011) 467–472. https://doi.org/10.1038/nchem.1032.

[24] G. Baffou, I. Bordacchini, A. Baldi, R. Quidant, Simple experimental procedures to distinguish photothermal from hot-carrier processes in plasmonics, Light Sci. Appl. 9 (2020). https://doi.org/10.1038/s41377-020-00345-0.

[25] M.A. Henderson, Complexity in the decomposition of formic acid on the TiO_2(110) surface, J. Phys. Chem. B. 101 (1997) 221–229. https://doi.org/10.1021/jp961494i.

[26] M. Bellardita, R. Fiorenza, L. D'Urso, L. Spitaleri, A. Gulino, G. Compagnini, S. Scirè, L. Palmisano, Exploring the Photothermo-Catalytic Performance of Brookite TiO_2-CeO_2 Composites, Catalysts. 10 (2020) 765. https://doi.org/10.3390/catal10070765.

[27] R. Fiorenza, R.A. Farina, E.M. Malannata, F. Lo Presti, S.A. Balsamo, VOCs Photothermo-Catalytic Removal on MnO_x-ZrO_2 Catalysts, Catalysts. 12 (2022) 85. https://doi.org/10.3390/catal12010085.

[28] M. Zhang, S. Cai, J. Li, E.A. Elimian, J. Chen, H. Jia, Ternary multifunctional catalysts of polymeric carbon nitride coupled with Pt-embedded transition metal oxide to enhance light-

driven photothermal catalytic degradation of VOCs, J. Hazard. Mater. 412 (2021) 125266. https://doi.org/10.1016/j.jhazmat.2021.125266.

[29] E. Yu, J. Chen, H. Jia, Enhanced light-driven photothermocatalytic activity on selectively dissolved $LaTi_{1-x}Mn_xO_{3+\delta}$ perovskites by photoactivation, J. Hazard. Mater. 399 (2020) 122942. https://doi.org/10.1016/j.jhazmat.2020.122942.

[30] S. Kwon, T.C. Lin, E. Iglesia, Formic Acid Dehydration Rates and Elementary Steps on Lewis Acid-Base Site Pairs at Anatase and Rutile TiO_2Surfaces, J. Phys. Chem. C. 124 (2020) 20161–20174. https://doi.org/10.1021/acs.jpcc.0c05721.

[31] X. Zhang, X. Li, D. Zhang, N.Q. Su, W. Yang, H.O. Everitt, J. Liu, Product selectivity in plasmonic photocatalysis for carbon dioxide hydrogenation, Nat. Commun. 8 (2017) 14542. https://doi.org/10.1038/ncomms14542.

[32] H. Song, X. Meng, Z.J.Z. Wang, Z.J.Z. Wang, H. Chen, Y. Weng, F. Ichihara, M. Oshikiri, T. Kako, J. Ye, Visible-Light-Mediated Methane Activation for Steam Methane Reforming under Mild Conditions: A Case Study of Rh/TiO2 Catalysts, ACS Catal. 8 (2018) 7556–7565. https://doi.org/10.1021/acscatal.8b01787.

[33] L. Zhou, J.M.P. Martirez, J. Finzel, C. Zhang, D.F. Swearer, S. Tian, H. Robatjazi, M. Lou, L. Dong, L. Henderson, P. Christopher, E.A. Carter, P. Nordlander, N.J. Halas, Light-driven methane dry reforming with single atomic site antenna-reactor plasmonic photocatalysts, Nat. Energy. 5 (2020) 61–70. https://doi.org/10.1038/s41560-019-0517-9.

[34] H. Song, X. Meng, T.D. Dao, W. Zhou, H. Liu, L. Shi, H. Zhang, T. Nagao, T. Kako, J. Ye, Light-Enhanced Carbon Dioxide Activation and Conversion by Effective Plasmonic Coupling Effect of Pt and Au Nanoparticles, ACS Appl. Mater. Interfaces. 10 (2018) 408–416. https://doi.org/10.1021/acsami.7b13043.

[35] D. Mateo, J.L. Cerrillo, S. Durini, J. Gascon, Fundamentals and applications of photo-thermal catalysis, Chem. Soc. Rev. 50 (2021) 2173–2210. https://doi.org/10.1039/D0CS00357C.

[36] D.J. Morgan, Resolving ruthenium: XPS studies of common ruthenium materials, Surf. Interface Anal. 47 (2015) 1072–1079. https://doi.org/10.1002/sia.5852.

[37] B. Folkesson, ESCA studies on the charge distribution in some dinitrogen complexes of rhenium, iridium, ruthenium, and osmium, Acta Chem. Scand. 27 (1973) 287–302.

[38] C.L. Bianchi, V. Ragaini, M.G. Cattania, An XPS study on ruthenium compounds and catalysts, Mater. Chem. Phys. 29 (1991) 297–306. https://doi.org/10.1016/0254-0584(91)90025-P.

[39] S.J. Tauster, S.C. Fung, R.L. Garten, Strong metal-support interactions. Group 8 noble metals supported on titanium dioxide, J. Am. Chem. Soc. 100 (1978) 170–175. https://doi.org/10.1021/ja00469a029.

[40] X. Du, Y. Huang, X. Pan, B. Han, Y. Su, Q. Jiang, M. Li, H. Tang, G. Li, B. Qiao, Size-dependent strong metal-support interaction in TiO_2 supported Au nanocatalysts, Nat. Commun. 11 (2020) 1–8. https://doi.org/10.1038/s41467-020-19484-4.

[41] J. Zhang, H. Wang, L. Wang, S. Ali, C. Wang, L. Wang, X. Meng, B. Li, D.S. Su, F.S. Xiao, Wet-Chemistry Strong Metal-Support Interactions in Titania-Supported Au Catalysts, J. Am. Chem. Soc. 141 (2019) 2975–2983. https://doi.org/10.1021/jacs.8b10864.

[42] H. Tang, Y. Su, B. Zhang, A.F. Lee, M.A. Isaacs, K. Wilson, L. Li, Y. Ren, J. Huang, M. Haruta, B. Qiao, X. Liu, C. Jin, D. Su, J. Wang, T. Zhang, Classical strong metal–support interactions between gold nanoparticles and titanium dioxide, Sci. Adv. 3 (2017) 1–9.

https://doi.org/10.1126/sciadv.1700231.

[43] Z. Wu, Y. Li, W. Huang, Size-Dependent Pt-TiO_2 Strong Metal-Support Interaction, J. Phys. Chem. Lett. 11 (2020) 4603–4607. https://doi.org/10.1021/acs.jpclett.0c01560.

[44] B. Han, Y. Guo, Y. Huang, W. Xi, J. Xu, J. Luo, H. Qi, Y. Ren, X. Liu, B. Qiao, T. Zhang, Strong Metal–Support Interactions between Pt Single Atoms and TiO_2, Angew. Chem. - Int. Ed. 59 (2020) 11824–11829. https://doi.org/10.1002/anie.202003208.

[45] O. Dulub, W. Hebenstreit, U. Diebold, Imaging cluster surfaces with atomic resolution: The strong metal-support interaction state of pt supported on TiO_2(110), Phys. Rev. Lett. 84 (2000) 3646–3649. https://doi.org/10.1103/PhysRevLett.84.3646.

[46] Y. Gao, Y. Liang, S.A. Chambers, Thermal stability and the role of oxygen vacancy defects in strong metal support interaction - Pt on Nb-doped TiO_2(100), Surf. Sci. 365 (1996) 638–648. https://doi.org/10.1016/0039-6028(96)00763-7.

[47] V.A. de la Peña O'Shea, M. Consuelo Álvarez Galván, A.E. Platero Prats, J.M. Campos-Martin, J.L.G. Fierro, Direct evidence of the SMSI decoration effect: the case of Co/TiO_2 catalyst, Chem. Commun. 47 (2011) 7131. https://doi.org/10.1039/c1cc10318k.

[48] F. Bertella, P. Concepción, A. Martínez, TiO_2 polymorph dependent SMSI effect in Co-Ru/TiO2 catalysts and its relevance to Fischer-Tropsch synthesis, Catal. Today. 289 (2017) 181–191. https://doi.org/10.1016/j.cattod.2016.08.008.

[49] J. Lee, S.P. Burt, C.A. Carrero, A.C. Alba-Rubio, I. Ro, B.J. O'Neill, H.J. Kim, D.H.K. Jackson, T.F. Kuech, I. Hermans, J.A. Dumesic, G.W. Huber, Stabilizing cobalt catalysts for aqueous-phase reactions by strong metal-support interaction, J. Catal. 330 (2015) 19–27. https://doi.org/10.1016/j.jcat.2015.07.003.

[50] B. Ealet, E. Gillet, Metal-alumina interface: influence of the metal electronegativity and of the substrates stoichiometry, Surf. Sci. 367 (1996) 221–230. https://doi.org/10.1016/S0039-6028(96)00865-5.

[51] T. Chen, G. Wu, Z. Feng, G. Hu, W. Su, P. Ying, C. Li, In Situ FT-IR Study of Photocatalytic Decomposition of Formic Acid to Hydrogen on Pt/TiO2 Catalyst, Chinese J. Catal. 29 (2008) 105–107. https://doi.org/10.1016/S1872-2067(08)60019-4.

[52] T. Kecskés, J. Raskó, J. Kiss, FTIR and mass spectrometric study of HCOOH interaction with TiO2 supported Rh and Au catalysts, Appl. Catal. A Gen. 268 (2004) 9–16. https://doi.org/10.1016/j.apcata.2004.03.021.

[53] C.-C. Chuang, W.-C. Wu, M.-C. Huang, I.-C. Huang, J.-L. Lin, FTIR Study of Adsorption and Reactions of Methyl Formate on Powdered TiO2, J. Catal. 185 (1999) 423–434. https://doi.org/10.1006/jcat.1999.2516.

[54] R.C. Millikan, K.S. Pitzer, The Infrared Spectra of Dimeric and Crystalline Formic Acid, J. Am. Chem. Soc. 80 (1958) 3515–3521. https://doi.org/10.1021/ja01547a007.

[55] K. Kobl, L. Angelo, Y. Zimmermann, S. Sall, K. Parkhomenko, A.C. Roger, In situ infrared study of formate reactivity on water-gas shift and methanol synthesis catalysts, Comptes Rendus Chim. 18 (2015) 302–314. https://doi.org/10.1016/j.crci.2015.01.003.

[56] B.E. Hayden, A. King, M.A. Newton, Fourier transform reflection - Absorption IR spectroscopy study of formate adsorption on TiO2(110), J. Phys. Chem. B. 103 (1999) 203–208. https://doi.org/10.1021/jp983581b.

[57] L. Österlund, Structure-reactivity relationships of anatase and rutile TiO2 nanocrystals

measured by in situ vibrational spectroscopy, Solid State Phenom. 162 (2010) 203–219. https://doi.org/10.4028/www.scientific.net/SSP.162.203.

[58] A. Mattsson, S. Hu, K. Hermansson, L. Österlund, Infrared spectroscopy study of adsorption and photodecomposition of formic acid on reduced and defective rutile TiO2 (110) surfaces , J. Vac. Sci. Technol. A Vacuum, Surfaces, Film. 32 (2014) 061402. https://doi.org/10.1116/1.4898568.

[59] S.Y. Chin, C.T. Williams, M.D. Amiridis, FTIR studies of CO adsorption on Al2O3- and SiO2-supported Ru catalysts, J. Phys. Chem. B. 110 (2006) 871–882. https://doi.org/10.1021/jp053908q.

[60] E. Guglielminotti, G.C. Bond, Effect of oxidation-reduction treatments on the infrared spectra of carbon monoxide chemisorbed on a Ru/TiO2 catalyst, J. Chem. Soc. Faraday Trans. 86 (1990) 979–987. https://doi.org/10.1039/FT9908600979.

CHAPTER 4: Influence of the support in photothermal catalysts for FA decomposition

Introduction

Following the first demonstration of a beneficial dual thermal/photo excitation of Ru/TiO_2 catalysts for the hydrogen production via formic acid decomposition, but also the intrinsic limitation resulting from the dehydration activity of the TiO_2 semiconductor support itself, this chapter investigates to which extent the behavior of photothermal catalysts can be modified depending on the support used. To this end, this chapter is devoted to $Ru/g\text{-}C_3N_4$ (graphitic carbon nitride) and Ru/SiO_2 (fumed silicon dioxide) catalysts, in comparison to the Ru/TiO_2 reference catalysts from chapter 3.

$g\text{-}C_3N_4$ has been selected as it is a semiconductor material like TiO_2, but with a narrower band gap of 2.7 e.V., that can have promising application under solar irradiation. Being not a metal oxide support and strongly differing from TiO_2 in terms of surface properties, it may solve the intrinsic drawback of the use of the dehydrating TiO_2 support. For comparison, SiO_2 has being selected as support as it is a bulk metal oxide support like TiO_2, but that displays insulating properties. In consequence, as it cannot be activated by the incident UV-A photons, it allows for the study of the unique interaction between the UV-A photons and the supported ruthenium nanoparticles.

Both Ru/SiO_2 and $Ru/g\text{-}C_3N_4$ catalysts have been tested in the same conditions as the Ru/TiO_2 reference systems in the previous chapter for the formic acid decomposition, as a function of the light irradiance at different reaction temperatures. Like in chapter 3, DRIFTS has been used to characterize in-situ the FA decomposition and the H_2 production at the catalyst surface in photothermal conditions.

This chapter is divided into 6 sections. The two first sections are devoted to the main physico-chemical characterization of the supports and of the Ru/SiO_2 and $Ru/g\text{-}C_3N_4$ catalysts, in comparison to the Ru/TiO_2 reference system. To have a suited understanding of the properties of the bare supports and of the ruthenium based catalysts that have been used for FA decomposition, characterization techniques such as e.g. BET, XRD, XPS, TPR and TEM are employed, as well as NH_3-TPD and CO_2-TPD techniques (gas adsorption) to get knowledge on the acidity and basicity of the catalyst surface. The photothermal catalytic properties of the different catalysts for the formic acid decomposition are shown in the following third section, while the fourth section is devoted to the in-situ DRIFT spectroscopy study.

1. The bare supports: $g\text{-}C_3N_4$, TiO_2 and SiO_2

Aeroxide TiO_2 P25 (Evonik) and SiO_2 (Sigma-Aldrich, >99.98%).) were used as received. Graphitic carbon nitride was synthesized via melamine decomposition followed by a thermal exfoliation at 550°C for 4 h, as described in the Chapter 2. **Fig. 62**A and **Fig. 62**B show the X-ray diffractograms and the N_2 sorption isotherms recorded for the three supports. Obviously, the pattern for the TiO_2 P25 support shows the presence of both anatase and rutile phases, with reflexes indexed in the I41/amd and P42/mnm tetragonal unit cells of anatase and rutile TiO_2, respectively (21-1272 and 21-1276 JCPDS files, respectively). As expected, the pattern obtained for SiO_2 exhibits a very broad diffraction peak located at 22.5°, characteristic of a disordered silica support and with small size particles. As regards of $g\text{-}C_3N_4$, two main diffraction peaks were identified. The highest intensity peak at 28.0° corresponds

to the (002) plane (87-1526 JCPDS) with a d-spacing of 0.319 nm, currently described as the interplanar distance between sheets. The secondary-order peak at 13.1° is ascribed to the (100) reflection, with a d-spacing of 0.675 nm, corresponding to in-plane diffraction (intralayer d-spacing) [1–3]. **Fig. 62**B reveals the usual aspect of the N_2 adsorption/desorption isotherms and of the associated hysteresis form for the three support materials, in agreement with the relative values of specific surface area, SSA. g-C_3N_4, TiO_2 and SiO_2 displayed specific surface area of 84 m²/g, 57m²/g and 322 m²/g, respectively. In addition, the surface area from BET model was compared with that of the t-plot external surface area model. It confirmed the non-microporous nature of the TiO_2 support. As regards of g-C_3N_4 and SiO_2, the comparison showed that the supports might contain a minority fraction of micropores (ca. 10% of the surface area), that however remained difficult to estimate due to the accuracy of the models.

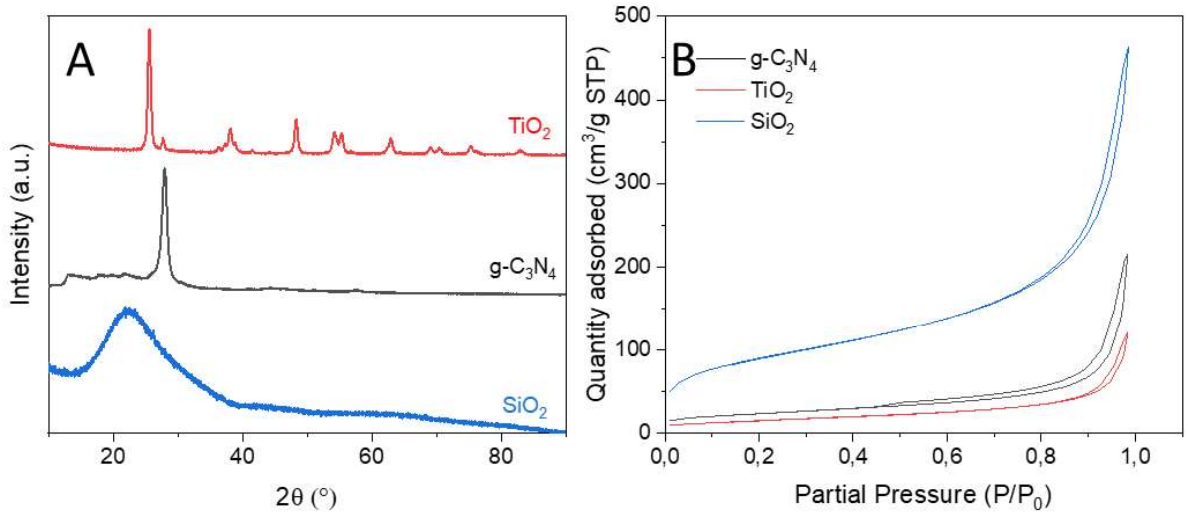

Fig. 62 A) *X-Ray diffractograms and* ***B)*** *N_2 physisorption isotherms at 77K of bare TiO_2 (red), g-C_3N_4 (black) and SiO_2 (blue).*

2. Synthesis and characterization of Ru/g-C_3N_4 and Ru/SiO_2 catalysts.

2.1. Ru/g-C_3N_4 catalysts.

UV-Vis photospectrometry was used for monitoring the photoassisted synthesis of the Ru/g-C_3N_4 catalysts, using the time-evolution of the absorbance of the ruthenium precursor in the g-C_3N_4 methanolic aqueous suspension, as shown in Fig. 2A. After the adsorption step in the dark at the modified pH of 8 (same protocol than for the photoassisted synthesis on the TiO_2 support), 60% of the Ru precursor was adsorbed at the surface of the g-C_3N_4 support. Almost complete disappearance of the Ru precursor (main peak at 324 nm) was observed upon UV-A illumination of the g-C_3N_4 support suspension for a photoirradiation time of 2 h. The higher charge carrier recombination rate of g-C_3N_4 compared to TiO_2 P25 under UV-A light is proposed to explain the lower rate of disappearance of the Ru precursor in the suspension, as less photo-induced electrons are available to participate in the reduction step of the Ru cations adsorbed at the surface of the semiconductor support.

A content of 0.6 wt.% Ru was determined by ICP-OES, in good agreement with the nominal targeted value of 0.5 wt.% Ru. **Fig. 63**B and **Fig. 63**D show TEM images of the Ru/g-C_3N_4 material where well-dispersed ruthenium nanoparticles are observable on the surface of the semiconductor. No formation of aggregates was observed. Statistical analysis of the Ru nanoparticle diameter (size) is shown **Fig. 63**C, with a mean particle size of 1.6 nm $\pm$ 0.7 nm, being slightly larger than that of the Ru/TiO_2 reference catalyst, and with a broader particle size distribution. Interplanar spacing in the dispersed ruthenium nanoparticles was observable in **Fig. 63**F with values of 0.21 nm that corresponds to the (101) planes of metallic Ru. This confirmed the efficiency of the photoassisted synthesis to form metallic Ru nanoparticles in the case of the Ru/g-C_3N_4 materials.

Fig. 63E depicts the X-Ray Photoelectron spectrum in the C 1s and Ru 3d orbital energy range. Two doublet contributions were evidenced at 280.8 and 282.2 eV with a 4.1 eV spin orbit splitting constant, corresponding to Ru 3d5/2-Ru 3d3/2 orbital doublet contributions, assigned to Ru^0 and $Ru^{\delta+}$ species, respectively. At higher binding energies is possible to observe the adventitious carbon peak (284.6 eV) and the main core level peak at 287.6 eV. that corresponds to sp^2 carbon ($C-(N)_3$) from the tri-s-triazine rings, in agreement with the literature [1,4,5].

Metallic ruthenium peaks were shifted to higher binding energy values in comparison to the Ru(0.5%)/TiO_2 (PA)catalyst (280.4 eV). Ru/C surface atomic ratio (calculated from the Ru 3d orbitals and the C1s orbital contribution associated to the sp^2 carbon ($C-(N)_3$) from g-C_3N_4) was calculated at 0.044. The catalyst surface displayed a lower $Ru^0/Ru^{\delta+}$ ratio compared to the Ru/TiO_2 (PA) counterpart catalyst, at 54:46, vs. 79:21. This can be seen as resulting from the larger Ru nanoparticle size compared to the sub-nanometric ones for the Ru/TiO_2 (PA) reference, taking into account the analysis depth for those kinds of samples. Therefore, oxidized Ru species could be present, for example, as amorphous particles on the surface or as isolated atoms in the g-C_3N_4 lattice.

Table 6 shown in the next section summarizes the main properties described here for the three Ru-based catalysts investigated. Obviously, no change in the XRD patterns was observed for the three catalysts in comparison to those of the bare supports, due to the small size of the nanoparticles and the very low loading.

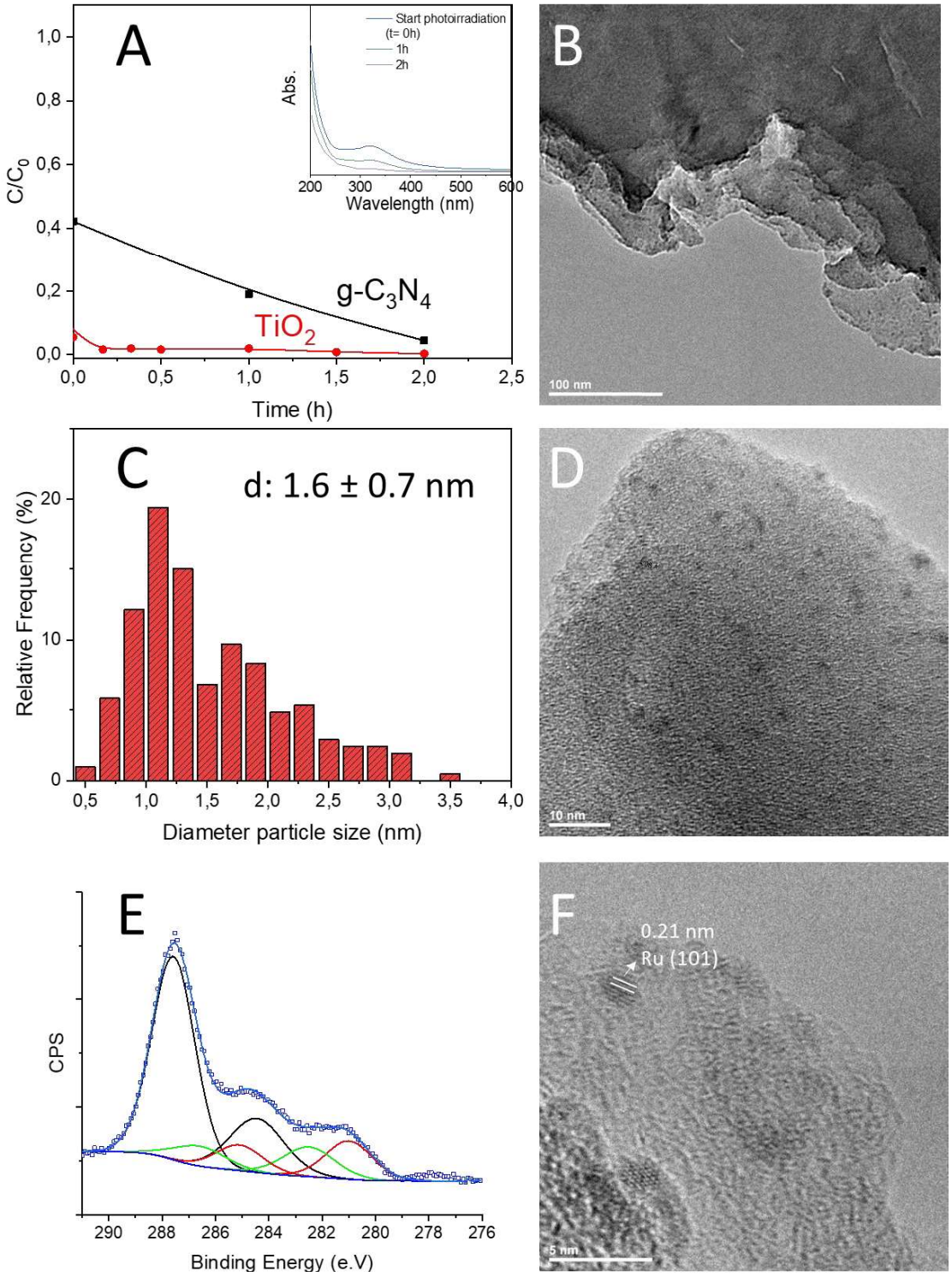

Fig. 63 A) *Photo-assisted synthesis of the Ru(0.5%)/g-C_3N_4 (PA) catalyst followed by UV-Vis spectrophotometry where the remaining Ru precursor was assigned to the peak at wavelength λ=324 nm (comparison with the preparation of the Ru(0.5%)/TiO_2 (P25) (PA) reference). Insert graph corresponds to UV-Vis absorbance spectra recorded upon UV-A illumination in the case of the Ru(0.5%)/g-C_3N_4 (PA) catalyst.* ***B,D,F)*** *TEM images of Ru/g-C_3N_4 (PA) catalyst with visible interplanar distance of (101) planes of metallic Ru in Ru nanoparticles in the F image.* ***C)*** *Histogram of the Ruthenium particle size distribution derived from TEM analysis (over 160 nanoparticles).* ***E)*** *X-ray photoelectron spectrum of the C 1s + Ru 3d orbitals where red, green and black lines are related to Ru^0, $Ru^{\delta+}$ and carbon species, respectively. C 1s contributions correspond to both adventious carbon at 284.6 eV and that from the g-C_3N_4 surface at 287.6 eV.*

2.2. Ru/SiO_2 catalysts.

Ru nanoparticles were synthesized at the surface of the SiO_2 support by the wet impregnation method with an external H_2 gas flow at 500°C. A content of 0.5 wt.% Ru was determined by ICP-OES, in agreement with the nominal targeted value of 0.5 wt.% Ru. TEM pictures in Fig3A and 3C show spherical well-dispersed ruthenium particles at the silica surface. Compared to the Ru/TiO_2 synthesized via wet impregnation with similar H_2 treatment at 500°C, a higher mean particle size was observed for the Ru/SiO_2 catalyst with a mean diameter value of 1.7 nm $\pm$ 0.7 nm. **Fig. 64**B depicts the X-Ray photoelectron spectrum in the Ru 3d + C1s orbital energy range. Ru^0 and $Ru^{\delta+}$ peaks are located at 280.3 eV and 281.7 eV, respectively. Ru/Si surface atomic ratio (calculated from Ru 3d and Si 2p orbital signals) was calculated at 0.022, while a $Ru^0/Ru^{\delta+}$ ratio of 52:48 was obtained.

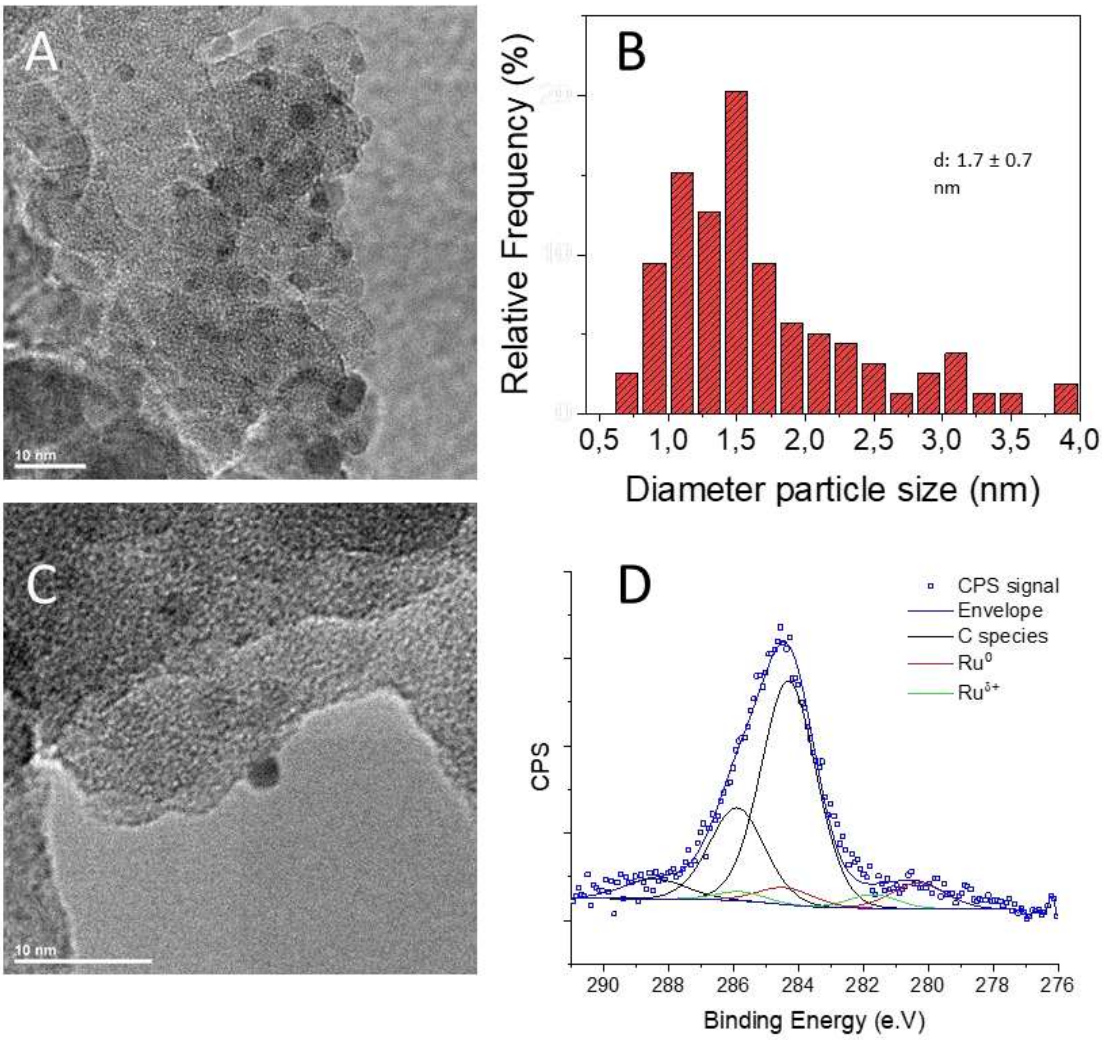

Fig. 64 *Characterization of the Ru(0.5%)/SiO_2 catalyst.* ***A,C)*** *TEM images ;* ***B)*** *histogram of particle size distribution derived from TEM analysis (over 210nanoparticles, and* ***D)*** *X-ray photoelectron spectrum of the C 1s + Ru 3d orbitals where red, green and black lines are related to Ru^0, $Ru^{\delta+}$ and carbon species, respectively.*

Ru nanoparticle size and distribution analysis derived from TEM was in agreement with the CO-pulses chemisorption study, that estimated the dispersion of ruthenium at the surface of the supports.

Results confirmed the better dispersion of Ru nanoparticles on TiO_2 than over g-C_3N_4 and SiO_2, with calculated values of dispersion of 90 %, 28.7 % and 20.8 %, respectively, as shown in **Table 6**, in agreement with the mean particle size derived from electron microscopy, considering the accuracy of the measurements.

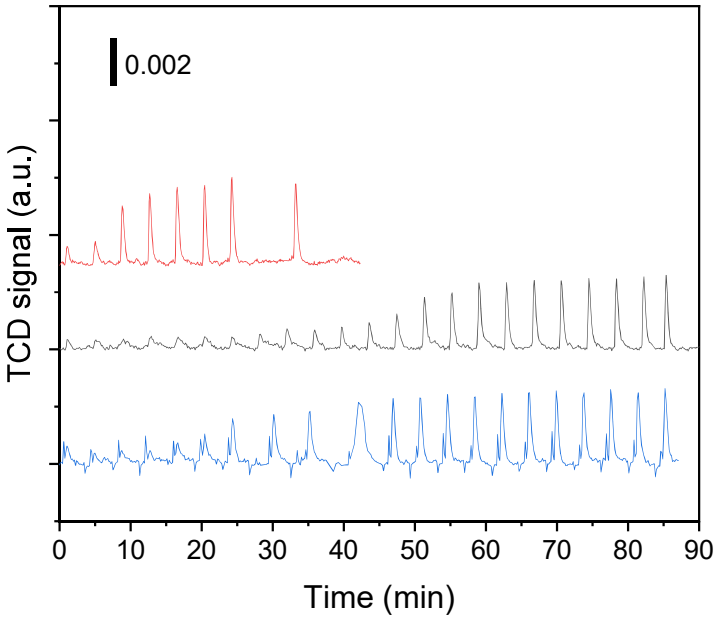

Fig. 65 TCD signal during CO pulses-chemisorption analysis on the Ru/SiO_2 (blue), Ru/TiO_2 (black), Ru/g-C_3N_4 (red) catalysts (Ru content of 0.5 wt.%).

Catalyst	Dispersion (%)[1]	Mean particle size (nm)[2]	Ru^0 B.E. (e.V.)[3]	Ru^0:$Ru^{\delta+}$ [3]	SAR
Ru/TiO_2	90.0	0.6 ± 0.2	280.4	79:21	0.037
Ru/SiO_2	28.7	1.7 ± 0.7	280.3	52:48	0.022
Ru/g-C_3N_4	20.8	1.6 ± 0.7	280.8	54:46	0.044

Table 6 *Data of different properties of the Ru(0.5%)/TiO_2 (PA) catalyst obtained by: 1. CO pulses chemisorption, 2. TEM, 3 and 4. XPS characterization techniques.*

UV-Vis reflectance spectrophotometry was performed for the bare supports and the Ru-based catalysts, as shown in **Fig. 66**. Ruthenium nanoparticles are reported be a light-sensitive material that can absorbs photon from the IR [6] and visible light [7,8] to the UV [9].

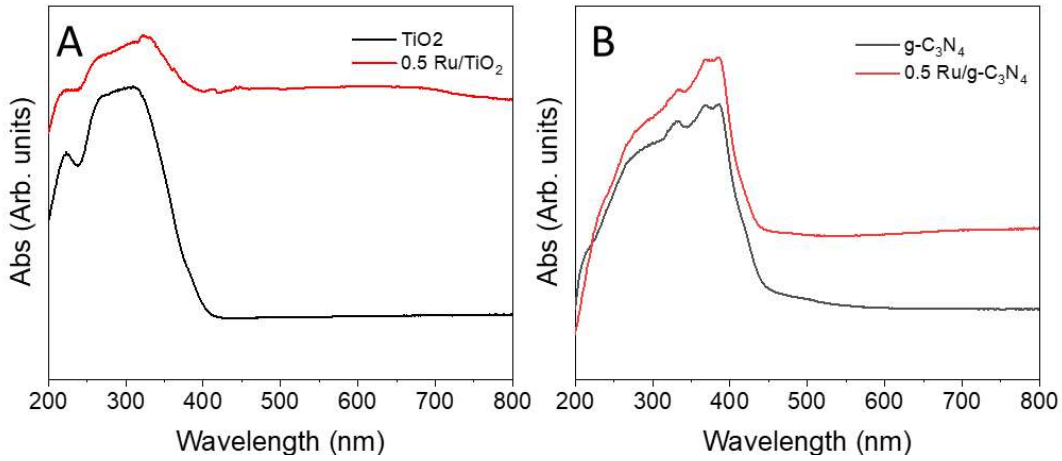

Fig. 66 *UV-Vis spectra of the bare TiO_2 and g-C_3N_4 supports, and of both Ru/TiO_2 and $Ru/g\text{-}C_3N_4$ catalysts.*

2.3. Additional complementary characterization

For obtaining more information about the ruthenium state at the support surface, temperature-programed reduction, TPR, experiments have been further carried out. **Fig. 67** depicts the TCD signal recorded during the TPR experiments performed on the Ru/TiO_2, Ru/SiO_2 and $Ru/g\text{-}C_3N_4$ catalysts after an in-situ oxidation pre-treatment at 200°C under air. Such a pre-treatment was necessary for cleaning (as much as possible) the surface from residual atmospheric CO_2, as Ru can catalyse the CO_2 methanation in the TPR conditions, without altering too much the surface properties (except its oxidation). The increase of the TCD signal corresponds to the consumption of H_2 from the H_2/Ar gas flow. In pre-oxidized Ru/TiO_2, ruthenium oxide particles are clearly reduced at 125-200°C with a maximum TCD signal at 157°C. In the case of the $Ru/g\text{-}C_3N_4$ systems, a broad band was observed, that resulted from the reduction of the ruthenium oxide nanoparticles and the progressive degradation of the g-C_3N_4 supports with release of CH_4 that started already at low temperature (ca. 150°C), although a peak maximum was observed around 350°C. In the case of the Ru/SiO_2 catalyst, the reduction occurred at 80-175°C with a peak maximum at 120°C, at slightly lower values than for Ru/TiO_2. Generally, the nanoparticle reduction temperature is influenced by the metal size and the interaction with the support [10]. As a smaller ruthenium particle size was determined by electron microscopy in the Ru/TiO_2 (PA) catalysts (see Chapter 3), this might suggest a stronger interaction between the TiO_2 support and the metal, that will cause a higher reduction temperature [11]. For instance, we know that this shift to higher reduction temperature is favored on titania supports containing the rutile phase vs. pure anatase-based supports. So, even a slight oxidative treatment at the temperature of 200°C might *a priori* not only influence in the chemical state of the Ru species but also the metal/support interface. This was confirmed by performing TPR analysis on Ru/TiO_2 (PA) sample with a pretreatment at 100°C as shown in **Fig. 68**, as well as XPS analysis (see below). Effectively, the reduction temperature was shifted to lower temperatures with a maximum intensity peak at 95°C, which supports the hypothesis of an increase in the support-metal interaction during the oxidative pre-treatment for the TiO_2 support. At higher temperatures, additional peaks were found in the 250-370°C range. These peaks were

attributed to the conversion of residual CO_2 non-removed from the surface into methane as shown in **Fig. 68**B.

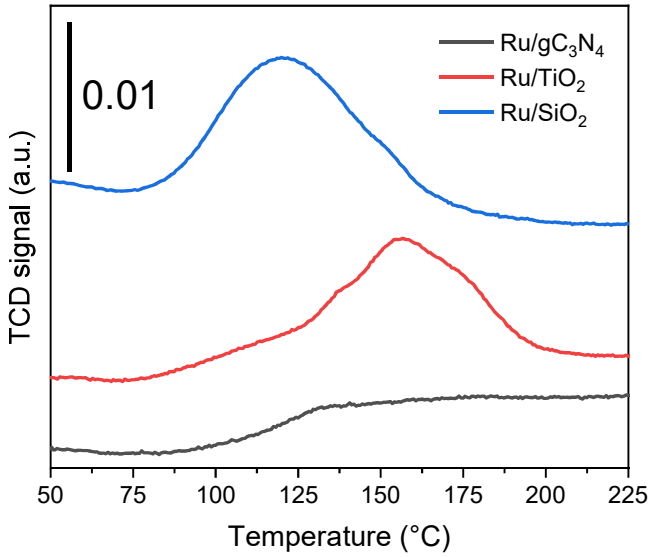

Fig. 67 *Temperature-programmed reduction results in the temperature range of 50-225°C with Ru/g-C_3N_4 (black), Ru/TiO_2 (red) and Ru/SiO_2 (blue) catalysts using 10% H_2/Ar as carrier gas (after an in-situ oxidative pre-treatment at 200°C).*

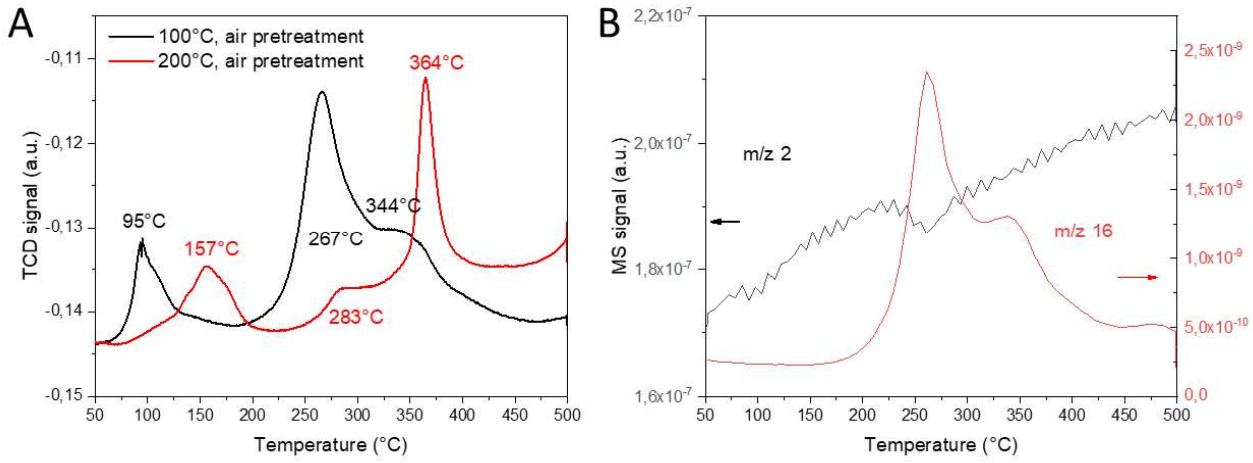

Fig. 68 *TCD signal during the Temperature-Programmed Reduction in the temperature range of 50-500°C of the Ru(0.5%)/TiO_2 (PA) materials with different oxidation pre-treatments at 100°C (black) and at 200°C (red) using 10% H_2/Ar as carrier gas* ***(A)*** *; MS signal of m/z 2 (black) and 16 (red) attributed to hydrogen and methane signal, respectively, in the case of the catalyst with an oxidation pre-treatment at 100°C* ***(B)****.*

In addition, the surface chemical state of the ruthenium species was followed by X-Ray photon spectroscopy, which verified changes in the ruthenium 3d. In **Table 7** is possible to find the Ru:$Ru^{+\delta}$ ratio and the Ru^0 $3d_{5/2}$ orbital binding energy values for the Ru(0.5%)/TiO_2 (PA) catalyst after a series of treatments (in-situ oxidative pre-treatment at 100°C and 200°C, and after the TPR analysis of the sample pre-treated at 200°C). It must be said that the binding energy of the Ru $3d_{5/2}$ orbital for the Ru^0 contribution was shifted to lower values, from 280.6 eV to 280.1 eV, with the increase of the pre-

treatment temperature (the $Ru:Ru^{+\delta}$ ratio also logically slightly decreased after the oxidative pre-treatment at 200°C). The binding energy decreased further down to 279.7 eV after the TPR analysis (till 500°C), as a result of the subsequent increase in the temperature-driven interaction with the support surface.

Sample	$Ru:Ru^{+\delta}$	Ru^0 $3d_{5/2}$ binding energy (e.V.)
Ru/TiO_2 preox. 100°C	79:21	280.6
Ru/TiO_2 preox. 200°C	58:42	280.1
Ru/TiO_2 preox. 200°C post-TPR	65:35	279.7

***Table 7**. Values of the $Ru:Ru^{+\delta}$ surface ratio and binding energy of the Ru^0 $3d_{5/2}$ orbital for the $Ru(0.5\%)/TiO_2$ (PA) catalyst, after in-situ oxidative pre-treatment at 100°C and 200°C, and after TPR analysis of the sample pre-treated at 200°C.*

2.4. CO_2-TPD and NH_3-TPD experiments

Among the gases that are commonly used for surface adsorption, CO_2 is an amphoteric molecule used to analyse the basicity of metal oxides, but that also could be used for surface acidity of titania [12] as their oxygen atoms are weakly basic and the carbon is acidic. On metal oxides, CO_2 can act as acid compound if the carbon interacts with the oxygen atom on the surface to produce bonds. In addition, this carbon can be bonded to the surface generating M-C bonds that are favourable when the metal acts as a basic Lewis site and it provides electron to the carbon of CO_2 (acidic site). CO_2 can also act as a basic species if the oxygen atoms (one or two) bonds the metal sites producing monodentate and bidentate species.

For evaluating the basic Lewis sites on the surfaces and to which extent the ruthenium presence affects them, CO_2-TPD experiments were carried out. The CO_2 desorption graphs are depicted in **Fig. 69**, for bare supports and the Ru-based catalysts. In regards of g-C_3N_4-based systems, no significant differences were observed between the support and the catalyst. Bare g-C_3N_4 and the Ru/g-C_3N_4 catalyst desorbed CO_2 at the same temperature, namely 142°C as shown in **Fig. 69**A. In both cases, at higher temperature, the MS signal m/z = 44 might not result only from CO_2 desorption, but also from the possible thermal decomposition of the surface of the graphitic carbon nitride. Therefore, only the CO_2 desorbed at 142°C is considered. According to literature, CO_2 can be adsorbed on the basic sites of the g-C_3N_4 such as "≡N", in the C-N-C six-membered rings, and at the surface edges on the groups "=NH" and "-NH_2" [13]. The slight differences observed (tail at higher temperatures, slight low-temperature shift) might suggest that the ruthenium species might act as catalyst for degrading the support. So, in the Ru/g-C_3N_4 catalyst, the basicity is directly provided by the support itself and the creation of interfaces with Ru does not create any new surface basicity.

For SiO_2 and TiO_2-based systems, the difference in basicity for the surface is more evident when it contains Ru particles. For instance, Ru/SiO_2 improved the CO_2 adsorption, which is observable from lower to higher temperatures ranges. Higher CO_2 desorption temperatures corresponded to stronger bonds between CO_2 and the surfaces. As soon as the strength of the bond is related to the basicity of the surface sites, higher CO_2 desorption temperatures are linked to the presence of stronger basic sites at the catalyst surface [14–16]. Ru/SiO_2 presented stronger interaction with CO_2 than bare SiO_2 material, which did not adsorb a significant quantity of CO_2 as shown in **Fig. 69**B. Beside the desorption

peak at 120°C that can be assigned to CO_2 adsorbed on the SiO_2 surface, the two main desorption peaks at 400°C and 650°C corresponded to mild and strong basicity sites at the catalytic surface [17]. This enhancement can be attributed to the adsorption of CO_2 on the ruthenium metal surfaces and/or at the Ru-support interfaces. Zagli and Falconer suggested that the activated ruthenium surface can dissociate CO_2 into CO and O [17]. However, this dissociation can be reversible, with the oxidation of the carbon monoxide species to CO_2 and desorption from the catalyst surface. Similarly to Ru/SiO_2, Fig 8C depicts the CO_2 desorption on Ru/TiO_2 and TiO_2, where the Ru presence enhances the CO_2 adsorption. In contrary to SiO_2, TiO_2 has been reported as a metal oxide that bonds to CO_2 onto the surface as this molecule can interact with both acidic and basic centers [18]. The peak observed at ca. 150°C corresponds to linearly-physisorbed CO_2 at the catalyst surface. When ruthenium nanoparticles are synthesized on the support surface, two high-intensity CO_2 desorption peaks appeared at 370°C and 620°C, with a larger amount of CO_2 is adsorbed after the Ru deposition, also associated to stronger basic centers.

To sum up, the metal surface (including the metal-support interface) is suggested to enhance the CO_2 adsorption, where the CO_2 is preferentially adsorbed with stronger bonds than on the bare support surface for Ru/SiO_2 and Ru/TiO_2. This enhancement is not visible for the Ru/g-C_3N_4 material, for which the bare support surface is already basic for CO_2 adsorption.

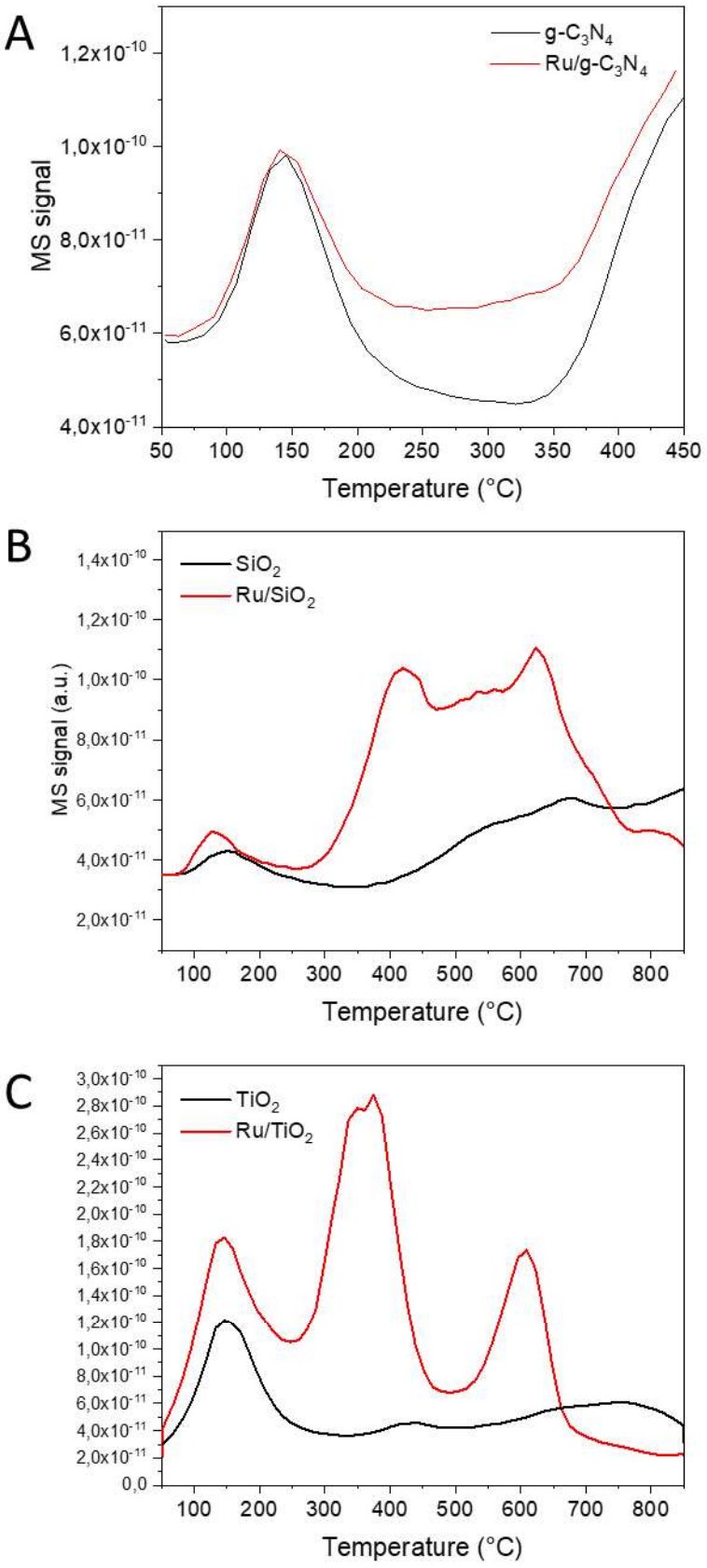

Fig. 69 *CO_2-TPD spectra recorded on bare supports and on the Ru-based catalysts, for **A)** g-C_3N_4, **B)** SiO_2 and **C)** TiO_2. MS signal m/z = 44.*

NH_3-TPD experiments were carried out similarly as CO_2 desorption tests. The results from the TCD signal and MS for NH_3-TPD are gathered in **Fig. 70** for Ru/TiO_2. Analysing the m/z=17 signal, Ru/TiO_2 did not have a high number of acidic sites onto the surface, as reported [19]. In fact, the m/z=17 signal is influenced by the condensation of surface hydroxides with the release of water (dehydration), so that both m/z=17 and m/z=18 signals are related. Nevertheless, the fraction ratio between parent m/z=18 and fragment m/z=17 in water is 1:0.2 [20]. Therefore, the fragment m/z=17 signal contained contributions from surface dehydration as well as desorbed NH_3. In addition, the peaks at mild (300-500°C) and high (550-800°C) temperatures observed for the TCD signal for Ru/TiO_2 are following the evolution of the m/z=2 and m/z=28 signals, that may corresponds to H_2 and N_2, respectively. This is in agreement with the ability of ruthenium based materials to act as catalysts for decomposing ammonia [21,22]. No traces of H_2 or N_2 being observed in the case of the bare support, this supports that the ammonia decomposition is relied on the presence of ruthenium. For ammonia detection, the m/z=16 fragment signal can also be used [23], and a very low signal was observed, lower than the intensity ratio of 16:17 fractions from ammonia (0.825:1) [20]

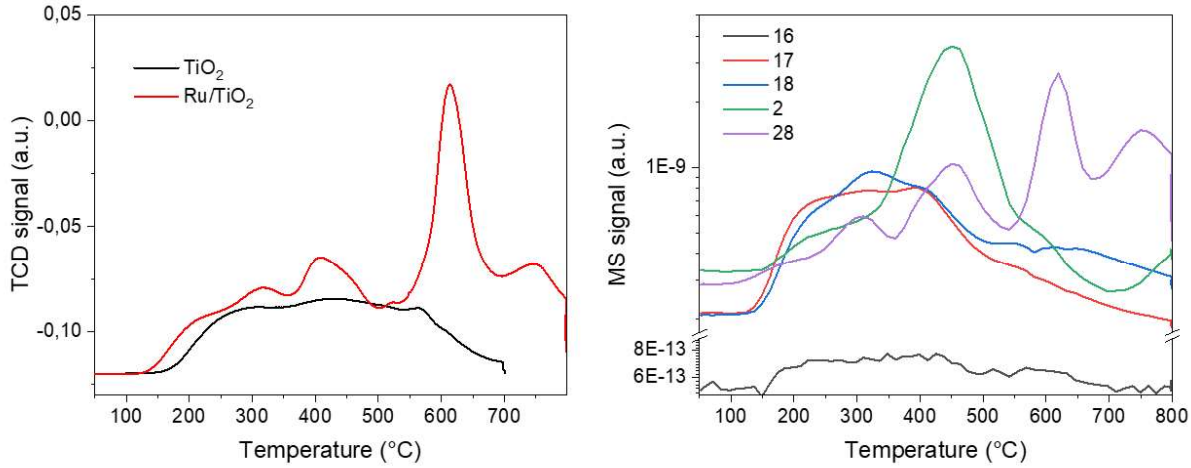

Fig. 70 *TCD signal (left) during the NH_3-TPD of the bare TiO_2 support (black) and the Ru/TiO_2 catalyst (red) ; MS signals (right) during the NH_3-TPD on Ru/TiO_2.*

Fig. 71 depicts the ammonia desorption from Ru/SiO_2 by TCD and mass spectrometry. In this case, the influence of the surface hydroxide condensation with release of water (m/z=18) is strongly visible in the TCD signal. This difference with the Ru/TiO_2 can be related to the higher specific surface area of the material and hence the higher concentration of surface hydroxide species. However, the desorption peak at 200°C detected by TCD correlates with the m/z=17 peak, with a higher intensity than the parent m/z=18 in that temperature range, so that it can be attributed to ammonia desorption. In addition, the intensity of m/z=2 and 28 signals does not increase as strongly as in the case of Ru/TiO_2, suggesting that the decomposition of ammonia is less favourable on this catalyst. According to literature, the maximum ammonia desorption peaks are observed at temperatures lower than 250°C [24], and are attributed to weak acid sites on the Ru/SiO_2 surface.

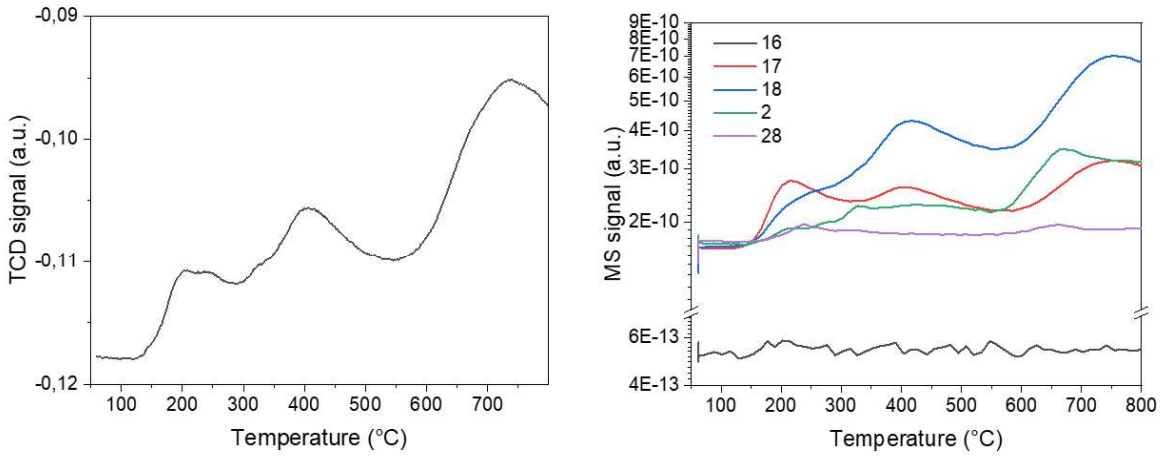

Fig. 71 *TCD signal (left) during the NH_3-TPD of the Ru/SiO_2 catalyst ; MS signals (right) during the NH_3-TPD.*

The TCD signals recorded during the ammonia-TPD measurements over g-C_3N_4-based materials are gathered in the following **Fig. 72**. Like for CO_2-TPD analysis, no significant difference was observed at low temperature, with a desorption peak centered on 175°C for both the support and the catalyst. At higher temperatures, the thermal decomposition of the surface of the graphitic carbon nitride was observed, at a slightly lower temperature and with higher intensity in the presence of Ru nanoparticles, that can be associated with Ru acting as catalyst, as described above. The surface decomposition of the g-C_3N_4 material and the release of water are here also complexifying the analysis, but the low temperature TCD peak was associated to a broad band for m/z=16 fragment, that was ascribed to ammonia desorption.

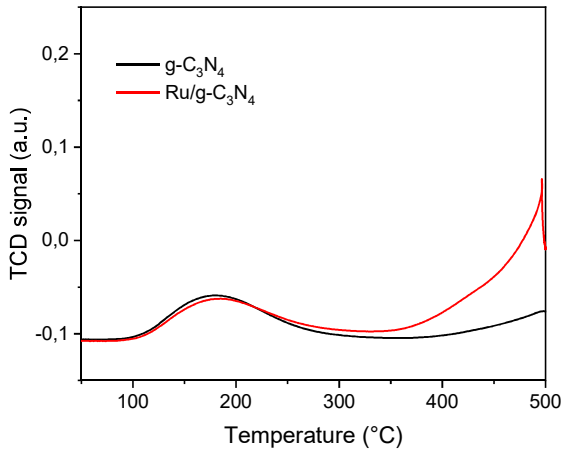

Fig. 72 *TCD signal during the NH_3-TPD of the bare g-C_3N_4 support (black) and the Ru/g-C_3N_4 catalyst (red).*

3. Photothermal FA decomposition on Ru/g-C_3N_4 and Ru/SiO_2 catalysts

This section presents and compares results obtained in the FA decomposition over both Ru/g-C_3N_4 (PA) and Ru/SiO_2 catalysts.

3.1. Ru(0.5%)/g-C_3N_4 (PA) photothermal catalysts

This subsection shows the results of formic acid decomposition obtained on the Ru(0.5%)/g-C_3N_4 catalyst. First **Table 8** reports the results obtained in dark conditions over the 25-150°C range, and expressed as FA conversion, and productions of H_2, CO and CO_2. Like for the counterpart based on TiO_2, no deactivation was observed with time on stream whatever the temperature conditions. Values of H_2 and CO_2 production were obtained in an equimolar ratio, meaning that no side reactions occurred (in the reaction conditions). In dark conditions, independently of the reaction temperature, higher FA conversions and higher H_2 productions were achieved in comparison to the Ru/TiO_2 reference catalyst reported in the Chapter 3, e.g. 36.9% and 24.5 $mmol g^{-1}h^{-1}$ at 150°C vs. 5.1% and 0.5 $mmol g^{-1}h^{-1}$, respectively. By contrast to the Ru/TiO_2 catalysts, the decomposition of formic acid was totally selective to the dehydrogenation reaction, no CO production being recorded, producing only CO_2 and H_2 as products. Carbon balance within the 97–102 % range was calculated regardless of the temperature.

Temperature	FA conversion	H_2 production	CO Production	CO_2 production	H_2 selectivity
°C	%	$mmol g^{-1}h^{-1}$	$mmol g^{-1}h^{-1}$	$mmol g^{-1}h^{-1}$	%
25	0.0	0.0	0.0	0.0	-
50	0.0	0.0	0.0	0.0	-
70	0.0	0.0	0.0	0.0	-
90	0.0	0.7	0.0	0.0	100.0
100	2.3	1.8	0.0	1.5	100.0
110	5.4	3.8	0.0	3.6	100.0
120	12.0	8.3	0.0	8.0	100.0
130	17.3	11.5	0.0	11.6	100.0
150	36.9	24.5	0.0	24.8	100.0

***Table 8**. Formic acid decomposition values over Ru(0.5%)/g-C_3N_4 (PA) at dark conditions. Reaction conditions: [FA]=4600 ppm_v, total Ar flow of 14.7 mL, 1.8 mg of catalyst, FA specific molar rate of 67.2 mmol $g^{-1}h^{-1}$.*

Fig. 73 show the influence of the reaction temperature and of the UV-A light irradiance (0-365 mW/cm²). All data are summarized in **Table A 2** in annex (to not duplicate here with the different graphs). **Fig. 73**A and **Fig. 73**B depicts the FA conversion dependency with light irradiance and temperature, respectively, while the evolution of the H_2 production is shown in **Fig. 73**C and **Fig. 73**D, respectively. The results showed that the FA conversion and the H_2 production are strongly enhanced under illumination in comparison to dark conditions, independently of the temperature reaction. The higher the light irradiance, the stronger the enhancement of both the FA conversion and the H_2 production upon illumination. For instance, a conversion higher than 80% was achieved at 150°C with maximum light irradiance (365 mW/cm²), while it remained at 36.9% in dark conditions.

Bare g-C_3N_4 was tested as (photo)-thermal catalyst for formic acid decomposition in similar reaction conditions of temperature (25-150°C) and irradiance (0-365 mW/cm²) Reaction conditions were

[FA]=4600 ppm_v, total Ar flow of 14.7 mL, 1.8 mg of g-C_3N_4 support, FA specific molar rate of 67.2 mmol $g^{-1}h^{-1}$. It must be said that, in contrary to the TiO_2 P25 reference support, that g-C_3N_4 did not exhibit any activity, no H_2, CO or CO_2 products being observed, neither at dark or at illuminating conditions, whatever the temperature and the irradiance.

The highest performances for the Ru(0.5%)/g-C_3N_4 catalyst in the dark benefitted from the inactivity of the support itself, a clear asset, that can be related to the absence of network oxygen as mentioned in the proposed mechanisms. We must said that the highest performances in the dark can origin from several factors that are still under investigation in thermal catalysis nowadays (size-effect, metal-support interaction, surface poisoning, etc.). We know from the literature that too small-size Ru nanoparticles are not necessarily beneficial for FA dehydrogenation, as notably (i) they can induce specific electronic properties resulting from the exposed facets and edges, and also related to the interaction with the support surface, and potentially driving the reaction towards CO, (ii) they can be more easily poisoned by the CO molecules (if formed). In the case of Ru(0.5%)/g-C_3N_4, the slightly larger Ru nanoparticle size might therefore be favourable. The slightly δ+ (electro-deficient) nature of the surface metallic Ru atoms could also act positively to provide beneficial electronic properties to the active metal, as well as the specific acido/basic properties of the g-C_3N_4 support itself.

So, strongly higher FA conversion and H_2 production values were obtained with the Ru(0.5%)/g-C_3N_4 catalyst in comparison to the Ru(0.5%)/TiO_2 reference, whatever the way of preparation (photoassisted synthesis or wet impregnation with thermal reduction in H_2). For instance, 60% of FA conversion was achieved at 90°C at 365 mW/cm² irradiance with the carbon nitride based catalyst, while only 55% was obtained at 110°C on the Ru/TiO_2 reference at similar irradiance (see Chapter3). It must be said that similarly to dark conditions, full H_2 selectivity was observed, with only the formation of the dehydrogenation products H_2 and CO_2 in an equimolar ratio.

As far as the H_2 production was concerned, the superiority of the Ru(0.5%)/g-C_3N_4 catalyst is even more significant, as the FA conversion is fully selective to H_2, no CO being formed. For instance, 23.8 $mmolg^{-1}h^{-1}$ of H_2 were produced at 110°C at a 365 mW/cm² light irradiance with the Ru/TiO_2 catalyst while 46.4 $mmolg^{-1}h^{-1}$ was produced with the Ru/g-C_3N_4 catalyst under same photo-thermal conditions. At 70°C under 290 mW/cm², the H_2 production over the Ru/g-C_3N_4 catalyst was even more than three times higher than that obtained over the Ru/TiO_2 reference, at 16.7 and 4.8 $mmolg^{-1}h^{-1}$ of H_2, respectively.

In this case, in terms of light irradiance dependency, superlinear regimes were observed from room temperature to 90°C, before turning into linear and further sublinear for higher temperatures. The superlinear and linear regimes can suggest the predominance of an electron-driven mechanism. Similarly to the case of the Ru/TiO_2 catalysts, the change towards a sublinear regime could result from the very high conversions of formic acid achieved in those conditions.

The influence of the light irradiance on the H_2 production was analysed as Arrhenius plots as shown in **Fig. 73**E and the apparent activation energies for the dehydrogenation reaction derived from those data are reported in **Fig. 73**F. The apparent activation energy for the dehydrogenation reaction is clearly dependent of the photon irradiance and decreased from 68.4 kJ/mol at dark conditions to 13.3 kJ/mol at the highest irradiance of 365 mW/cm². The decrease in activation energy upon illumination is relatively linear over the full irradiance range, in contrary to the trend observed for the Ru/TiO_2 reference that is only linear for the irradiances within the 38-365 mW/cm² range.

To sum up, the Ru(0.5%)/g-C_3N_4 catalyst has been demonstrated to be a very performant photothermal catalyst for the fully selective production of H_2 through the decomposition (dehydrogenation) of formic acid. It overcomes clearly the Ru(0.5%)/TiO_2 reference catalyst both in terms of conversion and H_2 selectivity, and in consequence of H_2 production. The inactivity of the g-C_3N_4 support it-self at dark conditions and under light is promising for inhibiting the CO formation and achieving a H_2 selectivity of 100% in photothermal conditions. Thanks to the photothermal enhancement, FA dehydrogenation into CO-free H_2 flow could also be obtained at by-far more sustainable reaction conditions.

The surface of the Ru/g-C_3N_4 systems will be further investigated by in-situ DRIFTS in the next section as a possible way to get information on the mechanisms taking place in photothermal conditions..

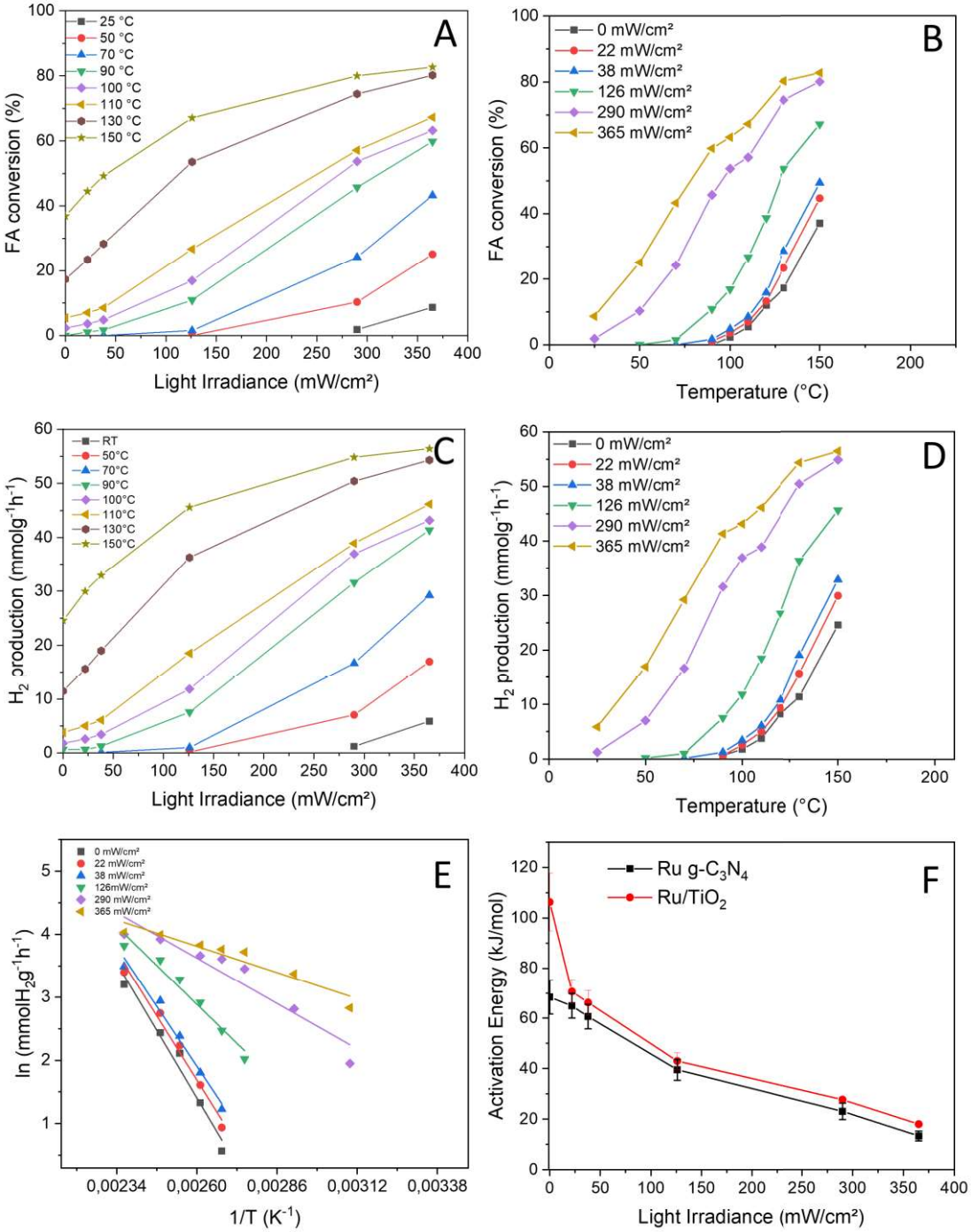

Fig. 73 *Influence of the UV-A light irradiance in the 0-365 mW/cm² range and of the reaction temperature on the photothermal formic acid decomposition on the Ru(0.5%)/g-C_3N_4 (PA) catalyst prepared by the photo-assisted synthesis method.* ***A-B)*** *FA conversion,* ***C-D)*** *Production of H_2,* ***E)*** *Arrhenius plot graph for H_2 production at different irradiating conditions and* ***F)*** *light-dependency of the apparent activation energy for H_2 production. Reaction conditions: [FA]= 4600 ppm_v, total Ar flow of 14.7 mL, 1.8 mg of catalyst, FA specific molar rate of 67.2 mmol $g^{-1}h^{-1}$.*

3.2. Ru(0.5%)/SiO_2 photothermal catalysts

Table 9 shows the results of FA conversion into H_2, CO_2 and CO products from 25°C to 190°C obtained in dark conditions on the Ru(0.5%)/SiO_2 catalyst. No deactivation was observed with time on stream, H_2 and CO_2 production values were obtained in an equimolar ratio. Carbon balance within the 98–102

% range was calculated regardless of the temperature. FA conversion was observed in the dark for reaction temperatures higher than 130°C, with a 6.7 % conversion and a selectivity of 62.8 % towards dehydrogenation reaction (H_2). FA conversions and H_2 productions were globally higher than those achieved with the Ru/TiO_2 reference catalyst reported in the Chapter 3, e.g. 31.7% and 15.7 $mmolg^{-1}h^{-1}$ at 190°C vs. 12.2% and 2.9 $mmolg^{-1}h^{-1}$, respectively. This might result from the larger Ru nanoparticle size, less sensitive to potential CO poisoning, or to specific interaction with the support surface. They were however lower than those obtained with the $Ru(0.5\%)/g\text{-}C_3N_4$ catalyst.

In contrary to $Ru/g\text{-}C_3N_4$ catalyst, CO production was obtained in the dark. Selectivity toward H_2 of 62.8 % was obtained at 130°C, which very moderately increased with the temperature to reach 76.9 % at 190°C.

It must be said, that bare SiO_2 did not exhibit any activity neither at dark conditions nor under light in photothermal conditions. In our experimental conditions, the absence of dehydrating properties of the bare SiO_2 surface in the dark can be attributed to the surface properties of the SiO_2 support, as in general the surface properties of metal oxides (e.g. IEP around 3 for SiO_2, acido/basic properties) are known to orientate (or not) the catalytic activity towards dehydration in the case of formic acid. It means that in this case, the CO formation resulted from the electronic properties of the supported Ru nanoparticles, and not from the dehydration properties of the support.

Temp	**H_2 prod**	**CO prod.**	**CO_2 prod.**	**H_2 selec.**	**FA conv.**
°C	$mmolg^{-1}h^{-1}$	$mmolg^{-1}h^{-1}$	$mmolg^{-1}h^{-1}$	%	%
25	0.0	0.0	0.0	-	0.0
90	0.0	0.0	0.0	-	0.0
110	0.0	0.0	0.0	-	0.0
130	2.0	1.7	2.8	62.8	6.7
150	7.1	3.4	7.9	70.1	16.8
170	15.7	5.5	15.7	74	31.7
190	30.0	8.8	29.4	76.9	57.0

***Table 9**. Formic acid decomposition values over $Ru(0.5\%)/SiO_2$ at dark conditions. Reaction conditions: [FA]=4600 ppm_v, total Ar flow of 14.7 mL, 1.8 mg of catalyst, FA specific molar rate of 67.2 mmol $g^{-1}h^{-1}$.*

Under illuminating conditions, FA conversion considerably increased as it is shown in **Fig. 74**A and **Fig. 74**B. The values obtained demonstrate that; the higher the light irradiance, the higher the conversion of formic acid. For instance, the conversion at 130°C in dark conditions (6.7 %) is boosted to values as high as 16.5 % and 64.5 % when the catalyst is illuminated with a UV-A light irradiance of 126 mW/cm² and 365 mW/cm², respectively. FA conversion was observed at lower temperatures values under light illumination. In consequence, in the case of SiO_2 also, the combined photonic/thermal excitation allowed the reaction temperature to be lowered. For instance, a conversion of 0.5% was detected at room temperature (25°C) at 365 mW/cm², while at 126 mW/cm², a conversion of 8.2 % was obtained at 110°C, lowering in both cases the temperature to get the same conversion values at dark conditions. The enhancement under light is also visible for the H_2 production, as it is shown in **Fig. 74**C and **Fig.**

74D. For instance, the value of 15.7 mmol H_2 $g^{-1}h^{-1}$ obtained at 170°C in dark conditions is boosted to 30.5 and further 43.7 mmol H_2 g^{-1} h^{-1} when the light irradiance raised values of 126 mW/cm² and 365 mW/cm², respectively. Therefore, the lowering of the temperature under illuminating conditions was also observed for the hydrogen production. For instance, a value of 2 mmolH_2 $g^{-1}h^{-1}$ obtained at 130°C in dark conditions is lower than those obtained at 110°C with the moderate irradiance of 126 mW/cm² (2.5 mmol H_2 $g^{-1}h^{-1}$) or at 90°C at 290 mW/cm² (5.7 mmol H_2 $g^{-1}h^{-1}$).

Fig. 74E and **Fig. 74**F depict the CO production achieved with the Ru/SiO_2 catalyst as a function of both light irradiance and temperature, respectively. Similarly to the H_2 production, the CO values obtained increased under illuminating conditions whatever the reaction temperature. At high conversion and H_2 production rate, the enhancement of the CO production rate was hindered by the high FA conversion achieved at high irradiance.

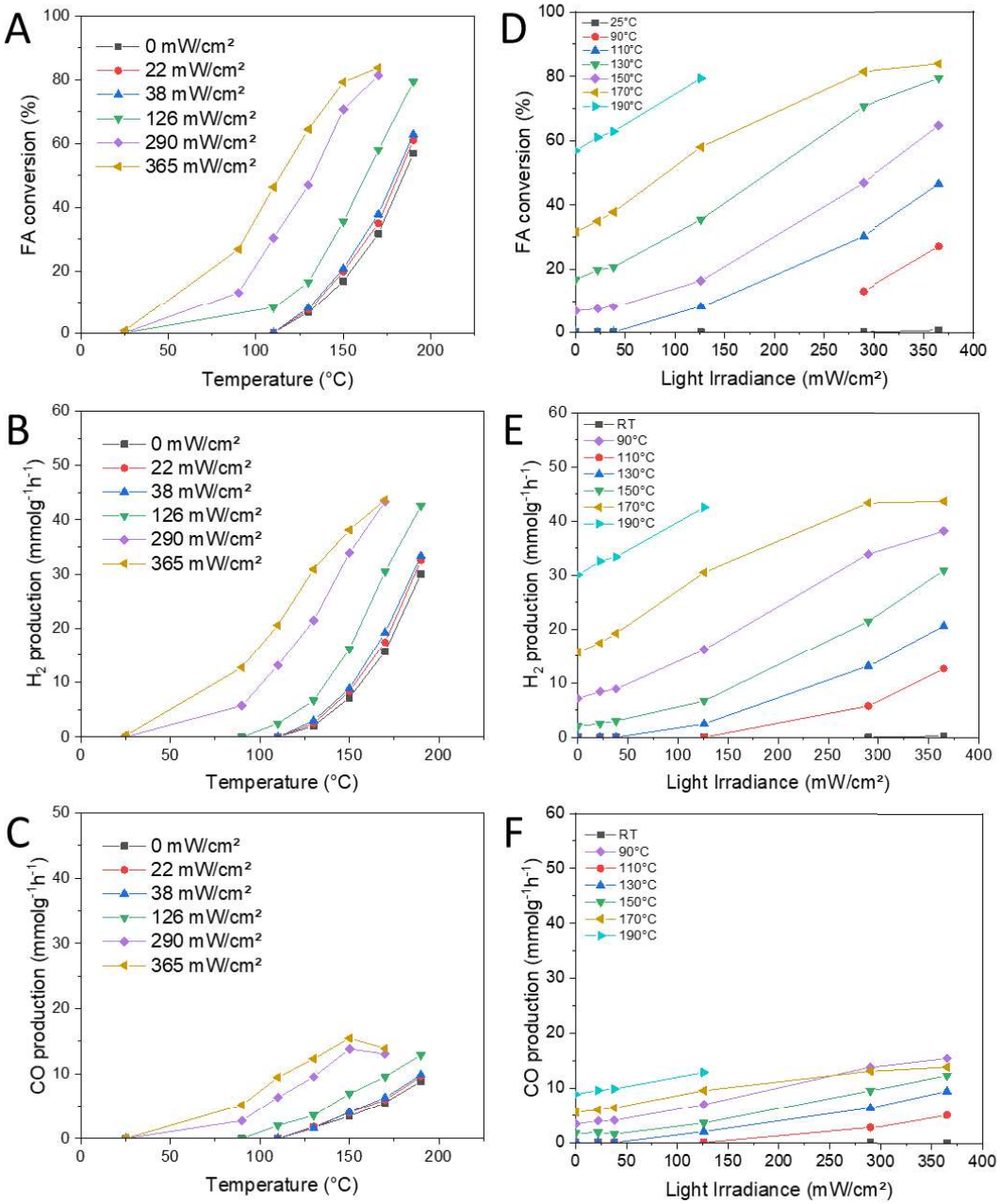

Fig. 74 *Influence of the UV-A light irradiance in the 0-365 mW/cm² range and of the reaction temperature on the photothermal formic acid decomposition on the Ru(0.5%)/SiO_2 catalyst prepared by the wet impregnation method.* ***A-B)*** *FA conversion,* ***C-D)*** *Production of H_2,* ***E-F)*** *Production of CO. Reaction conditions: [FA]= 4600 ppm_v, total Ar flow of 14.7 mL, 1.8 mg of catalyst, FA specific molar rate of 67.2 mmol $g^{-1}h^{-1}$.*

In general, the light irradiation does not affect in a large extent the selectivity with the Ru/SiO_2 catalyst, the selectivity to CO (dehydration) being not strongly impacted by the additional photonic excitation . The CO selectivity at dark conditions (22-38%) remained mainly unchanged over the whole light irradiance range, as it is shown in **Fig. 75**A. This is particularly visible when the temperature is increased. For instance, the CO selectivity values oscillate slightly from 26.0 % to 24.7 % at 170°C from 0 mW/cm² to 365 mW/cm², respectively. At lower temperatures, i.e. at lower FA conversions, a slight decrease in CO selectivity may be observed, but we must say that the amount of CO produced remained low, so that the accuracy of the data also. These results may suggest that the photon

absorption and the following processes such as local heating, electron-driven reaction, etc. equally contributed to the production of hydrogen and carbon monoxide. The relative absence of sensitivity to light irradiance of the CO selectivity was in agreement with the fact that the support surface was not playing directly an active role in the CO formation. No photothermal enhancement being observed at the support surface, the enhancement was only taking place at the surface of the catalytic Ru nanoparticles, by contrast to the case of the Ru/TiO_2 catalyst.

Fig. 75B and **Fig. 75**C depict the linear tendency of the Arrhenius plot graphs for both CO and H_2 productions, respectively. The derived apparent activation energies in **Fig. 75**D linearly for both dehydration and dehydrogenation reactions with increasing the light irradiance from dark conditions to 365 mW/cm², following a stronger slope for the dehydrogenation reaction.

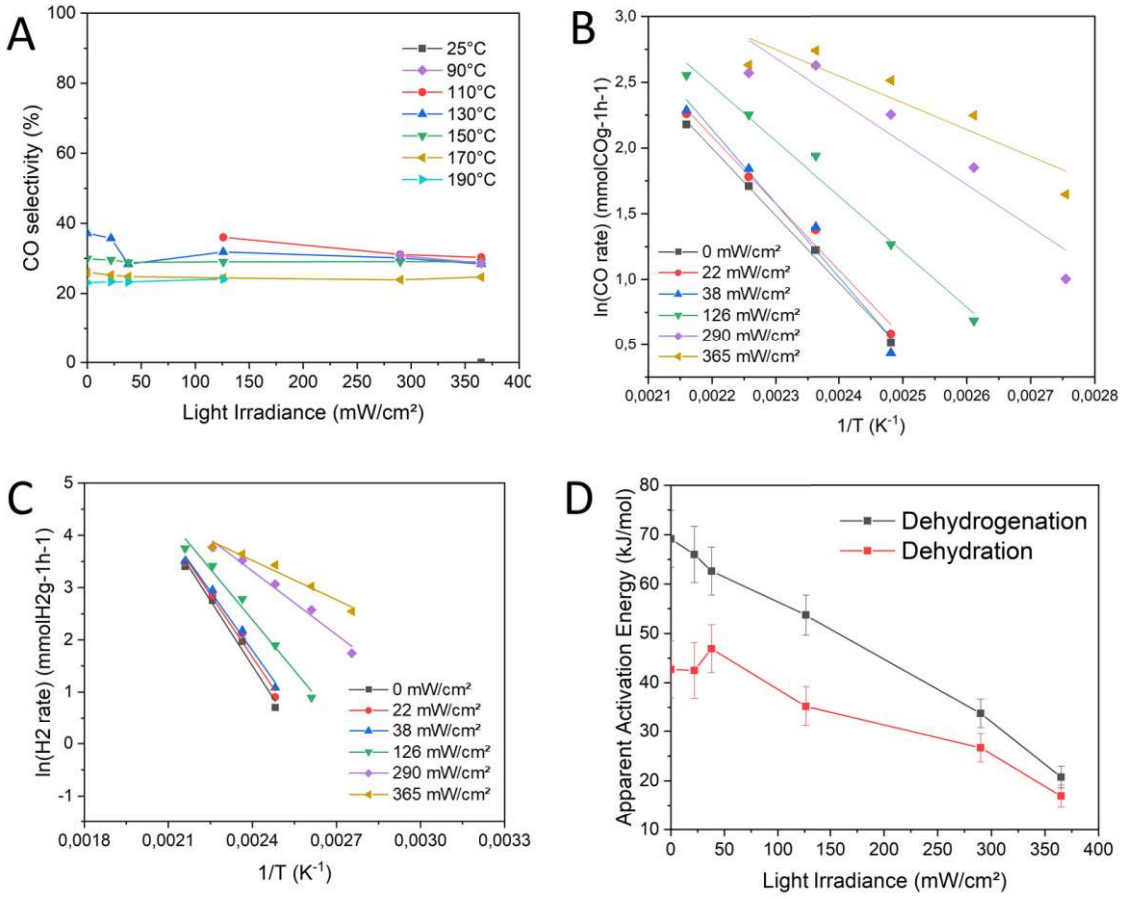

Fig. 75 *Influence of the UV-A light irradiance in the 0-365 mW/cm² range and of the reaction temperature on the photothermal formic acid decomposition on the Ru(0.5%)/SiO_2 catalyst prepared by the wet impregnation method.* ***A)*** *CO selectivity values,* ***B)*** *Arrhenius plot graphs of CO production at different irradiating conditions,* ***C)*** *Arrhenius plot graphs of H_2 production at different irradiating conditions,* ***D)*** *Light-dependency of the apparent activation energies of dehydrogenation and dehydration reactions.*

To sum up, Ru/SiO_2 demonstrated also to benefit from a combined photonic/thermal excitation and inconsequence can be considered as a photothermal catalyst for FA conversion into H_2 and CO_2 products via dehydrogenation. The obtained results showed that catalysts based on isolating supports like SiO_2 can be considered as photothermal catalysts. In contrast to the $Ru/g\text{-}C_3N_4$ catalysts the Ru/SiO_2 systems unfortunately also catalysed the dehydration reaction, producing CO and H_2O. While

both H_2 and CO productions were enhanced under UV-A light excitation, selectivity is not dependent on the light irradiance. These similar selectivity values from dark conditions to 365 mW/cm² is quite different of what it was observed when FA decomposition on Ru/TiO_2 catalyst.

3.3. Summary graphs for the photothermal catalytic decomposition of FA over the three Ru catalysts

The low-temperature shifts for achieving similar FA conversion and H_2 production rate under combined photonic/thermal excitation than that obtained at dark conditions are represented in **Fig. 76** for the three catalysts. As previously observed for the Ru/TiO_2 catalysts, the lowering of the temperature was well evidenced with $Ru/g\text{-}C_3N_4$ and Ru/SiO_2 catalysts.

It was worth noting that the low-temperature shift upon irradiation remained independent of the reaction temperature (in the dark) in the case of the $Ru/g\text{-}C_3N_4$ catalysts, the slopes being identical whatever the temperature plotted in the 100-150°C range. Obviously, on the $Ru/g\text{-}C_3N_4$ catalyst, similar trend has been observed for FA conversion and H_2 production rate as the reaction was fully selective towards the dehydrogenation route (see **Fig. 76**E). We suggested for the first time, that this behaviour could be the evidence of a thermal-driven mechanism, with thermalization of hot carriers from the Ru nanoparticles.

In the case of the Ru/SiO_2 catalyst, **Fig. 76**F depicts the different slopes at each temperature for H_2 production, and **Fig. 76**C for the FA conversion. In contrary to the Ru/TiO_2 catalyst, the low-temperature shift observed for the FA conversion was not much depending on the reaction temperature, while the low-temperature shift observed for the H_2 production was depending on the temperature.

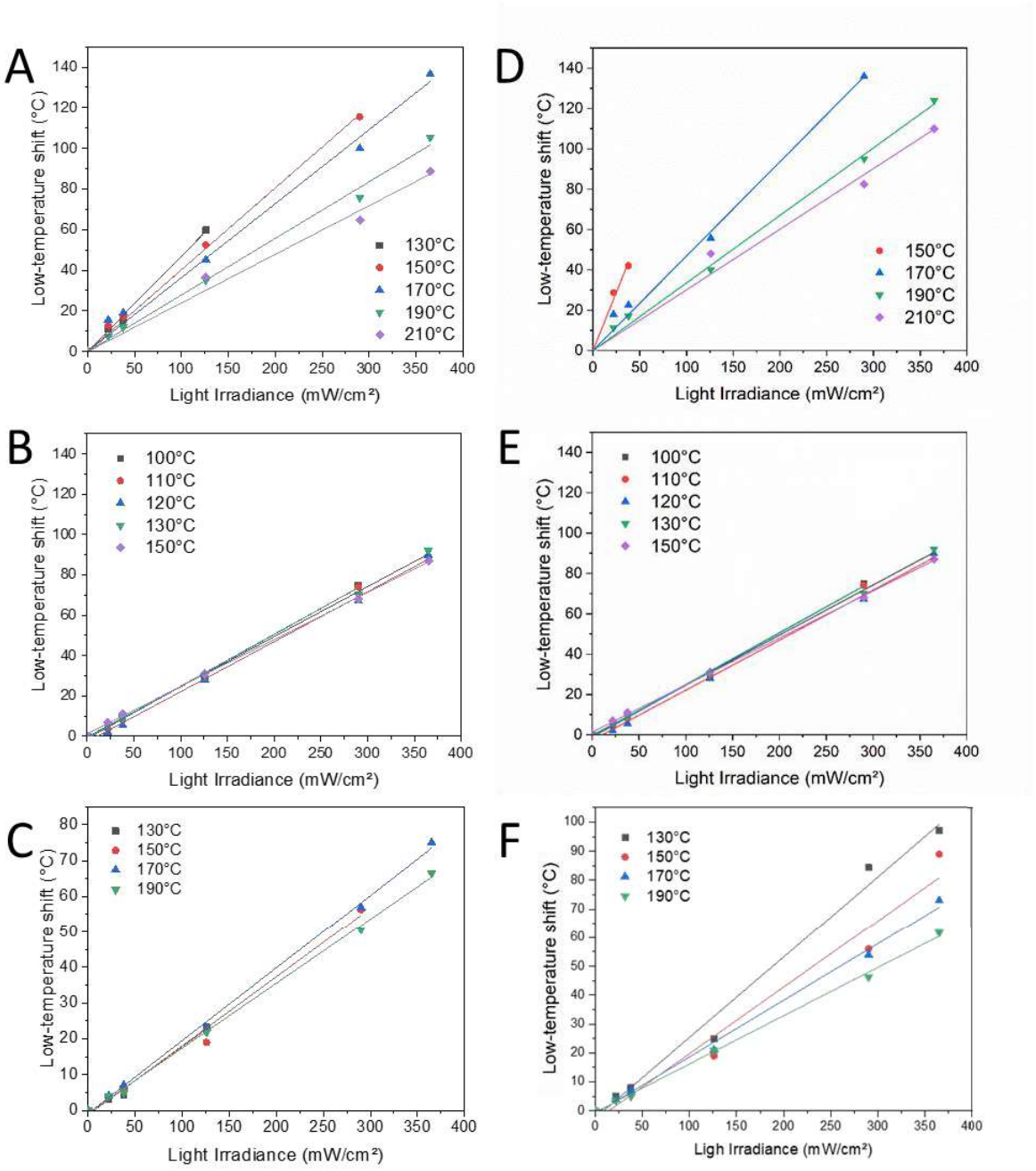

Fig. 76 *Results extrapolated results from the FA conversion and H_2 productions over Ru(0.5%)/TiO_2 (PA), Ru(0.5%)/g-C_3N_4 (PA) and Ru(0.5%)/SiO_2 catalysts shown in Fig 6A,B (chapter 3), Fig 13B,C and Fig. 15A,B (chapter 4), in order to evidence the influence of the irradiance on the low-temperature shift while achieving* ***(left) a similar FA conversion*** *as that in the dark and* ***(right) a similar H_2 production*** *rate conversion as that in the dark. In both cases, the low-temperature shift is represented by referring to the different reaction temperatures in the dark.*

(***A-D)*** *Ru(0.5%)/TiO_2 (PA),* ***(B-E)*** *Ru(0.5%)/g-C_3N_4 (PA) and* ***(C-F)*** *Ru(0.5%)/SiO_2 catalysts*

In the **Fig. 77** is shown the evolution with the light irradiance of the different apparent activation energies of the dehydrogenation and dehydration reactions for the three catalysts (the pseudo-activation energy calculated from the Arrhenius plot graphs for the FA conversion is shown in **Fig. A 1** in Annex).

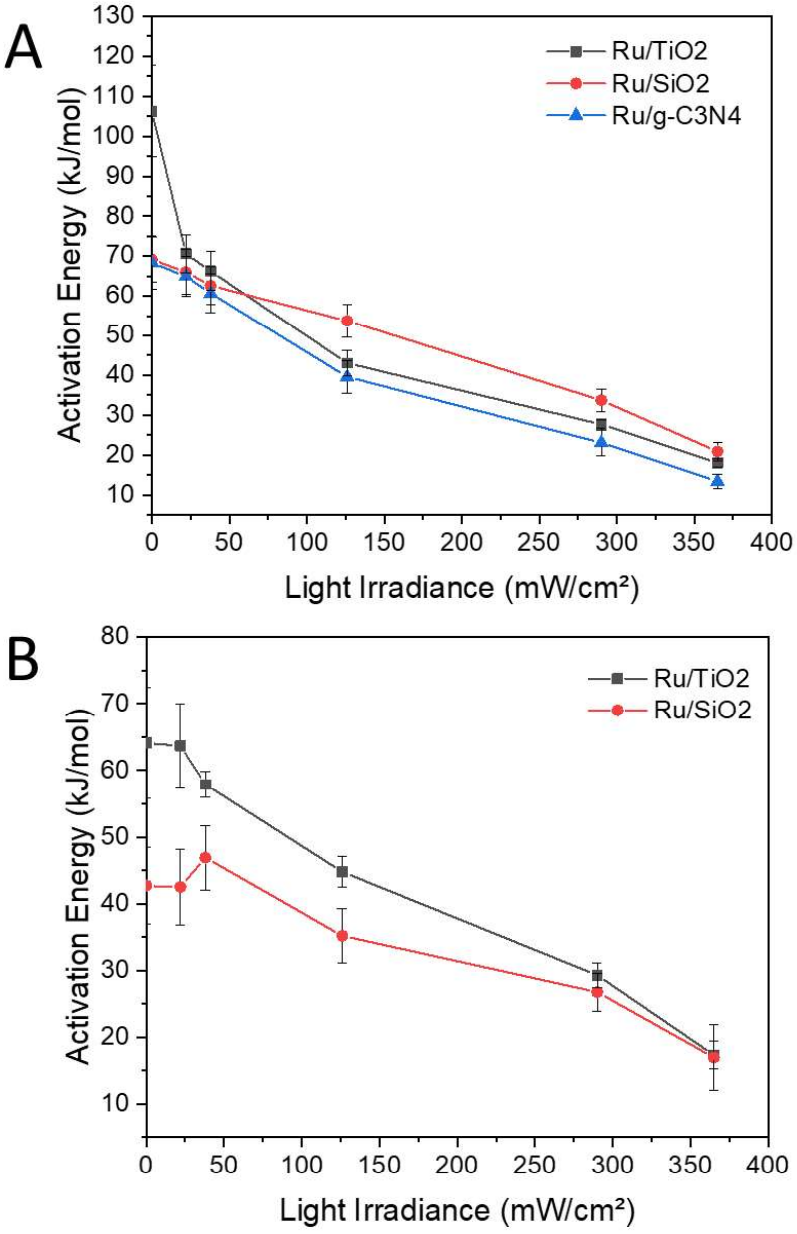

Fig. 77 *Evolution with the light irradiance of the apparent activation energies for* ***(A)*** *dehydrogenation and* ***(B)*** *dehydration reactions, over (black) Ru/TiO_2, (red) Ru/SiO_2 and (blue) Ru/g-C_3N_4 catalysts.*

We must said that this way to plot the influence of the light irradiance on the catalytic indicators for deriving mechanistic aspects is not accepted by all authors in the literature. For instance, the decrease of the activation energy with increasing the light irradiance that is usually reported for electron-driven reactions, has been questioned by the group of Jain about the original work of Dubi [25,26]. The authors suggested that a linearity of the activation energy decrease upon irradiation might be in fact also correlated to an increase of the surface temperature produced by the "photothermal" contributions (thermalization of hot carriers at metal surface), and that it is possible to correlate the temperature of the surface to the light irradiance. This points out that many questions still remained under debate in this emerging field.

In our case, for instance, in the case of the Ru/g-C_3N_4 catalyst, a decrease of the apparent activation energy for the dehydrogenation reaction has been observed, and what is more with a linear relationship, what suggest the predominance of electron-driven mechanisms. However, the low-temperature shift we observed with maintain of a similar H_2 production rate was very interestingly independent of the bulk temperature at which we operated, what might suggest the predominance of thermalization mechanisms. This confirmed that unravelling mechanistic aspects in photothermal catalysis require implementing a wide span of (advanced) characterization tools.

3.4. Influence of the Ru content in Ru/g-C_3N_4 catalysts

Similarly to the Ru/TiO_2 (PA) catalyst, it must be said the a Ru loading of 0.5 wt.% was optimal in terms of H_2 production also in the case of the g-C_3N_4-based catalysts. Without providing here details, **Fig. 78** depicts the influence of the light irradiance at different temperatures for Ru loadings of 0.25% and 1.5% (using a similar UV-A light driven photo-assisted synthesis method). Additional TEM and XPS analyses displayed that the mean Ru nanoparticle size and the distribution were not significantly influenced, probably due to the large specific surface area of the g-C_3N_4 support. A beneficial photothermal enhancement was observed in terms of H_2 production rate, whatever the Ru loading, here again with no formation of CO by-product. The evolution of the apparent activation energy upon irradiation is also reported.

We can suggest that under light the activation of the g-C_3N_4 support by UV-A photons is playing a role for modifying the electronic properties of the Ru nanoparticles, e.g. through electron transfer from the semiconductor surface to the supported Ru nanoparticles. Indeed, in the absence of any specific role, except that to support and stabilize the nanoparticles, the increase in the Ru loading should lead to an increase in the conversion and H_2 production rate upon irradiation. By contrast an optimum content was observed, as often reported for semiconductors decorated with noble metal nanoparticles, due to an optimum charge transfer at the different support/metal interfaces.

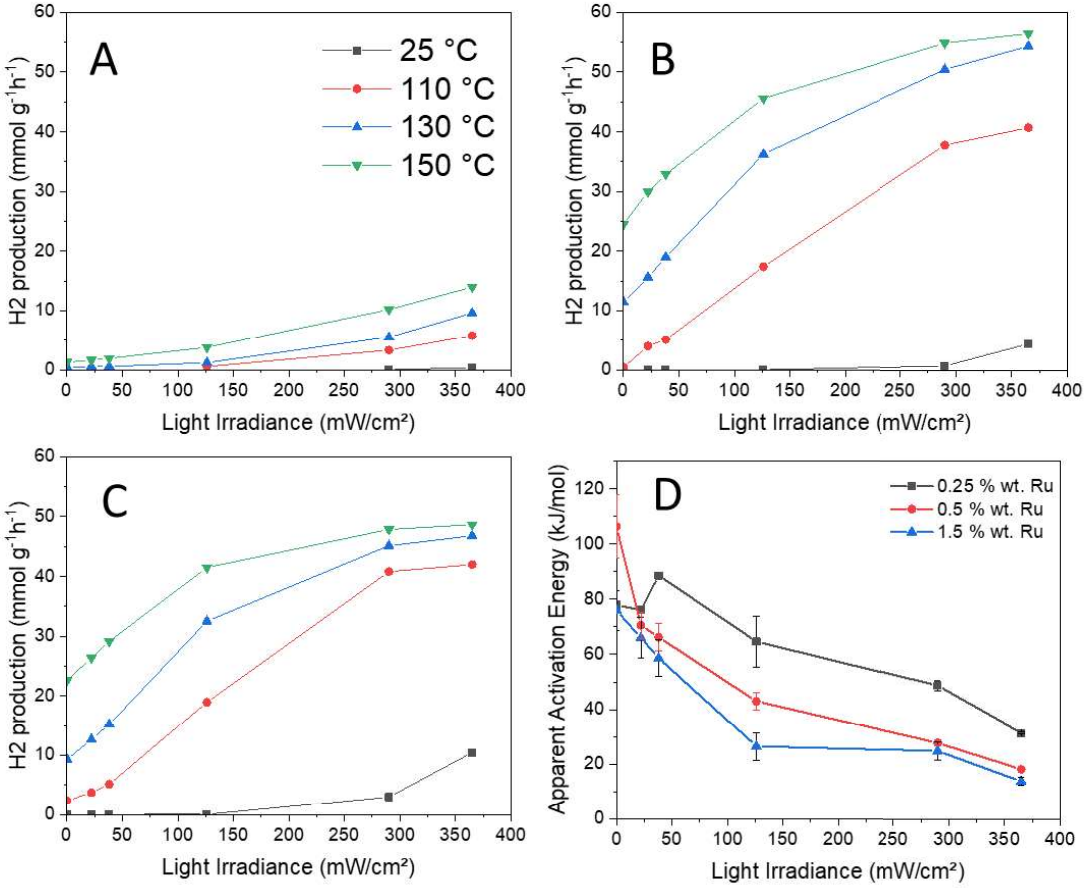

Fig. 78 *Photothermal H_2 production from FA decomposition over the Ru/g-C_3N_4 (PA) catalysts with Ru loadings of* ***(A)*** *0.25 %,* ***(B)*** *0.5% and* ***(C)*** *1.5% wt.* ***(D)*** *influence of the light irradiance on the apparent activation energy of the dehydrogenation reaction over the mentioned catalysts.*

4. In-situ DRIFT spectroscopy study of the formic acid decomposition

This section is subdivided into three parts, namely first the study of the adsorption of formic acid in the dark on the three catalysts, and subsequently the in-situ DRIFTS study of the formic acid decomposition over the Ru/SiO_2 catalyst, and over the Ru/g-C_3N_4 catalyst, in both cases in the dark and in photothermal conditions.

As in the previous study, in-situ infrared spectroscopy has been used to provide useful information on the way formic acid interacts with the catalytic surface and further how it is catalytically decomposed.

4.1. Adsorption of formic acid

In **Fig. 79**, the different spectra of in-flow formic acid over the Ru/SiO_2, Ru/g-C_3N_4 and Ru/TiO_2 catalysts are collected after the subtraction of the bare catalyst spectra. Unfortunately, bare SiO_2 material absorbs infrared light at wavenumbers values lower than 1700 cm^{-1} [27]. Therefore, any signal below this value would not be visible in that range, with in consequence a redhibitory "noise" observed in the differential spectra that does not allow any absorbance band to be distinguished. Similar limitation was observed for the Ru/g-C_3N_4 catalyst, for which the saturation ranges are between 1750 cm^{-1} and 1250 cm^{-1} due to the C–N stretching and bending vibrations of the N-heterocycles of the g-C_3N_4 support that absorb in that region, and between 900 cm^{-1} and 600 cm^{-1} for the tri-s-triazine vibrations [1]. In

consequence, we extended the range of the different spectra for trying to analyse the adsorption, as the wavenumber region that corresponds to carbonates and formates is unobservable.

At high wavenumbers (4000-2500 cm^{-1}) it is possible to observe the O-H bonds at the surface of the metal oxide materials. Negative absorbance values at 3750-3680 cm^{-1} can correspond to the consumption of surface hydroxyl groups [28,29], being this band assigned to the O-H stretching of free silanol (in the case of Ru/SiO_2 catalyst) [28] and isolated hydroxyl groups coordinated with Ti^{4+} atoms (in the case of Ru/TiO_2) [29]. In addition, a broad (ill-defined) band was observed in the range of 3500-2500 cm^{-1}. This band is attributed to the hydrogen bond formation between the hydroxyl groups of the formic acid and the oxygen atoms of the metal oxide surface [28]. Therefore, formic acid is adsorbed at the oxygen of the free silanol (or from hydroxide of TiO_2), breaking the O-H bond of the surface, meanwhile its hydroxyl groups is hydrogen bonded to other oxygen atom, this two mechanistic steps are visual in the spectra. In addition, the band at 2940 cm^{-1} is assigned to the gas-phase formic acid, concretely to the vibrational frequency of the C-H stretch, and the band at 2875 cm^{-1} is assigned to the vibrational frequency of the stretch C-H of adsorbed formate species onto the surface [34].

As the absorbance bands for carboxylate and formate species are in the 1900-1300 cm^{-1} range, observing adsorbate and intermediate species over both Ru/SiO_2 and $Ru/g\text{-}C_3N_4$ catalysts remained difficult. However, there is a narrow range, namely between 1220 cm^{-1} and 900 cm^{-1}, where it was possible to observe bands at 1217 cm^{-1} and 913 cm^{-1} in the case of the $g\text{-}C_3N_4$ based catalyst, which are attributed to dimer formic acid in gas phase, and the band at 1104 cm^{-1} assigned to gaseous HCOOH monomer species [30–33]. Similarly to in-situ formic acid decomposition over Ru/TiO_2, a mixture of formic acid as monomer and dimer species was observed in the gas flow with absorbance bands at 1790 cm^{-1} and 1740 cm^{-1}.

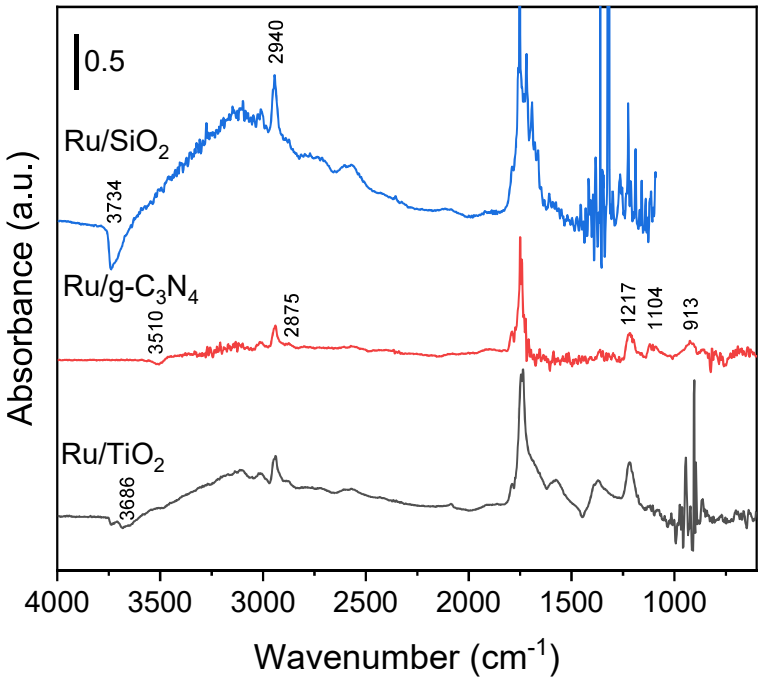

Fig. 79 *Differential DRIFT spectra (after subtraction of the reference spectrum recorded in the absence of FA flow) in the case of the Ru/SiO_2 (blue), $Ru/g\text{-}C_3N_4$ (red) and Ru/TiO_2 (black) catalysts in the dark at 25°C (Formic acid flow: 14.7 ml/min, 0.044 bar).*

4.2. In-situ DRIFTS study of the formic acid decomposition over the Ru/SiO_2 catalyst in photothermal conditions.

Fig. 80 shows the differential infrared spectra recorded in-situ during the photothermal FA decomposition over the Ru/SiO_2 catalyst (subtracted from the spectra recorded at 25°C at dark conditions). Spectra in dark conditions are first shown in **Fig. 80**A-B. There, it is possible to appreciate the high absorbance values of the silanol band at 3734 cm^{-1} that occurs during the decomposition of formic acid, being the -OH species part of the mechanism to produce CO_2, H_2, H_2O and CO. The decomposition of gas dimer formic acid is assigned to the negative values of the bands at 2940 cm^{-1}, 2580 cm^{-1} and 1746 cm^{-1}, while the absorbance of the band assigned to the monomer formic acid species at 1790 cm^{-1} increased at mild temperatures (110-150°C) and decreased at high temperatures (170-190°C). The absorbance at 2400-2300 cm^{-1} increased with increasing the temperature, what was assigned to the CO_2 production from the dehydrogenation reaction. In the 2100-1900 cm^{-1} range it was possible to appreciate the increase of absorbance with the temperature, which was assigned to the Ru-CO bonds as part of intermediate species that adsorb at the ruthenium surface to finally produce CO_2, CO, H_2 and H_2O.

Fig. 80C-D show the FA decomposition under UV-A light irradiation in the full spectral range and in the region of interest, respectively. As similarly occurred at dark conditions, a high concentration of hydroxide species occurred over the catalyst surface. In the concrete wavenumber range for the physisorbed CO_2 and Ru-CO bands (2400-1900 cm^{-1}), bands assigned to CO_2 started to raise at temperatures above 130°C to 170°C, the maximum temperature analysed. Ru-CO bands increased in absorbance at illuminating conditions with the temperature with two distinguishable bands at 2080 cm^{-1} and 2020 cm^{-1}:

- the band at 2080 cm^{-1} corresponds to the vibrational frequencies of linear Ru^{n+}-CO and/or trycarbonyl species CO species on Ru^{n+}-$(CO)_n$ (where n=1-3). The band at 2080 cm^{-1} was not observed in the dark and only appears at illuminating conditions, so that it can be considered as a **light band**, as defined in Chapter 3.
- the band at 2020 cm^{-1} corresponds to dicarbonyl CO species on Ru^0, Ru^0-$(CO)_2$, and/or CO linearly adsorbed on Ru defects or isolated Ru^0 atoms over a ruthenium partially-oxidized surface [35]. The band obtained at 2020 cm^{-1} has been observed in dark conditions also as the broad band at 2100-1900 cm^{-1}, previously described before. Therefore, it could be considered as a **thermal band**. However, the intensity of this band is similar under dark and light conditions, which means that, instead of a possible surface *thermalization* (local temperature), this band emerges with the increase of the bulk temperature.

The co-existence of two kinds of bands suggested that both electron-driven and thermal-driven processes (but without thermalization) might occur under combined photonic/thermal excitation of the Ru/SiO_2 catalysts.

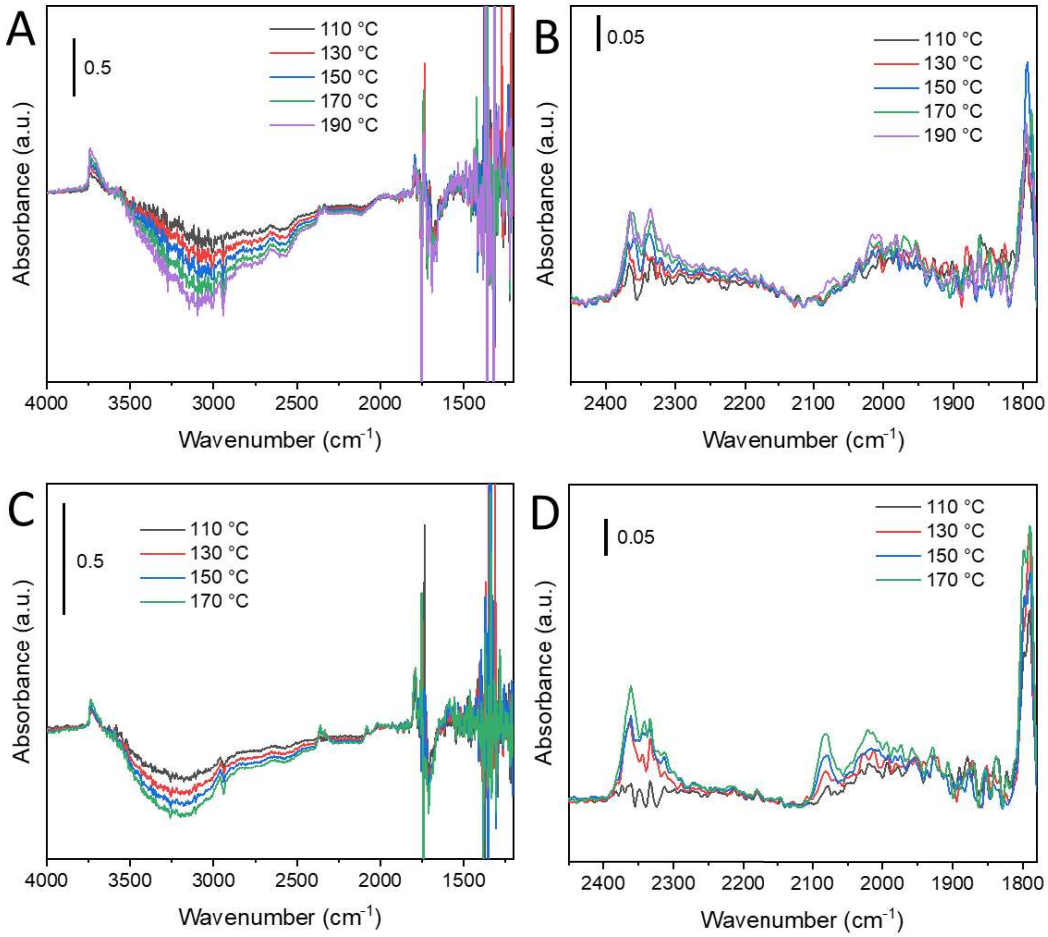

Fig. 80 *DRIFT differential spectra recorded for the formic acid decomposition over the Ru/SiO_2 catalyst (subtracted from the reference spectra at room temperature and dark conditions) at 110-190°C at* ***dark*** *conditions in the range of* ***(A)*** *4000-1100 cm^{-1} and* ***(B)*** *2500-1780 cm^{-1}, and at 110-170°C at* ***illuminating*** *conditions in the range of* ***(C)*** *4000-1100 cm^{-1} and* ***(D)*** *2500-1780 cm^{-1}. (Formic acid flow: 14.7 ml/min, 0.044 bar, Irradiance: ca. 365 mW/cm^2)*

The following **Fig. 81** compares directly the differential spectra recorded in-situ in the range of 2400-1780 cm^{-1} during the FA decomposition over Ru/SiO_2 at dark (black) and illuminating (red) conditions. While the absorbance in the physisorbed CO_2 bands and the monomer formic acid does not show any clear difference between dark and light conditions, the Ru-CO bonds spectra are influenced. On one hand, the band at 2080 cm^{-1} was only visible in the spectra under light irradiation conditions, and its intensity increased with the temperature. This suggested an electron-driven mechanism. On the other hand, the broad band at 2020 cm^{-1} have similar values under light irradiation and at dark conditions, which can be related to a pure thermal-driven mechanism ; however this thermal catalysis was not enhanced upon irradiation, so this mechanism is not considered as thermalization of hot carriers. Therefore, the reaction under light irradiation might be considered as a combination of light- and thermal-driven processes where both photons and heat activate the ruthenium active sites, respectively, to decompose formic acid into dehydrogenation (and dehydration) products. Upon irradiation, the presence of the band at 2080 cm^{-1} is clearly a sign of photo-enhanced intermediates species over the ruthenium surface, in contrary to the similar intensity of the band at 2020 cm^{-1} with and without light. The photons would induce an electron-driven mechanism, and no thermalization.

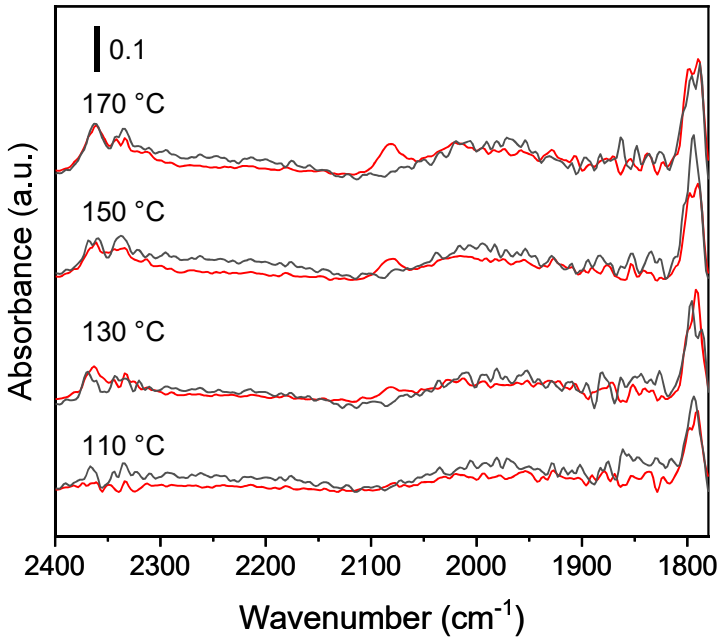

Fig. 81 *DRIFT spectra in the range from 2400-1780 cm^{-1} recorded during the formic acid decomposition over the Ru/SiO_2 catalyst at dark (black) and illuminating (red) conditions. (Formic acid flow: 14.7 ml/min, 0.044 bar, Irradiance: ca. 365 mW/cm^2)*

4.3. In-situ DRIFTS study of the formic acid decomposition over the Ru/g-C_3N_4 catalyst in photothermal conditions.

The infrared spectra recorded in-situ during the photothermal FA decomposition on the Ru/g-C_3N_4 catalyst are shown for the 2500-1900 cm^{-1} and 1300-800 cm^{-1} ranges, as shown in **Fig. 82**. Similar to the previous experiments, the reference spectrum recorded with FA/Ar flow over the catalyst at 25°C was subtracted. **Fig. 82**A depicts the spectra recorded in the dark in the wavenumber range of bands assigned to physisorbed CO_2 and Ru-CO bonds. Bands at 2043 cm^{-1} and 2016 cm^{-1} appeared at 150°C. They are assigned to linearly bonded Ru-CO and dicarbonyl species on Ru^{2+} [Ru^{2+}-$(CO)_2$], respectively. The shoulder appearing simultaneously at 1959 cm^{-1} was assigned to Ru-CO linearly adsorbed over partially-oxidized ruthenium surface and/or bridge-bonded CO to two atoms of ruthenium [Ru_2-(CO)] [35]. Band at 1210 cm^{-1} indicates the consumption of gas dimer formic acid as it shows negative absorbance at 150°C meanwhile bands at 1125 cm^{-1} and 1086 cm^{-1} increased in absorbance with temperature until 130°C. Then, absorbance values decreased at 150°C. Therefore, we can suggest that these bands can be assigned to intermediates of the formic acid decomposition due to their appearance with the temperature increase and their vanishing at 150°C when the conversion of FA reached high values.

At illuminating conditions, Ru-CO bonds were observable even at 110°C with an almost no visible CO_2 production. However, the CO_2 bands increased in absorbance with the temperature increase. Ru-CO bands increased in terms of absorbance under light but no additional bands were detected. This can suggest the absence of a predominant electron-driven mechanism, and the predominant occurrence

of a thermalization (i.e. thermal-driven) mechanism to produce H_2 and CO_2 from the formic acid decomposition.

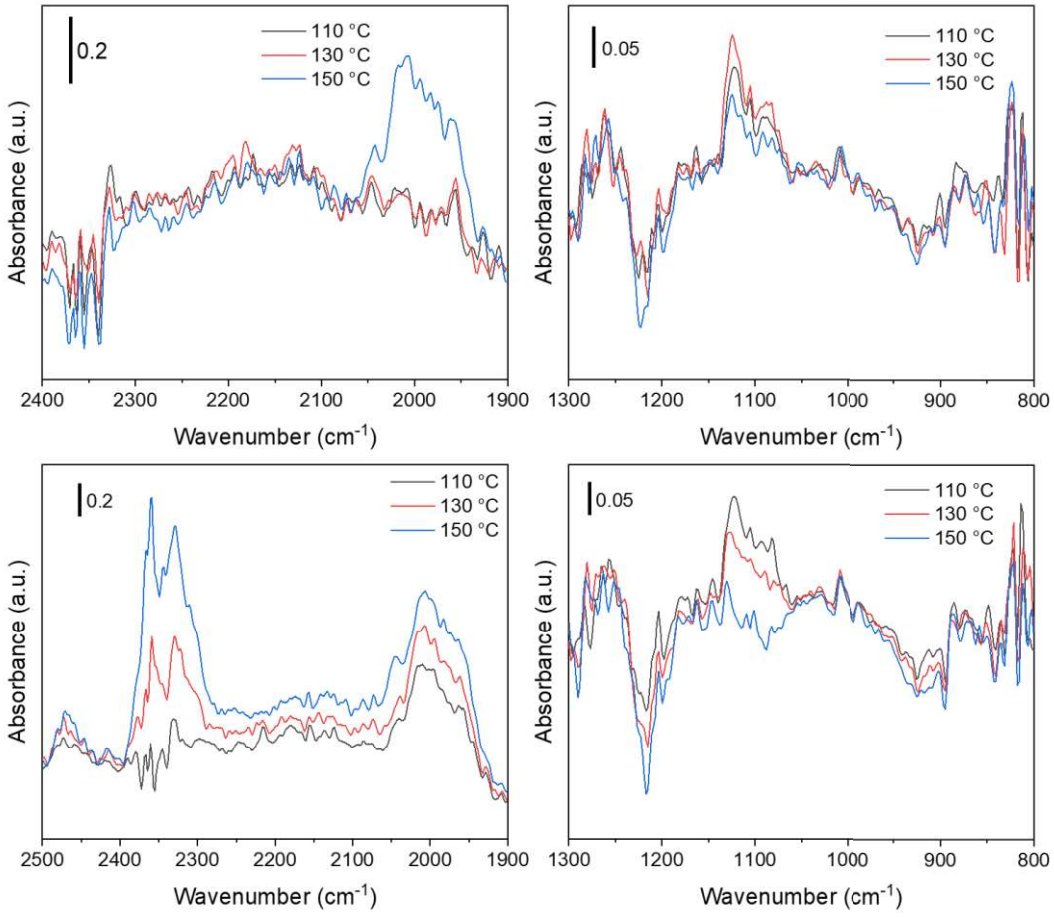

Fig. 82 *DRIFT differential spectra recorded for the formic acid decomposition over the Ru/g-C_3N_4 catalyst (subtracted from the reference spectra at room temperature and dark conditions) at 110-150°C at* ***dark*** *conditions in the range of* ***(A)*** *2400-1900 cm^{-1} and* ***(B)*** *1300-800 cm^{-1}, and at 110-150°C at* ***illuminating*** *conditions in the range of* ***(C)*** *2500-1900 cm^{-1} and* ***(D)*** *1300-800 cm^{-1}. (Formic acid flow:14.7 ml/min, 0.044 bar Irradiance: ca. 365 mW/cm^2)*

In **Fig. 83**, the infrared spectra recorded for the in-situ formic acid decomposition over the Ru/g-C_3N_4 catalyst are directly compared under illuminating and dark conditions. There, the absorbance of CO_2 bands at 2400-2300 cm^{-1} increased with increasing the temperature only under UV-A photon irradiation, which was not observed at dark conditions. In addition, the absorbance of the bands assigned to the characteristic frequency of Ru-CO bonds are different at 110°C and 130°C (being higher under light irradiation) but similar at 150°C. This could suggest again that Ru-CO bonds activation is produced by the increase in temperature of the metal surface, localized increased under illuminating conditions via photothermal processes. Therefore, the Ru-CO bands observed during the FA decomposition can correspond to thermal bands following our terminology. Then, the light absorption by the metal would increase the local temperature around the Ru nanoparticles and enhance the thermal-driven mechanisms over the catalyst for the FA decomposition into hydrogen. This can be in agreement with the particular constant low-temperature shift reported for the Ru/g-C_3N_4 catalyst in **Fig. 77**, only observed Ru/g-C_3N_4 catalyst, in contrary to the temperature dependent low-temperature shift observed for both Ru/TiO_2 and Ru/SiO_2 catalysts.

We said that this conclusion differs from what suggested the decrease of the apparent activation energy with the increase in the light irradiance, what is usually assigned to electron-driven mechanisms. This points out that many questions still remained under debate in this emerging field, that unravelling mechanistic aspects in photothermal catalysis require implementing a wide span of (advanced) characterization tools.

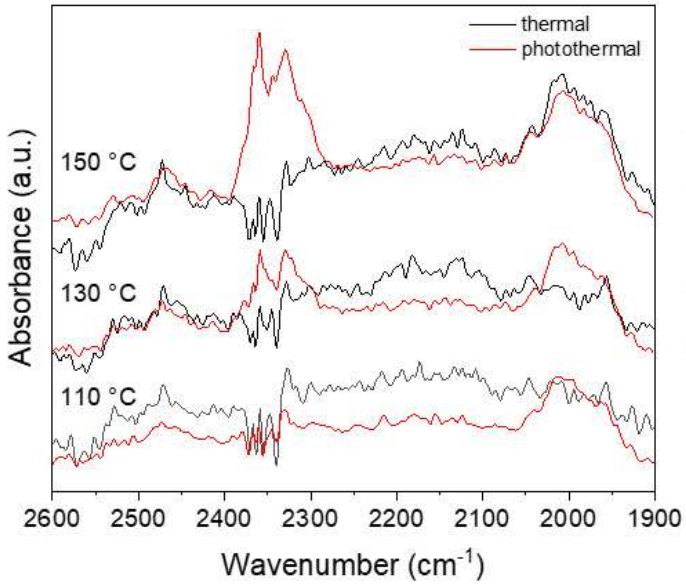

Fig. 83 *DRIFT differential spectra in the range of 2600-1900 cm^{-1} recorded during the FA decomposition over the Ru/g-C_3N_4 catalyst (subtraction of the reference spectrum at 25°C (FA adsorption) at dark (black) and illuminating (red) conditions (Formic acid flow:14.7 ml/min, 0.044 bar, Irradiance: ca. 365 W/cm^2)*

DRIFTS as an in-situ technique provided useful information on the influence of the light for the formic acid decomposition over the different catalytic surfaces. The support material, being different in Ru/TiO_2, Ru/SiO_2 and Ru/g-C_3N_4 catalysts, influences the bonds between ruthenium and the carbonyls during the reaction. In addition, new bonds between ruthenium and carbonyl appeared under UV-A photon irradiation even at low temperature for Ru/SiO_2 with an increase of absorbance for the bands assigned to CO_2. As this band is assigned to the characteristic frequency of linear Ru^{n+}-CO, it might be induced by the migration of electrons from the metal to the molecule as intermediate step of the final conversion of formic acid into dehydrogenation and dehydration products. For Ru/g-C_3N_4, more bonds were detected like bridge Ru_2-CO, which can confirm a different mechanism that contributed to the full selectivity to dehydrogenation products in addition to the properties of the support surface. In this case, the bands that were detected under light conditions are similar to those observed at high temperatures at dark conditions; which might indicate that the formic acid decomposition would be mainly activated by thermal-driven processes after *thermalization* of the light induced-charge carriers.

5. Conclusions

Following the first evidence of a beneficial photothermal effect under UV-A in the case of the Ru/TiO_2 catalysts, this chapter aimed at studying to which extent the performances and the photothermal

enhancement effect might be influenced and improved through the choice of other support materials. Mainly Ru/g-C_3N_4 and Ru/SiO_2 catalysts were investigated, even if other supports such as $LaFeO_3$ or β-SiC among others have been investigated. The catalysts have been tested in the same conditions as the Ru/TiO_2 reference systems in the previous chapter for the formic acid decomposition, as a function of the light irradiance at different reaction temperatures.

We showed that both Ru/g-C_3N_4 and Ru/SiO_2 catalysts exhibited a positive photothermal effect, allowing the H_2 production rate to be increased under light in comparison to the dark conditions, and in consequence allowing an important low-temperature shift to be obtained while maintaining a similar H_2 production rate.

Medium surface area g-C_3N_4 prepared by a double-step thermal treatment synthesis at 550°C was shown to allow the elaboration of excellent Ru/g-C_3N_4 photothermal catalysts, through a UV-A light driven photoassisted synthesis method. We demonstrated for the first time that Ru/g-C_3N_4 catalysts are remarkable photothermal catalysts, that clearly outperformed the Ru/TiO_2 reference catalysts in terms of hydrogen production, as well as selectivity to H_2. An optimum Ru content of 0.5 wt.% was observed. The Ru/g-C_3N_4 catalyst allowed to obtain a selectivity to H_2 of 100%, the reaction occurring only via the dehydrogenation route, no dehydration being observed with no CO formed, whatever the reaction temperature and the light irradiance. The surface properties of the g-C_3N_4 support was proposed to play an important role in the full selectivity towards dehydrogenation, and allowed to overcome the intrinsic limitation resulting from the dehydration activity of the TiO_2 semiconductor support itself.

In that case, we suggsted a photothermal enhancement through a thermal-driven process, with thermalization of the light induced-charge carriers generated at the supported Ru nanoparticles. However, this remains under debate are the different results collected might sound contradictory.

Interestingly, an isolating support like SiO_2 can also be considered as support in photothermal catalysis, and the photothermal enhancement was attributed to the activation of the Ru nanoparticles upon irradiation with no contribution of the support, in contrary to both Ru/TiO_2 and Ru/g-C_3N_4 catalysts. We proposed a combined electron-driven and pure thermal mechanism, with the involvement of hot carriers from Ru (with no thermalization). However, the Ru/SiO_2 systems unfortunately also catalysed the dehydration reaction, i.e. also producing CO and H_2O.

References

[1] E.M. Dias, K.C. Christoforidis, L. Francàs, C. Petit, Tuning Thermally Treated Graphitic Carbon Nitride for H2 Evolution and CO2 Photoreduction: The Effects of Material Properties and Mid-Gap States, ACS Appl. Energy Mater. 1 (2018) 6524–6534. https://doi.org/10.1021/acsaem.8b01441.

[2] F. Fina, S.K. Callear, G.M. Carins, J.T.S. Irvine, Structural investigation of graphitic carbon nitride via XRD and neutron diffraction, Chem. Mater. 27 (2015) 2612–2618. https://doi.org/10.1021/acs.chemmater.5b00411.

[3] L. Ge, Synthesis and photocatalytic performance of novel metal-free g-C3N4 photocatalysts, Mater. Lett. 65 (2011) 2652–2654. https://doi.org/10.1016/j.matlet.2011.05.069.

[4] A.. Dementjev, A. de Graaf, M.C.. van de Sanden, K.. Maslakov, A.. Naumkin, A.. Serov, X-Ray photoelectron spectroscopy reference data for identification of the C3N4 phase in carbon–nitrogen films, Diam. Relat. Mater. 9 (2000) 1904–1907. https://doi.org/10.1016/S0925-9635(00)00345-9.

[5] Y. Zhang, Z. Schnepp, J. Cao, S. Ouyang, Y. Li, J. Ye, S. Liu, Biopolymer-activated graphitic carbon nitride towards a sustainable photocathode material, Sci. Rep. 3 (2013) 1–5. https://doi.org/10.1038/srep02163.

[6] M. Bonn, S. Funk, C. Hess, D.N. Denzler, C. Stampfl, M. Scheffler, M. Wolf, G. Ertl, Phonon-versus electron-mediated desorption and oxidation of CO on Ru(0001), Science. 285 (1999) 1042–1045. https://doi.org/10.1126/science.285.5430.1042.

[7] X.Y.X.N. Guo, Z.F. Jiao, G.Q. Jin, X.Y.X.N. Guo, Photocatalytic fischer-tropsch synthesis on graphene-supported worm-like ruthenium nanostructures, ACS Catal. 5 (2015) 3836–3840. https://doi.org/10.1021/acscatal.5b00697.

[8] P.G. O'Brien, A. Sandhel, T.E. Wood, A.A. Jelle, L.B. Hoch, D.D. Perovic, C.A. Mims, G.A. Ozin, Photomethanation of gaseous CO2 over ru/silicon nanowire catalysts with visible and near-infrared photons, Adv. Sci. 1 (2014) 1–7. https://doi.org/10.1002/advs.201400001.

[9] J.M. Sanz, D. Ortiz, R. Alcaraz de la Osa, J.M. Saiz, F. González, A.S. Brown, M. Losurdo, H.O. Everitt, F. Moreno, UV Plasmonic Behavior of Various Metal Nanoparticles in the Near- and Far-Field Regimes: Geometry and Substrate Effects, J. Phys. Chem. C. 117 (2013) 19606–19615. https://doi.org/10.1021/jp405773p.

[10] J.L. Eslava, X. Sun, J. Gascon, F. Kapteijn, I. Rodríguez-Ramos, Ruthenium particle size and cesium promotion effects in Fischer-Tropsch synthesis over high-surface-area graphite supported catalysts, Catal. Sci. Technol. 7 (2017) 1235–1244. https://doi.org/10.1039/c6cy02535h.

[11] P.G.J. Koopman, A.P.G. Kieboom, H. van Bekkum, Characterization of ruthenium catalysts as studied by temperature programmed reduction, J. Catal. 69 (1981) 172–179. https://doi.org/10.1016/0021-9517(81)90139-1.

[12] A. Fahmi, C. Minot, A theoretical study of CO adsorption on TiO2, J. Organomet. Chem. 478 (1994) 67–73. https://doi.org/10.1016/0022-328X(94)88158-8.

[13] J. Zhu, P. Xiao, H. Li, S.A.C. Carabineiro, Graphitic carbon nitride: Synthesis, properties, and applications in catalysis, ACS Appl. Mater. Interfaces. 6 (2014) 16449–16465. https://doi.org/10.1021/am502925j.

[14] H. Liu, P. Da Costa, H.B. Hadj Taief, M. Benzina, M.E. Gálvez, Mg-promotion of Ni natural clay-

supported catalysts for dry reforming of methane, RSC Adv. 8 (2018) 19627–19634. https://doi.org/10.1039/c8ra02615g.

[15] R.K. Singha, A. Yadav, A. Agrawal, A. Shukla, S. Adak, T. Sasaki, R. Bal, Synthesis of highly coke resistant Ni nanoparticles supported MgO/ZnO catalyst for reforming of methane with carbon dioxide, Appl. Catal. B Environ. 191 (2016) 165–178. https://doi.org/10.1016/j.apcatb.2016.03.029.

[16] D. Li, R. Li, M. Lu, X. Lin, Y. Zhan, L. Jiang, Carbon dioxide reforming of methane over Ru catalysts supported on Mg-Al oxides: A highly dispersed and stable Ru/Mg(Al)O catalyst, Appl. Catal. B Environ. 200 (2017) 566–577. https://doi.org/10.1016/j.apcatb.2016.07.050.

[17] E. Zağli, J.L. Falconer, Carbon dioxide adsorption and methanation on ruthenium, J. Catal. 69 (1981) 1–8. https://doi.org/10.1016/0021-9517(81)90122-6.

[18] C. Morterra, E. Fisicaro, F. Boccuzzi, A spectroscopic study of anatase properties, Zeitschrift Fur Phys. Chemie. 124 (1981) 211–222. https://doi.org/10.1524/zpch.1981.124.2.211.

[19] R. Wang, L. Chen, X. Zhang, Q. Zhang, Y. Li, C. Wang, L. Ma, Conversion of levulinic acid to γ-valerolactone over Ru/Al2O3-TiO2 catalyst under mild conditions, RSC Adv. 8 (2018) 40989–40995. https://doi.org/10.1039/C8RA07938B.

[20] W.E. Wallace, NIST Chemistry WebBook, NIST Standard Reference Database Number 69, (n.d.). https://doi.org/10.18434/T4D303.

[21] W. Tsai, W.H. Weinberg, Steady-state decomposition of ammonia on the ruthenium(001) surface, J. Phys. Chem. 91 (1987) 5302–5307. https://doi.org/10.1021/j100304a034.

[22] F. Hayashi, Y. Toda, Y. Kanie, M. Kitano, Y. Inoue, T. Yokoyama, M. Hara, H. Hosono, Ammonia decomposition by ruthenium nanoparticles loaded on inorganic electride C12A7:e-, Chem. Sci. 4 (2013) 3124–3130. https://doi.org/10.1039/c3sc50794g.

[23] A.W. Chester, E.G. Derouane, Zeolite Characterization and Catalysis: a tutorial, Springer, Dordrecht Heidelberg London New York, 2010. https://doi.org/10.1016/s1351-4180(10)70329-9.

[24] I. V. Shamanaev, I. V. Deliy, E.Y. Gerasimov, V.P. Pakharukova, E.G. Kodenev, P. V. Aleksandrov, G.A. Bukhtiyarova, Synergetic effect of Ni2P/SiO2 and γ-Al2O3 physical mixture in hydrodeoxygenation of methyl palmitate, Catalysts. 7 (2017) 19–24. https://doi.org/10.3390/catal7110329.

[25] P.K. Jain, Comment on “Thermal effects – an alternative mechanism for plasmon-assisted photocatalysis” by Y. Dubi, I. W. Un and Y. Sivan, Chem. Sci. , 2020, 11 , 5017, Chem. Sci. 11 (2020) 9022–9023. https://doi.org/10.1039/D0SC02914A.

[26] Y. Dubi, I.W. Un, Y. Sivan, Thermal effects – an alternative mechanism for plasmon-assisted photocatalysis, Chem. Sci. 11 (2020) 5017–5027. https://doi.org/10.1039/C9SC06480J.

[27] K. Li, J. Jianguo, S. Tian, F. Yan, Influence of Silica Types on Synthesis and Performance of Amine–Silica Hybrid Materials Used for CO2 Capture, J. Phys. Chem. C. (2014). https://doi.org/10.1021/jp408354r.

[28] M. Navlani-García, M. Martis, D. Lozano-Castelló, D. Cazorla-Amorós, K. Mori, H. Yamashita, Investigation of Pd nanoparticles supported on zeolites for hydrogen production from formic acid dehydrogenation, Catal. Sci. Technol. 5 (2015) 364–371. https://doi.org/10.1039/c4cy00667d.

[29] J. Araña, C. Garriga I Cabo, J.M. Doña-Rodríguez, O. González-Díaz, J.A. Herrera-Melián, J.

Pérez-Peña, FTIR study of formic acid interaction with TiO 2 and TiO 2 doped with Pd and Cu in photocatalytic processes, Appl. Surf. Sci. 239 (2004) 60–71. https://doi.org/10.1016/j.apsusc.2004.04.039.

[30] L.F. Liao, W.C. Wu, C.Y. Chen, J.L. Lin, Photooxidation of formic acid vs formate and ethanol vs ethoxy on TiO2 and effect of adsorbed water on the rates of formate and formic acid photooxidation, J. Phys. Chem. B. 105 (2001) 7678–7685. https://doi.org/10.1021/jp003541j.

[31] R.C. Millikan, K.S. Pitzer, The Infrared Spectra of Dimeric and Crystalline Formic Acid, J. Am. Chem. Soc. 80 (1958) 3515–3521. https://doi.org/10.1021/ja01547a007.

[32] T. Hou, Q. Luo, Q. Li, H. Zu, P. Cui, S. Chen, Y. Lin, J. Chen, X. Zheng, W. Zhu, S. Liang, J. Yang, L. Wang, Modulating oxygen coverage of Ti3C2Tx MXenes to boost catalytic activity for HCOOH dehydrogenation, Nat. Commun. 11 (2020). https://doi.org/10.1038/s41467-020-18091-7.

[33] R.C. Millikan, K.S. Pitzee, Infrared spectra and vibrational assignment of monomeric formic acid, J. Chem. Phys. 27 (1957) 1305–1308. https://doi.org/10.1063/1.1743996.

[34] J. Raskó, T. Kecskés, J. Kiss, Formaldehyde formation in the interaction of HCOOH with Pt supported on TiO2, J. Catal. (2004). https://doi.org/10.1016/j.jcat.2004.03.025.

[35] S.Y. Chin, C.T. Williams, M.D. Amiridis, FTIR studies of CO adsorption on Al2O3- and SiO 2-supported Ru catalysts, J. Phys. Chem. B. 110 (2006) 871–882. https://doi.org/10.1021/jp053908q.

CHAPTER 5: CO_2 Methanation over Ru based photothermal catalysts

Introduction

Photothermal heterogeneous CO_2 methanation has been reported as a potential emerging process that might boost the methane yield and improve the selectivity to methane in comparison with thermal catalysis [1,2] and photocatalysis. Following the work performed on the photothermal enhancement of gas phase formic acid dehydrogenation into hydrogen, this chapter is a short (preliminary) study investigating the ability of Ru-based catalysts to be also used as photothermal catalysts under UV-A light in a second reaction of interest, i.e. the photothermal CO_2 hydrogenation into methane.

First, methanation experiments are performed using Ru(5%)/TiO_2-P25 (PA) as our catalyst reference. The investigations are further extended mainly to Ru/g-C_3N_4 and Ru/SiO_2 catalysts, as well as to a span of commercially available titania materials used as supports for Ru nanoparticles.

1. Ru/TiO_2 (P25) as reference catalyst for the CO_2 photothermal methanation

As in the previous studies for the gas-phase decomposition of formic acid, Ru/TiO_2 (P25) is selected as reference catalyst for introducing the photothermal CO_2 methanation. After a series of screening experiments at different Ru loadings and gas flows, the Ru loading has been increased to 5 wt.% Ru to allow for a suited conversion of CO_2 and a sensitive detection of any potential reaction by-products (including CO and light oxygenated hydrocarbons if any).

1.1. Synthesis of the Ru(5%)/TiO_2 (P25) catalyst

The Ru(5%)/TiO_2-P25 catalyst was synthesized via the photo-assisted method described in Chapter 2 and already reported in Chapter 3 for Ru loadings till 1 wt.%, here with a synthesis time under UV-A light of 30 min. The sample is labelled as Ru(5%)/TiO_2-P25 (PA). **Fig. 84**A shows the evolution of the relative Ru precursor concentration in the dark and upon irradiation, with a similar trend than that previously reported for a Ru content of 0.5 wt.%. 15% of ruthenium precursor from aqueous dispersion of Titania P25 (10 % v/v methanol) was adsorbed on the TiO_2 surface without adjustment to pH 8, while the Ru precursor signal in UV-Vis spectrophotometry remained negligible at pH 8. ICP-AES results certified a ruthenium loading of 5.9 wt.% in the catalyst. TEM pictures, as the one shown in **Fig. 84**B, demonstrated the synthesis of well-dispersed, small size ruthenium nanoparticles at the titanium dioxide surface, with a mean diameter size of 0.8 ± 0.3 nm visualized in the histogram of the **Fig. 84**C, based on the statistical analysis of TEM images. The CO pulses chemisorption study confirmed (**Fig. 84**D) the high Ru dispersion at the support surface, with a 62 % of dispersion, with a crystallite size calculated from the dispersion value of 1.5 nm. Like previously mentioned in Chapter 3 for lower loadings, this difference finds its origin in the assumption used in the model, and the presence of oxidized ruthenium species surface at the surface of metallic Ru nanoparticles, that resulted from the natural surface passivation when exposed to air. X-ray photon spectroscopy confirmed the metallic and partially oxidized nature of the ruthenium species at the TiO_2-P25 support surface with a ratio of 68:32, respectively, as shown in **Fig. 84**E, with similar conclusion than for the lower loadings in the Chapter 3. Although the Ru loading increased from a magnitude order from the original 0.5 wt.% to 5

wt.%, no peaks assigned to the diffraction of Ru-based phases were observed in the X-Ray diffractograms as shown in **Fig. 84**F.

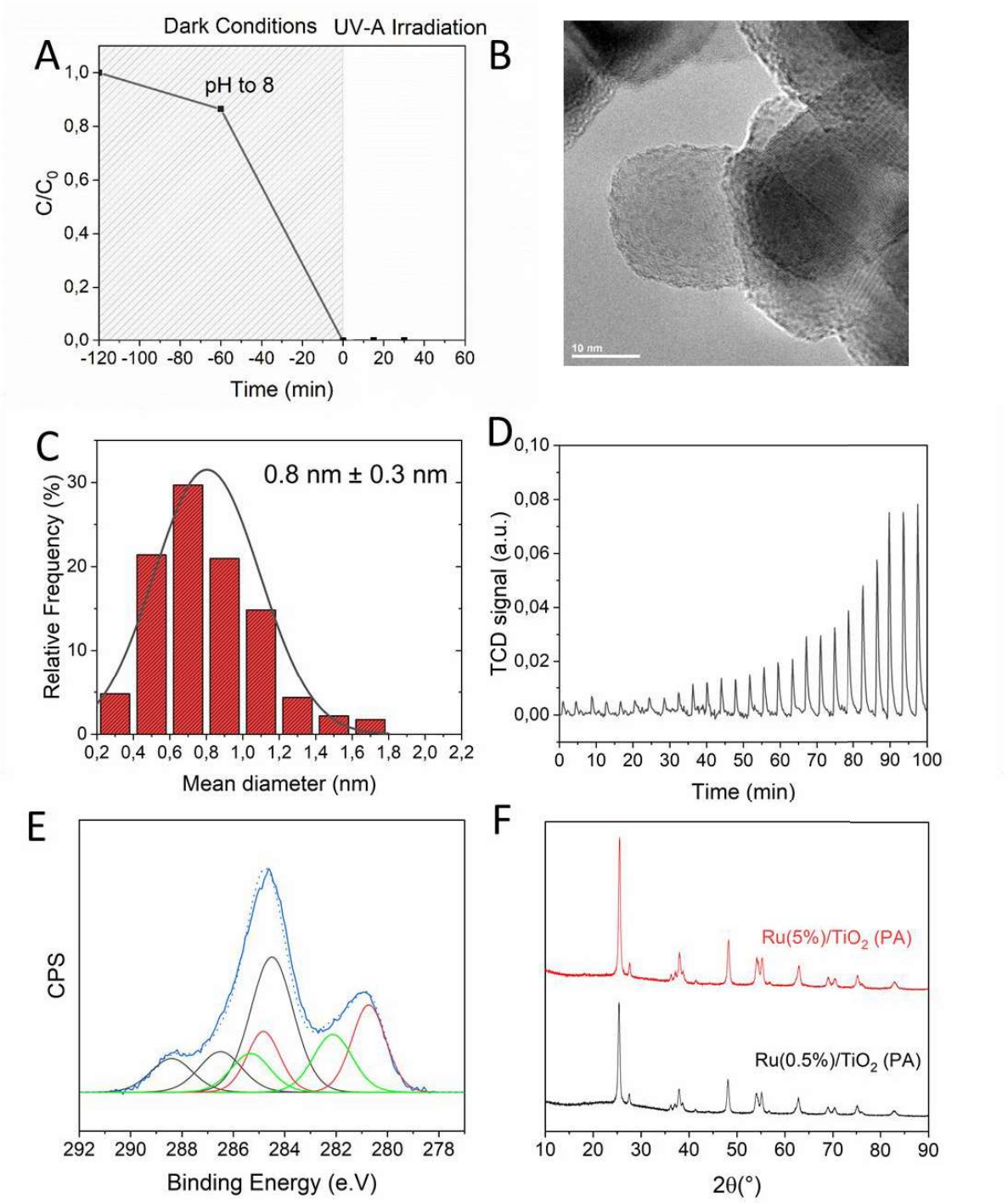

***Fig. 84 A**) Relative Ru precursor concentration during the photo-assisted synthesis of Ru nanoparticles at the TiO_2 surface, **B)** TEM image of the Ru(5%)/TiO_2-P25 (PA) catalyst, **C)** Ru nanoparticle size distribution histogram derived from the statistical analysis of TEM images (over 230 nanoparticles), **D)** TCD signal of the CO pulses during the chemisorption test, **E)** C1s + Ru 3d orbital XPS spectra where red: Ru^0 (3d); green: oxidized $Ru^{\delta+}$ (3d); black: multi-contribution envelope of adventious carbon (1s) and **F)** X-Ray diffractograms of Ru(0.5%)/TiO_2-P25 (PA) (black) and Ru(5%)/TiO_2-P25 (PA) (red).*

The Ru(5%)/TiO_2-P25 (PA) catalyst was submitted to a temperature-programmed reduction experiment as shown in **Fig. 85** in comparison with the Ru(0.5%)/TiO_2-P25 (PA) reference counterpart.

In both cases the as-synthesized catalysts were pre-treated under air at 200°C. It must be said that similar TPR patterns were obtained whatever the Ru wt.% content. At high temperature, similar peaks were obtained at 293°C and 364°C, which correspond to the desorption of methane, as a result from the Ru-catalyzed methanation of residual traces of CO_2 remaining adsorbed at the catalyst surface despite the pre-treatment applied, as it is evidenced on the mass spectrometry signals for m/z= 16 (production) and m/z=2 (consumption), corresponding to methane and H_2, respectively (**Fig. 85**B). At low temperature, the reduction peak recorded around 160°C (within the 75-220°C temperature range) for the ruthenium oxide species in both samples confirmed a rather similar Ru nanoparticle size distribution and similar interactions with the TiO_2 support, and we suggest that the catalysts differ only in terms of Ru content (0.5-5 wt.%), as visualized by the difference in signal intensity.

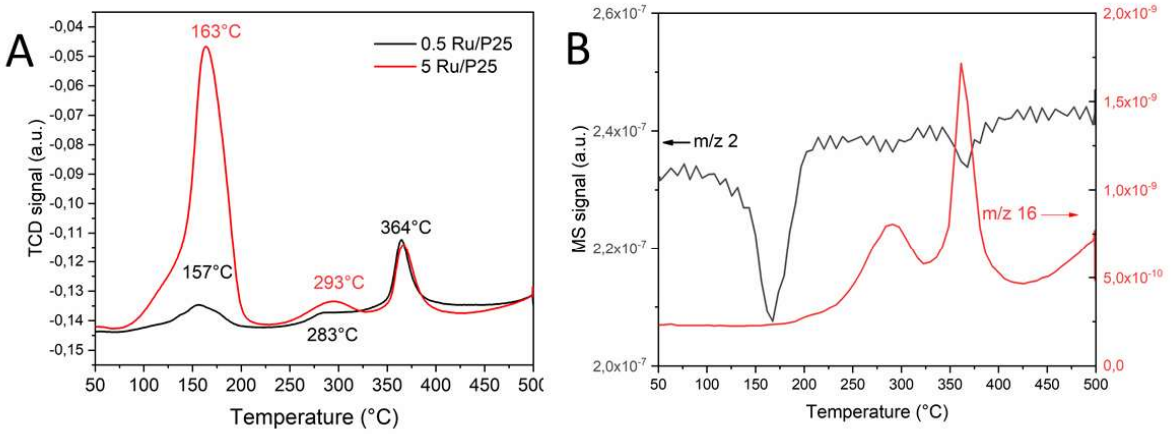

Fig. 85 (A) *TCD signal of the temperature-programmed reduction of both Ru(0.5%)/TiO_2 (PA) (black) and Ru(5%)/TiO_2 (PA) (red) catalysts after a slight oxidative pre-treatment at 200°C, and* ***(B)*** *both m/z 2 (black) and m/z 16 (red) signals that correspond to hydrogen and methane in MS, respectively, during the TPR of the Ru(5%)/TiO_2 (PA) sample.*

1.2. CO_2 methanation with 0.2 vol. % of CO_2 in Ar over the Ru/TiO_2 photothermal catalyst.

The first series of tests of CO_2 photothermal methanation were carried out with a gas concentration of CO_2 and H_2 in Ar flow at 0.2 $\%_{v/v}$ and 0.8 $\%_{v/v}$, respectively, corresponding to the stoichiometrical ratio 1:4. The aim here was to study the influence of the light irradiance within the 40-400 mW/cm^2 range on the catalytic yield to methane over the Ru/TiO_2 (PA) catalyst, as depicted in **Fig. 86**, and **in Fig. 87.** for the conversion. We demonstrated that a combined photonic/thermal excitation strongly enhanced both CO_2 conversion and yield to methane. No other reaction products were detected, and we can consider the reaction being fully selective to CH_4. This enhancement was remarkably visible at low temperature, for which both CO_2 conversion and yield to methane were very low at dark conditions. For instance, the CH_4 yield at 0.1 mmol $g^{-1}h^{-1}$ at 120°C at dark conditions, was increased to 2.4 mmol $g^{-1}h^{-1}$ under light at an irradiance of 400 mW/cm². A strong low-temperature shift was therefore observed. At higher temperatures, for which the conversion was already important, the enhancement was in consequence by far less pronounced.

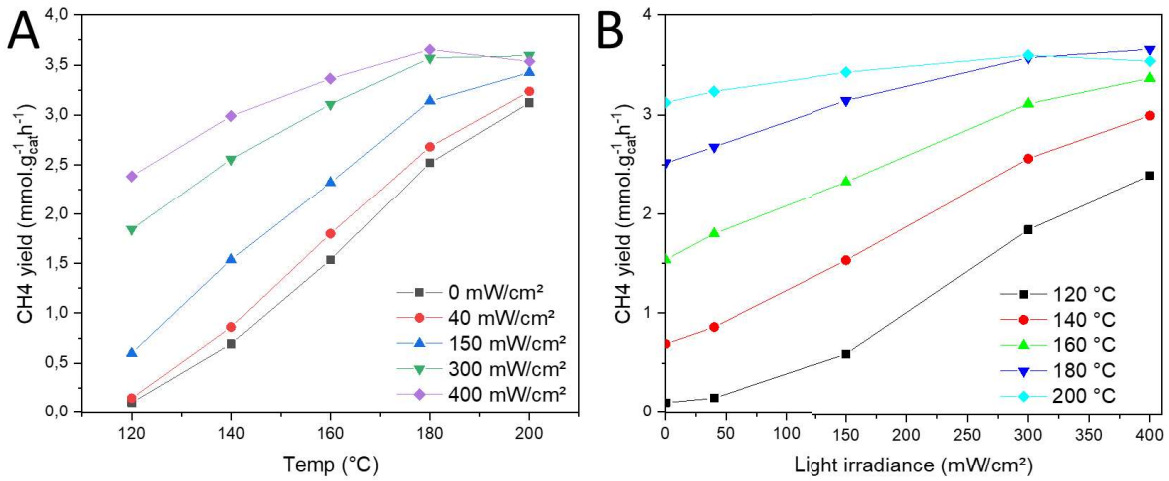

Fig. 86 *Methane yield from the CO_2 methanation over the Ru(5%)/TiO_2 (PA) catalyst with* ***(A)*** *temperature-dependency and* ***(B)*** *irradiance-dependency. Reaction conditions: [CO_2] = 2000 ppm_v, [H_2] = 8000 ppm_v total Ar flow of 5.8 mL/min, 5.0 mg of catalyst, CO_2 specific molar rate of 5.7 mmol g^{-1} h^{-1}.*

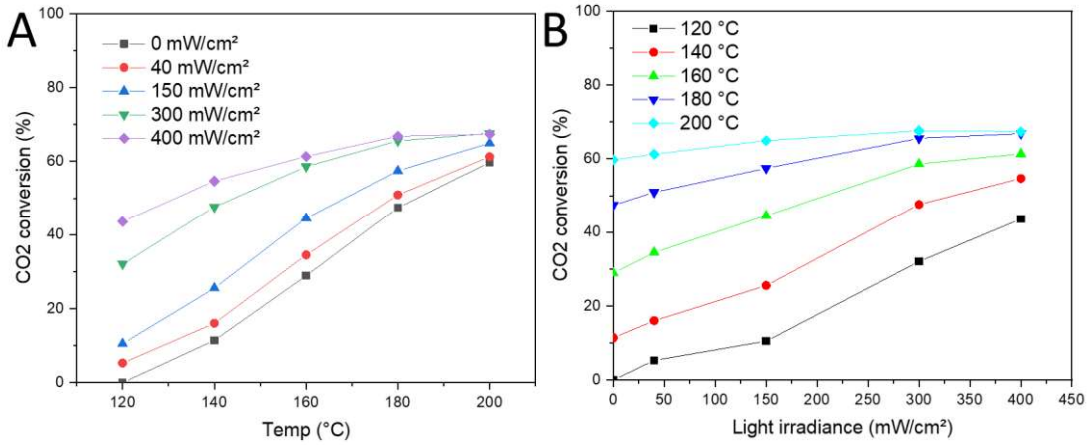

Fig. 87 *CO_2 conversion over the Ru (5%)/TiO_2 (PA) catalyst with* ***(A)*** *temperature-dependency and* ***(B)*** *irradiance-dependency. Reaction conditions: [CO_2] = 2000 ppm_v, [H_2] = 8000 ppm_v total Ar flow of 5.8 mL/min, 5.0 mg of catalyst, CO_2 specific molar rate of 5.7 mmol g^{-1} h^{-1}.*

The ratio between the consumed H_2 and CO_2 reactants is depicted in **Fig. 88**. The H_2/CO_2 consumed ratio was calculated to be ca. 3.9, independently of the light irradiance and of reaction temperature, in good agreement with the theoretical value of 4. The minor difference could be most probably attributed to the experimental error, rather than to the formation of traces of compounds that would require less hydrogen, like carbon, CO or HCOOH, as the difference remained relatively independent of the experimental conditions [3].

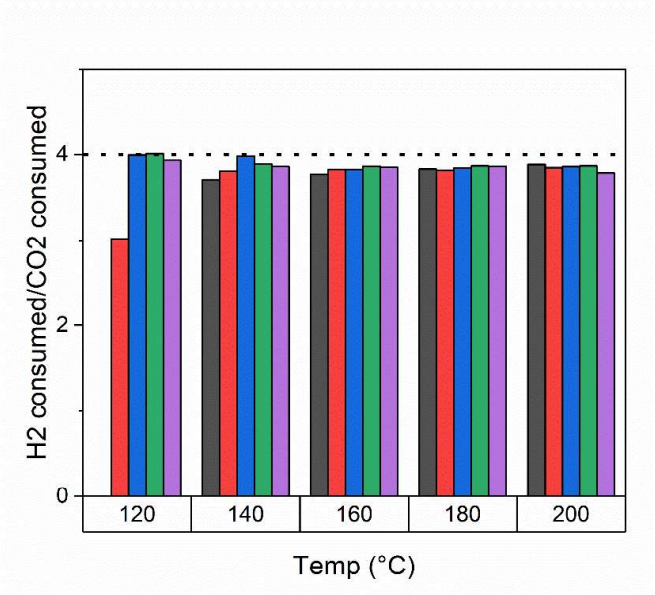

Fig. 88 *-The ratio between consumed H_2 and CO_2 in the CO_2 photothermal methanation over the Ru(5%)/TiO_2 (PA) catalyst. Reaction conditions: [CO_2] = 2000 ppm_v, [H_2] = 8000 ppm_v total Ar flow of 5.8 mL/min, 5.0 mg of catalyst, CO_2 specific molar rate of 5.7 mmol g^{-1} h^{-1}.*

Physical and chemical deactivation mechanisms have been reported for CO_2 methanation [4,5]. Among them, we can find the sintering of the catalyst by the metal agglomeration (which affects to the decrease of the active surface sites) [6,7] and the fouling (physical deposition and blocking of the active sites), in this case, by the carbon deposition [8]. This effect might be enhanced and favoured by the exothermicity of the reaction. To demonstrate that the light irradiation does not contribute to such mechanisms potentially already occurring at dark conditions, a preliminary study was conducted, in which the Ru(5%)/TiO_2 (PA) catalyst was tested again at dark conditions after having been previously tested at illuminating conditions for some hours.

Fig. 89 depicts the methane yield at dark conditions, obtained before (black) and after (red) irradiation at the maximum irradiance of 400 mW/cm², within the temperature range from 140°C to 200°C. It must be said that submitting the catalyst to the irradiation of 400 mW/cm² at different temperatures did not result in any significant change in the CH_4 yield at dark conditions. This suggested that the photonic excitation of the catalyst had only a positive effect on the catalytic activity. The excursion at high temperatures, especially for an exothermic reaction, can introduce catalyst changes in thermal catalysis (dark conditions), but we can suggest that performing the reaction under light also did not contribute additionally to those changes. By lowering the reaction temperature, and therefore allowing the catalyst to operate at a lower (bulk) reaction temperature, it can further reduce those negative (thermal) effects.

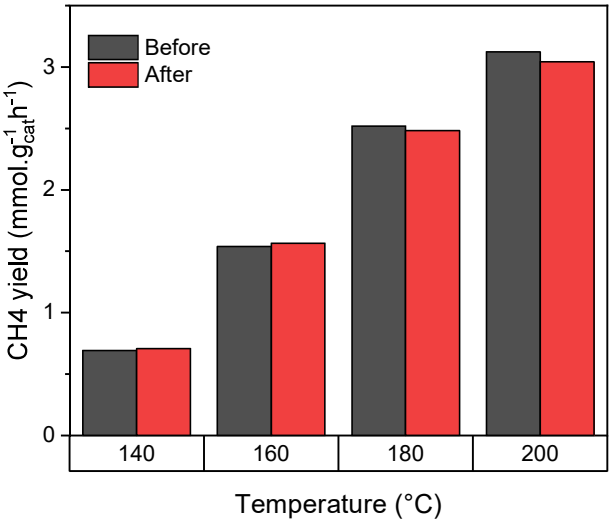

Fig. 89 *Methane yield obtained from the CO_2 hydrogenation over the Ru(5%)/TiO_2 (P25) (PA) catalyst at dark conditions before* ***(black)*** *and after* ***(red)*** *light irradiation. Reaction conditions: [CO_2] = 2000 ppm_v, [H_2] = 8000 ppm_v total Ar flow of 5.8 mL/min, 5.0 mg of catalyst, CO_2 specific molar rate of 5.7 mmol g^{-1} h^{-1}.*

The methane yields obtained were used for deriving the influence of the light irradiance on the Arrhenius plots and on the apparent activation energy, as shown in **Fig. 90**A and **Fig. 90**B. For the CO_2 methanation reaction on the Ru/TiO_2 catalyst, the graphs showed the positive influence of the photonic excitation to lower the apparent activation energy for the CH_4 formation, that linearly decreased from values around 40 kJ/mol under dark conditions down to less than 10 kJ/mol at 400 mW/cm² irradiance. We are aware that some values, in particular at high irradiances, remain relatively approximate.

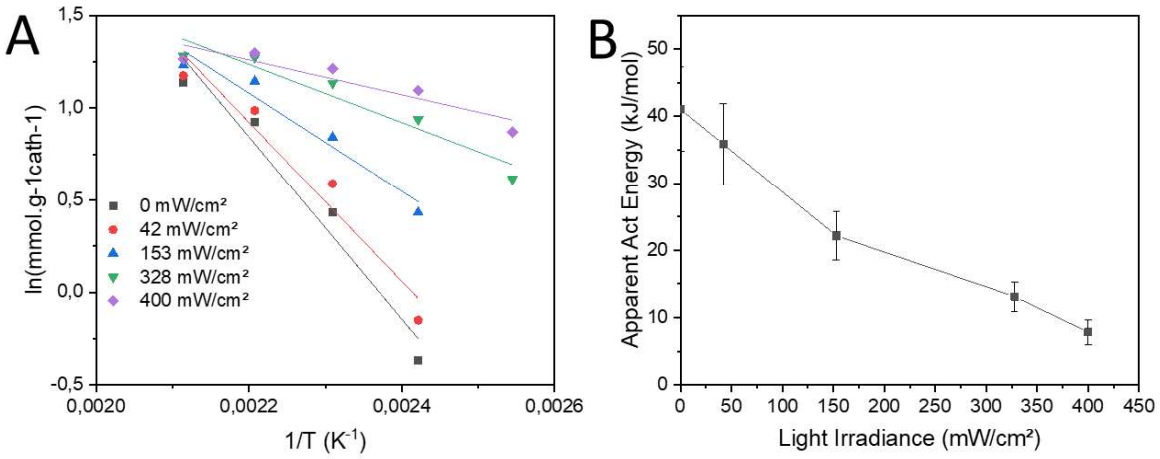

Fig. 90 (A) *Arrhenius plot for the methane yield obtained over the Ru(5%)/TiO_2 (PA) catalyst and* ***(B)*** *Light-dependency of the apparent activation energy of CO_2 conversion to CH_4. Reaction conditions: [CO_2] = 2000 ppm_v, [H_2] = 8000 ppm_v total Ar flow of 5.8 mL/min, 5.0 mg of catalyst, CO_2 specific molar rate of 5.7 mmol g^{-1} h^{-1}.*

The results obtained in this subsection demonstrated that Ru/TiO_2 can act as photothermal catalyst for the selective CO_2 conversion into methane.

1.3. Optimization of the CO_2 concentration in gas flow for methanation over Ru/TiO_2

This short subsection investigates to which extent the methane yield and the photothermal enhancement were influenced by the carbon dioxide concentration in the flow. In consequence, the photothermal methanation tests have been carried out with two other percentages of CO_2 (and H_2), namely with 2 and 20 $\%_{v/v}$ of carbon dioxide concentration in the flow. It is important to remark that initial hydrogen concentration in flow was always four folds that of carbon dioxide, i.e. with a stoichiometrical ratio. In this comparison, the influence of the light irradiance on the methane yield is shown under the three different conditions in **Fig. 91**. Higher values of methane yield were obtained at dark conditions with an inlet concentration of 2% CO_2 compared to 0.2% CO_2, with also a strong photothermal enhancement effect. Values approximately 10 times higher than at 0.2% CO_2 were achieved at maximum reaction conditions (T=200°C, I=400 mW/cm²), e.g. 33.1 $mmol_{CH4}\ g^{-1}h^{-1}$ vs. 3.5 $mmol_{CH4}\ g^{-1}h^{-1}$). Obviously this was accompanied by a drop in the overall conversion with the increase in the CO_2 concentration. Higher methane yields can be further achieved at the maximum CO_2 concentration of 20 $\%_v$ (and 80$\%_v$ H_2), also with a remarkable photothermal enhancement, reaching under 400 mW/cm² values of CH_4 production of 87.3 mmol g^{-1} h^{-1} and 341 mmol g^{-1} h^{-1} at 200°C and 240°C, respectively. However experiments in non-diluted reaction conditions were difficult to implement, due to the significant change in the molar flow composition, as four moles of hydrogen are used to convert one mole of CO_2 into one mole of methane and of water, as well as to the production of water in high amounts.

In consequence, we selected 2% as initial concentration of CO_2, and 8% of H_2, for the further experiments in CO_2 photothermal methanation.

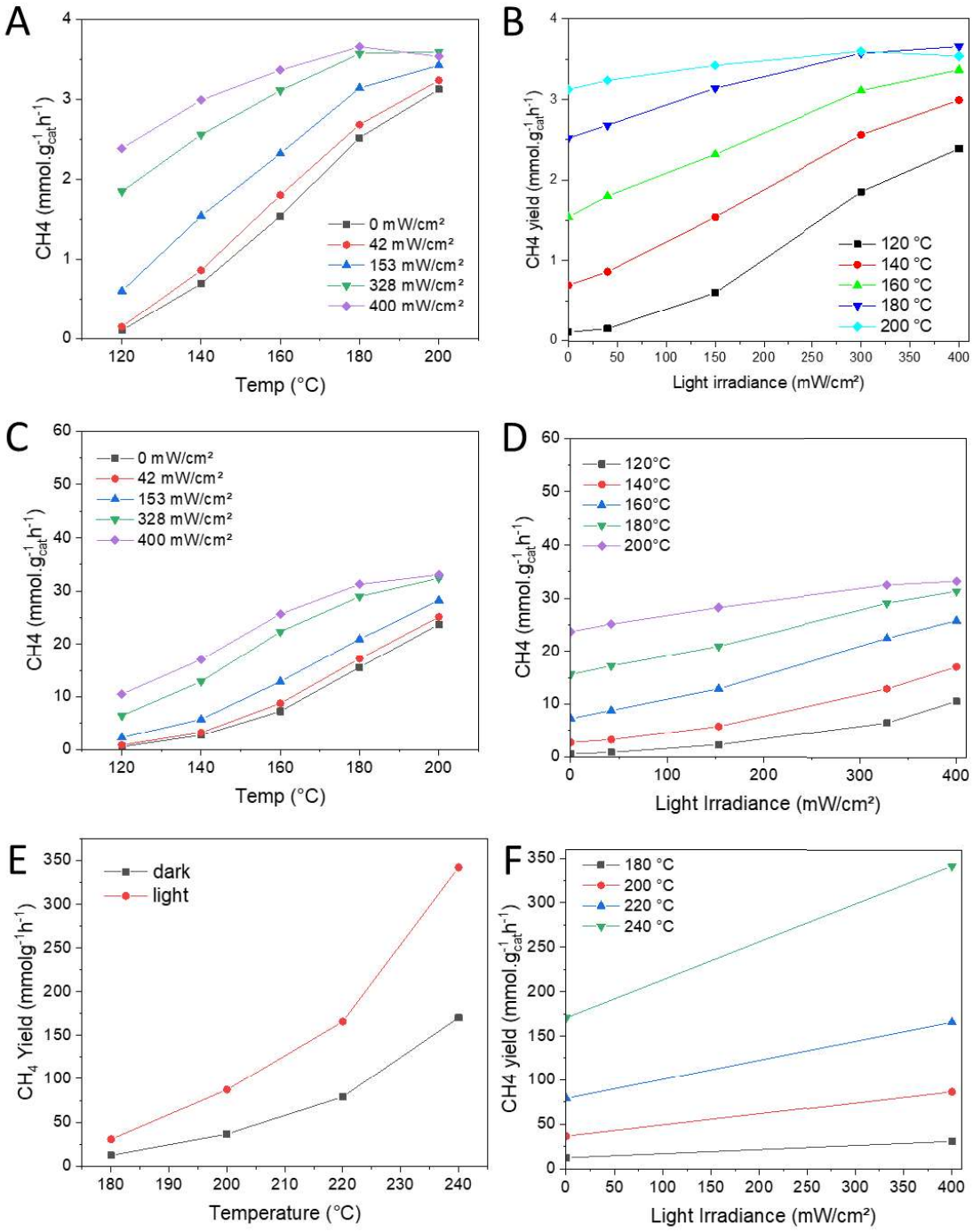

Fig. 91 *Influence on the methane yield of the light irradiance at different CO_2 concentrations in the flow: 0.2%$_v$ (**A,B**), 2% (**C,D**) and 20 % (**E,F**) with the Ru(5 %)/TiO_2 (PA) catalyst. Total flow around 5 mL/min, 5.0 mg of catalyst.*

2. Influence of the supports in the CO_2 photothermal methanation: g-C_3N_4 and SiO_2.

As we developed in the previous chapter for the photothermal formic acid decomposition, supported Ru particles on graphitic carbon nitride and SiO_2 can have influence on the selectivity and conversion features of the photo thermal reaction. In addition, g-C_3N_4 have been very recently reported as efficient support for CO_2 photothermal reduction in 2021 and 2022 (not necessarily for the methanation reaction) [9–11] as well as SiO_2 [12,13].

In this subsection, Ru/g-C_3N_4 and Ru/SiO_2 have been studied as photothermal catalysts for the CO_2 methanation. Both catalysts were prepared with the same ruthenium loading of 5 wt.%. Ru. Metallic Ru nanoparticles were synthesized on g-C_3N_4 by the UV-A driven photo-assisted method, and on SiO_2 via wet impregnation, as reported in Chapters 3 and 4.

In regards of the Ru nanoparticles synthesis onto the g-C_3N_4 surface, after a 2 h adsorption period in the dark to reach the adsorption/desorption equilibrium state at the carbon nitride surface (remaining value of 60%) and the subsequent adjustment of the pH value to 8 (remaining value of 12%), complete disappearance of the ruthenium precursor from the aqueous phase was observed after 2 h under UV-A light irradiation, as shown in **Fig. 92**A. TEM pictures shown in **Fig. 92**B demonstrated the presence of well-dispersed ruthenium particles on the graphitic carbon nitride, with a mean particle size of 1.8 nm and a standard deviation of 0.7 nm. **Fig. 92**C depicts the results of the TPR experiments (performed on the ruthenium species pre-oxidized at 200°C as in chapter 4) for Ru loadings of 0.5% and 5% on the g-C_3N_4 support. At low temperature, similar patterns are obtained for the TCD signal, with the main difference that the reduction peak is more visible due to the higher loading and therefore is better separated from the foot of the peak corresponding to methane formation (around 175°C). The methane formation might here be observed at slightly lower temperature due to the higher Ru content that acts as catalyst. Moreover, X-ray photon spectroscopy has been performed on the Ru(5%)/g-C_3N_4 catalyst, as shown in **Fig. 92**D. A similar pattern for the Ru3d and C1s orbitals region has been observed in comparison to that of the catalyst loading with 0.5 wt.%, the main peak of Ru^0 being observed at a binding energy of 280.8 eV, which is common when Ru nanoparticles are synthesized on g-C_3N_4 by the photo-assisted synthesis method. It must be said that performing XPS on the sample after TPR revealed a shift of main Ru^0 peak to lower binding energies values, at 280.3 eV. This suggested that the metal-support interaction was probably strengthen during the overall reduction profile process at higher temperatures (till 500°C).

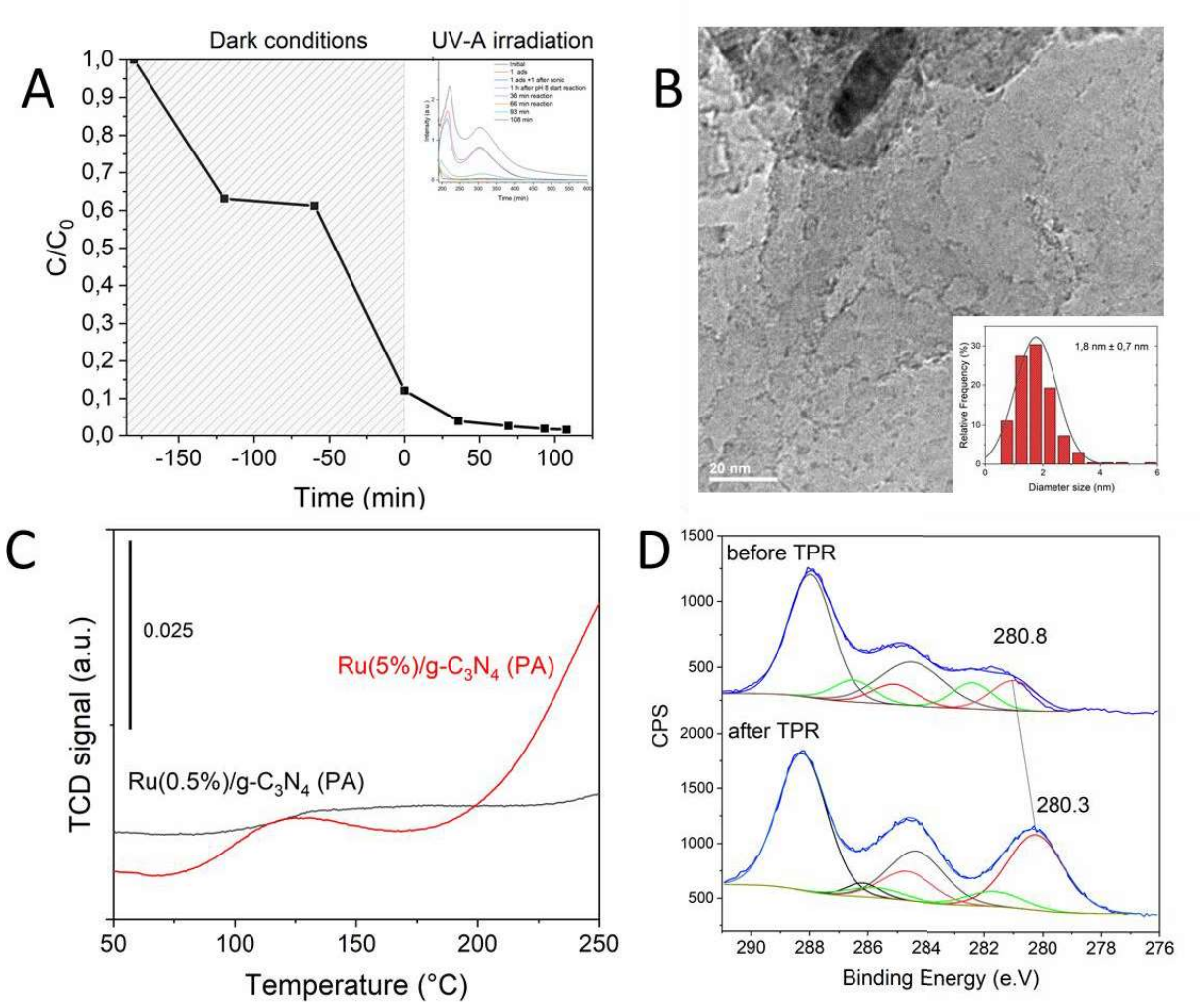

Fig. 92 (A) *Evolution with time of the relative Ru precursor concentration in the suspension during the photo-assisted synthesis of the Ru(5%)/g-C_3N_4 catalyst ;* ***(B)*** *TEM image of Ru(5%)/g-C_3N_4 (PA) catalyst with the Ru nanoparticle size distribution histogram after statistical analysis of the images (over 250 nanoparticles) ;* ***C)*** *TPR of Ru(0.5%)/g-C_3N_4 (PA) (black) and Ru(5%)/g-C_3N_4 (PA) (red) and* **D)** *X-ray photon spectroscopy before (top) and after (bottom) TPR: C1s + Ru 3d orbitals with red: Ru^0 (3d); green: oxidized $Ru^{\delta+}$ (3d); black: C 1s carbon species, with contributions corresponding to both adventious carbon at low binding energy and to the g-C3N4 surface at higher binding energy.*

The Ru/SiO_2 catalyst was synthesized by classical wet impregnation method at 500°C in pure hydrogen flow. TEM pictures in **Fig. 93** demonstrated ruthenium nanoparticles on amorphous silica with a uniform dispersion over the surface. A mean particle size was determined by the statistical analysis with 1.5 ± 0.6 nm.

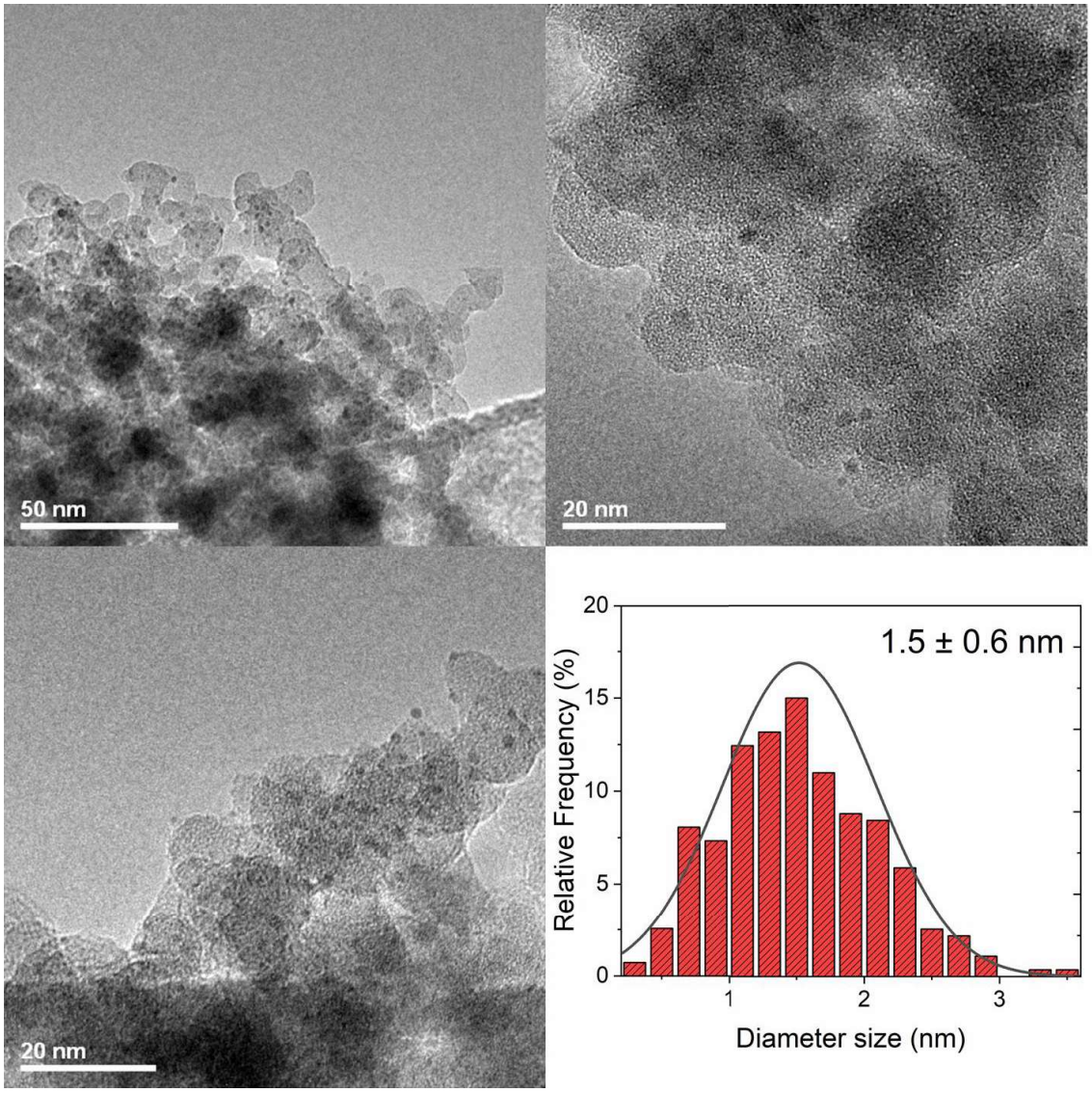

Fig. 93 *TEM images of the Ru(5%)/SiO_2 (WI) catalyst with the Ru nanoparticle size distriubtion histogram derived from the statistical analysis of the images (over 270 nanoparticles).*

Fig. 94 and **Fig. 95**. depict the influence of the light irradiance at different temperatures for the CO_2 methanation on both Ru/g-C_3N_4 and Ru/SiO_2 catalysts, expressed in terms of yield to methane and CO_2 conversion, respectively. First, it was shown that both catalysts exhibited similar activity at dark conditions over the whole range of temperatures tested, as it is shown in **Fig. 94**A and **Fig. 95**A. But they were characterized by very low conversions and CH_4 yields compared to the reference Ru/TiO_2 catalyst. For instance, no production of CH_4 was obtained in the dark for temperatures lower than 160°C, and the high temperature of 200°C was requested to get a CH_4 yield of 0.7 mmol $g^{-1}h^{-1}$ vs. 23.7 mmol $g^{-1}h^{-1}$ for the reference system. This explained why the temperature range was extended till 240°C in those tests. No other reaction products than CH_4 were observed.

However, both catalysts exhibited a different behavior upon illumination (**Fig. 94**B and **Fig. 95**B). Indeed, the Ru/g-C_3N_4 catalyst displayed only a moderate enhancement of the CH_4 yield under irradiation in comparison to the performances in the dark, even at the maximum irradiance of 400 mW/cm². For instance, the production of methane slightly increased from 0.7 mmol $g^{-1}h^{-1}$ at 200°C up to 1.2 mmol $g^{-1}h^{-1}$ at 400 mW/cm². By contrast, a significant enhancement was observed for the

Ru/SiO_2 catalyst in photothermal conditions, although we have to stress that the CH_4 yield and the CO_2 conversion remained low in comparison to the reference Ru/TiO_2 counterpart. Production of methane is in consequence observable at a lower temperature, while at 200°C, it increased from 0.7 mmol $g^{-1}h^{-1}$ up to 3.1 mmol $g^{-1}h^{-1}$ at 400 mW/cm². At illuminating conditions, no formation of additional products was observed, and the reaction was considered to be selective in photothermal conditions.

A similar behavior was observed for the CO_2 conversion, but with a lower accuracy of the measurement, as the CO_2 conversion remained globally low. In consequence, the evolution of the methane yield was more suited for expressing the influence of the light irradiance and deriving the apparent activation energies from the Arrhenius plots at dark and illuminating conditions, as shown in **Fig. 96**A and **Fig. 96**B for the $Ru/g\text{-}C_3N_4$ and Ru/SiO_2 catalysts, respectively.

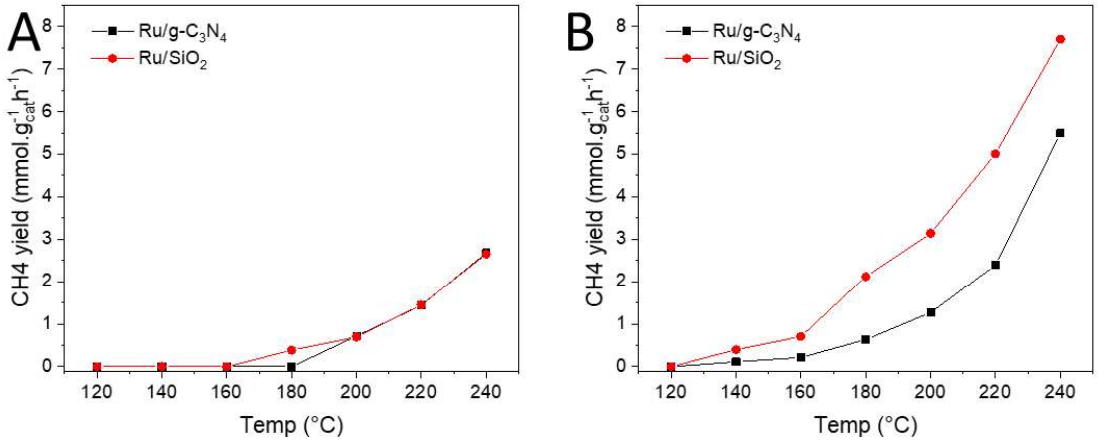

Fig. 94 *Influence of the light on the methane yield of the CO_2 methanation over the Ru(5%)/g-C_3N_4 (PA) (black) and Ru(5%)/SiO_2 (WI) (red) catalysts.* ***(A)*** *dark and* ***(B)*** *light (I=400 mW/cm²) conditions. Reaction conditions: [CO_2] = 2 %ᵥ, [H_2] = 8 %ᵥ total Ar flow of 5.2 mL/min, 5.0 mg of catalyst. CO_2 specific molar rate of 48.5 mmol g^{-1} h^{-1}.*

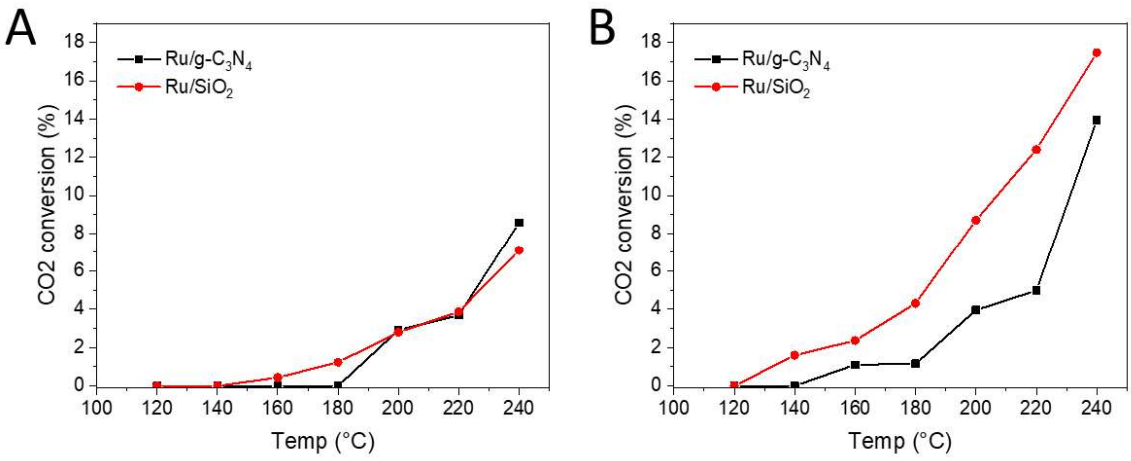

Fig. 95 *Influence of the light on the CO_2 conversion obtained over the Ru(5%)/g-C_3N_4 (PA) (black) and Ru(5%)/SiO_2 (WI) (red) catalysts.* ***(A)*** *dark and* ***(B)*** *light (I=400 mW/cm²) conditions. Reaction conditions: [CO_2] = 2 %ᵥ, [H_2] = 8 %ᵥ total Ar flow of 5.2 mL/min, 5.0 mg of catalyst. CO_2 specific molar rate of 48.5 mmol g^{-1} h^{-1}.*

Both Ru/g-C_3N_4 and Ru/SiO_2 catalysts differentiate in regards of the influence of the light irradiance on the apparent activation energy. For the Ru/SiO_2 catalyst, a decrease from 63 kJ/mol to 41.9 kJ/mol under maximum illuminating conditions was observed, however, this decrease remained moderate upon irradiation in comparison to that obtained with the Ru/TiO_2 reference catalyst. By contrast, although a small (but observable) enhancement was obtained under combined photonic/thermal excitation in the case of the Ru/g-C_3N_4 catalyst, no change was observed in terms of apparent activation energy between dark and illuminating conditions. Therefore, we suggest that the process where light plays a role over these two catalysts might be different. For instance, Zhang and co-workers observed something similar over Au/CeO_2 in the photothermal reverse-water-gas-shift reaction [14]. They observed that the CO_2 conversion into CO had the same Arrhenius plot slope under dark conditions than when the catalyst was irradiated despite the CO_2 conversion was 14 times higher under light. They proposed that this could be related to a different hydrogen dissociation mechanism under light vs. dark conditions, rather than to the carbon dioxide activation. They suggested that H_2 is much more easily dissociated over the metal surface through a photon-induced mechanism, in consequence enhancing the production of CO from CO_2.

Since the particle sizes over both materials were similar, we might correlate this phenomenon to the support influence (including different Ru-support interfaces) and the different ways that CO_2 and H_2 could be adsorbed onto the catalytic surface. Furthermore, additional analysis must be done over these catalysts to obtain a more clear conclusion about the mechanism.

Here we can also propose that the Ru/g-C_3N_4 catalyst is subjected to a thermal-driven mechanism, as the thermalization of hot carriers is reported not to lead to any changes in the apparent activation energy of the reaction.

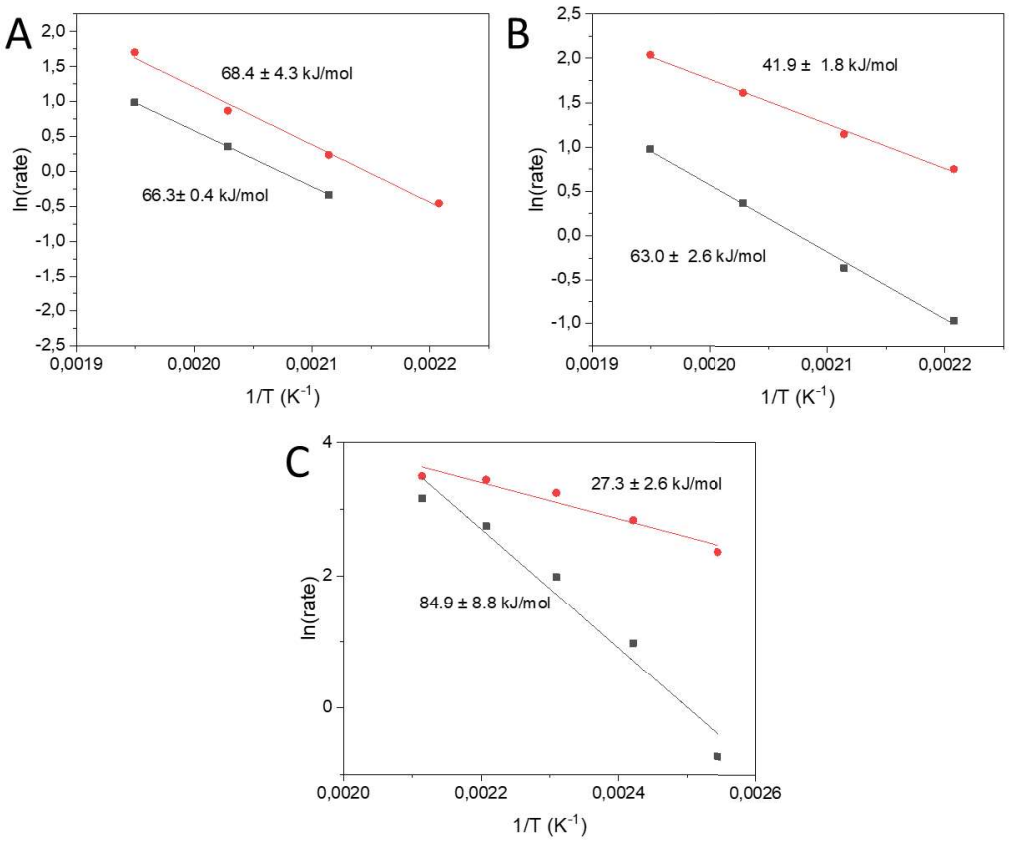

Fig. 96 *Arrhenius plot graphs for the methane yield obtained over the Ru/g-C_3N_4* ***(A)****, Ru/SiO_2* ***(B)*** *and Ru/TiO_2* ***(C)*** *catalysts. Reaction conditions: [CO_2] = 2 %$_v$, [H_2] = 8 %$_v$ total Ar flow of 5.2mL/min, 5.0 mg of catalyst. CO_2 specific molar rate of 48.5 mmol g^{-1} h^{-1}.*

2.1. CO_2 methanation over the Ru/CeO_2 photothermal catalyst.

In addition to Ru/TiO_2, Ru/g-C_3N_4 and Ru/SiO_2 catalysts, for which the observed photothermal effect benefitted to the CO_2 conversion and CH_4 yield with no change in terms of CH_4 selectivity (100%), CeO_2 (ceria) was also tested as support for ruthenium nanoparticles to investigated to which extent the selectivity pattern might also be influence by the combined photonic/thermal excitation. Indeed, itis a known support for CO_2 conversion in thermal catalysis [15–17] and also recently in photothermal catalysis [14,18,19], that can lead to CO production.

A Ru/CeO_2 catalyst has been prepared via the UV-A light driven photo-assisted synthesis method, with a UV-A irradiation of 2 h. A protocol similar to that used for other supports was implemented. Using CeO_2 (HSA 5, Solvay), a Ru content of 3.1 wt.% was obtained.

Fig. 97 depicts the influence of the light on the catalytic CO_2 methanation over the Ru/CeO_2 catalyst. There is a clear evidence of the CO_2 conversion enhancement under light irradiation, reaching values at 240°C of 37.8% vs. 5.0 % at dark conditions. The photothermal enhancement was very pronounced for the formation of methane, and remained more limited for the CO formation, with values increasing from 2.8 $mmol_{CH4}$ $g^{-1}h^{-1}$ to 16.8 $mmol_{CH4}$ $g^{-1}h^{-1}$ at 240°C under light in comparison to the small increase from 0.5 mmol $g^{-1}h^{-1}$ to 1.2 mmol $g^{-1}h^{-1}$ for the CO production. At dark conditions, conversions were observed for temperatures higher than 200°C, with a selectivity largely towards the methane product, reaching values in the 85-97% range, CO being formed in relatively small proportion. By contrast, a low

selectivity to methane was observed under light at a low temperature (140-160°C), i.e. 40-45%, CO being formed as secondary product ; the selectivity to methane under light increased with the temperature for reaching approximatively similar values at higher temperatures than those obtained at dark conditions, or even slightly higher at 240°C (94%).

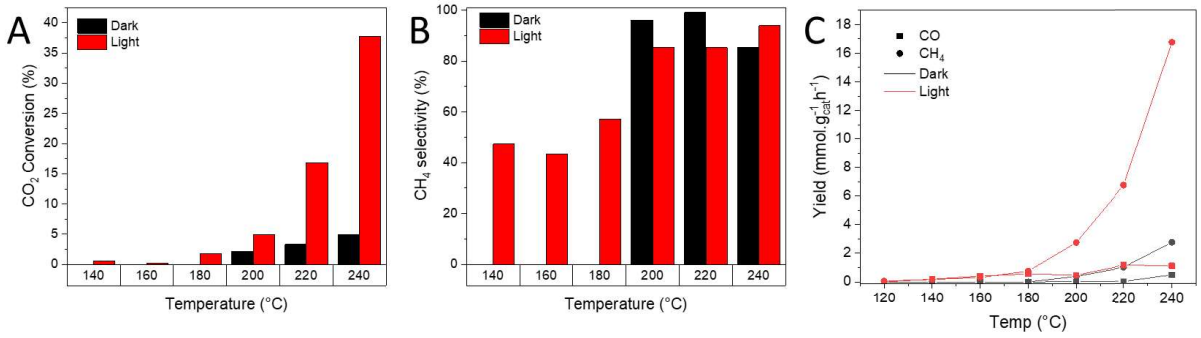

Fig. 97 *Influence of the light on* ***(A)*** *CO_2 conversion and* ***(B)*** *CH_4 selectivity in the CO_2 methanation over Ru(5%)/CeO_2 as photothermal catalyst.* ***(C)*** *Yields to methane (square) and CO (circle) obtained under dark (black) and light (red) conditions. Reaction conditions: [CO_2] = 2 %$_v$, [H_2] = 8 %$_v$ total Ar flow of 5.2 mL/min, 5.0 mg of catalyst, (I=400 mW/cm²). CO_2 specific molar rate of 48.5 mmol g^{-1} h^{-1}.*

The influence of the light on the apparent activation energy for the yield to methane was obtained from the Arrhenius plot shown in **Fig. 98**. Similar values were obtained at dark and light conditions around 93-99 kJ/mol, although a significant improvement was observed in terms of methane yield upon irradiation. By analogy with the results obtained by with Zhang and co-workers on Au/CeO_2 [14], this may indicate an enhancement of the H_2 dissociation on the Ru metal under light irradiation rather than an effect in key-limiting step or CO_2 activation. The occurrence of a thermalization mechanism is however also possible.

Many factors may explain the difference in activity and selectivity over this catalyst, that behaves differently in comparison to the others, such as e.g. the reactant adsorption, the role of oxygen vacancies [15,17], as well as different mechanisms enhanced by the light irradiation, etc. For instance, other parameters as support-metal interaction or H spillover can affect to the catalytic properties on Ru/CeO_2 [16]. Jiang and co-workers suggested that the CO_2 methanation enhancement over Ru/CeO_2 under light conditions could result from a possible photo-generated electron migration from the ceria to the ruthenium. This migration would increase the electron density at the metal surface and facilitates the H_2 dissociation. Then, H atoms could migrate to the ceria surface promoting the oxygen vacancies that facilitates the CO_2 dissociation [19]. In another study with 1.5 wt.% Ru/CeO_2, Quan et al. observed an improvement of the CO_2 hydrogenation being 6 times higher under Xe lamp light irradiation at 160°C than in dark conditions, this enhancement being assigned to the photon absorption of the metal oxide that promotes the activation of intermediates and overcome the energy barrier to the following conversion [18].

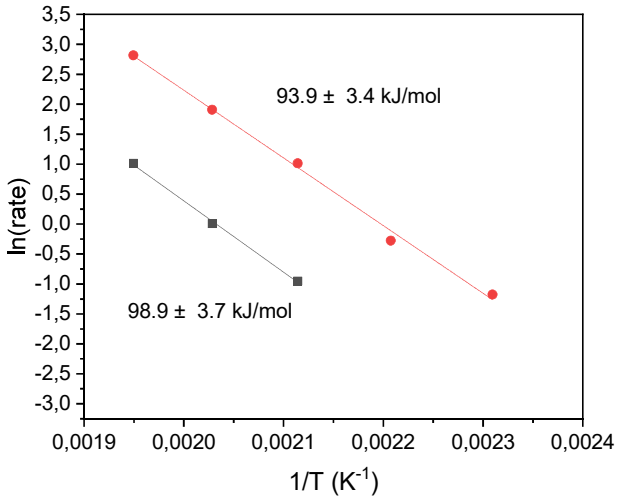

Fig. 98 *Influence of the light on the Arrhenius plot for the methane yield obtained over the Ru/CeO_2 catalyst under dark (black) and light (red) conditions (irradiance of 400 mW/cm²). Reaction conditions: [CO_2] = 2 %$_v$, [H_2] = 8 %$_v$ total Ar flow of 5.2 mL/min, 5.0 mg of catalyst. CO_2 specific molar rate of 48.5 mmol g^{-1} h^{-1}.*

The superiority of the Ru/TiO_2 photothermal catalyst in comparison to the Ru/g-C_3N_4, Ru/SiO_2 or Ru/CeO_2 catalysts, with e.g. 31.3 $mmol_{CH4}$ g^{-1} h^{-1} obtained at 180°C at 400 mW/cm² irradiance with a CO_2 conversion of 66%, led us to investigate in the next section to which extent the nature of the TiO_2 support might play a role for improving the performances and the photothermal effect. r

3. Influence of the TiO_2 nature in Ru/TiO_2 photothermal catalysts.

3.1. The TiO_2 supports

A wide span of commercially-available TiO_2 materials has been used as support for the Ru nanoparticles in this study: Hombikat UV-100 (Sachtleben Chemie GmbH), Aeroxide TiO_2 P90 and P25 (Degussa-Evonick) and TiO_2 MPT-625 (Ishihara Sangyo Kaisha, ISK). The main physico-chemical properties of the TiO_2 supports used are listed In **Table 10** and their XRD patterns are shown in **Fig. 99**. The TiO_2 supports differ in terms of phase composition, average crystallite size, as well as with regard to the specific surface area. It has to be mentioned that the phase composition corresponds to the composition among the crystalline TiO_2 phases, and differs from pure anatase for UV-100 to pure rutile phase for MPT-625, the P25 and P90 being TiO_2 with mixed anatase-rutile phases, with an approximate ratio of 80:20 and 90:10, respectively. No brookite phases were observed in any commercial TiO_2 sample. BET specific surface areas were ranging from 56 m^2/g to 330 m^2/g, in relationship with the average crystallite size. Difference in the amorphous content was also observed, within the 7-30% range, as determined by the approximate methods used by the group of Lillo-Rodenas and Roman-Martinez for TiO_2 samples [20].

Fig. 100A and **Fig. 100**B show the UV-Vis spectroscopy results as absorption spectrogram and as Tauc plot using the Kubelka-Munk function, respectively. Taking into account the accuracy of the measurements, the main difference lies in the slight red-shift of the absorption edge for the TiO_2 MPT625 sample that is composed of pure rutile phase, in comparison to the TiO_2 supports composed

of pure anatase or of anatase as majority phase. The corresponding bandgap values determined from the Tauc plots are collected in **Table 10**, in agreement with the phase composition, the narrowest bandgap being for the rutile MPT-625 (3.0 eV), and the others composed of (mainly) anatase being at ca. 3.2. eV.

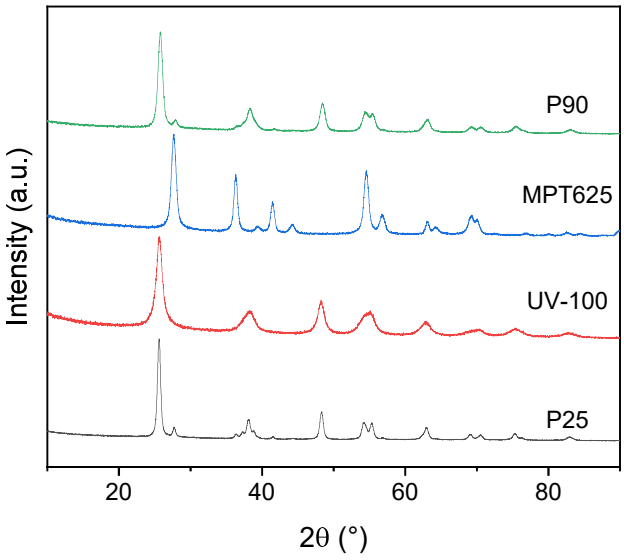

Fig. 99 *X-Ray diffractograms of the different commercial TiO_2 materials used as supports for the Ru nanoparticles. The XRD patterns have been normalized to the intensity of the (101) diffraction peak of the anatase phase at 25.7°.*

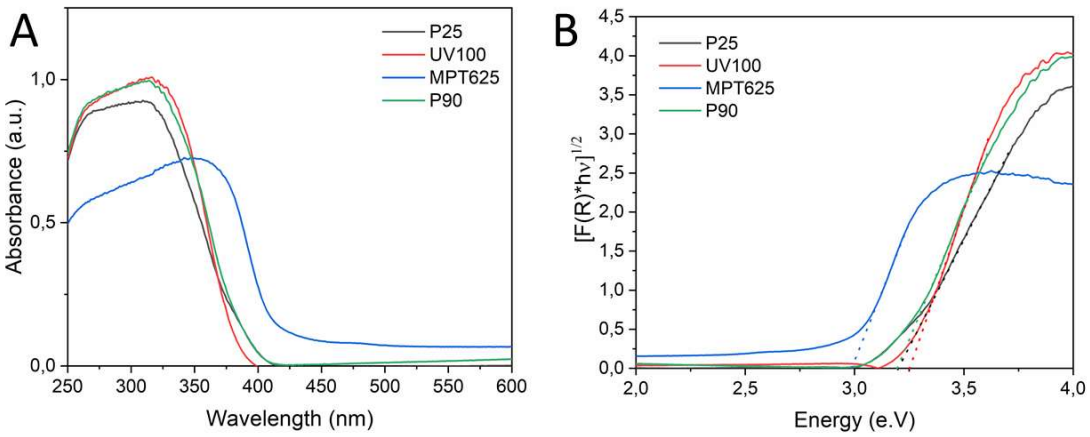

Fig. 100 (A) *UV-Vis spectra of the different commercial titanium dioxide and* ***(B)*** *Corresponding plots used to estimate the band gap of the materials using the K-M function (F(r)), considering TiO_2 as indirect semiconductor.*

TiO_2	Bandgap (eV)	Anatase:Rutile [1]	Amorphous phase [%] [2]	Average crystallite size [nm] [3]	SSA (m^2/g)
P25	3.2	80:20	7	32 (A) : 22 (R)	56
UV100	3.2(5)	100:0	26	9 (A)	330
MPT-625	3.0	0:100	10	10 (R)	103
P90	3.2	90:10	29	13 (A) : 23 (R)	90

Table 10 *Main physico-chemical properties of the TiO_2 used as supports for the Ru nanoparticles.*

***1** the phase composition corresponds to the composition within the crystallized TiO_2 phases (without considering the amorphous TiO_2) ; **2** determined by using the method developed by the group of Lillo-Rodenas and Roman-Martinez* [20]*; **3** determined by applying the Scherrer equation to the (101) and (110) peaks of anatase and rutile, at 25.7° and 27.5°, respectively, A and R representing the anatase and rutile content in the TiO_2 phase composition, respectively.*

Fig. 101 depicts the CO_2 adsorption measurements onto the different titanium dioxide materials after a previous dehydration treatment at 400°C under Ar flow. The band patterns recorded under diluted 10% CO_2/Ar with a flow rate of 5.5 ml/min, were in agreement with the species and the adsorption configuration reported in the literature, and collected in **Table 11**. In general, there is a good match between the specific surface area of the materials and the band intensity for the CO_2 adsorption, the larger the absorbance, the higher the specific surface area. Adsorption modes were observed as monodentate carbonates and bicarbonates, as well as monodentate bicarbonates.

At highest wavenumber values, a band with a maximum absorbance at 1673 cm^{-1} were detected on P90 and P25 materials. As it is explained it corresponds to the presence of bonded bidentate bicarbonates species [21]. However, these species were less clearly detected on pure anatase (UV100) or pure rutile (MPT625), what suggests that these species are favourable onto anatase/rutile frontiers. In addition, these species bands have a high absorbance in particular on P25, whose anatase/rutile interphases are more frequent in the surface as its composition of anatase:rutile is 80:20.

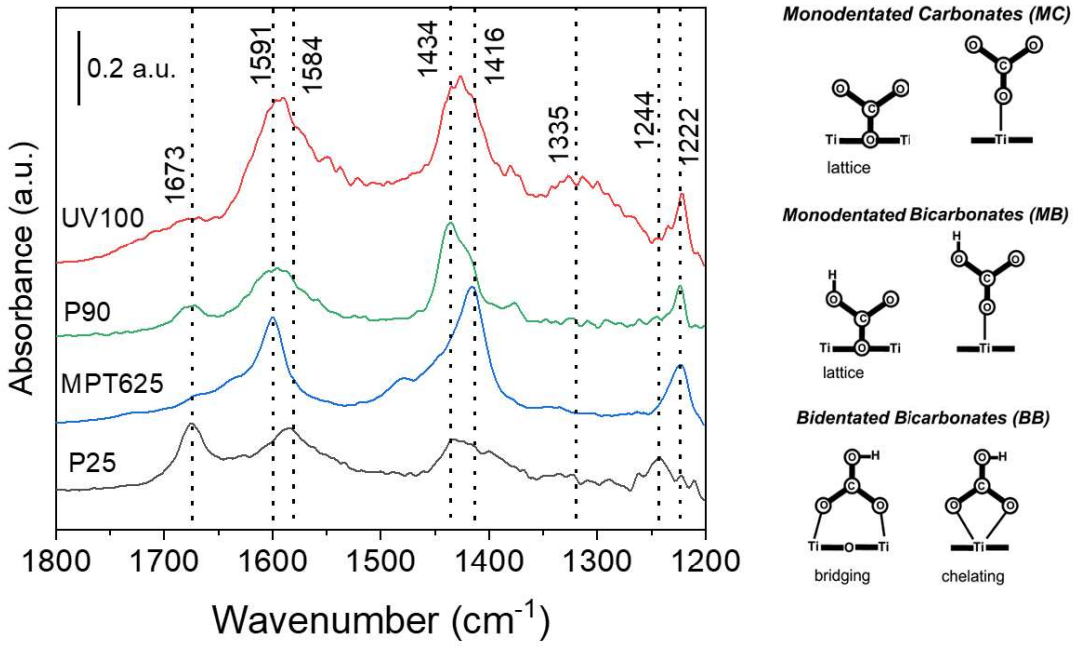

***Fig. 101** DRIFT spectra recorded under continuous gas flow of 10% CO_2/Ar (5.5 ml/min) over the different titanium dioxide materials. **(right)** drawings of the species and adsorption configurations on the TiO_2 surface based on the ref* [21].

Band wavenumber (cm^{-1})	Carbon species assigned
1673	Monodentate bicarbonates
1591-1584	Monodentate carbonates
1434-1416	Bidentate bicarbonates
1244	Monodentate bicarbonates
1222	Bidentate bicarbonates

***Table 11.** Main absorption bands and carbon species assigned in refs [21, 22] during CO_2 adsorption over TiO_2 followed by DRIFTS analysis.*

CO_2-TPD experiments (**Fig. 102**A) have been carried out with bare TiO_2 materials as it was described in the previous chapters. In all the samples, a main CO_2 desorption peak was observed by MS at low temperature around 150°C. UV100 was the titania sample that desorbed the largest quantity of CO_2 in in comparison with the other titanium dioxide materials, as a result of its higher specific surface area. All samples were pre-treated at 300°C before the analysis to clean the surface, so the higher temperature m/z=44 signal was not assigned to CO_2 desorption from the measurement, but might find its origin in the oxidative cleaning of the TiO_2 surface, that requires higher temperatures than 300°C. However, those values remained low.

In addition, a similar procedure have been implemented by DRIFT Spectroscopy on UV100 as shown in **Fig. 102**B. Tuning the temperature from room temperature until 500°C as maximum temperature of work of the DRIFTS set-up, it was possible to observe the negative absorbance values at 1586 cm^{-1} and 1426 cm^{-1} wavenumbers. These bands are assigned to mono- and bidentate bicarbonates species, respectively, being easier desorbed the bicarbonates in monodentate vs. bidentate configuration.

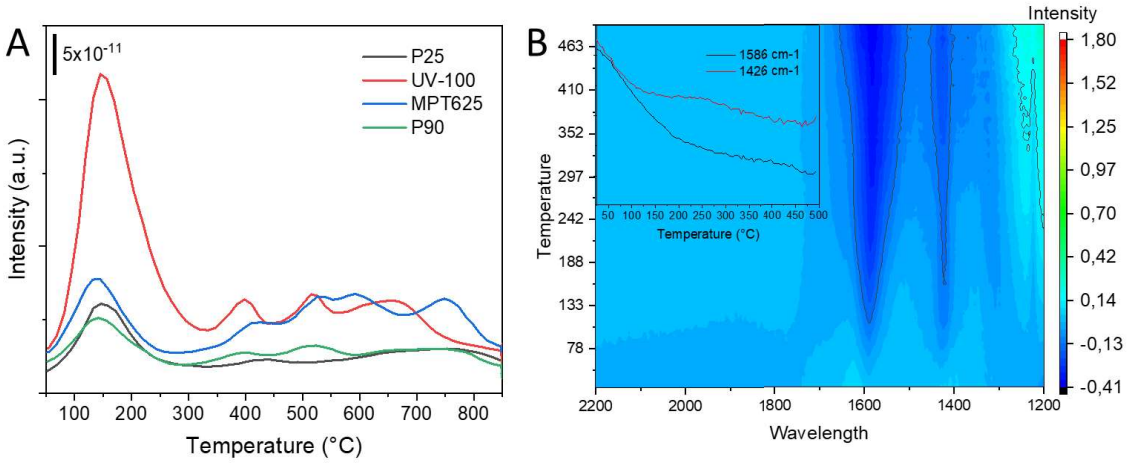

Fig. 102 *CO_2 desorption tests over TiO_2 commercial materials **A**) by CO_2-TPD and **B**) by DRIFT (only UV100).*

3.2. The Ru/TiO_2 catalysts

The photo-assisted synthesis method was employed for preparing the Ru/TiO_2 catalysts with different titania supports, according to a similar protocol as previously described. As in the previous chapters, the relative concentration of the Ru precursor in the support suspension was followed by UV-VIS spectrophotometry along the course of the photo-assisted process (**Fig. 103**). The adsorption step at dark conditions is related to the specific surface area of the support, as the different TIO_2 used did not differ significantly in terms of IsoElectric Point (IEP) and zeta potential (net surface charges), e.g. measured at 6.5 for TiO_2-P25 and 5.5. for both TiO_2-P90 and UV100. So, larger the specific surface area (and the number of Ti-OH surface group, as TiO^- or $TiOH_2^+$), more pronounced the precursor adsorption in the dark, ranging from 40% to 86%). The syntheses were performed under light for 30-40 min, with the complete disappearance of the Ru precursor signal.

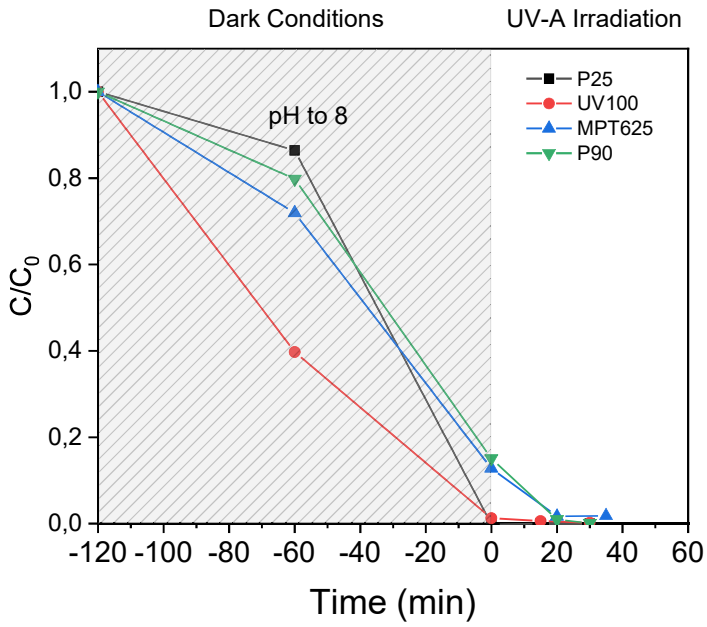

Fig. 103 *Evolution with time of the relative Ru precursor concentration during the photo-assisted synthesis of Ru nanoparticles at the surface of the different TiO_2 supports.*

The main properties of the Ru-based catalysts are collected in Table 12. All catalysts exhibited a Ru content in the range 5-6%, except for the Ru/MPT625 systems. In that case, a lower Ru content of 3.7 wt.% was observed by ICP-OES chemical analysis. This might be attributed to the higher recombination rate of the TiO_2 rutile phase under UV-A light in comparison to the TiO_2 anatase counterpart, that would result in a lower availability of the photogenerated electrons at the rutile surface, with in consequence a lower rate in the reduction of the adsorbed Ru cations. They have as well as a slightly lower reduction power (ca. 0.2 V), but this should not be a major factor considering the favourable position of the associated redox couple involving Ru^{3+}. The non-reduced Ru cations remaining adsorbed at the surface of the TiO_2 at the end of the synthesis would be removed from the surface during the washing step.

The TEM pictures recorded for the different Ru/TiO_2 catalysts and the corresponding Ru nanoparticle size distribution histograms derived from the statistical analysis of the images are shown in **Fig. 104**. These TEM images demonstrated the sub-nanometric sized Ru particles on the different titania supports. Ru/P25 and Ru/UV100 demonstrated to have a mean particle diameter size of 0.8 and 0.7 nm, respectively. However, the ruthenium particle size was higher on MPT625 and P90 with values of 1.0 and 1.1, respectively. CO-pulses demonstrated a dispersion of the catalyst according to the particle size observed by electron microscopy and the Ru wt.% content, as shown in **Table 13**.

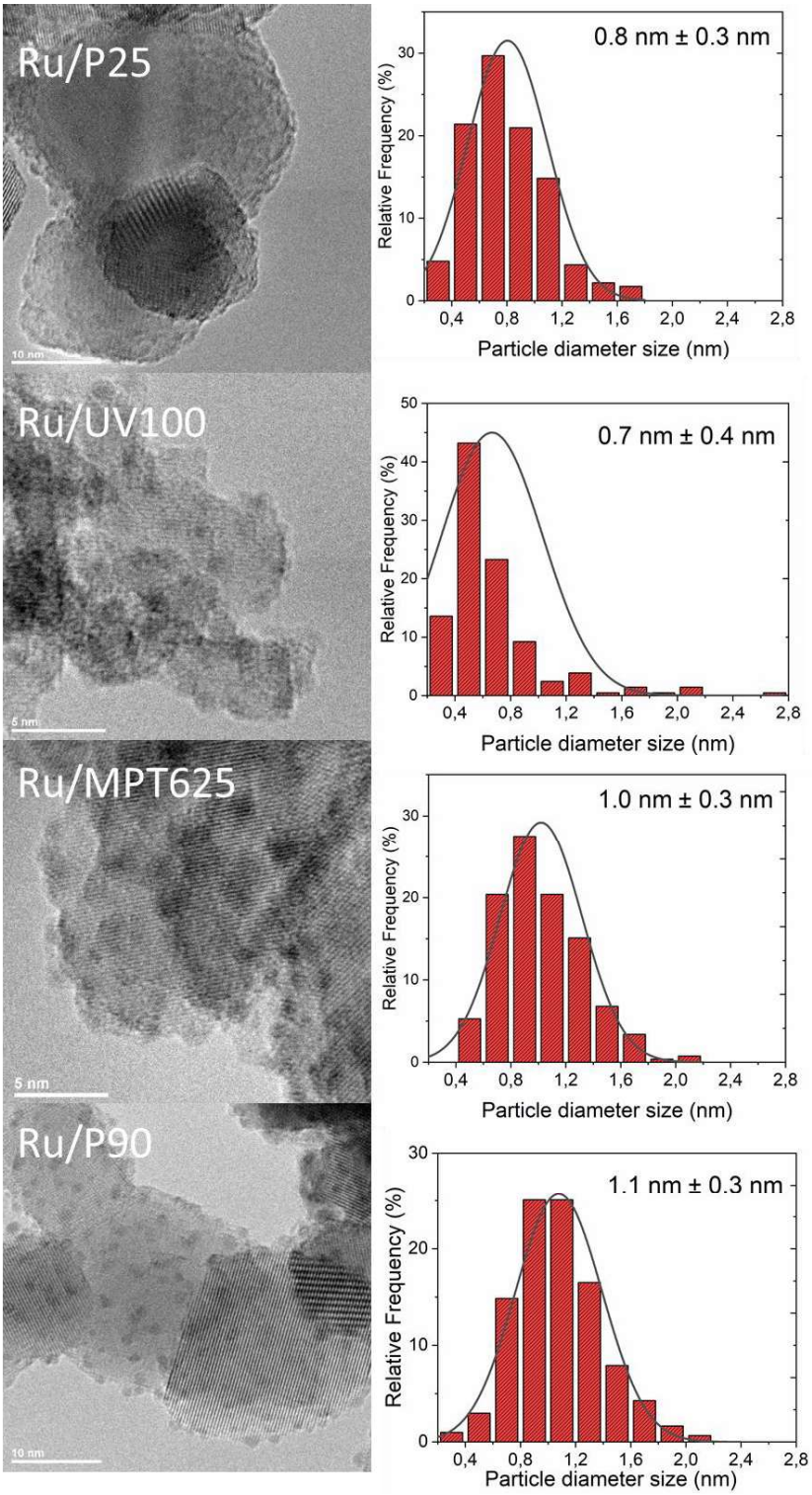

Fig. 104 *On the left, TEM images of Ru/P25, Ru/UV100, Ru/MPT625 and Ru/P90 catalysts, and, on the right, their respective nanoparticle size distribution histograms derived from the statistical analysis of the images (over 230, 206, 265, and 303 nanoparticles).*

Ruthenium chemical state of the different Ru/TiO_2 photothermal catalysts was studied by XPS, as summarized in **Table 13**. Classical XPS patterns were obtained for the Ru 3d and C 1s orbital region, with a similar binding energy of 280.8 eV recorded for the main Ru^0 peak (3d 5/2 orbital) independently of the TiO_2 nature. Some differences in terms of Ru^0:Ru^+ ratios was observed, the Ru/UV100 sample exhibiting the lowest fraction of the metallic species.

Catalyst	Loading Ru (wt. %)[1]	NP size (nm)[2]	Dispersion (%)[3]	Ru^0:$Ru^{\delta+}$ [4]	B.E. (e.V.)
Ru/P25	5.9	0.8 ± 0.3	60	61:39	280.7
Ru/UV100	5.1	0.7 ± 0.4	91	38:62	280.9
Ru/MPT625	3.7	1 ± 0.3	37.5	64:36	280.8
Ru/P90	5.7	1.1 ± 0.3	55.5	59:41	280.7

Table 13. *Ru based catalyst properties obtained by, 1: ICP-OES analysis ; 2:TEM statistical particle counting ;* 3: CO pulses chemisorption *; 4: XPS analysis*

Fig. 105 collects the CO_2 temperature-programmed desorption graphs over the different Ru/TiO_2 catalysts. In comparison with the bare supports, strongly larger quantity of desorbed CO_2 was observed on the Ru-based catalysts. The main fraction corresponded to a mid- and high-temperature desorption, in comparison to the low-temperature desorption observed on the TiO_2 surface it-self. This is related to the strength of the interaction with the catalytic surface. The distribution between mid- and high-temperature desorbed CO_2 was dependent on the catalyst, and can be related to Ru size effect, location of Ru nanoparticles (e.g. anatase, rutile, anatase/rutile interface, amorphous phase), that influence the adsorption mode and strength of the CO_2 adsorption. Also it is known that ruthenium on metal oxide materials can dissociate CO_2 into CO and O atom on its surface, and this dissociation can also be reflected on CO desorption. CO desorption was followed by MS in the line m/z=28 as it is plotted in the **Fig. A 2** of the Annex. However, the CO desorption will be discarded from the quantification of adsorbed CO_2 as m/z=28 can be a fragment of m/z=44 [22]. The values obtained from the integrated CO_2-TPD signals are collected in **Table 14**, normalized with the reference Ru/P25 catalyst. While Ru/P90 did not have strong adsorption bonds with CO_2 (no high-temperature contribution), it showed the larger quantity of CO_2 adsorbed, with 2.6 times that of Ru/P25, followed by Ru/UV100 with 2.1 times and Ru/MPT625 with 1.2 times the reference.

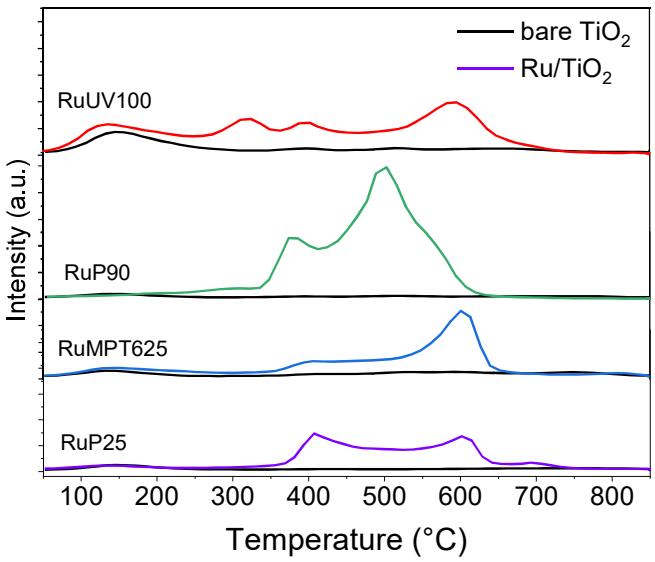

Fig. 105 *CO_2-TPD graphs of the bare TiO_2 supports (black) and the different Ru/TiO_2 catalysts (colour).*

Catalyst	Normalized CO_2 adsorption
Ru/P25	1
Ru/UV100	2.1
Ru/MPT625	1.2
Ru/P90	2.6

Table 14 *Values of CO_2 adsorption normalized with Ru/P25 reference.*

In conclusion, the characterization results confirmed the preparation of well-dispersed ruthenium nanoparticles onto the titania surface, independently of the TiO_2 nature, although slightly smaller sizes were obtained on the TiO_2 P25 and UV100 supports, with sub-nanometric size distribution. CO_2 adsorption on Ru/TiO_2 catalysts was boosted by the presence of ruthenium nanoparticles.

3.3. CO_2 photothermal methanation over Ru/TiO_2 catalysts.

In this subsection, 5 wt.% Ru/TiO_2 are studied for the CO_2 photothermal conversion into methane with H_2 as reducing reactant with a flow composition of 2%$_{v/v}$ CO_2, 8%$_{v/v}$ H_2 and 90%$_{v/v}$ Ar. **Fig. 106** Influence of the light irradiance on the methane yield obtained on the Ru/P25 (black), Ru/UV100 (red), Ru/MPT625 (blue) and Ru/P90 (green) from 120°C to 200°C. Reaction conditions: [CO_2] = 2 %$_v$, [H_2] = 8 %$_v$ total Ar flow of 5.2 mL/min, 5.0 mg of catalyst. CO_2 specific molar rate of 48.5 mmol g^{-1} h^{-1}, (I=0-400 mW/cm²). depicts the influence of the light irradiance (0-400 mW/cm²) on the CH_4 yield over each catalyst from 120°C to 200°C. Both series of graphs expressed the results as a function of the light irradiance and of the temperature. It must be said that among the different catalyst, one sample, namely Ru/MPT625, displayed a significantly lower content of Ru in comparison to the other catalysts. That is why here we preferred to normalize the methane yield per gram of Ru rather than per gram of catalyst, for not potentially introducing a significant external bias to the results.

All the Ru/TiO_2 catalysts exhibited a beneficial photothermal effect upon the combined photonic/thermal excitation, independently of the bulk reaction temperature. Whatever the operating conditions (irradiance and temperature), the reaction was fully selective to methane. Ru/UV100 demonstrated to have the highest methane yield over the whole light irradiance range at 120°C, followed by Ru/P25, Ru/P90 and last Ru/MPT625, with methane yield values of 257, 199, 136 and 103 $mmol_{CH4}$ g_{Ru}^{-1} h^{-1} at an irradiance of 400 mW/cm², respectively. However, this behaviour is changed at higher temperatures, and the Ru/UV100 catalyst lost its superiority. The higher the temperature, more similar are the performances and the photo-enhancement on the Ru/UV100 and Ru/P90 catalysts. By contrast, Ru/MPT625 catalyst demonstrated a higher photo-enhancement than Ru/UV100 and Ru/P90 above 180 °C. Despite the methane yield obtained at lower temperatures over Ru/MPT-625 were the lowest in comparison with the other catalysts, the highest values of methane production were also obtained over this catalyst. For instance, methane yield values at 200 °C and irradiance of 400 mW/cm² were 776 $mmol_{CH4}$ g_{Ru}^{-1} h^{-1} by Ru/MPT625, followed by Ru/P25 with 626 $mmol_{CH4}$ g_{Ru}^{-1} h^{-1} and Ru/UV100 and Ru/P90 with 497 and 492 $mmol_{CH4}$ g_{Ru}^{-1} h^{-1}, respectively. Ru/P25 catalyst demonstrated high methane yield in all the temperature range analysed, being in the most active catalyst rank.

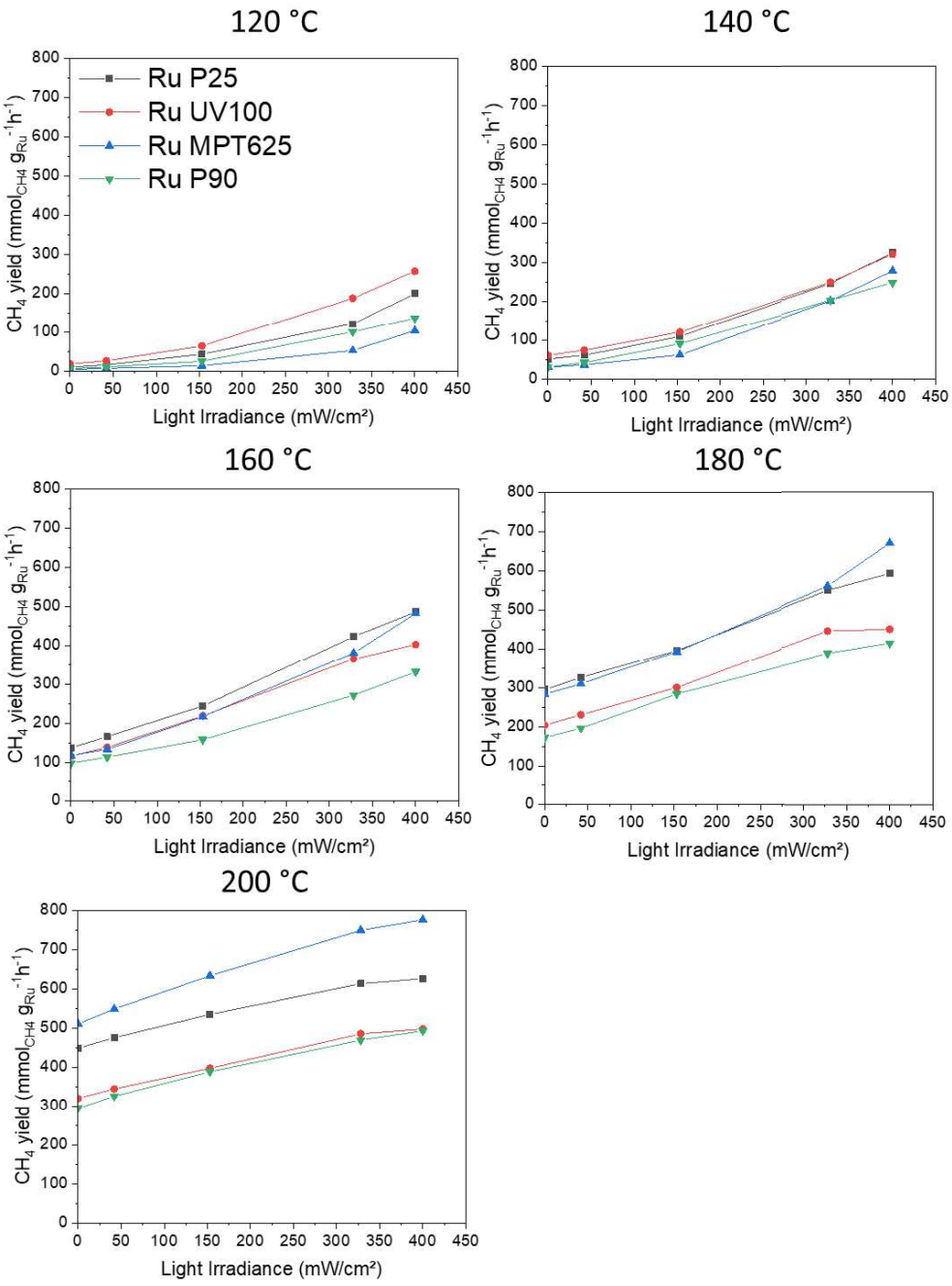
120 °C
140 °C
160 °C
180 °C
200 °C
Ru P25
Ru UV100
Ru MPT625
Ru P90
CH4 yield (mmolCH4 gRu-1h-1)
Light Irradiance (mW/cm²)

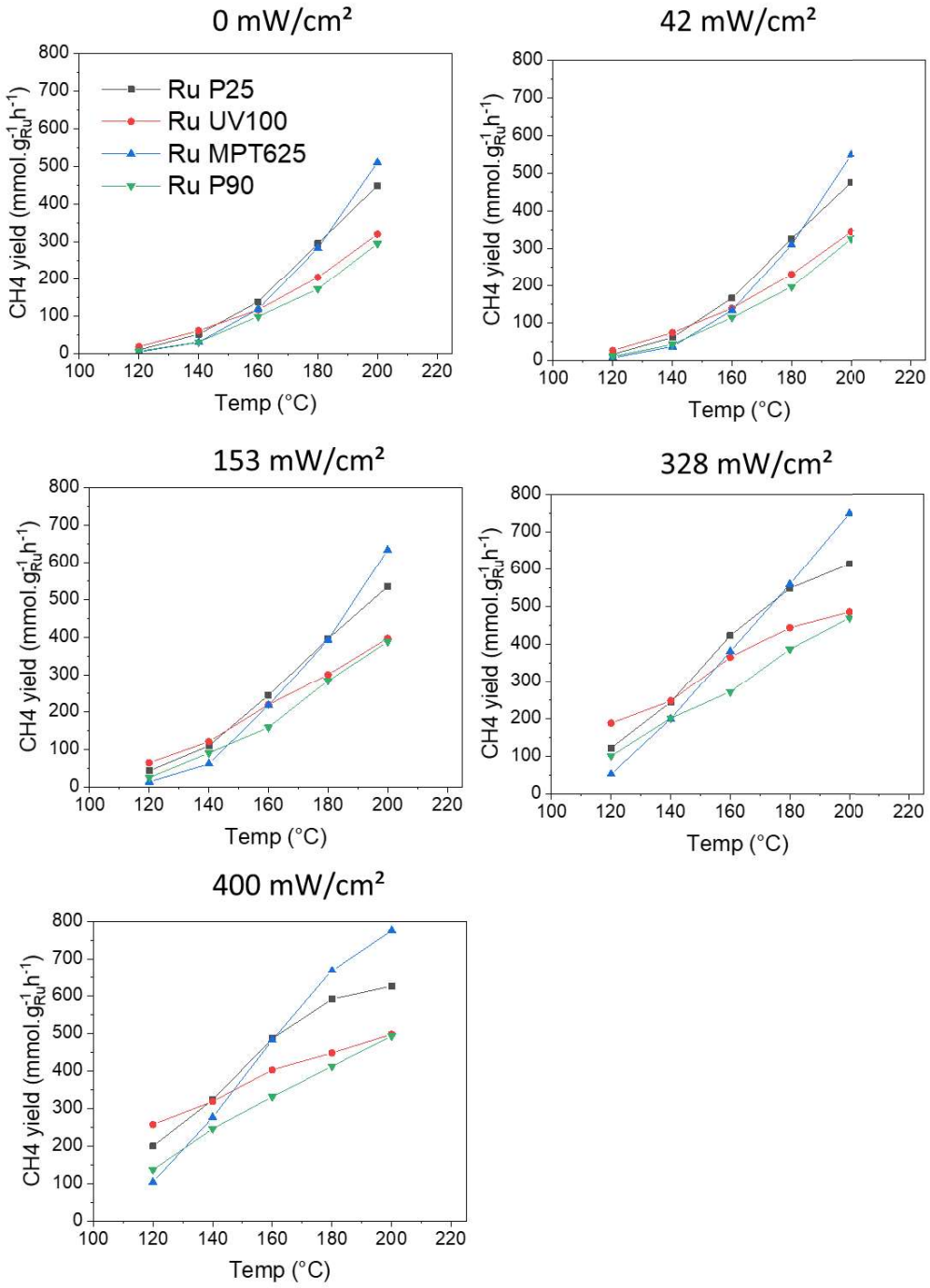

Fig. 106 *Influence of the light irradiance on the methane yield obtained on the Ru/P25 (black), Ru/UV100 (red), Ru/MPT625 (blue) and Ru/P90 (green) from 120°C to 200°C. Reaction conditions: [CO_2] = 2 %$_v$, [H_2] = 8 %$_v$ total Ar flow of 5.2 mL/min, 5.0 mg of catalyst. CO_2 specific molar rate of 48.5 mmol g^{-1} h^{-1}, (I=0-400 mW/cm²).*

Top graphs : *expressed as a function of the light irradiance –* ***bottom graphs*** *: expressed as a function of the temperature*

The apparent activation energies have been calculated from the Arrhenius plot graphs of the methane yield for each catalyst, as shown in **Fig. 107**. They have been calculated based on the real Ru wt.% content. For all the catalysts, a linear decrease in the apparent activation energy was observed with increasing the light irradiance, as also shown in **Table 15** with the appropriate slope obtained for each catalyst. A similar slope was observed when using P25, MPT625 and P90 as support, meanwhile UV100

exhibited the less pronounced one. There are so many parameters that can influence in this result. For instance, the ruthenium chemical state on titania surface, carbonates intermediates or light absorption from the support.

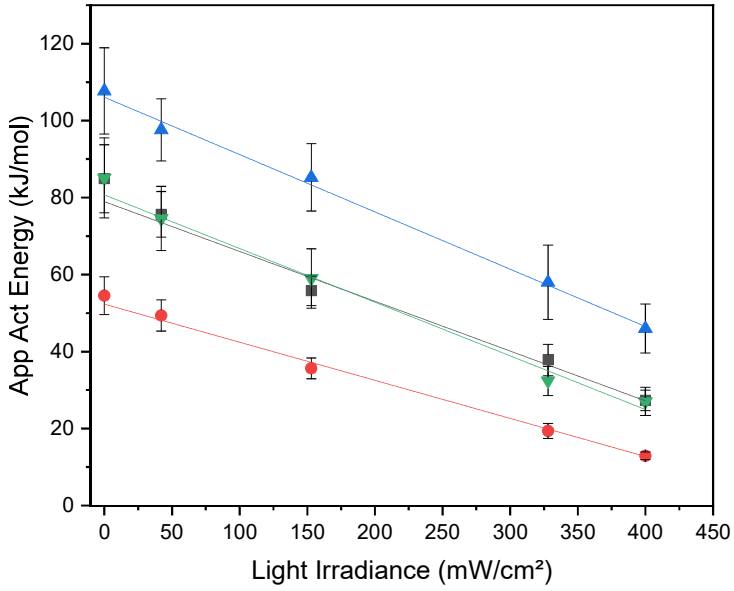

Fig. 107 *Influence of the light irradiance on the apparent activation energy for the methane yield in the CO_2 methanation over Ru/P25 (black), Ru/UV100 (red), Ru/MPT625 (blue), Ru/P90 (green) catalysts. Reaction conditions: [CO_2] = 2 %$_v$, [H_2] = 8 %$_v$ total Ar flow of 5.2 mL/min, 5.0 mg of catalyst. CO_2 specific molar rate of 48.5 mmol g^{-1} h^{-1}.*

Catalyst	0 mW/cm²	156 mW/cm²	400 mW/cm²	Slope (-kJ cm²/mol mW)
Ru/P25	84.9 ± 8.8	55.8 ± 3.8	27.3 ± 2.6	0.129
Ru/UV100	54.5 ± 4.9	35.6 ± 2.7	12.9 ± 1.0	0.099
Ru/MPT625	107.7 ± 11.2	85.2 ± 8.7	46.0 ± 6.4	0.149
Ru/P90	85.1 ± 10.4	59.0 ± 7.7	27.0 ± 3.7	0.139

Table 15 *Apparent activation energy for the methane yield in the CO_2 methanation over the different Ru/TiO_2 catalysts at different light irradiances and the associated slope. Reaction conditions: [CO_2] = 2 %$_v$, [H_2] = 8 %$_v$ total Ar flow of 5.2 mL/min, 5.0 mg of catalyst. CO_2 specific molar rate of 48.5 mmol g^{-1} h^{-1}.*

To sum up, CO_2 methanation was successfully carried out over the different Ru/TiO_2 catalysts with a selective production of methane and high CO_2 conversion at low temperature and under UV-A photon irradiation conditions. Ru/UV100 demonstrated to be the most efficient catalyst at low temperatures under light irradiation. However, as much as the temperature increase, methane production was much more boosted over Ru/MPT625, being the most active catalyst at 200 °C followed by Ru/P25. Even Ru/UV100 was the worst catalyst at high temperatures, the apparent activation energy on it decreased reaching the lowest obtained value of 12.9 ± 1.0 kJ/mol at 400mW/cm².

3.4. In-situ DRIFT spectroscopy study over the Ru/TiO_2 catalysts for CO_2 methanation.

In this subsection, the CO_2 photothermal methanation is studied over the different Ru/TiO_2 catalysts by in-situ DRIFT spectroscopy. First tests were performed with the Ru/TiO_2-P25 catalyst at dark conditions with a non-diluted sample from 200°C to 400°C and with a pure flow of CO_2 and H_2 (1:4) as it is shown in **Fig. 108**. It is possible to observe in the high wavenumber range an intense band at 3015 cm^{-1} that increased in absorbance as much as the temperature increased. This band is assigned to methane physisorbed on the surface as similarly was assigned to 1300 cm^{-1} [23–25]. Ru-CO bands were detected in the 2100-1900 cm^{-1} range. However, the high noise in the spectra avoid to the detection of carbonates/formates intermediates species adsorbed on the titanium dioxide surface. This can be attributed to the high absorption of the material over all the infrared spectrum, which saturates the detector and makes the subtraction of the Ru/P25 spectrum recorded under inert gas from the "methanation" spectrum more difficult and increase the noise of the different spectra in **Fig. 108**. Therefore, to avoid these problems in the next experiments, it is important to dilute the sample into an inert matrix that does not adsorb CO_2 and H_2 and does not absorb IR light.

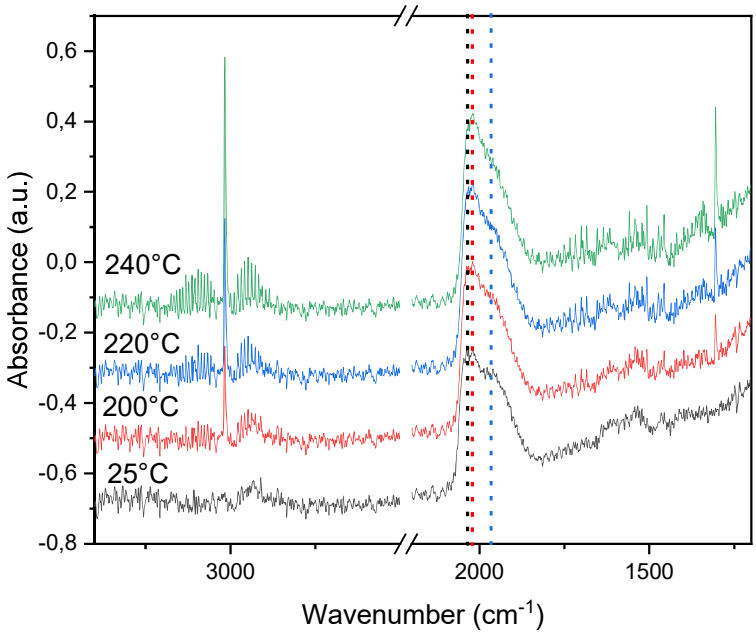

Fig. 108 *In-situ DRIFT spectra in dark conditions over the Ru/P25 catalyst. Reaction conditions: [CO_2]= 20%$_v$, [H_2]= 80%$_v$, flow rate: 5.8 ml/min, catalyst mass=27.9 mg.*

Wavenumber (cm^{-1})	Species	References
3015	Methane	[23–25]
2060-1994	Ru_x-CO	[23,24,26]
1906 (shoulder)	CO at metal/support interfaces	[23,24]
1550-1535	Bidentate formate	[27]
1441	Bidentate bicarbonate	[27]

Table 16 *Carbon species (formates, carbonates and carbonyl) detected in the in-situ DRIFT spectra of CO_2 over the Ru/TiO_2 catalysts surface.*

The previous experiment was repeated using as a sample, 10 wt.% Ru/P25 diluted into a matrix of KBr and with a flow composed of 10 $\%_{v/v}$ CO_2, 40$\%_{v/v}$ H_2 and 50$\%_{v/v}$ Ar. The spectra are plotted in **Fig. 109**. It is possible to observe that, under dark and illuminating conditions, there are no bands assigned to the presence of methane, as during the in-situ experiment on Ru/P25 under inert gas. This can be explained by the decrease of the amount of active material in the sample, reducing the CO_2 conversion to methane. However, the bands assigned to Ru-CO bonds and carbonates/formates adsorbed onto catalytic surface are observed in these conditions, which can be potentially methane precursor species [24]. In addition, some bands at high wavenumber are also reported. These absorbance bands are assigned to physisorbed CO_2 onto the material surface. Furthermore, the influence of the UV-A light irradiation did not result into the appearance of new absorbance bands or into an absorbance increase on Ru/P25 surface when the DRIFTS experiments were conducted under photon irradiation.

Unfortunately, despite the implementation of a large span of experimental conditions for the DRIFTS analysis, the difficulties of observing any difference by the UV-A photon irradiation can be related to the dilution of the catalyst in the KBr matrix. Since potassium bromide material is opaque to the ultraviolet light, it avoids the transmission of photons to the catalyst that is not on the top of the cup. Therefore, we will be more focused on other parameters apart of the light irradiation such as CO_2 activation , hydrogen spillover or metal/support interface.

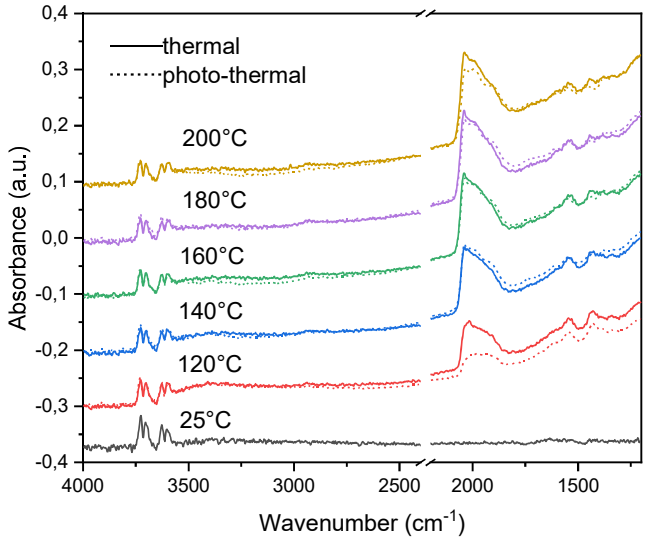

Fig. 109 *In-situ DRIFT spectra in dark (solid line) and light (dashed line) conditions over Ru/P25 catalyst. Irradiance set at 400 mW/cm². Reaction conditions: [CO_2] = 10%$_v$, [H_2] = 40%$_v$ in Ar, flow rate: 5.8 ml/min, sample mass=28.0 mg, catalyst mass=2.45 mg.*

In the range of 2200-1200 cm^{-1} the different recorded infrared bands were analysed in **Fig. 110**. In the range of carbonates/formates it is possible to distinguish two main bands from 120°C to 200°C with maximum absorbance at 1537 and 1441 cm^{-1}. These bands are assigned to bidentate formate and bidentate bicarbonate species, respectively ([27]). In addition, bidentate formate species on anatase band is shifted to higher wavenumbers (ca. 1550 cm^{-1}). This might suggest that bidentate species are preferentially obtained on the rutile phase of the P25 support [28,29]. Bands assigned to Ru-CO bonds increased in absorbance as much as the temperature increased till 200°C. 2038 cm^{-1} and 2014 cm^{-1} bands have been identified as linear Ru^0-CO bond. However, at higher temperatures a new band

emerged at 1994 cm^{-1}. Literature has reported a shift of carbonyl-ruthenium bands in the spectra when the bonds are weaker due to the presence of electron-donating species in the vicinity of Ru adsorption sites [23,30]. However, this band at 1994 cm^{-1} can also be assigned to partially-oxidized Ru bonded carbonyls (Ru^{n+}-CO)[31]. In this case, no band at 1673 cm^{-1} was observed, while during the CO_2 adsorption on bare P25 it was the most characteristic of the sample. During the CO_2 adsorption experiments by Mino and co-workers, they observed that the species assigned to this band was easily desorbed with the outgassing at room temperature, which certifies that the bond of this specie with the TiO_2 surface is very weak [21].

According to literature [23], the mechanistic route from CO_2 to CH_4 over Ru/P25 catalyst can have intermediate steps as hydrogenates species as shown in Eq. 5.1,5.2:

$$CO_2 + H_{(Ru)} \rightarrow (COOH)_{(Ru\text{-}TiO2)} \rightarrow CO_{(Ru)} + OH_{(TiO2)} \quad (5.1)$$

$$CO_{(Ru)} + H_{(Ru)} \rightarrow (CHOH)_{ads} + S \rightarrow (CH_x)_{(S)} + (OH_x)_{(S)} \rightarrow CH_4 + H_2O \quad (5.2)$$

being S an active site on the catalytic surface. The bands in the range from 1700-1200 cm^{-1} can point out the Eq. 1 as the dissociative pathway of CO_2 into CO. However, additional bands assigned to CH_x should appear at 3000-2800 cm^{-1} range. The absence of CH_x species can be justified by a small population of these species on the surface, being insufficient for the detection.

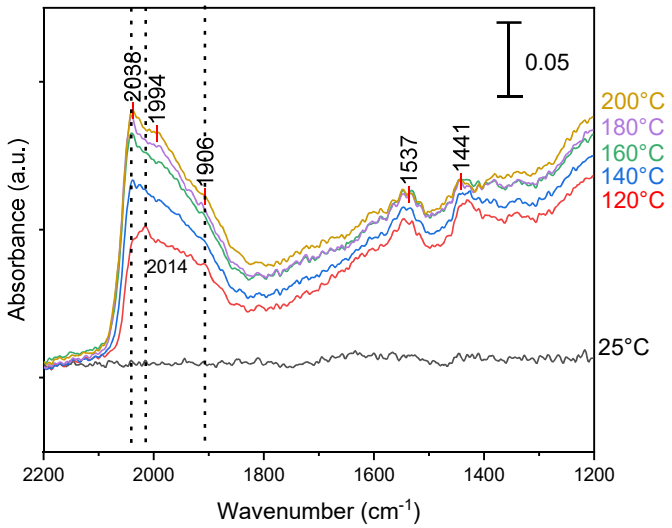

Fig. 110 *In-situ DRIFT spectra in dark conditions over Ru/P25 catalyst at 25°C (grey), 120°C (red), 140°C (blue), 160°C (green), 180°C (violet), 200°C (yellow). Reaction conditions: [CO_2] = 10%$_v$, [H_2] = 40%$_v$ in Ar, flow rate: 5.8 ml/min, sample mass=28.0 mg, catalyst mass=2.5 mg.*

The DRIFT spectra during photothermal and thermal methanation over Ru/MPT625 are depicted in the next **Fig. 111**. Formate/carbonate bands were weaker at lower temperature. However, high absorbance bands were detected upper 140°C, which has connection with the catalytic activity observed in the previous subsection. What it is highlighting is the new bands that emerged at 2970 cm^{-1}, 2930 cm^{-1} and 2860 cm^{-1}, which can be assigned to the C-H stretching vibration of methyl groups ($CH_{3,ad}$) and to the symmetric and asymmetric stretching of C-H bonds of methylene groups ($CH_{2,ad}$), respectively [23].

Moreover, it is possible to observe an intense broad band in the range of 3500-3000 cm^{-1} assigned to the presence of hydroxyl groups on the surface.

Ru-CO bands have different shape and wavenumber than in the previous spectra over Ru/P25 material. In this case, it is found a broad shape band at 1930 cm^{-1}. Since there is any band assigned to 1930 cm^{-1}, we can attribute this broad band to an overlapping of bands between Ru^{n+}-CO, Ru-CO bonds at NPs edges and bridged Ru-CO-Ti bonds [23,24,26]. Similar to Ru/P25, band assigned to linear Ru^0-CO bond was observed at 2038 cm^{-1}. However, this band is only distinguishable at higher temperatures, which can explain the enhancement of the catalytic rate at these reaction conditions. In the range of carbonates/formates we found bands assigned to formate and bidentate bicarbonate species at 1542 cm^{-1} and 1427 cm^{-1}, respectively [21], which are the species that CO_2 is adsorbed onto rutile phase surface in presence of hydrogen flow.

In comparison with Ru/P25, we can observe hydrogenate carbonyl species bands shew high absorbance than ruthenium carbonyl species when temperature increase. Among the Ru-CO bonds, linear Ru^0-CO bond is not the predominant specie during the CO_2 methanation reaction. The high absorbance of carbonyl onto Ru particle edges and (TiO_2)Ru-CO bands indicates it is at particle surrounds where the CO_2 easily dissociates into hydrogenated carboxylates and formates followed by the decomposition into CO and, then, into methyl and methylene intermediates as it is shown in Eq.1, 2.

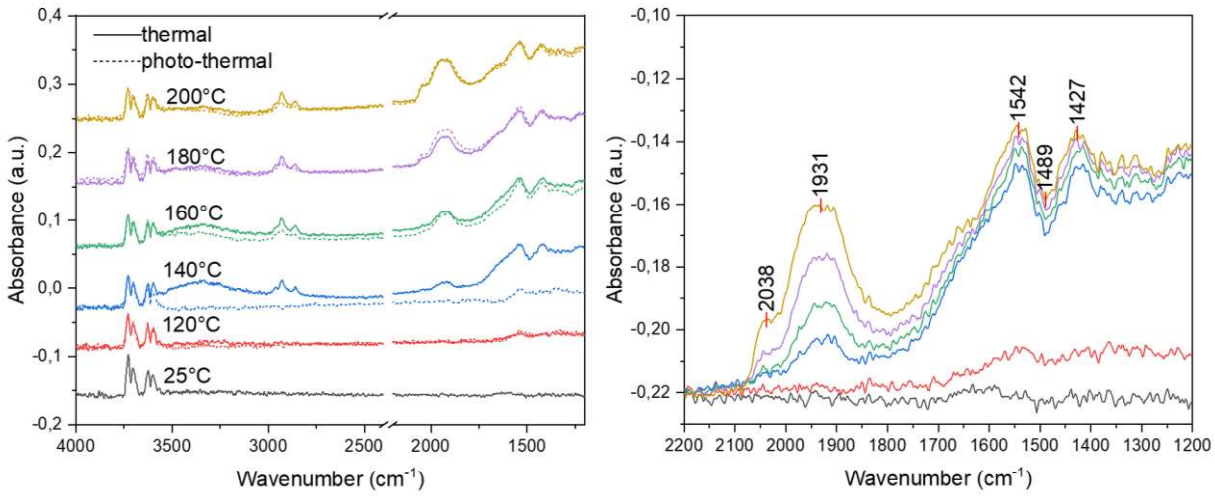

Fig. 111 *In-situ DRIFT spectra over Ru/MPT625 catalyst. On the left, full spectra in dark (solid line) and light (dashed line) conditions. In the right, comparison of the spectra in dark conditions at 25 °C (grey), 120 °C (red), 140 °C (blue), 160 °C (green), 180 °C (violet), 200 °C (yellow) Reaction conditions: [CO_2]= 10%$_v$, [H_2]= 40%$_v$ in Ar, flow rate: 5.8 ml/min, sample mass=24.5 mg, catalyst mass=2.1 mg*

A similar broad band was observed during the DRIFT spectra over Ru/UV100 (**Fig. 112**) in the range from 2000-1900 cm^{-1} attributed to several bonds between ruthenium species and carbonyls (between Ru^{n+}-CO, Ru-CO bonds at NPs edges and bridged Ru-CO-Ti bonds). These Ru-CO bands, in comparison with Ru-CO assigned bands over Ru/MPT625 ones, are shifted to higher wavenumber frequencies. This effect can be related to the CO covering of the surface [25]. At high CO covering on Ru particles, the Ru-CO bonds weaken and, therefore, the stretching of C=O is stronger [25,32]. In addition, the bands located at 1550 cm^{-1} and 1369 cm^{-1} are assigned to ν_a(OCO) and ν_s(OCO) in bidentate formate species, $HCOO_{ad}$, respectively [33,34].

Another band was detected at 1679 cm^{-1} related to the v_{as}(CO) modes of monodentate bicarbonate specie [21,35] but also can be assigned to molecularly adsorbed formic acid [33,34]. 1635 cm^{-1} band was detected at room temperature, which is attributed to carbonates species [24]. However, the literature in which they were supported to assign this band is not reporting this band [21,36–38]. Other research groups classified this peak as water [39,40].

As it occurred over the rutile catalyst, high frequency bands at 2930 cm^{-1} and 2860 cm^{-1} demonstrate methyl and methylene groups during the CO_2 methanation.

As it is shown in the Fig. of the left, there is a clear increase in absorbance of formates and Ru-CO bands under light irradiation from 120°C to 160 °C. This activation of the catalytic surface did not affect only to Ru related species, also to titania surface. In the right of the Fig it is possible to observe that absorbance values of the Ru-CO bands increased from 120°C to 180°C as it also occurred with the band at 1679 cm^{-1}. However, similar absorbance is recorded at 180 °C and 200 °C for these bands meanwhile the bands at 1369 cm^{-1} and 1420 cm^{-1} increased its absorbance value when the temperature was increased to 200 °C.

According to the results obtained during the methanation test, the stabilization of the absorbance for Ru-CO bonds at high temperatures meanwhile formates and carbonates band increased in absorbance with the temperature, might suggest the CO hydrogenation (Eq.2) as the rate-determining step, which is supported in the literature [35,40].

Li and co-workers believed that the difficulty to hydrogenate CO into methane over Ru/anatase can be related to the hydrogen spillover and electron transfer from metal to titanium dioxide [35]. If H_2 is dissociated onto the ruthenium surface and H atom migrates to the O lattice of the anatase surface (Ti-O(H)-Ti), the population of formates and carbonates species increase instead of reduce the CO into CH_4 on ruthenium active sites. Simultaneously, the H spillover leads the electron transfer from metal to TiO_2, which weakens the Ru-carbonyl bonds and strengthen the C=O one and hinders the CH_x species production [35,41,42].

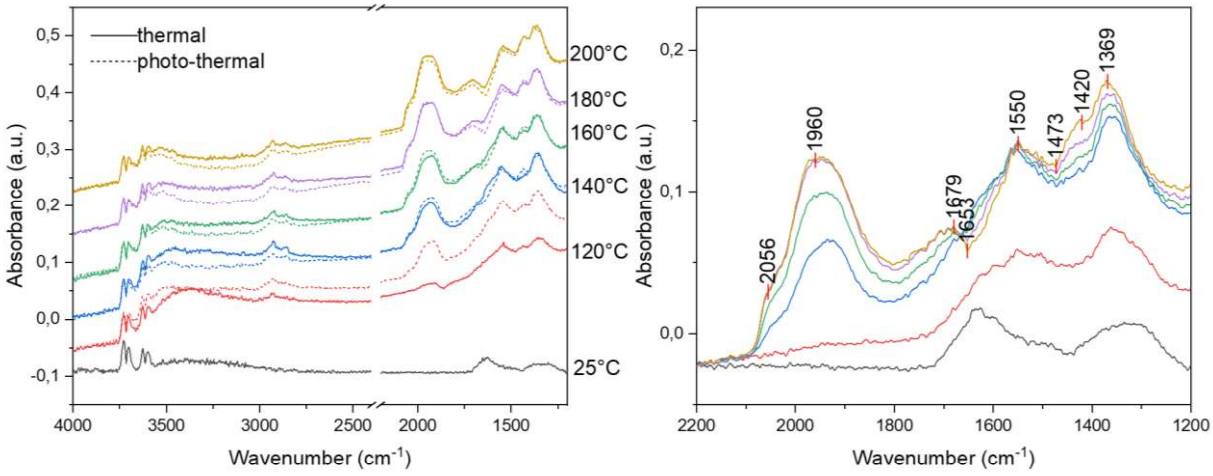

Fig. 112 *In-situ DRIFT spectra over Ru/UV100 catalyst. On the left, full spectra in dark (solid line) and light (dashed line) conditions. In the right, comparison of the spectra in dark conditions at 25 °C (grey), 120 °C (red), 140 °C (blue), 160 °C (green), 180 °C (violet), 200 °C (yellow) Reaction conditions: [CO_2]= 10%$_v$, [H_2]= 40%$_v$ in Ar, flow rate: 5.8 ml/min, sample mass=24.5 mg, catalyst mass=2.1 mg*

Finally, in regards of the Ru/P90 catalyst (**Fig. 113**), similar to Ru/UV100 a band ca. 1620 cm^{-1} assigned to water emerged at room temperature. At 140°C, bands at 1500 cm^{-1} and 1350 cm^{-1} and assigned to bicarbonates were observed, as well as a broad band in the range of Ru-CO modes. At higher temperatures, the broad band at ca. in 1350 cm^{-1} had two maximum peaks of absorbance at 1370 cm^{-1} and 1340 cm^{-1}, which are assigned to carbonates and formates species. The appearance of new bands at 1720 cm^{-1} and 1462 cm^{-1} might be related to the presence of formaldehyde or even oxymethylene [43,44], respectively, on the catalytic surface.

Similarly to Ru/P25, a high absorbance band is observed at 2039 cm^{-1}. However, the band at 1993 cm^{-1} is better distinguished (less overlapping) with Ru/P90. In addition, this band has more absorbance than the main one at 2039 cm^{-1} at 140°C and similar at high temperatures. These differences between both catalysts might be explained in terms of metal-support interaction, and by the higher percentage of anatase phase in P90 than in P25. As it was previously mentioned, electron transfer from metal to anatase phase is stronger than in rutile [40]. Therefore, a higher presence of anatase than rutile may induce a higher electron transfer from ruthenium, generating more Ru partially oxidized species and, then, Ru^{n+}-CO bonds.

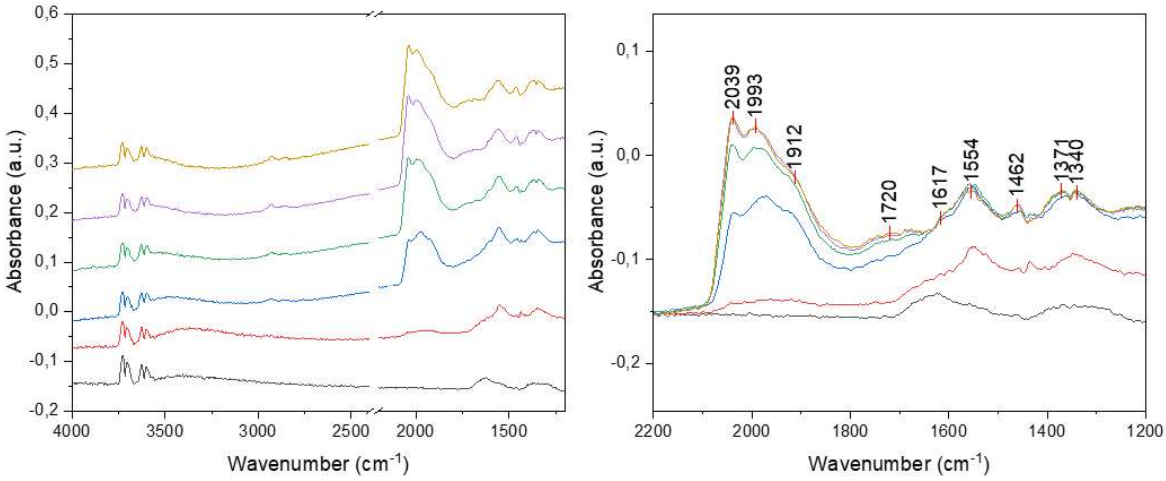

Fig. 113 *In-situ DRIFT spectra over Ru/P90 catalyst. On the left, full spectra in dark conditions. In the right, comparison of the spectra in dark conditions at 25 °C (grey), 120 °C (red), 140 °C (blue), 160 °C (green), 180 °C (violet), 200 °C (yellow) Reaction conditions: [CO_2]= 10%$_v$, [H_2]= 40%$_v$ in Ar, flow rate: 5.8 ml/min, sample mass=24.5 mg, catalyst mass=2.1 mg*

This preliminary study on the use of Ru/TiO_2 catalysts for the photothermal CO_2 methanation is promising. The results demonstrated that TiO_2 is an efficient support for CO_2 adsorption and conversion into formates and adsorbates as the first step. The decoration of the TiO_2 support with small size Ru nanoparticles increases the interfaces between the metal and the metal oxide, which might enhance the CO adsorption, in consequence improving the conversion of CO_2 into CH_4, as suggested by in situ DRIFTS for some catalysts. However, the anatase phase demonstrated not to be the best support in our experimental conditions. Among the different explanations, the role of hydrogen spillover effect might be proposed, as reported in the literature for some other systems. This phenomenon weakens the Ru bond with the carbonyls and hinder the hydrogenation of CO species.

Although being just in its infancy in this emerging field of photothermal catalysis, the need of deeper understanding of mechanistic aspects will require in particular the implementation of more suited

experimental conditions allowing for the visualization of significant effects upon the combined photonic/thermal excitation.

4. Conclusions

In this chapter, we demonstrated that photothermal catalysis on Ru-based systems cannot only be applied efficient for dehydrogenation processes such as in the gas phase formic acid conversion, but also for the CO_2 hydrogenation. Ruthenium has been reported as an active metal for the CO_2 hydrogenation with high selectivity to methane. We evidenced a pronounced photothermal enhancement upon the combined photonic/thermal excitation, and under UV-A light irradiation, the methane yield considerably increased, the effect being all the more marked than the light irradiance increased. It was observed that the catalytic behaviour of the supported Ru differs strongly depending on the used support. Notably, the Ru/g-C_3N_4 catalyst exhibited only a very small photothermal enhancement, while the enhancement under UV-A light shown by the Ru/SiO_2 catalyst remained by far moderate in comparison to that obtained for the Ru/TiO_2 reference systems. Catalytic results obtained on Ru/CeO_2 suggested, although there is no significant change in the activation energy values under light/dark conditions and that a thermalization mechanism might occur simultaneously, that electron-driven processes might take place upon light irradiation, with a change in the selectivity from CO (reverse gas shift water reaction) to methane production.

However, the Ru/TiO_2 catalysts demonstrated to be the most efficient systems among those tested for the CO_2 conversion into methane. The study about the influence of the different commercial titanias used as support points out the importance of the crystallographic nature of the titania (polymorphs). Despite the good results in terms of methane yield obtained under light at low temperatures when ruthenium is supported on anatase, the presence of the rutile phase appeared to be a key-factor at higher temperatures. Preliminary mechanistic studies by DRIFTS suggested that CO_2 is first activated over the titanium dioxide surface as formate and carbonates species that decompose into CO as first step of the methanation. This step would be followed by the hydrogenation of the carbonyl onto ruthenium surface or at the TiO_2/Ru interface.

References

[1] B. Xie, E. Lovell, T.H. Tan, S. Jantarang, M. Yu, J. Scott, R. Amal, Emerging material engineering strategies for amplifying photothermal heterogeneous CO2 catalysis, J. Energy Chem. 59 (2021) 108–125. https://doi.org/10.1016/j.jechem.2020.11.005.

[2] M. Ghoussoub, M. Xia, P.N. Duchesne, D. Segal, G. Ozin, Principles of photothermal gas-phase heterogeneous CO2 catalysis, Energy Environ. Sci. 12 (2019) 1122–1142. https://doi.org/10.1039/c8ee02790k.

[3] C. Mebrahtu, F. Krebs, S. Abate, S. Perathoner, G. Centi, R. Palkovits, CO2 Methanation: Principles and Challenges, in: Stud. Surf. Sci. Catal., 1st ed., Elsevier B.V., 2019: pp. 85–103. https://doi.org/10.1016/B978-0-444-64127-4.00005-7.

[4] N. Takezawa, H. Terunuma, M. Shimokawabe, H. Kobayashib, Methanation of carbon dioxide: preparation of Ni/MgO catalysts and their performance, Appl. Catal. 23 (1986) 291–298. https://doi.org/10.1016/S0166-9834(00)81299-3.

[5] R. Spinicci, A. Tofanari, Comparative study of the activity of titania- and silica-based catalysts for carbon dioxide methanation, Appl. Catal. 41 (1988) 241–252. https://doi.org/10.1016/S0166-9834(00)80395-4.

[6] J.. Moulijn, A.. van Diepen, F. Kapteijn, Catalyst deactivation: is it predictable?, Appl. Catal. A Gen. 212 (2001) 3–16. https://doi.org/10.1016/S0926-860X(00)00842-5.

[7] J. Gao, Q. Liu, F. Gu, B. Liu, Z. Zhong, F. Su, Recent advances in methanation catalysts for the production of synthetic natural gas, RSC Adv. 5 (2015) 22759–22776. https://doi.org/10.1039/C4RA16114A.

[8] J. Kopyscinski, Production of synthetic natural gas in a fluidized bed reactor, ETH, 2010.

[9] X. Han, M. Li, Y. Ma, Y. Li, H. Ma, C. Wang, Thermal coupled photocatalysis to enhance CO2 reduction activities on Ag loaded g-C3N4 catalysts, Surfaces and Interfaces. 23 (2021) 101006. https://doi.org/10.1016/j.surfin.2021.101006.

[10] N. Sun, Y. Zhu, M. Li, J. Zhang, J. Qin, Y. Li, C. Wang, Thermal coupled photocatalysis over Pt/g-C3N4 for selectively reducing CO2 to CH4 via cooperation of the electronic metal–support interaction effect and the oxidation state of Pt, Appl. Catal. B Environ. 298 (2021). https://doi.org/10.1016/j.apcatb.2021.120565.

[11] X. Zhang, H. Liu, Y. Wang, S. Yang, Q. Chen, Z. Zhao, Y. Yang, Q. Kuang, Z. Xie, Hot-electron-induced CO2 hydrogenation on Au@AuRu/g-C3N4 plasmonic bimetal–semiconductor heterostructure, Chem. Eng. J. 443 (2022) 136482. https://doi.org/10.1016/j.cej.2022.136482.

[12] C. Kim, S. Hyeon, J. Lee, W.D. Kim, D.C. Lee, J. Kim, H. Lee, Energy-efficient CO2 hydrogenation with fast response using photoexcitation of CO2 adsorbed on metal catalysts, Nat. Commun. 9 (2018). https://doi.org/10.1038/s41467-018-05542-5.

[13] P.G. O'Brien, K.K. Ghuman, A.A. Jelle, A. Sandhel, T.E. Wood, J.Y.Y. Loh, J. Jia, D. Perovic, C.V. Singh, N.P. Kherani, C.A. Mims, G.A. Ozin, Enhanced photothermal reduction of gaseous CO2 over silicon photonic crystal supported ruthenium at ambient temperature, Energy Environ. Sci. 11 (2018) 3443–3451. https://doi.org/10.1039/c8ee02347f.

[14] B. Lu, F. Quan, Z. Sun, F. Jia, L. Zhang, Photothermal reverse-water-gas-shift over Au/CeO2 with high yield and selectivity in CO2 conversion, Catal. Commun. 129 (2019) 105724. https://doi.org/10.1016/j.catcom.2019.105724.

[15] F. Wang, C. Li, X. Zhang, M. Wei, D.G. Evans, X. Duan, Catalytic behavior of supported Ru

nanoparticles on the {100}, {110}, and {111} facet of CeO2, J. Catal. 329 (2015) 177–186. https://doi.org/10.1016/j.jcat.2015.05.014.

[16] Y. Guo, S. Mei, K. Yuan, D.J. Wang, H.C. Liu, C.H. Yan, Y.W. Zhang, Low-Temperature CO2 Methanation over CeO2-Supported Ru Single Atoms, Nanoclusters, and Nanoparticles Competitively Tuned by Strong Metal-Support Interactions and H-Spillover Effect, ACS Catal. 8 (2018) 6203–6215. https://doi.org/10.1021/acscatal.7b04469.

[17] F. Wang, S. He, H. Chen, B. Wang, L. Zheng, M. Wei, D.G. Evans, X. Duan, Active Site Dependent Reaction Mechanism over Ru/CeO2 Catalyst toward CO2 Methanation, J. Am. Chem. Soc. 138 (2016) 6298–6305. https://doi.org/10.1021/jacs.6b02762.

[18] F. Quan, G. Zhan, C. Mao, Z. Ai, F. Jia, L. Zhang, H. Gu, S. Liu, Efficient light-driven CO2 hydrogenation on Ru/CeO2 catalysts, Catal. Sci. Technol. 8 (2018) 6503–6510. https://doi.org/10.1039/c8cy01787e.

[19] R. Jiang, X. Yue, K. Wang, Z. Yang, W. Dai, X. Fu, Photothermal-Catalyzing CO2 Methanation over Different-Shaped CeO2 -Based Ru Nanoparticles, Energy & Fuels. (2022). https://doi.org/10.1021/acs.energyfuels.2c00560.

[20] L. Cano-Casanova, A. Amorós-Pérez, M. Ouzzine, M.A. Lillo-Ródenas, M.C. Román-Martínez, One step hydrothermal synthesis of TiO2 with variable HCl concentration: Detailed characterization and photocatalytic activity in propene oxidation, Appl. Catal. B Environ. 220 (2018) 645–653. https://doi.org/10.1016/j.apcatb.2017.08.060.

[21] L. Mino, G. Spoto, A.M. Ferrari, CO2 capture by TiO2 anatase surfaces: A combined DFT and FTIR study, J. Phys. Chem. C. 118 (2014) 25016–25026. https://doi.org/10.1021/jp507443k.

[22] W.E. Wallace, NIST Chemistry WebBook, NIST Standard Reference Database Number 69, (n.d.). https://doi.org/10.18434/T4D303.

[23] P. Panagiotopoulou, D.I. Kondarides, X.E. Verykios, Mechanistic aspects of the selective methanation of CO over Ru/TiO 2 catalyst, Catal. Today. 181 (2012) 138–147. https://doi.org/10.1016/j.cattod.2011.05.030.

[24] P. Panagiotopoulou, Methanation of CO2 over alkali-promoted Ru/TiO2 catalysts: II. Effect of alkali additives on the reaction pathway, Appl. Catal. B Environ. 236 (2018) 162–170. https://doi.org/10.1016/j.apcatb.2018.05.028.

[25] S. Cisneros, A. Abdel-Mageed, J. Mosrati, S. Bartling, N. Rockstroh, H. Atia, H. Abed, J. Rabeah, A. Brückner, Oxygen vacancies in Ru/TiO2 - drivers of low-temperature CO2 methanation assessed by multimodal operando spectroscopy, IScience. 25 (2022). https://doi.org/10.1016/j.isci.2022.103886.

[26] P. Panagiotopoulou, D.I. Kondarides, X.E. Verykios, Mechanistic study of the selective methanation of CO over Ru/TiO 2 catalyst: Identification of active surface species and reaction pathways, J. Phys. Chem. C. 115 (2011) 1220–1230. https://doi.org/10.1021/jp106538z.

[27] C. Morterra, E. Fisicaro, F. Boccuzzi, A spectroscopic study of anatase properties, Zeitschrift Fur Phys. Chemie. 124 (1981) 211–222. https://doi.org/10.1524/zpch.1981.124.2.211.

[28] B.E. Hayden, A. King, M.A. Newton, Fourier transform reflection - Absorption IR spectroscopy study of formate adsorption on TiO2(110), J. Phys. Chem. B. 103 (1999) 203–208. https://doi.org/10.1021/jp983581b.

[29] L. Österlund, Structure-reactivity relationships of anatase and rutile TiO2 nanocrystals measured by in situ vibrational spectroscopy, Solid State Phenom. 162 (2010) 203–219.

https://doi.org/10.4028/www.scientific.net/SSP.162.203.

[30] O.S. Alexeev, S.Y. Chin, M.H. Engelhard, L. Ortiz-soto, M.D. Amiridis, Effects of Reduction Temperature and Metal - Support Interactions on the Catalytic Activity of Pt/γ-Al2O3 and Pt/TiO2 for the Oxidation of CO in the Presence and Absence, J. Phys. Chem. B. 109 (2005) 23430–23443. https://doi.org/10.1021/jp054888v.

[31] N.M. Gupta, V.S. Kamble, R.M. Iyer, K.R. Thampi, M. Gratzel, The transient species formed over RuRuOx/TiO2 catalyst in the CO and CO + H2 interaction: FTIR spectroscopic study, J. Catal. 137 (1992) 473–486. https://doi.org/10.1016/0021-9517(92)90174-G.

[32] J. Robbins, Chemistry of supported Ru: CO-induced oxidation of Ru at 310 K, J. Catal. 115 (1989) 120–131. https://doi.org/10.1016/0021-9517(89)90012-2.

[33] S. Kwon, T.C. Lin, E. Iglesia, Formic Acid Dehydration Rates and Elementary Steps on Lewis Acid-Base Site Pairs at Anatase and Rutile TiO2Surfaces, J. Phys. Chem. C. 124 (2020) 20161–20174. https://doi.org/10.1021/acs.jpcc.0c05721.

[34] S. Kwon, T.C. Lin, E. Iglesia, Elementary steps and site requirements in formic acid dehydration reactions on anatase and rutile TiO2 surfaces, J. Catal. 383 (2020) 60–76. https://doi.org/10.1016/j.jcat.2019.12.043.

[35] X. Li, J. Lin, L. Li, Y. Huang, X. Pan, S.E. Collins, Y. Ren, Y. Su, L. Kang, X. Liu, Y. Zhou, H. Wang, A. Wang, B. Qiao, X. Wang, T. Zhang, Controlling CO2 Hydrogenation Selectivity by Metal-Supported Electron Transfer, Angew. Chem. - Int. Ed. 59 (2020) 19983–19989. https://doi.org/10.1002/anie.202003847.

[36] L.F. Liao, C.F. Lien, D.L. Shieh, M.T. Chen, J.L. Lin, FTIR study of adsorption and photoassisted oxygen isotopic exchange of carbon monoxide, carbon dioxide, carbonate, and formate on TiO2, J. Phys. Chem. B. 106 (2002) 11240–11245. https://doi.org/10.1021/jp0211988.

[37] M. Marwood, R. Doepper, A. Renken, In-situ surface and gas phase analysis for kinetic studies under transient conditions The catalytic hydrogenation of CO2, Appl. Catal. A Gen. 151 (1997) 223–246. https://doi.org/10.1016/S0926-860X(96)00267-0.

[38] A. Karelovic, P. Ruiz, Mechanistic study of low temperature CO2 methanation over Rh/TiO2 catalysts, J. Catal. 301 (2013) 141–153. https://doi.org/10.1016/j.jcat.2013.02.009.

[39] D.A. Panayotov, J.T. Yates, Spectroscopic detection of hydrogen atom spillover from Au nanoparticles supported on TiO2: Use of conduction band electrons, J. Phys. Chem. C. 111 (2007) 2959–2964. https://doi.org/10.1021/jp066686k.

[40] J. Zhou, Z. Gao, G. Xiang, T. Zhai, Z. Liu, W. Zhao, X. Liang, L. Wang, Interfacial compatibility critically controls Ru/TiO2 metal-support interaction modes in CO2 hydrogenation, Nat. Commun. 13 (2022) 1–10. https://doi.org/10.1038/s41467-021-27910-4.

[41] T. Avanesian, G.S. Gusmão, P. Christopher, Mechanism of CO2 reduction by H2 on Ru(0 0 0 1) and general selectivity descriptors for late-transition metal catalysts, J. Catal. 343 (2016) 86–96. https://doi.org/10.1016/j.jcat.2016.03.016.

[42] W.E. Kaden, T. Wu, W.A. Kunkel, S.L. Anderson, Electronic Structure Controls Reactivity of Size-Selected Pd Clusters Adsorbed on TiO2 Surfaces, Science. 326 (2009) 826–829. https://doi.org/10.1126/science.1180297.

[43] G.Y. Popova, T. V Andrushkevich, Y.A. Chesalov, E.S. Stoyanov, In situ FTIR Study of the Adsorption of Formaldehyde, Formic Acid, and Methyl Formiate at the Surface of TiO2 (Anatase), Kinet. Catal. 41 (2000) 885–891.

[44] F.S. Feil, J.G. Van Ommen, J.R.H. Ross, Infrared Investigation of the Adsorption and Reactions of Methanol on V2O5/TiO2 Catalysts, Langmuir. 3 (1987) 668–673. https://doi.org/10.1021/la00077a015.

Conclusions and perspectives

The main objective of this thesis was to demonstrate the ability of Ru-based catalysts to be used as photothermal catalysts under UV-A light for two gas-phase reactions of interest, as main reaction the formic acid dehydrogenation to produce hydrogen, and as secondary reaction the hydrogenation of CO_2 to methane (Sabatier reaction). We aimed at obtaining a proof of evidence of a beneficial photothermal effect under UV-A for both reactions, and that photothermal catalysis can soften the reaction conditions and increase the reaction yield through the dual photo/thermal excitation of Ru-based catalysts for developing more sustainable processes.

We described first the advances realized for the gas-phase formic acid dehydrogenation as a sustainable process for hydrogen production.

First, Ru/TiO_2 was considered as reference catalyst under UV-A light. The main conclusions are:

- combining (dual) photonic/thermal excitation of the Ru/TiO_2 catalyst has been proved to boost the decomposition of gaseous formic acid towards dehydrogenation under UV-A light irradiation, with a significant increase in the hydrogen yield.
- it lowers the formic acid decomposition temperature, increases the H_2 production rate as well as the selectivity towards dehydrogenation, thanks to a differentiated (light-enhanced) mechanisms for H_2 and CO productions.
- Ru demonstrated to be related to the H_2 production, with an optimum content of 0.5 wt.%.
- TiO_2 acting as photothermal catalyst selective for the dehydration reaction, the TiO_2 support itself is an intrinsic limitation for the photothermal performances.

Different methodologies were used to access the possible light-induced mechanisms, e.g. photon-dependency experiments, apparent activation energy evaluation or in situ DRIFT spectroscopy:

- in-situ DRIFT spectroscopy spectra in photothermal conditions confirmed the enhancement features attributed to the bare TiO_2 support itself and to the supported Ru nanoparticles, for dehydration and dehydrogenation reactions.
- it shows that Ru can be differently bonded to carbon species under light and dark conditions, with new bands assigned to Ruthenium-carbonyl bonds under illuminating conditions, suggesting a new electron-driven mechanism under UV-A light, in addition to a thermal-driven (thermalization) mechanism.
- Photon-dependency experiments and apparent activation energy determination supported the hypothesis of dominant electron-driven processes vs. thermalization.

Second, we aimed at studying to which extent the performances and the photothermal enhancement effect might be influenced and improved through the choice of other support materials. In this part of the thesis, the main conclusions are:

- a positive photothermal effect was obtained on both $Ru/g\text{-}C_3N_4$ and Ru/SiO_2 catalysts, allowing the H_2 production rate to be increased under UV-A light vs. dark conditions, and the temperature to be lowered while maintaining a similar H_2 production rate.
- the isolating SiO_2 can be used as support in photothermal catalysis, the enhancement being shown to rely only on the activation of Ru nanoparticles, with both H_2 and CO formation.

- we demonstrated that Ru/g-C_3N_4 were remarkable photothermal catalysts that outperformed the Ru/TiO_2 reference catalysts in terms of H_2 production and with a 100% selectivity over the whole temperature and irradiance range. An optimum Ru content of 0.5 wt.% was observed
- the features of the -C_3N_4 surface allowed the intrinsic limitation of the TiO_2 semiconductor to be overcome.
- By contrast to Ru/TiO_2, in situ DRIFT spectra over Ru/SiO_2 suggested possible electron-driven mechanism under light irradiation in addition to pure thermal catalysis. We suggested a thermalization mechanism for hot carriers over Ru/g-C_3N_4.

Third, we aimed at showing in a preliminary study the ability of supported Ru-based systems to be also used as photothermal catalysts under UV-A in another reaction of interest, the photothermal CO_2 hydrogenation into methane. In this part of the thesis, the main conclusions are:

- Ru-based catalysts with a 5 wt.% content can also be used efficiently for the CO_2 hydrogenation into methane using H_2 as reducing reactant in photothermal conditions with a selectivity of 100 %. UV-A light irradiation promoted strongly higher methane yields than under dark conditions in the case of the Ru/TiO_2 catalysts, that overcome all the catalysts studied.
- the performances under light were less interesting on the Ru/SiO_2 catalyst, and by far worst on the Ru/g-C_3N_4 catalyst, although a photothermal enhancement was observed for all catalysts.
- Different light-induced mechanisms were suggested depending on the nature of the support, related to the evolution of the apparent activation energy.
- Results showed than the nature of the TiO_2 support used influenced the photo, although a photothermal enhancement was observed independently of the TiO_2 support used.
- Anatase phase demonstrated good results at low temperature conditions. However, the most enhanced methane yield with the temperature was over rutile-phase supported ruthenium. Several factors like metal/support interaction, hydrogen spillover or CO_2 activation are affecting in these results.

As perspectives opened by the work, our results paved the way for further studies and the development of new photothermal catalysts, under UV-A light as well as under solar light.

Ruthenium is an excellent metal for elaborating supported photothermal catalysts. However, as one of the objectives remains to lower further the temperature, the study of other materials should be contemplated. Other noble metals like Au, Ag or Pt can be promising metals for a photothermal enhancement, with a wide range of spectral responses, that in addition can be tuned from the UV-A to the visible part of the spectra depending on the nanoparticle size. In fact, under pure UV-A light, promising preliminary results already obtained by substituting Ru by Pt demonstrated that, even at room temperature, high FA conversion values can be obtained under light irradiation, as shown in **Fig. 114**. Under maximum light irradiance, FA conversion of 23% was achieved over a Pt(0.5%)/g-C_3N_4 (PA) catalyst with 100% selectivity towards H_2, vs. only 8.8% with our reference Ru(0.5%)/TiO_2 (PA) catalyst. H_2 production with the Pt catalyst reached 16.3 mmol g^{-1} h^{-1}, strongly overcoming the 4.2 mmol $g^{-1}h^{-1}$ obtained with the reference Ru catalyst in similar conditions.

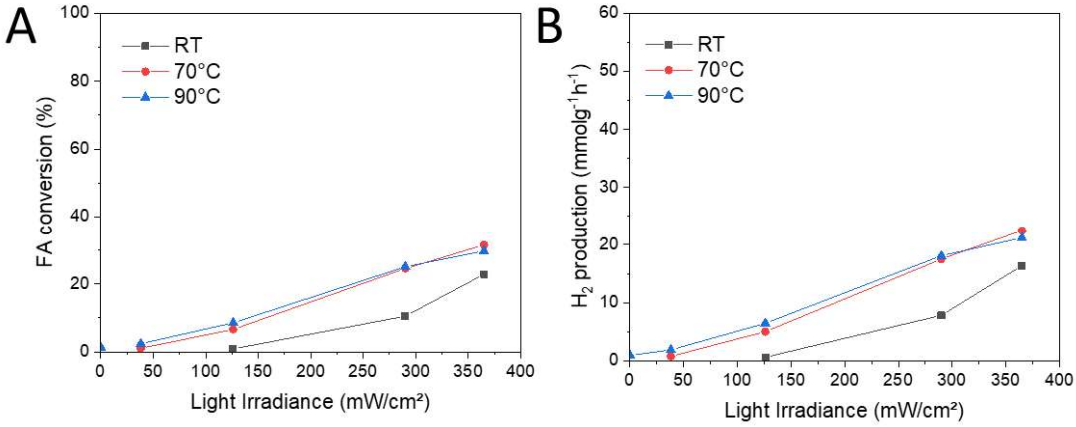

Fig. 114 *Representation as a function of the light irradiance of the photothermal FA decomposition over the Pt(0.5 %)/g-C_3N_4 (PA) reference catalyst prepared by the photo-assisted synthesis method.* ***A)*** *FA conversion and* ***B)*** *production of H_2. Reaction conditions: [FA]=5500 ppm_v, total Ar flow of 14.7 mL, 2.1 mg of catalyst, FA specific molar rate of 68.8 mmol $g^{-1}h^{-1}$.*

Another strategical route for further experiments is the study of non-noble, earth-abundant metals. For instance, without any exclusive, Cu, Ni, Co are less expensive materials that, in the determined photon wavelength, are sensitive to light irradiation.

In particular, a highly innovative strategy might rely on the use of bi-metallic systems allowing favourably to extend the operating spectral range. The concept would be to associated a metal with an suited absorption in the visible spectral range, and thermalization the hot carriers for thermally activating an efficient (thermal) metallic catalyst.

As we demonstrated in this work, the influence of the support plays a crucial role during the photothermal reaction. The search of alternative supports that might enhance further the catalytic properties of the materials, notably by allowing a synergistic, double activation of both the support surface and the supported metals, is of prime interest.

In the literature chapter, several methodologies were described to analyse the different mechanisms taking place during the photothermal conditions with combined photonic/thermal excitation. In the following studies, the search of collaboration and the expansion of the set-up are vital to determine the influence of photon-driven and thermal-driven processes during the reactions. For instance, are targeted wavelength-dependency experiments, nano-thermal measurements and kinetic isotopic exchange experiments.

Last perspective relies on the exploration of other reactions of high interest for the synthesis of high value-added chemicals in the bio-(solar)-refinery field. Notably, we previously mentioned that formic acid can act as internal hydrogen supplier for hydrogenation reactions, for instance for the hydrogenation of levulinic acid issued from the direct conversion of cellulosic biomass into γ-valerolactone. The strong photothermal enhancement in the H_2 production rate that we reported on the Ru catalyst would allow providing in-situ large amount of H_2 for the coupled hydrogenation reaction, for which Ru is known to be a very good catalyst.

Annex

Temperature	Light Irradiance	H_2 production	CO production	CO_2 production	FA conversion	H_2 selectivity
°C	mW/cm²		mmol g^{-1} h^{-1}		%	%
25	0	0.0	0.0	0.0	0.0	--
	22	0.2	0.0	0.0	0.0	--
	38	0.3	0.0	0.0	0.0	--
	126	0.6	0.0	0.6	0.9	--
	290	2.4	0.0	2.3	3.4	--
	365	4.2	1.5	4.4	8.8	73.1
70	0	0.0	0.0	0.0	0.0	--
	22	0.0	0.0	0.0	0.0	--
	38	0.0	0.0	0.0	0.0	--
	126	0.8	0.0	0.8	1.2	100.0
	290	4.8	3.0	4.8	11.5	62.1
	365	10.7	6.3	10.8	25.5	62.9
90	0	0.0	0.0	0.0	0.0	--
	22	0.0	0.0	0.0	0.0	--
	38	0.0	0.0	0.0	0.0	--
	126	1.6	1.0	1.7	4.0	61.8
	290	9.1	5.8	9.3	22.5	61.0
	365	16.8	10.3	16.8	40.4	62.1
110	0	0.0	0.0	0.0	0.0	--
	22	0.4	0.0	0.4	0.5	--
	38	0.6	0.0	0.5	0.7	--
	126	2.4	1.9	2.6	6.8	55.8
	290	12.4	8.5	12.9	31.9	59.3
	365	23.8	12.5	24.8	55.5	65.6
130	0	0.1	1.0	0.1	1.6	8.3
	22	0.7	1.1	0.6	2.6	38.0
	38	1.0	1.6	1.0	3.9	39.2
	126	4.6	4.2	4.9	13.6	51.8
	290	21.6	14.3	22.1	54.2	60.3
	365	30.8	16.1	31.0	70.2	65.6
150	0	0.6	2.8	0.6	5.1	18.0
	22	2.3	3.8	2.6	9.5	37.7
	38	3.1	3.9	3.4	10.9	43.9
	126	10.0	9.2	10.5	29.3	52.1
	290	31.1	12.9	31.9	66.6	70.7
	365	36.3	17.6	36.3	80.2	67.3
170	0	2.9	4.2	4.0	12.2	40.9
	22	5.9	6.3	7.2	20.1	48.4
	38	8.6	7.5	9.3	25.0	53.5
	126	26.4	13.2	27.2	60.3	66.6

	290	44.2	12.7	43.4	83.5	77.7
	365	46.4	11.7	45.8	85.6	79.9
	0	10.1	13.4	11.3	36.8	43.0
190	22	15.4	14.6	16.7	46.6	51.4
	38	18.7	15.7	19.8	52.8	54.4
	126	37.5	15.7	37.2	78.8	70.5
210	0	20.4	21.5	21.4	63.9	48.7

Table A 1*Influence of the UV-A light irradiance in the 0-365 mW/cm² range and of the reaction temperature on the photothermal FA decomposition on the Ru(0.5 %)/TiO_2 (PA) reference catalyst prepared by the photo-assisted synthesis method*

Temperature	**Light Irradiance**	**H_2 production**	**CO production**	**CO_2 production**	**FA conversion**	**H_2 selectivity**
°C	mW/cm²		mmol g^{-1} h^{-1}		%	%
	0	--	--	--	--	--
	22	--	--	--	--	--
25	38	--	--	--	--	--
	126	--	--	--	--	--
	290	1.2	0.0	1.2	1.8	100.0
	365	5.9	0.0	5.8	8.7	100.0
	0	--	--	--	--	--
	22	--	--	--	--	--
50	38	--	--	--	--	--
	126	0.2	0.0	0.0	0.0	100.0
	290	7.0	0.0	6.9	10.3	100.0
	365	17.0	0.1	16.7	25.1	99.2
	0	--	--	--	--	--
	22	--	--	--	--	--
70	38	0.1	0.0	0.0	0.0	100.0
	126	1.0	0.0	1.0	1.5	100.0
	290	16.7	0.0	16.3	24.2	100.0
	365	29.2	0.6	28.4	43.3	97.8
	0	0.7	0.0	0.0	0.0	100.0
	22	0.6	0.0	0.7	1.0	100.0
90	38	1.2	0.0	1.1	1.7	100.0
	126	7.5	0.0	7.3	10.9	100.0
	290	31.6	0.2	30.5	45.7	99.3
	365	41.3	0.3	39.9	59.8	99.2
	0	1.8	0.0	1.5	2.3	100.0
	22	2.6	0.0	2.4	3.6	100.0
100	38	3.4	0.0	3.2	4.8	100.0
	126	11.8	0.0	11.4	16.9	100.0
	290	36.9	0.7	35.4	53.7	98.1
	365	43.2	1.2	41.3	63.2	97.3

110	0	3.8	0.0	3.6	5.4	100.0
	22	5.0	0.0	4.7	7.0	100.0
	38	6.1	0.0	5.7	8.5	100.0
	126	18.5	0.0	18.0	26.7	100.0
	290	38.9	0.9	37.5	57.2	97.7
	365	46.2	0.7	44.5	67.3	98.6
120	0	8.3	0.0	8.0	12.0	100.0
	22	9.3	0.0	8.9	13.2	100.0
	38	10.9	0.0	10.6	15.9	100.0
	126	26.7	0.0	26.0	38.7	100.0
130	0	11.5	0.0	11.6	17.3	100.0
	22	15.6	0.0	15.7	23.4	100.0
	38	19.0	0.0	19.0	28.3	100.0
	126	36.3	0.0	36.0	53.5	100.0
	290	50.4	0.4	49.6	74.4	99.3
	365	54.3	0.8	53.0	80.2	98.5
150	0	24.5	0.0	24.8	36.9	100.0
	22	29.9	0.0	29.9	44.5	100.0
	38	32.9	0.0	33.1	49.3	100.0
	126	45.6	0.0	45.1	67.1	100.0
	290	54.8	0.0	53.7	80.0	100.0
	365	56.4	0.0	55.5	82.7	100.0

Table A 2 *Influence of the UV-A light irradiance in the 0-365 mW/cm² range and of the reaction temperature on the photothermal FA decomposition on the Ru(0.5 %)/g-C_3N_4 (PA) reference catalyst prepared by the photo-assisted synthesis method*

Temperature	**Light Irradiance**	**H_2 production**	**CO production**	**CO_2 production**	**CO selectivity**	**FA conversion**
°C	mW/cm²		mmol g^{-1} h^{-1}		%	%
25	0	0.0	0.0	0.0	--	0.0
	22	0.0	0.0	0.0	--	0.0
	38	0.0	0.0	0.0	--	0.0
	126	0.0	0.0	0.0	--	0.0
	290	0.0	0.0	0.0	--	0.0
	365	0.2	0.0	0.5	0.0	0.8
90	0	0.0	0.0	--	--	--
	22	0.0	0.0	--	--	--
	38	0.0	0.0	--	--	--
	126	0.0	0.0	--	--	--
	290	5.7	2.7	6.1	30.8	13.1
	365	12.7	5.2	12.9	28.6	26.9
110	0	0.0	0.0	0.0	--	0.0
	22	0.0	0.0	0.0	--	0.0
	38	0.0	0.0	0.0	--	0.0

	126	2.4	2.0	3.5	36.0	8.2
	290	13.1	6.3	14.0	31.1	30.3
	365	20.6	9.4	21.7	30.3	46.3
	0	2.0	1.7	2.8	37.2	6.7
	22	2.5	1.8	3.2	35.8	7.4
	38	3.0	1.5	3.9	28.3	8.1
130	126	6.7	3.5	7.5	31.9	16.5
	290	21.4	9.5	22.0	30.1	47.0
	365	30.9	12.3	31.0	28.4	64.5
	0	7.1	3.4	7.9	29.9	16.8
	22	8.4	3.9	9.4	29.6	19.8
	38	8.9	4.0	9.9	28.9	20.8
150	126	16.1	6.9	16.9	29.0	35.5
	290	33.9	13.8	33.7	29.1	70.7
	365	38.2	15.5	37.8	29.0	79.3
	0	15.7	5.5	15.7	26.0	31.7
	22	17.4	5.9	17.6	25.3	35.0
	38	19.2	6.3	19.1	24.8	37.9
170	126	30.5	9.5	29.4	24.4	58.0
	290	43.4	13.1	41.6	23.9	81.4
	365	43.7	13.9	42.4	24.7	83.8
	0	30.0	8.8	29.4	23.1	57.0
	22	32.6	9.6	31.4	23.3	61.1
190	38	33.4	9.8	32.4	23.3	62.9
	126	42.5	12.9	40.5	24.1	79.4

Table A 3 *Influence of the UV-A light irradiance in the 0-365 mW/cm² range and of the reaction temperature on the photothermal FA decomposition on the Ru(0.5 %)/g-C_3N_4 (PA) reference catalyst prepared by the photo-assisted synthesis method*

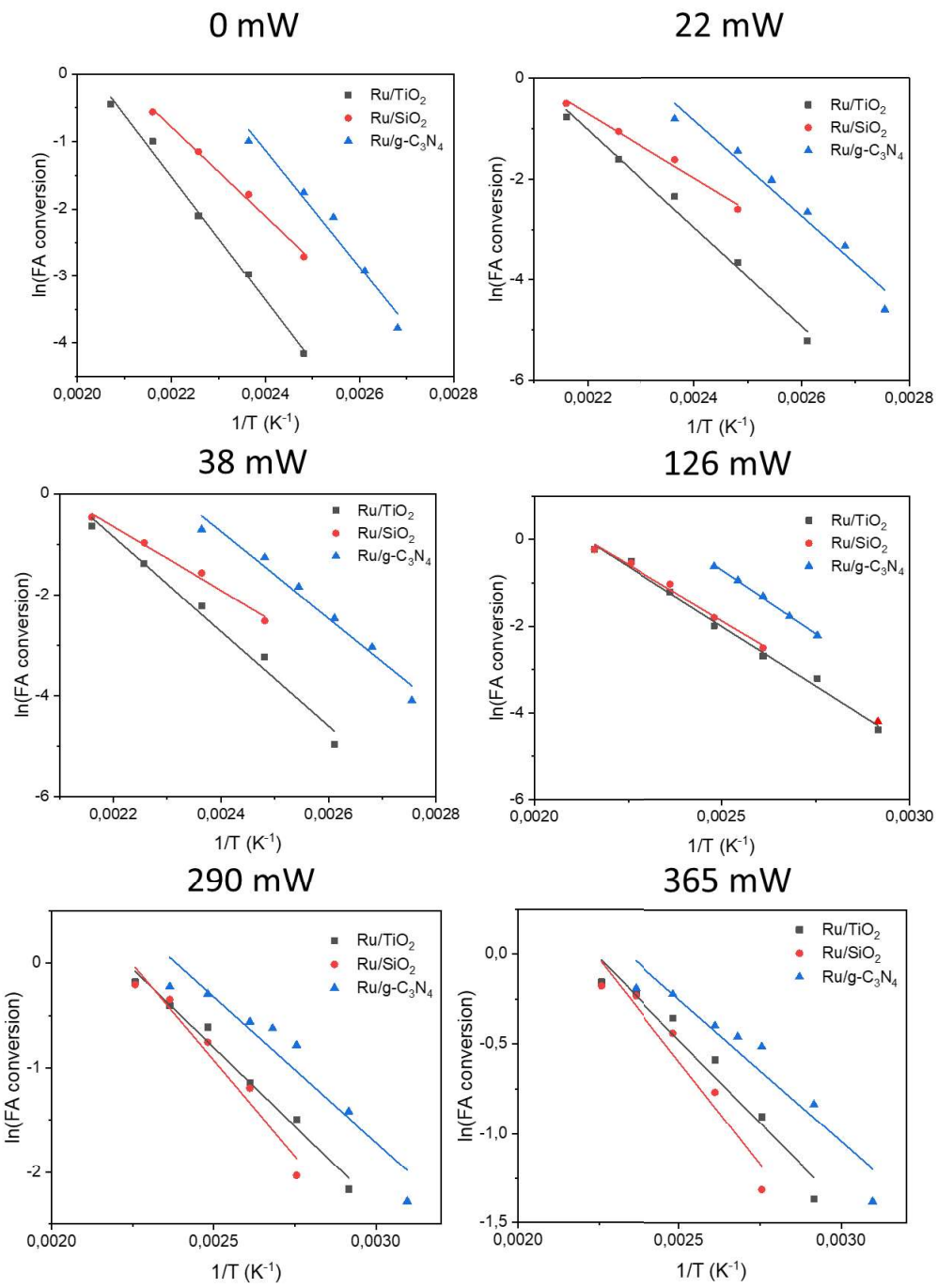

Fig. A 1 *Arrhenius plot graphs of formic acid conversion over (black) Ru/TiO_2, (red) Ru/SiO_2 and (blue) $Ru/g\text{-}C_3N_4$ catalysts for different light irradiances within the 0-365 mW/cm² range*

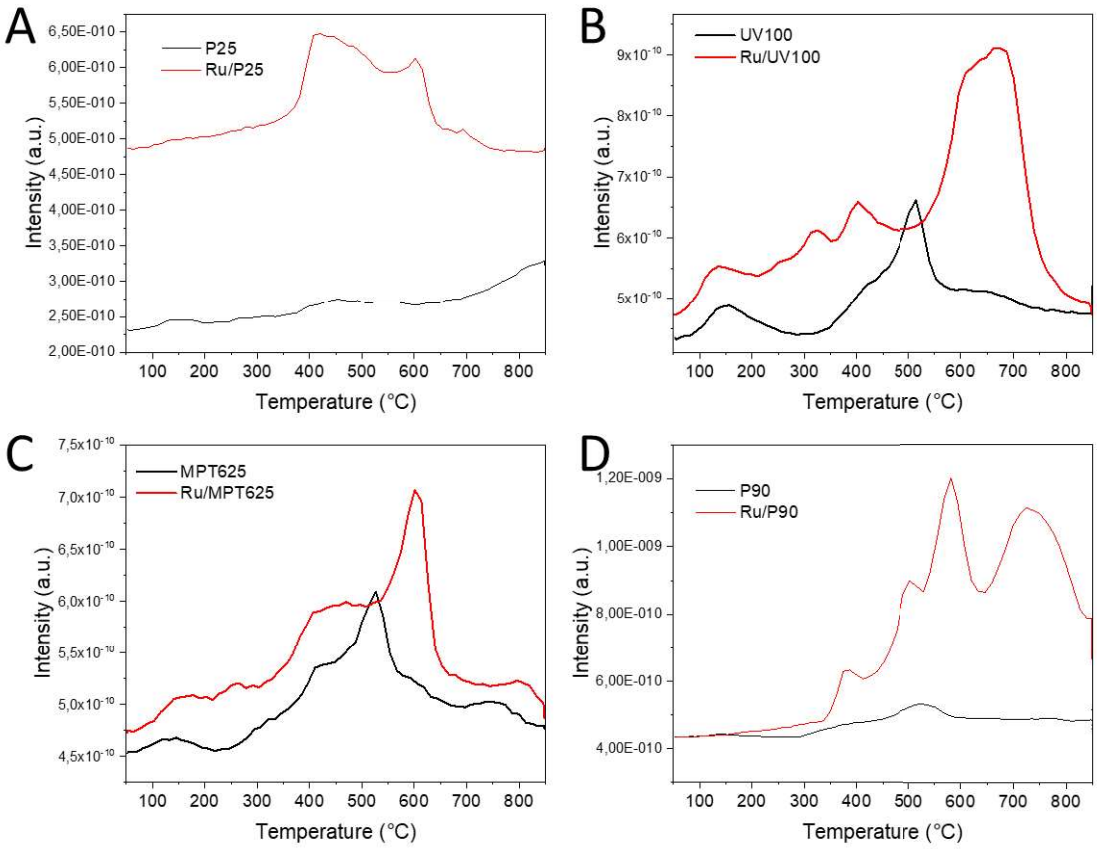

Fig. A 2 *CO_2-TPD graphs of the m/z=28 signal of bare TiO_2 supports (black) and supported Ru (red) on* ***A)****P25,* ***B)*** *UV100,* ***C)****MPT625 and* ***D)****P90.*

Résumé

1. Introduction

Au cours des dernières décennies, les questions environnementales et énergétiques ont suscité un intérêt croissant en raison du réchauffement de la planète et du changement climatique liés aux émissions de CO_2, ainsi que de l'épuisement des ressources fossiles. Par conséquent, l'industrie chimique et énergétique doit répondre à cette préoccupation sociétale en termes de durabilité des processus et doit opérer une transition environnementale et énergétique difficile, mais vitale, des ressources fossiles vers une économie chimique et énergétique durable et respectueuse de l'environnement. Cette politique vise à réduire la dépendance aux combustibles fossiles et à évoluer progressivement vers une économie neutre en carbone.

La catalyse hétérogène peut être considérée comme la science de la réduction des matériaux et de l'énergie en chimie. Elle joue un rôle central dans la recherche de voies durables et plus écologiques pour fournir de l'énergie (carburants) et produire des produits chimiques en réduisant l'empreinte environnementale et énergétique, avec une efficacité atomique maximale. La photocatalyse hétérogène est apparue au cours des dernières décennies comme une approche précieuse pour fournir des conditions de réaction durables afin de conduire sélectivement des réactions chimiques dans divers domaines liés à l'environnement ou à l'énergie.

Cependant, la photocatalyse hétérogène a démontré des taux de production ou de conversion plus faibles que la catalyse traditionnelle (thermique), ce qui est défavorable à son application dans un large éventail de domaines, et notamment pour l'industrie chimique. Néanmoins, la photocatalyse est un processus qui fonctionne à température ambiante et qui s'est révélé efficace dans des conditions plus durables que la catalyse (thermique). Ces dernières années, la stratégie consistant à combiner une double excitation photonique et thermique en une seule opération a émergé pour abaisser les conditions de température et améliorer la durabilité des processus, augmenter les taux de réaction et potentiellement orienter la sélectivité de la réaction. Cette approche a ouvert la porte à un nouveau domaine de la catalyse hétérogène, à savoir la catalyse photothermique.

La catalyse photothermique est donc un domaine émergent qui peut être considéré comme l'un des outils les plus prometteurs et durables pour réduire l'empreinte carbone dans l'industrie énergétique et chimique. Elle consiste en une activation photonique et thermique simultanée (lumière et chaleur) d'un catalyseur photosensible (c'est-à-dire sensible à la lumière). La plupart des systèmes reposent sur des matériaux semi-conducteurs, le plus souvent décorés de nanoparticules métalliques. Tout effet photothermique positif repose sur une synergie résultant potentiellement d'une activation combinée (double) du catalyseur qui a un impact sur le comportement (photo)catalytique et modifie la réaction catalytique à la surface.

Il existe trois possibilités différentes de combiner les sources d'énergie lumineuse et thermique :

- De source unique d'énergie photonique et thermique : La stratégie consiste à utiliser un source d'énergie unique qui peut fournir des énergies photonique et thermique (comme le soleil ou une source de lumière solaire simulée), comme le montre la Figure 1A. Les photons de haute énergie (UV-Vis) interagissent avec le catalyseur photo-thermique avec la promotion de « hot carriers », tandis que les photons de basse énergie (Vis-NIR) augmentent globalement la température à la surface catalytique. Dans ce cas, la température globale est contrôlée et limitée par la puissance optique et la dispersion de la source lumineuse (filtres, dispositifs monochromatiques, etc.). Néanmoins, l'optimisation de la conception du réacteur peut améliorer l'augmentation de la température, notamment grâce à des concentrateurs solaires adaptés.

- Des sources d'énergie photonique et thermique distinctes : Cette stratégie (voir Figure. 1B) est similaire à la précédente à l'exception du fait que globalement la température ne dépend pas de l'irradiation lumineuse mais peut être mieux ajustée par des processus de conduction et de convection depuis les parois du réacteur jusqu'à l'endroit où se trouve le catalyseur photo-thermique.

- Source de chaleur interne par irradiation par flux de photons (voir Figure. 1C) : Comme il a été décrit précédemment, certains matériaux peuvent augmenter la température locale par un processus de relaxation non-radiative après absorption du flux de photons. Dans ce cas, la source d'énergie thermique provient de l'interaction entre les matériaux et les photons. En cas d'irradiation photonique en régime permanent, un gradient thermique s'établit à la surface du catalyseur, qui dépend des propriétés thermiques (diffusion) du catalyseur et des réactifs. Pour assurer l'efficacité photo-thermique de la lumière à la chaleur, la plupart des matériaux de nanostructure plasmonique

ont été rapportés. Cependant, il est important de mentionner la capacité de plusieurs matériaux non plasmoniques à générer une augmentation de la température.

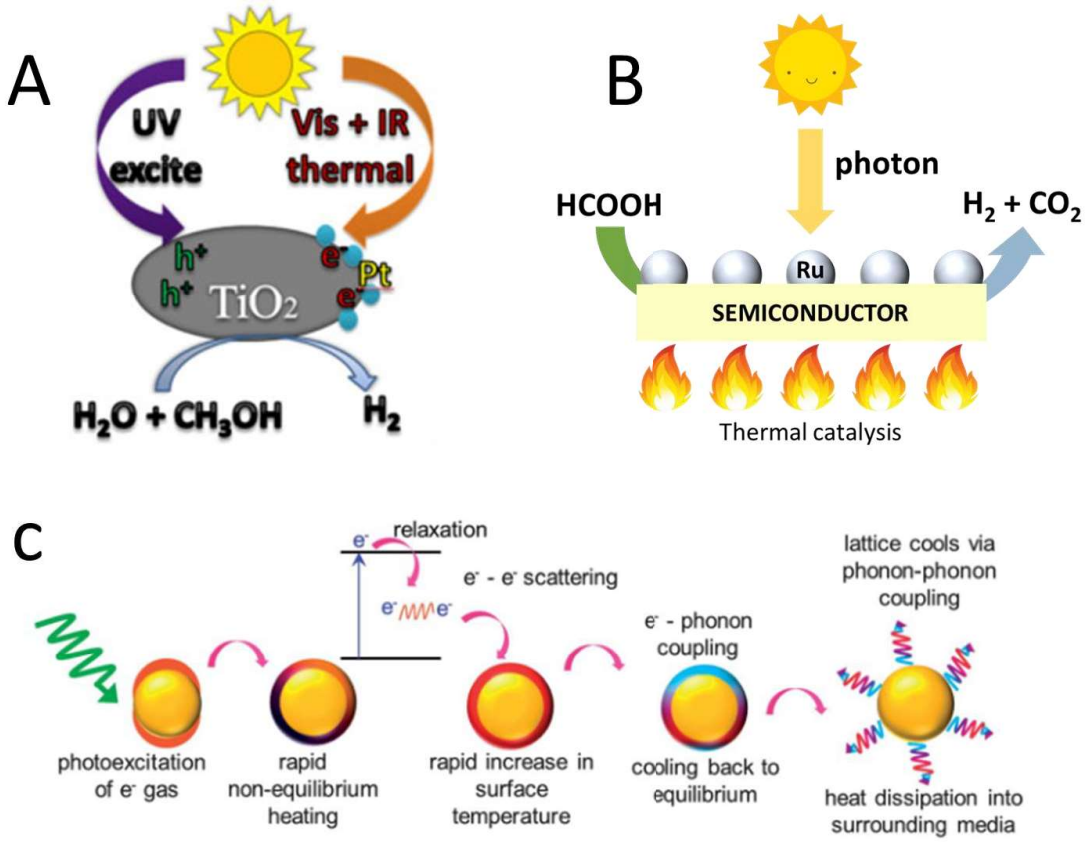

***Figure** 1(A) Première stratégie avec un fournisseur d'énergie photonique et thermique unique, **(B)** deuxième stratégie avec des fournisseurs d'énergie photonique et thermique distincts, et **(C)** troisième stratégie avec une source de chaleur interne par irradiation par flux de photons.*

Sur un métal dont la surface est propre, les électrons ne peuvent se retrouver qu'en se recombinant (Figure 2A).

Cette thermalisation est liée à la possibilité de recombinaison de l'électron dans le métal. Ainsi, si l'électron migre vers une orbitale moléculaire d'une espèce adsorbée (Figure 2B), il pourrait participer aux mécanismes électroniques des différentes réactions sur la surface du métal. Cependant, il peut aussi se recombiner dans le métal et augmenter la température.

La même chose pourrait se produire avec une hétérojonction d'un métal et d'un semi-conducteur (Figure 2C). Si le nouveau niveau d'énergie de l'électron excité est supérieur à la barrière Schottky créée à l'interface entre les deux matériaux, il peut être transféré dans la bande de conduction. De manière similaire à celle précédemment décrite. L'électron peut être retransféré au métal.

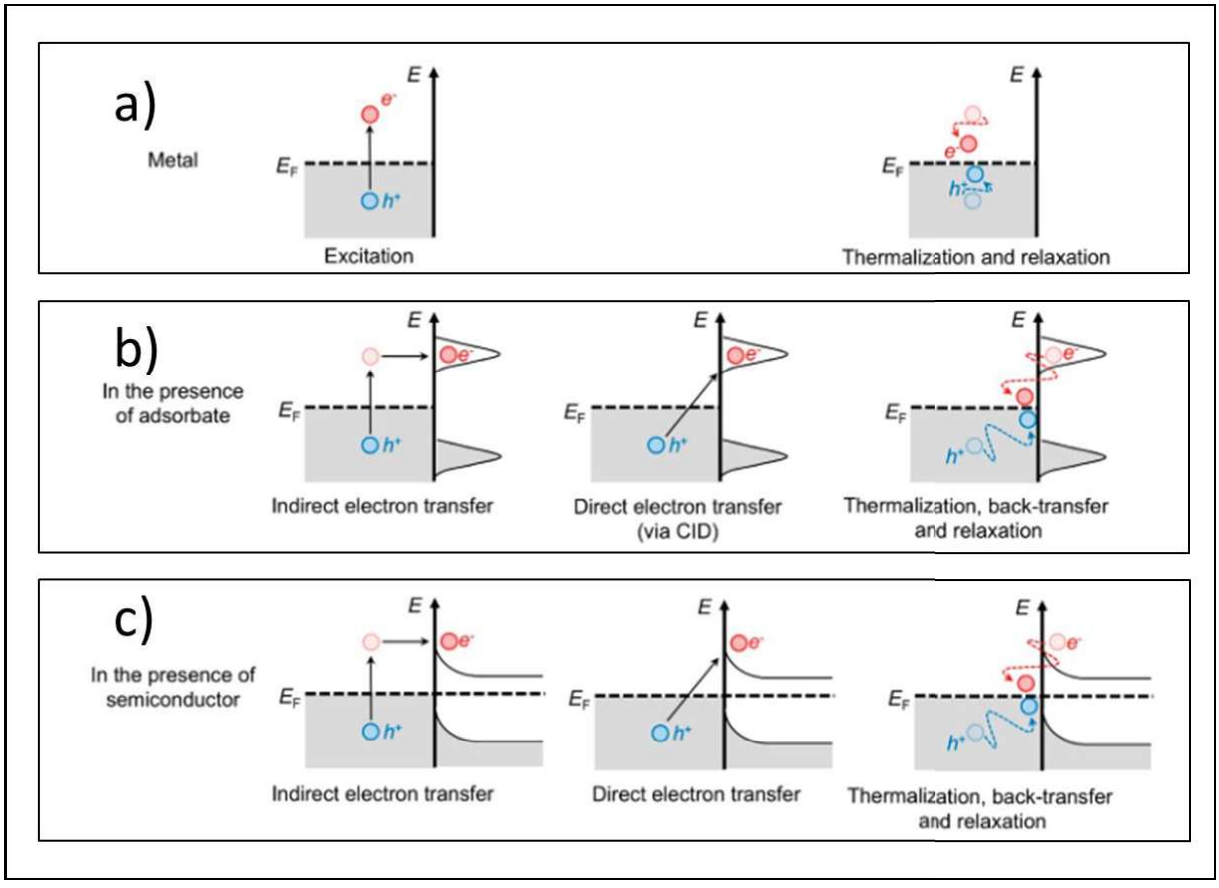

Figure 2 *Génération de « hot carriers » via le processus induit par les plasmons et processus de transfert/rétrotransfert d'électrons et de trous chauds dans différents scénarios.*

A) *métal propre,*

B) *métal/adsorbat,*

C) *métal/semi-conducteur.*

Dans chaque schéma, le côté gauche (par rapport à l'énergie, axe des y) représente le niveau de Fermi (E_F) du métal plasmonique. Le côté droit (par rapport à l'énergie, axe des y) illustre l'orbitale moléculaire la plus occupée (HOMO) et l'orbitale moléculaire inoccupée la plus basse (LUMO) pour l'adsorbat (b), ou la position des bandes de conduction et de valence du semi-conducteur. Les parties grises représentent la population d'états électroniques.

La catalyse photo-thermique est apparue comme un procédé prometteur pour réduire la consommation d'énergie afin d'effectuer une conversion chimique sans perte d'efficacité et de sélectivité. L'intérêt croissant des chercheurs du domaine consolide sa position de sujet brûlant au cours des dernières années. Cependant, un long chemin reste à parcourir pour développer tous les avantages de ce nouveau domaine dans les applications thermochimiques et photochimiques classiques. Dans ce but, nous avons sélectionné deux réactions différentes d'intérêt dans le domaine chimique où les processus assistés par la lumière peuvent être bénéfiques: La décomposition de l'acide formique et la methanation du CO_2.

L'acide formique est abondant dans les produits dérivés de la biomasse et constitue un vecteur d'hydrogène prometteur et renouvelable pour le stockage de l'hydrogène et comme source d'hydrogène interne (donneur d'hydrogène) pour effectuer des réactions d'hydrogénation par transfert catalytique. L'utilisation de l'hydrogène en tant que combustible énergétique présente des avantages bien connus, tels qu'une combustion à haute énergie avec zéro émission de carbone après la combustion (seulement H_2O comme sous-produit). Cependant, ses principales limites sont associées au stockage et au processus de livraison. C'est alors que l'acide formique, un dérivé du glucose issu de la chaîne de conversion hydrolytique de la biomasse lignocellulosique, a suscité l'intérêt car, contrairement à l'hydrogène, il est approprié pour le stockage et le transport. Il a une teneur volumétrique élevée en hydrogène dans des conditions ambiantes, à savoir 53 gH_2/L et l'H_2 peut être produit par une réaction de déshydrogénation/décarboxylation (1). Son application alternative en tant qu'approche médiée par un donneur d'hydrogène au lieu d'utiliser de l'hydrogène externe sous pression est un pas en avant dans la conception de procédés d'hydrogénation durables permettant la production de produits chimiques à haute valeur ajoutée. Néanmoins, l'acide formique peut aussi se décomposer en monoxyde de carbone et en eau par déshydratation/décarbonylation (2).

$$HCOOH \rightarrow CO_2 + H_2 \quad (1)$$

$$HCOOH \rightarrow CO + H_2O \quad (2)$$

L'absence de production d'hydrogène moléculaire et la présence de composés qui empoisonnent les catalyseurs tels que le CO par le processus de déshydratation rendent nécessaire la conception d'une voie catalytique qui inhibe cette réaction et favorise celle de la déshydrogénation.

La methanation du CO_2 (3) est un processus catalytique très difficile dans le cadre des progrès actuels de la chimie. L'hydrogénation du CO_2 pour produire du méthane, également appelée réaction de Sabatier, est une réaction exothermique spontanée qui convertit le CO_2 en un combustible gazeux précieux, le gaz naturel synthétique (GNS), bien qu'au prix d'une consommation élevée de H_2 renouvelable. Néanmoins, le seuil thermodynamique ne permet pas de réaliser la conversion du dioxyde de carbone à des températures élevées, et l'intensification du processus est par conséquent nécessaire.

$$CO_2 + 4H_2 \rightarrow CH_4 + 2H_2O \quad (3)$$

Un catalyseur photo-thermique doit contenir au moins un matériau ou un composant photo-réactif. Pour les deux réactions d'intérêt qui ont été décrites dans la section précédente, les nanostructures des métaux du groupe VIII ont été signalées comme étant des catalyseurs utiles dans des conditions d'obscurité et d'éclairage. En revanche, une grande variété de supports a été utilisée, allant des supports classiques d'oxyde métallique en vrac aux structures 2D ou aux matériaux à base de carbone.

Le ruthenium est un catalyseur métallique de choix pour plusieurs réactions (exemples), dont les deux réactions d'intérêt sélectionnées, à savoir la décomposition de l'acide formique et la méthanation du CO_2. Les catalyseurs à base de ruthénium semblent convenir à des applications photothermiques telles que l'hydrogénation du CO_2 ou la valorisation de la biomasse, avec la conversion de microcristallin.

En ce qui concerne le support, le dioxyde de titane, TiO_2, est un support d'intérêt en catalyse thermique pour plusieurs types de réactions. Il a été étudié au cours des dernières décennies pour une grande variété d'applications, en particulier dans le domaine de la photocatalyse avec une activation UV-A en raison de ses propriétés photoélectroniques en tant que matériau semi-conducteur. Néanmoins, le TiO_2 est un support d'intérêt en catalyse thermique pour plusieurs types de réactions telles que les réactions d'oxydation, les réactions de déshydrogénation ou encore les applications industrielles.

2. Objectifs

Les principaux objectifs de cette thèse étaient d'abord de démontrer la capacité des catalyseurs à base de Ru à être utilisés comme catalyseurs photothermiques sous lumière UV-A pour deux réactions d'intérêt en phase gazeuse, à savoir la déshydrogénation de l'acide formique pour former de l'hydrogène comme réaction principale et ensuite l'hydrogénation/méthanation du CO_2 (réaction de Sabatier). Nous avons donc cherché à obtenir la preuve d'un effet photothermique bénéfique sous lumière UV-A pour les deux réactions, et à mieux comprendre dans quelle mesure les propriétés des catalyseurs Ru supportés peuvent influencer le comportement photothermique et les mécanismes réactionnels associés qui ont lieu sous excitation photonique et thermique combinée. Notre objectif était d'ouvrir la voie à d'autres études et au développement de nouveaux catalyseurs photothermiques.

3. Discussion des résultats

Étant donné les excellentes propriétés électroniques du dioxyde de titane. Une méthode de synthèse alternative a été employée. Cette méthode photo-assistée est basée sur la décomposition et la réduction du précurseur métallique par les porteurs chauds générés par le TiO_2 sous irradiation de lumière ultraviolette. Après deux heures de photo-irradiation, le précurseur métallique $RuCl_3xH_2O$ a été décomposé et réduit en particules de ruthénium métallique à la main, comme le certifient la microscopie électronique (MET) et la photospectroscopie aux rayons X (PSX), avec la charge de ruthénium souhaitée (0,46 % contre 0,5 % idéal).

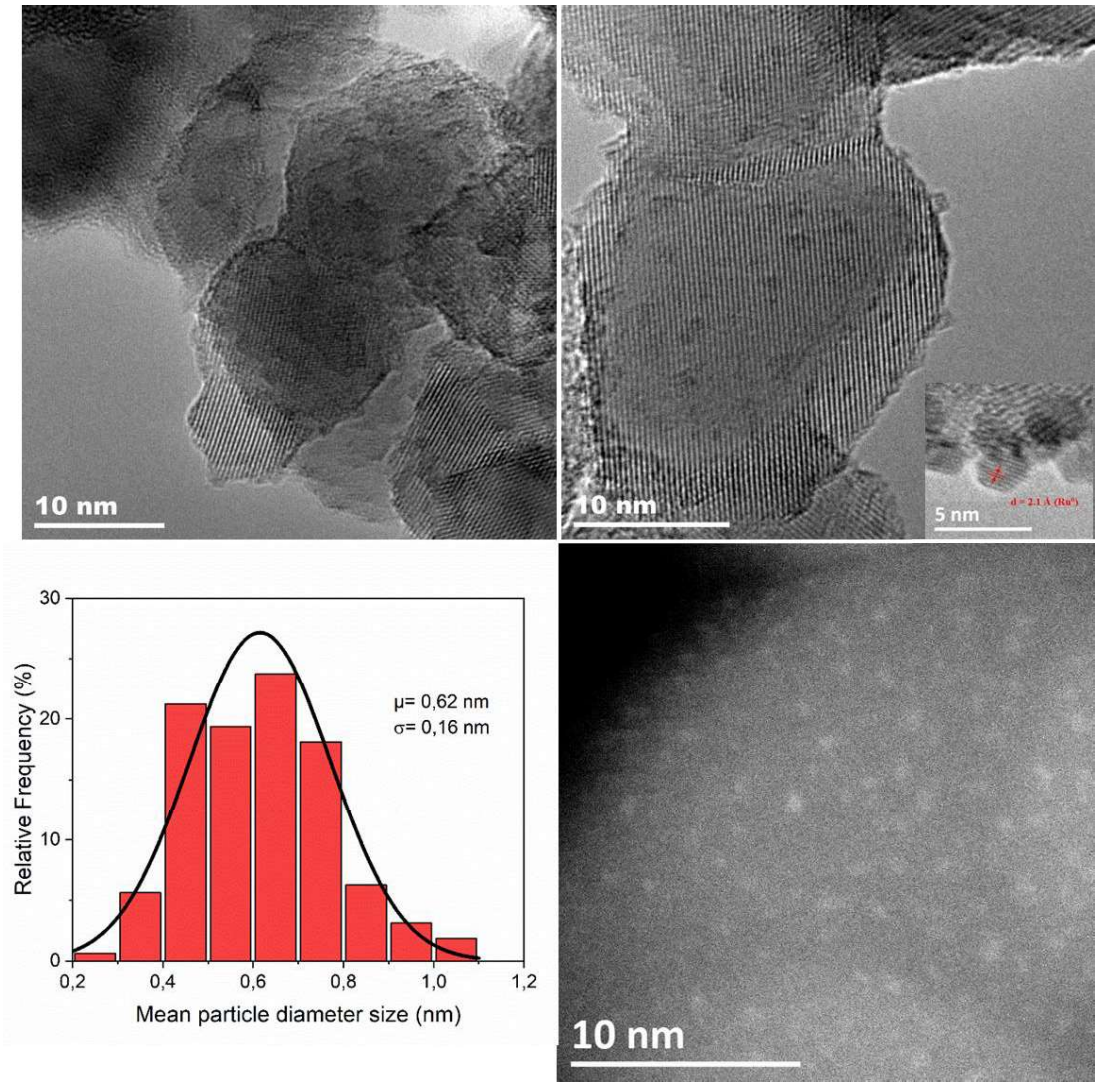

Figure 3 *Analyse MET du catalyseur de référence Ru(0,5 %)/TiO_2 (PA). En haut : Images METRH. En bas : histogramme de la distribution de la taille des particules de ruthénium et image METB.*

La première preuve de l'existence d'une double excitation photo/thermique a été apportée sur le catalyseur Ru(0.5%)TiO_2 PA pour la décomposition de l'acide formique (Figure 4). Dans ce cas, l'influence de la lumière a entraîné une conversion de l'acide formique à des températures plus basses que dans des conditions sombres. En outre, les valeurs de température pour la production d'hydrogène ont été abaissées. De plus, les graphiques en fonction de la température ont démontré que l'on n'obtenait pas seulement un déplacement à basse température. À des températures similaires à celles des conditions d'obscurité, la conversion de l'acide formique et la production d'hydrogène ont augmenté dans des conditions de lumière. Le test d'irradiation de la lumière a

prouvé que la production d'H_2 et la décomposition de l'acide formique sont proportionnelles au flux de photons.

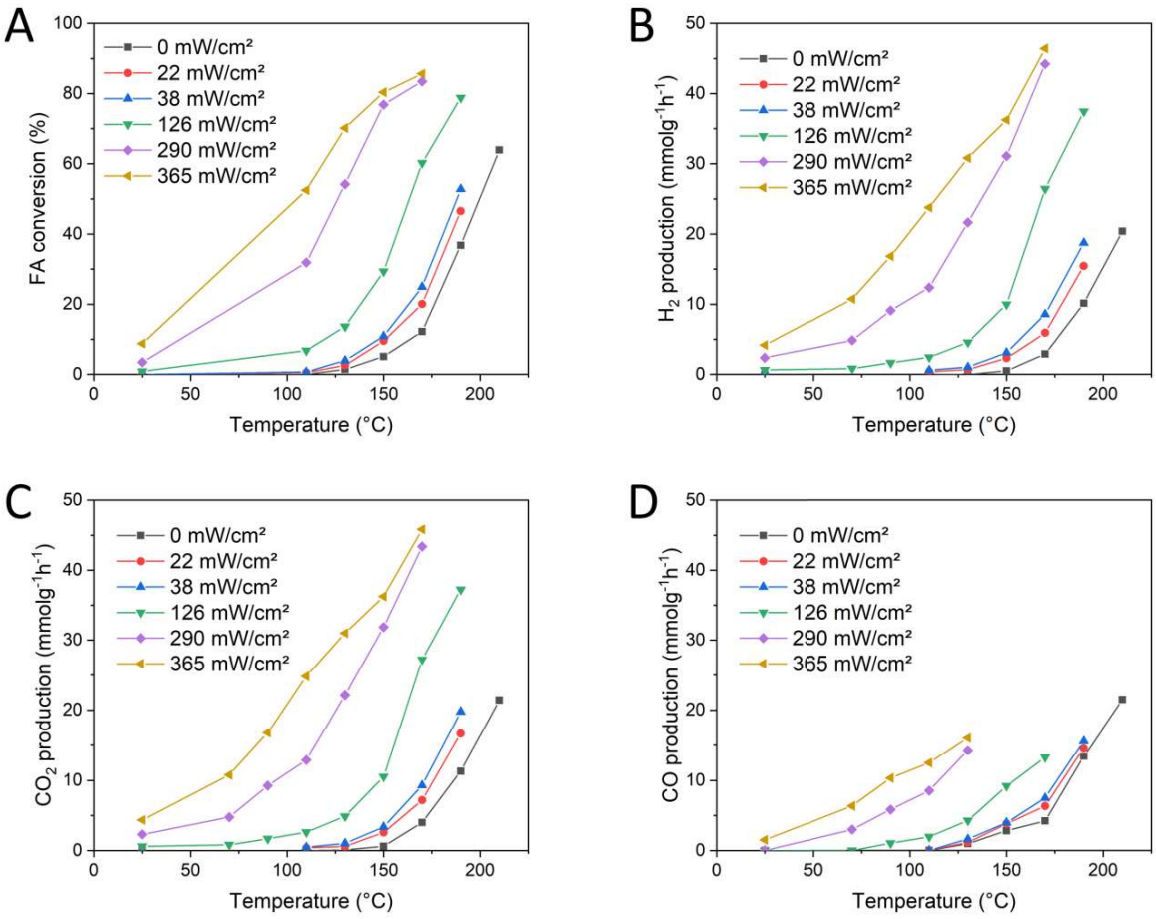

***Figure 4 A**)Conversion de l'AF, **B)** production de l'hydrogene, **C)** production du CO_2 et **D)** production du CO sur Ru(0.5%)TiO_2 PA.*

Comme l'acide formique peut également être décomposé en produits de déshydratation, les paramètres de sélectivité peuvent être affectés. En fait, il y a une influence positive vers les produits de déshydrogénation par l'irradiation lumineuse et la température. Pour déterminer comment le produit CO est produit, TiO_2 a été testé comme catalyseur photothermique pour la décomposition de l'AF dans des conditions similaires à celles du catalyseur de référence. Dans ce cas, l'AF a été converti avec succès mais en produits de déshydratation sans aucune trace de H_2. Des études complémentaires ont démontré (non présentées dans ce résumé) que FA seulement peut être décomposé en CO et H_2O sur la surface de TiO_2.

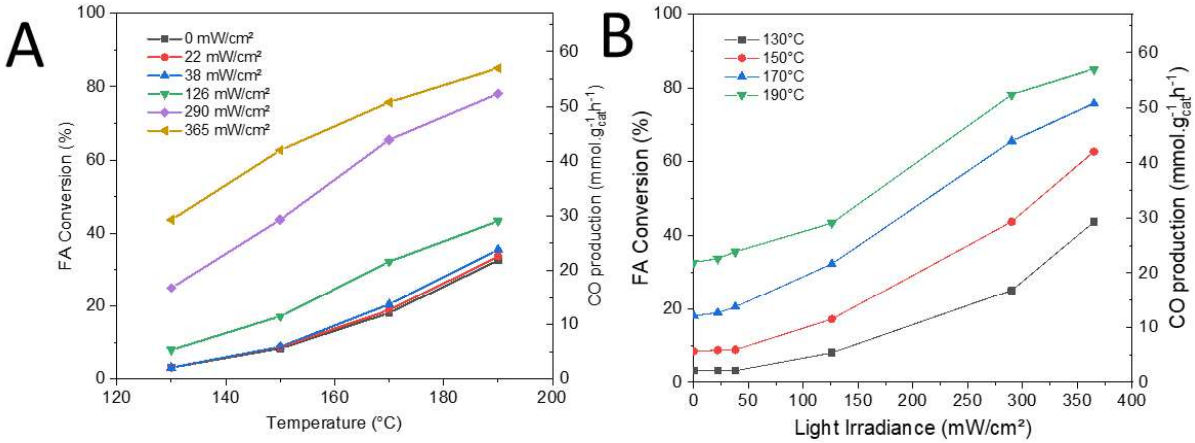

Figure 5 *Conversion de l'AF et production de CO par* ***A)*** *température et* ***B)*** *lumière sur TiO_2.*

D'autres catalyseurs Ru/TiO_2 ont été testés avec différentes propriétés telles que la charge en Ru, la taille des nanoparticules, l'interaction métal/support. Cependant, la production de CO n'a pas été affectée par ces changements dans les catalyseurs. Ceci est une conséquence claire de l'emploi du matériau TiO_2 comme support.

Dans ce cas, le fait qu'il y ait différentes valeurs de sélectivité pour la décomposition des AF est dû au fait qu'il y a deux processus parallèles pendant la décomposition. L'un est réalisé par le ruthénium qui produit de l'hydrogène et l'autre par le TiO_2 qui génère du CO. Par conséquent, un autre support doit être utilisé pour la décomposition photothermique des AF.

Les supports alternatifs sont SiO_2 et g-C_3N_4. SiO_2 est un matériau d'oxyde métallique comme TiO_2, largement rapporté comme support de catalyseur dans la catalyse thermique. Cependant, le SiO_2 présente des propriétés isolantes.

Le g-C_3N_4 est un photocatalyseur largement utilisé et un support prometteur pour la catalyse thermique. Avec une bande interdite de 2,7 eV, il peut promouvoir les porteurs chauds sous irradiation de lumière UV-Vis. Par conséquent, la méthode photo-assistée peut être utilisée pour développer des catalyseurs $Ru/g\text{-}C_3N_4$. Dans le cas de Ru/SiO_2, la méthode classique d'imprégnation humide a été utilisée.

L'image suivante (Figure 6) compare les résultats de ces deux catalyseurs alternatifs avec ceux obtenus avec le catalyseur de référence. Dans ce cas, l'utilisation d'un matériau isolant comme support n'a pas d'influence négative sur la décomposition de l'acide formique. Cela signifie que le

ruthénium est la partie active du matériau qui absorbe l'énergie des photons. Cette énergie favorise les « hot carriers » dans le métal qui sont impliqués dans les processus électriques et thermiques.

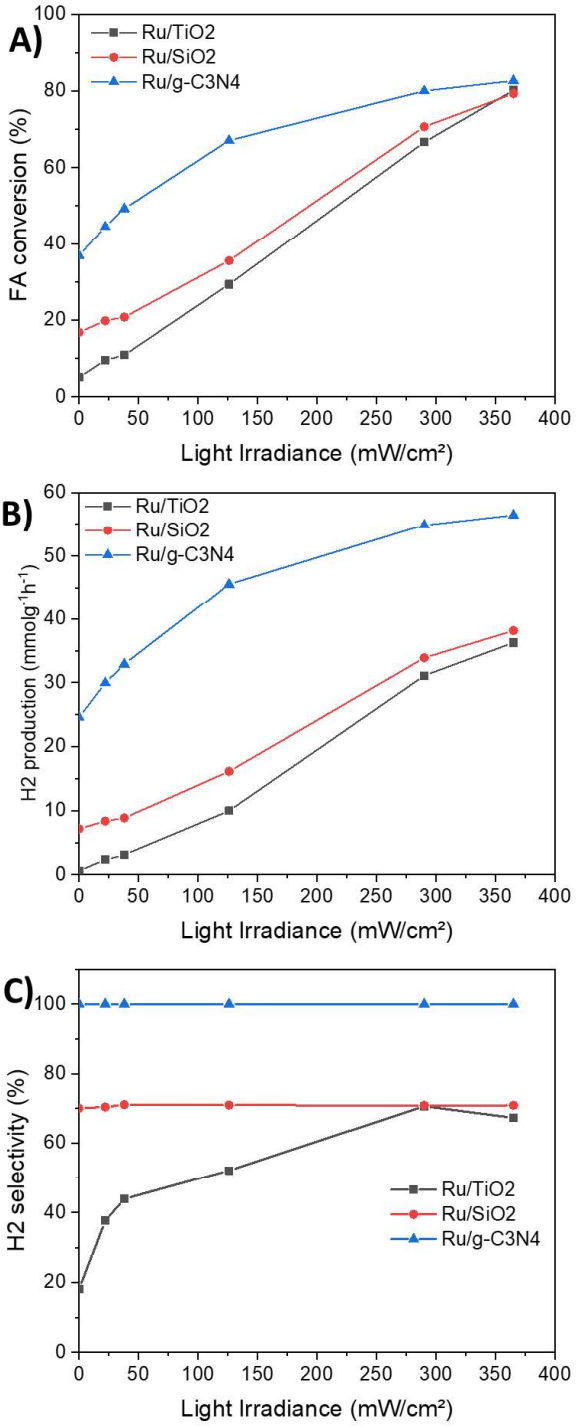

***Figure 6**. Résultats de la décomposition de l'acide formique à 150 °C ou A) est la conversion de l'AF, B) est la production de l'hydrogène et C) la sélectivité sur les trois catalyseurs.*

En outre, le catalyseur Ru/g-C_3N_4 a montré une production efficace d'hydrogène sur sa surface (Figure 6B). Les valeurs de sélectivité recueillies certifient une conversion totale de l'acide formique en produits de déshydrogénation. D'autre part, les valeurs de sélectivité lors de la décomposition de FA (Figure 6C) sur Ru/SiO_2 sont de l'ordre de 70% pour la production d'hydrogène. Ces valeurs ne varient pas en fonction de l'irradiance UV-A. Cela signifie que ce n'est que dans le cas de Ru/TiO_2 que ces valeurs sont favorisées par les conditions de lumière.

La spectroscopie DRIFTS in-situ a été utilisée pour analyser les différentes espèces obtenues lors de la décomposition de l'acide formique sur les trois types de catalyseurs. En regardant de Ru/TiO_2, on peut observer qu'il existe des bandes d'absorption qui n'apparaissent que dans des conditions de lumière (en bleu), que nous avons associées à des processus réalisés par des mécanismes électroniques. Ces bandes sont appelées bandes lumineuses. Cependant, d'autres bandes apparaissent également dans l'obscurité et sont favorisées par l'irradiation de la lumière ultraviolette (en rouge). Ces bandes peuvent être attribuées à des processus thermiques où les « hot carriers » se *thermalisent* en augmentant localement la température de surface. Ces bandes sont appelées "bandes thermiques".

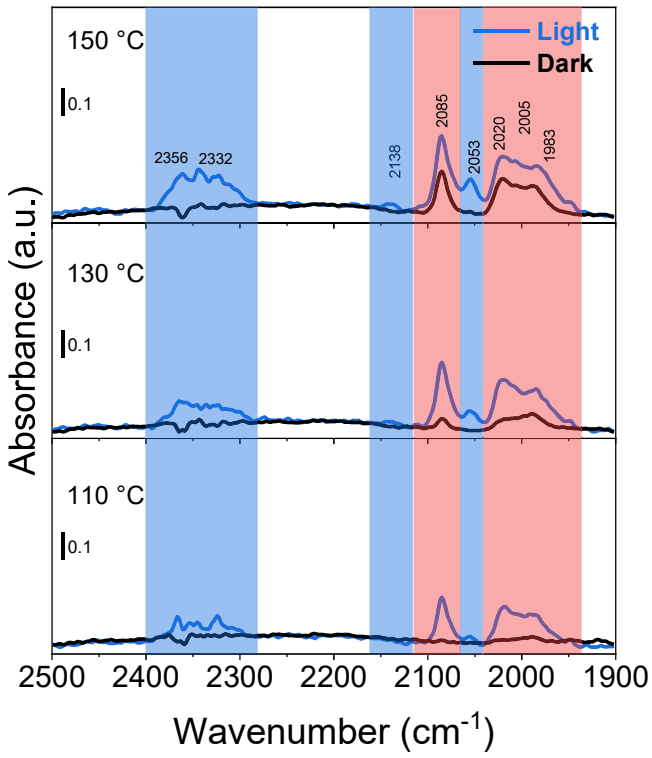

***Figure 7**. Spectrogrammes DRIFT in-situ pendant la décomposition de l'acide formique sur Ru/TiO_2 dans des conditions sombres (noir) et lumière (bleu).*

Dans le cas de Ru/SiO_2 et $Ru/g\text{-}C_3N_4$ (non présenté dans ce résumé) on peut voir que la situation est similaire au catalyseur de référence pour Ru/SiO_2. Cependant, $Ru/g\text{-}C_3N_4$ ne présente pas de bandes lumineuses. Cela pourrait être l'indication d'un processus clair dominé par des mécanismes thermiques grâce à l'irradiation par l'ultraviolet A.

Dans le cas de la methanation du CO_2, Ru/TiO_2 est toujours utilisé comme catalyseur de référence bien que la charge en ruthénium ait été multipliée par 10 pour assurer une efficacité catalytique élevée.

Malgré l'augmentation du précurseur pendant la synthèse, une synthèse efficace de nanoparticules de ruthénium sur la surface de l'oxyde métallique a pu être certifiée.

Les résultats en termes de production de méthane avec les autres catalyseurs basés sur d'autres supports sont présentés dans l'image suivante. Les données montrent une conversion effective du CO_2 en méthane beaucoup plus élevée sur Ru/TiO_2 que sur Ru/SiO_2 et Ru/gC_3N_4. Cette grande différence entre les catalyseurs peut être basée sur le matériau de support utilisé. Toutefois, il convient d'examiner de plus près les propriétés du titane qui en font le catalyseur le plus efficace dans des conditions de lumière et d'obscurité.

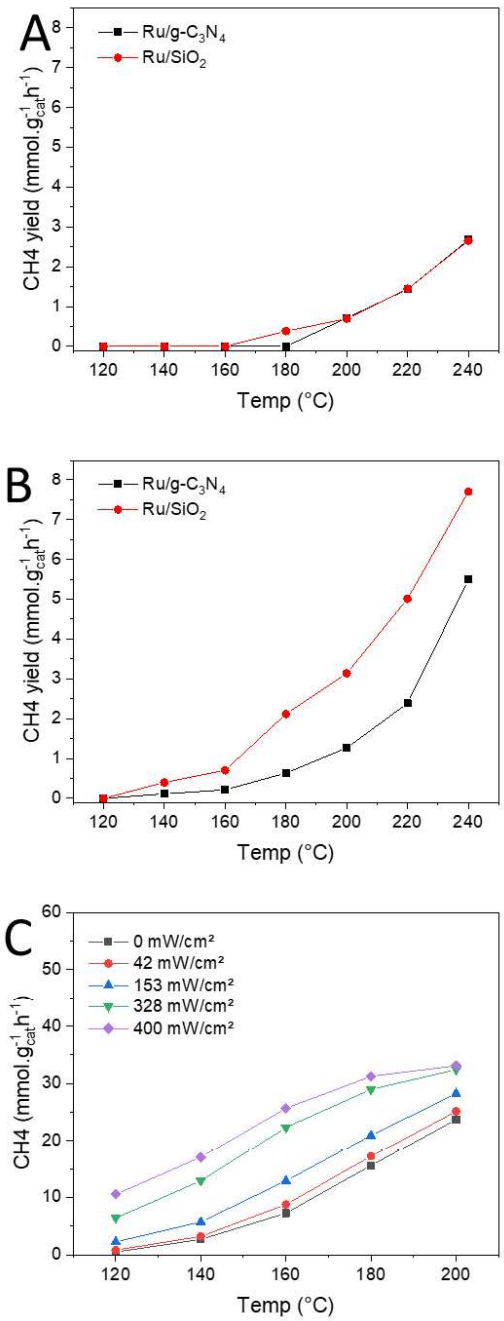

***Figure 8**. Résultats de la méthanisation du CO_2 sur des catalyseurs alternatifs où **A)** est dans des conditions sombres et **B)** sous lumière UV (I=400 mW/cm²). **C)** correspond aux valeurs du méthane sur Ru/TiO_2 à différentes irradiances.*

Pour le cas suivant, différents matériaux commerciaux à base de titane ont été utilisés. Parmi eux, il existe de nombreuses différences en termes de propriétés : phases cristallines, surface spécifique, etc. Les données sur les propriétés les plus importantes sont indiquées dans le tableau suivant :

TiO_2	Bandgap (eV)	Anatase:Rutile	Phase amorphe [%]	Taille moyenne des cristallites [nm]	SSA (m^2/g)
P25	3.2	80:20	7	32 (A) : 22 (R)	56
UV100	3.2(5)	100:0	26	9 (A)	330
MPT-625	3.0	0:100	10	10 (R)	103
P90	3.2	90:10	29	13 (A) : 23 (R)	90

Tableau 1 *Principales propriétés physico-chimiques du TiO2 utilisé comme support des nanoparticules de Ru.*

Puisque ces matériaux, comme le P25, absorbent la lumière ultraviolette à la longueur d'onde. La méthode photo-assistée a été utilisée pour la synthèse de nanoparticules de ruthénium sur les différents supports. Les résultats sur la base de la production de méthane certifient que les propriétés du titane ont une forte influence sur la méthanisation en termes de conditions de température. Par exemple, le Ru supporté sur anatase est le catalyseur le plus efficace à toutes les basses températures. Cependant, le Ru/UV100 perd sa dominance avec l'augmentation de la température. D'autre part, le catalyseur Ru supporté par MPT625, qui est du rutile pur, est le plus efficace aux températures les plus élevées, suivi par Ru/P25 qui est le second supporté par le rutile.

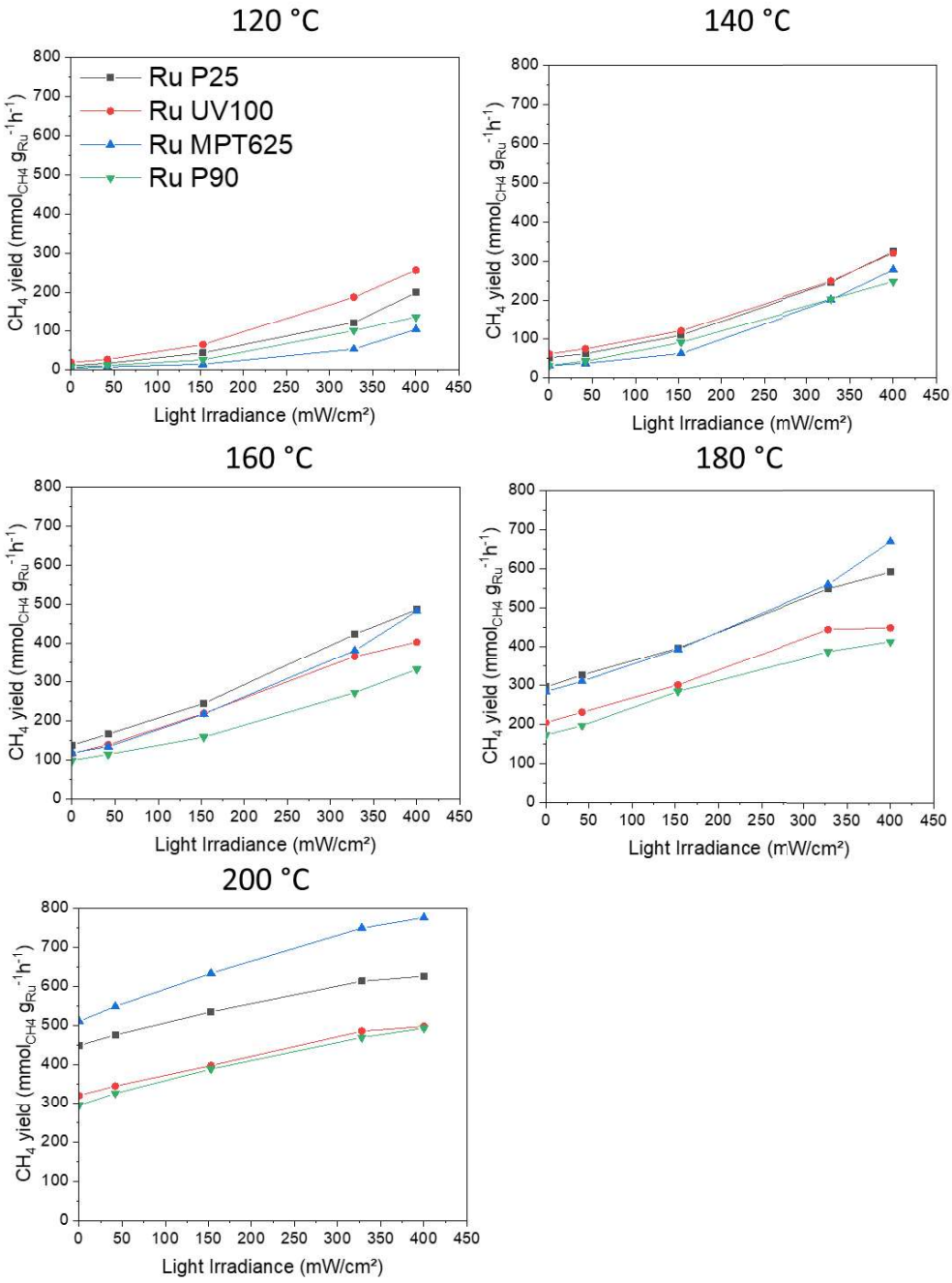

Figure 9. *Influence de l'irradiation lumineuse sur le rendement en méthane obtenu sur les Ru/P25 (noir), Ru/UV100 (rouge), Ru/MPT625 (bleu) et Ru/P90 (vert) de 120°C à 200°C.*

Dans ce cas, les phases cristallines du support jouent un rôle très important en termes de production de méthane à la surface des catalyseurs. D'autres études telles que la spectroscopie infrarouge ont corroboré le fait que, bien que tous les catalyseurs utilisés soient des Ru/TiO_2, les intermédiaires créés à la surface du catalyseur pendant l'hydrogénation du CO_2 et leur concentration varient en fonction du matériau.

4. Conclusions

Tout d'abord, Ru/TiO_2 a été considéré comme un catalyseur de référence sous lumière UV-A. Les principales conclusions sont les suivantes

- il a été prouvé que la combinaison (double) excitation photonique/thermique du catalyseur Ru/TiO_2 stimule la décomposition de l'acide formique gazeux vers la déshydrogénation sous irradiation de lumière UV-A, avec une augmentation significative du rendement en hydrogène.

- Il abaisse la température de décomposition de l'acide formique, augmente le taux de production de H2 ainsi que la sélectivité vers la déshydrogénation, grâce à des mécanismes différenciés (renforcés par la lumière) pour les productions de H_2 et de CO.

- Il a été démontré que le ru est lié à la production de H_2, avec une teneur optimale de 0.5 % en poids.

- TiO_2 agissant comme catalyseur photothermique sélectif pour la réaction de déshydratation, le support TiO_2 lui-même est une limitation intrinsèque pour les performances photothermiques.

Différentes méthodologies ont été utilisées pour accéder aux mécanismes possibles induits par la lumière, par exemple des expériences de dépendance aux photons, l'évaluation de l'énergie d'activation apparente ou la spectroscopie DRIFT in situ :

- les spectres de spectroscopie DRIFT in situ dans des conditions photothermiques ont confirmé les caractéristiques d'amélioration attribuées au support TiO2 nu lui-même et aux nanoparticules de Ru supportées, pour les réactions de déshydratation et de déshydrogénation.

- Elle montre que le Ru peut être lié différemment aux espèces de carbone dans des conditions de lumière et d'obscurité, avec de nouvelles bandes attribuées aux liaisons Ruthénium-carbonyle dans des conditions d'éclairage, ce qui suggère un nouveau mécanisme piloté par les électrons sous lumière UV-A, en plus d'un mécanisme piloté par la chaleur (thermalisation).

- Les expériences de dépendance aux photons et la détermination de l'énergie d'activation apparente ont soutenu l'hypothèse de processus dominants dirigés par les électrons par rapport à la thermalisation.

Deuxièmement, nous avons cherché à étudier dans quelle mesure les performances et l'effet d'amélioration photothermique pouvaient être influencés et améliorés par le choix d'autres matériaux de support. Dans cette partie de la thèse, les principales conclusions sont les suivantes :

- un effet photothermique positif a été obtenu à la fois sur les catalyseurs Ru/g-C_3N_4 et Ru/SiO_2, permettant d'augmenter le taux de production de H_2 dans des conditions de lumière UV-A par rapport à des conditions sombres, et d'abaisser la température tout en maintenant un taux de production de H_2 similaire.

- le SiO_2 isolant peut être utilisé comme support dans la catalyse photothermique, l'amélioration étant montrée comme reposant uniquement sur l'activation des nanoparticules de Ru, avec formation de H_2 et de CO.

- nous avons démontré que Ru/g-C3N4 sont des catalyseurs photothermiques remarquables qui surpassent les catalyseurs de référence Ru/TiO2 en termes de production de H2 et avec une sélectivité de 100% sur toute la gamme de température et d'irradiation. Une teneur optimale en Ru de 0,5 % en poids a été observée.

- les caractéristiques de la surface g-C_3N_4 ont permis de surmonter la limitation intrinsèque du semi-conducteur TiO_2.

- Contrairement à Ru/TiO_2, les spectres DRIFT in situ sur Ru/SiO_2 suggèrent la possibilité d'un mécanisme piloté par les électrons sous irradiation lumineuse en plus de la catalyse thermique pure. Nous avons suggéré un mécanisme de thermalisation pour les porteurs chauds sur Ru/g-C_3N_4.

Troisièmement, nous avons voulu montrer dans une étude préliminaire la capacité des systèmes supportés à base de Ru à être également utilisés comme catalyseurs photothermiques sous UV-A dans une autre réaction d'intérêt, l'hydrogénation photothermique du CO_2 en méthane. Dans cette partie de la thèse, les principales conclusions sont :

- Les catalyseurs à base de Ru avec une teneur de 5 % en poids peuvent également être utilisés efficacement pour l'hydrogénation du CO_2 en méthane en utilisant H_2 comme réactif réducteur dans des conditions photothermiques avec une sélectivité de 100 %. L'irradiation par la lumière UV-A a

favorisé des rendements en méthane fortement plus élevés que dans des conditions sombres dans le cas des catalyseurs Ru/TiO_2, qui surpassent tous les catalyseurs étudiés.

- Les performances sous lumière étaient moins intéressantes sur le catalyseur Ru/SiO_2, et de loin les pires sur le catalyseur $Ru/g\text{-}C_3N_4$, bien qu'une amélioration photothermique ait été observée pour tous les catalyseurs.

- Différents mécanismes induits par la lumière ont été suggérés en fonction de la nature du support, liés à l'évolution de l'énergie d'activation apparente.

- Les résultats ont montré que la nature du support TiO_2 utilisé a influencé la photo, bien qu'une amélioration photothermique ait été observée indépendamment du support TiO_2 utilisé.

- La phase anatase a montré de bons résultats dans des conditions de basse température. Cependant, le rendement en méthane le plus élevé avec la température a été obtenu avec le ruthénium supporté par la phase rutile. Plusieurs facteurs tels que l'interaction métal/support, le débordement d'hydrogène ou l'activation du CO_2 ont une incidence sur ces résultats.

Résumé

Ce travail se concentre sur l'étude des matériaux à base de ruthénium pour une utilisation en catalyse photothermique. À cette fin, différentes expériences ont été réalisées, depuis leur méthode de synthèse jusqu'à leurs applications pour l'obtention d'hydrogène ou la conversion du CO_2 via methanation. L'étude des différents matériaux, dans différentes conditions et sur différentes réactions montre que l'effet photothermique, principalement dû au ruthénium, peut contribuer à une amélioration des propriétés catalytiques. Les résultats montrent une orientation de la sélectivité vers les réactions souhaitées tout en augmentant l'activité catalytique à des températures plus basses grâce à l'irradiation lumineuse. Ce travail ouvre la voie à l'utilisation de catalyseurs photothermiques pour des processus plus durables dans le secteur énergétique et industriel.

Mot clés : Ruthénium, catalyse, photothermique, hydrogène, méthane, dioxyde du carbone, hydrogénation, methanation, acide formique

Résumé en anglais

This work is centered on the study of ruthenium-based catalysts for their use in photothermal catalysis. For this purpose, different experiments have been elaborated focusing from their synthesis method to their applications for obtaining hydrogen or CO_2 conversion via methanation. The study of the different materials, under different conditions and on different reactions shows that the photothermal effect, mainly generated by ruthenium, can contribute to an improvement of the catalytic properties. The results affirm a direction of selectivity to the desired reactions while increasing the catalytic activity at lower temperatures thanks to light irradiation. This work opens up the use of photothermal catalysts for more sustainable processes in the energy and industrial sectors.

Keywords: Ruthenium, catalysis, photothermal, hydrogen, methane, carbon dioxide, hydrogenation, methanation, formic acid